



HAL
open science

Grain motion and packing: application to metallic alloy solidification

Antonio Olmedilla González de Mendoza

► **To cite this version:**

Antonio Olmedilla González de Mendoza. Grain motion and packing: application to metallic alloy solidification. Materials. Université de Lorraine, 2017. English. NNT: 2017LORR0265. tel-01822597

HAL Id: tel-01822597

<https://theses.hal.science/tel-01822597>

Submitted on 25 Jun 2018

HAL is a multi-disciplinary open access archive for the deposit and dissemination of scientific research documents, whether they are published or not. The documents may come from teaching and research institutions in France or abroad, or from public or private research centers.

L'archive ouverte pluridisciplinaire **HAL**, est destinée au dépôt et à la diffusion de documents scientifiques de niveau recherche, publiés ou non, émanant des établissements d'enseignement et de recherche français ou étrangers, des laboratoires publics ou privés.



AVERTISSEMENT

Ce document est le fruit d'un long travail approuvé par le jury de soutenance et mis à disposition de l'ensemble de la communauté universitaire élargie.

Il est soumis à la propriété intellectuelle de l'auteur. Ceci implique une obligation de citation et de référencement lors de l'utilisation de ce document.

D'autre part, toute contrefaçon, plagiat, reproduction illicite encourt une poursuite pénale.

Contact : ddoc-theses-contact@univ-lorraine.fr

LIENS

Code de la Propriété Intellectuelle. articles L 122. 4

Code de la Propriété Intellectuelle. articles L 335.2- L 335.10

http://www.cfcopies.com/V2/leg/leg_droi.php

<http://www.culture.gouv.fr/culture/infos-pratiques/droits/protection.htm>

Grain motion and packing: application to metallic alloy solidification

THÈSE

Pour l'obtention du titre de :

DOCTEUR de L'UNIVERSITÉ DE LORRAINE

Sciences des Matériaux

Science et Ingénierie des Matériaux et Métallurgie

Présentée par :

Antonio Olmedilla González de Mendoza

11 Décembre 2017

<i>Rapporteurs :</i>	M. Andreas Ludwig	Professeur des universités Montanuniversität Leoben, Autriche
	Mme. Pascale Aussillous	Maître de conférences IUSTI, CNRS Aix-Marseille Université
<i>Examineurs :</i>	M. Christophe Martin	Directeur de recherche CNRS SIMaP, Université Grenoble Alpes
	Mme. Marie Bedel	Maître de Conférences Arts et Métiers ParisTech d'Aix-en-Provence, MSMP
<i>Directeur :</i>	M. Hervé Combeau	Professeur des universités IJL, Université de Lorraine, Nancy
<i>Co-directeur :</i>	M. Miha Založnik	Chargé de recherche CNRS IJL, Université de Lorraine, Nancy

This class is used with my own modifications

*A mi familia,
mi Daria,
y mis amigos.*

*También agradecer
a mi director, Hervé Combeau
a mi codirector, Miha Založnik
y a Bernard Rouat
por su tiempo dedicado,*

*en general,
a todos aquellos que
han tenido una actitud
profesionalmente constructiva
durante estos tres años,
como Walter Dal'Maz en
mis primeros días con
objetos en C++*

*También agradecer a
la Escuela Superior de
Ingenieros Aeronáuticos
por la excelente base
que nos proporcionan,
más que suficiente para
afrontar cualquier reto
profesional.*

*Por último agradecer
a mi máquina Linux
por darle a los cálculos
la chispa adecuada.*

¡Gracias totales!

Contents

Symbols and notation	vii
Introduction	1

First Part

Literature review

Chapter 1 State of the art	5
1.1 Introduction	5
1.2 Equiaxed grain packing in solidification	7
1.2.1 Analog experiments: transparent alloys	7
1.2.2 Solidification background	9
1.2.3 Why is the grain motion and packing important?	11
1.2.4 Experimental observation of metallic mushy zone	17
1.2.5 Dendritic grain growth	19
1.2.6 Conclusion of the solidification review	20
1.3 Particle packing	22
1.3.1 Fundamental concepts	22
1.3.2 Dry and fluidized packings of spheres	25
1.3.3 Arbitrary geometry particle packing	34

1.3.4	Experimental characterization techniques for packings	40
1.3.5	Conclusion of the particle packing review	42
1.4	Numerical techniques for packing modeling	44
1.4.1	Conclusion of the numerical techniques review	49

Second Part

Theoretical, experimental and modeling analysis

Introduction	53	
Chapter 2 Single grain approaching a packed grain bed: theoretical analysis	55	
2.1	Introduction	55
2.2	Approaching phase	56
2.2.1	Drag force	57
2.2.2	Particle-wall lubrication force	58
2.2.3	Particle growth	60
2.2.4	Particle motion equation	60
2.2.5	Dimensionless analysis	61
2.3	Rearrangement phase: single particle model	65
2.3.1	Dimensionless analysis	67
2.4	Application to casting processes	68
2.5	Theoretical conclusions	72

Chapter 3 Experimental analysis	73
3.1 Introduction	73
3.2 Setup conception	74
3.3 Particle selection	75
3.4 Fluid selection	78
3.4.1 Glycerol	78
3.4.2 Glycerol-water solution	79
3.4.3 Water	79
3.4.4 Air (dry packing)	80
3.5 Average packing fraction	80
3.5.1 Volume reconstruction technique	81
3.5.2 Influence of geometry and hydrodynamic conditions on the pack- ing fraction	81
3.6 Packing dynamics: Lagrangian description	83
3.7 Conclusions of the experimental analysis	90
 Chapter 4 Packing modeling	 91
4.1 Introduction	91
4.2 Geometrical packing model	92
4.2.1 Description	92
4.2.2 Sphere and dendrite packings	94
4.3 Discrete Element Method	97
4.3.1 Motivation	97
4.3.2 Rigid body dynamics	97
4.3.3 Particle geometry discretization	99
4.3.4 Contact model	99
4.3.5 Fluid model	103
4.3.6 Initial conditions	106
4.3.7 Particle-boundary interaction	106
4.3.8 Contact detection	108
4.4 DEM simulations	109
4.4.1 Low weight protocol	109
4.4.2 Fluid protocol	127
4.5 Modeling conclusions	145

Chapter 5 Application to packing during solidification	147
5.1 Packing fraction correlation	147
5.2 Packing dynamics	151
5.2.1 Lagrangian description	151
5.2.2 Eulerian description	152
Conclusions and perspectives	157
Résumé (long)	161
Appendix A Solidification modeling support	171
A.1 DC casting simulations	171
Appendix B Experimental analysis	173
B.1 Sedimentation column setup	173
B.2 Friction coefficient of PAQC	180
B.3 Theoretical sedimentation parameters	181
B.4 Average packing fraction measurement technique	182
B.5 Sigmoidal model of fitting	184
B.6 Particle contacts	185
B.6.1 Description	185
Appendix C Mathematical support	187
C.1 Geometrical particle packing algorithm: flowchart	188
C.2 Random sequential addition algorithm: RSA	189
C.3 Random orientation: Shoemaker algorithm	189
C.4 DEM numerical parameters	190
C.4.1 Low weight protocol	190
C.4.2 Fluid protocol	192
C.5 Polydispersity: mathematical relations	192
C.6 Initial conditions	195
Appendix D DEM simulations	197
Bibliography	205

Symbols and notation

Latin notations

Ar	Archimedes number	-
CN	Contacting Neighbors	-
D	Vessel diameter	$[m]$
d_{eq}	Particle equivalent diameter	$[m]$
\mathbf{g}_o	Standard gravity	9.81 m/s^2
g_s	Solid fraction in solidification	-
g_s^{pack}	Solid packing limit in solidification	-
g_{env}	Envelope fraction in solidification	-
g_{env}^{pack}	Envelope packing limit in solidification	-
\mathbf{I}_G	Particle inertia tensor about gravity center (in DEM)	$[kgm^2]$
l_c	Widest particle length	$[m]$
L_{trE}	Eulerian transition length	$[m]$
\bar{L}_{trE}^*	Dimensionless Eulerian transition length	-
L_{trL}	Lagrangian transition length	$[m]$
\bar{L}_{trL}^*	Dimensionless Lagrangian transition length	-
m	Particle mass (in DEM)	$[kg]$
N_{pt}	Granular system size	-
\hat{q}	Particle orientation quaternion (in DEM)	-
\mathbf{r}	Particle position vector (in numerical models)	$[m]$
Re	Reynolds number	-
RCP	Random Close Packing	
RLP	Random Loose Packing	
St	Stokes number	-
t	Time	$[s]$
\mathbf{v}	Particle velocity vector (in DEM)	$[m/s]$
\mathbf{v}_s	Solid (particle) velocity	$[m/s]$
\mathbf{v}_s^{sed}	Solid (particle) sedimentation velocity	$[m/s]$
\mathbf{v}^{front}	Packing front velocity	$[m/s]$
\mathbf{x}_i	Particle i position vector (in experiments)	$[m]$
Z	Mechanical contacts	-

Greek notations

α	Particle rotation	[rad]
Γ	Particle growth-to-motion characteristic time ratio	-
δ_p	Particle size polydispersity	-
$\Delta\rho$	Solid-liquid density difference	[kg/m ³]
Δt_{trL}	Transition time (Lagrangian specification)	[s]
Δt_{trL}^*	Transition dimensionless time (Lagrangian specification)	-
η	Particle principal section equivalent diameter to perimeter ratio	-
θ	Dendritic geometric model free parameter: apex-angle	[rad]
μ_{fr}	Friction coefficient	-
μ_f	Fluid dynamic viscosity	[kg/m/s]
ξ	Globular geometric model free parameter	-
ρ_s	Particle density	[kg/m ³]
ρ_f	Fluid density	[kg/m ³]
ϕ_s	Solid fraction (also simply ϕ)	-
ϕ_s^{sed}	Sedimentation solid fraction	-
ϕ_s^{pack}	Packing fraction (also simply ϕ)	-
$\langle\phi_s\rangle_\Omega$	Average solid fraction at volume Ω	-
Ψ	Particle sphericity	-
ω	Particle angular velocity vector (in DEM)	[rad/s]

Introduction

Context

Solidification of metal alloys is a complex issue due to the coupling between macro-scale phenomena, e.g. the transport of momentum, the transport of energy or the transport of solute; with microscale phenomena such as the crystal nucleation and growth. A better understanding of the preceding actors brings the enhancement of the quality of the solidification products via the control and removal of defects during the solidification process. The product quality depends on the microstructure, chemical segregation, porosity, etc.

In fact, the macrosegregation, porosity and hot tearing are the most important solidification defects. The porosity and the hot tearing are related to the lack of interdendritic liquid in the mushy zone. On the other hand, macrosegregation is the result of a heterogeneous distribution of alloying elements along the final product. Thereby, the heterogeneity of the alloying element concentrations can be detrimental for the final mechanical properties of the product. Moreover, if the solidification product is subsequently submitted to heat treatments, the mechanical properties could be even more deleterious, due to the heterogeneous distribution of precipitates as a result of the former macrosegregation.

Regarding the macrosegregation, this phenomenon is the consequence of the relative motion between the liquid and solid phases while they coexist. These two phases have different content of alloying elements due to the different solubility in liquid and solid. The macrosegregation can be caused by: a) solidification shrinkage, b) natural or forced convection, c) grain sedimentation and d) deformation of the mushy solid.

The free-floating solid equiaxed grains, nucleated in the melt, sediment and pack driven by a low solid-liquid density difference causing negative macrosegregation. After settling, the equiaxed grains randomly pack forming a porous structure. In this thesis, we investigate the phenomenon of equiaxed grain random packing, especially the grain packing fraction (also called packing limit) which is the volumetric solid fraction once the grains are in mechanical equilibrium. In this way, the nature of the momentum transport is identified through the solid fraction with slurry flow for solid fraction values lower than the packing fraction and porous flow otherwise.

Since the macrosegregation and other defects are strongly sensitive to the nature of the momentum transport, the packing fraction becomes an important parameter in solidification, particularly, in solidification multiphase multiscale modeling where the packing

fraction is an input parameter.

In the context of solidification, the grain packing phenomenon is characterized by a complex grain geometry, a grain size distribution, a particular packing hydrodynamic condition due to the melt presence, a grain growth, etc. Additionally, this phenomenon has a random nature, i.e. the orientation and position of the packed grains do not follow any pattern.

Objectives

In this thesis, the solid grain packing phenomenon during the solidification is investigated. To cope with the understanding of this phenomenon, some key questions are formulated:

- What is the packing fraction for settling equiaxed grains?
- How do the grain geometry and packing hydrodynamic conditions affect the equiaxed grain packing?
- What is the dynamics of transition (time, length) from a steady settling to a packed grain bed?

Means of research

A theoretical model, an experimental and a numerical approaches are developed from scratch for the investigation of the grain sedimentation and packing in the solidification context aforementioned.

We investigate the hydrodynamic dimensionless parameters that govern the sedimentation and packing phenomenon in a viscous fluid by means of the theoretical model.

The experimental approach is based on a sedimentation vertical column where several grain collections sediment and pack over a horizontal grid. This experimental model offers the possibility to measure the average packing fraction for each grain collection and packing hydrodynamic conditions visualizing the grain evolution from sedimentation to packing. A hydrodynamic similarity between the experiments and actual packing phenomenon is carried out by means of the hydrodynamic dimensionless parameters studied in the theoretical model.

A numerical solver based on the Discrete Element Method (DEM) is developed to model the particle dynamics during the grain packing. This model is validated by the packing fraction of the experiments. It allows us to investigate those variables of the granular system that we cannot access experimentally. Additionally, with this model we learn about the sensitivity of the packing to the grain geometry, the grain size polydispersity, the interparticle friction, and so on.

First Part

Literature review

Chapter 1

State of the art

1.1 Introduction

The State of the Art of this text firstly introduces the equiaxed grain packing in the solidification context. Subsequently, after acquiring a solidification background, the particle packing concept is understood in the context of Granular Media. To conclude, a final section is dedicated to build a brief modeling background of the particle packing phenomenon.

In industrial casting, the macrosegregation is an important defect so large efforts are done for a better comprehension and prevention of it. The numerical modeling is a fundamental tool to cope with the macrosegregation phenomenon. However, the available macrosegregation models need accurate auxiliary microscopic models, such as for the mushy zone permeability, dendritic grain packing, grain growth, etc. in order to provide realistic physical results.

In this way, the equiaxed grain packing in the context of solidification is presented as well as the fundamental solidification concepts. The importance of the grain packing limit is shown by means of the aluminum direct chill casting and steel static ingot casting comparing different packing limits chosen by the modeling authors. Finally, some actual images of the dendritic grain packing are shown for the case of metallic alloys.

Secondly, the particle packing is a topic of interest in plenty of research fields in physics such as the granular and powder materials, the porous and particle-laden flows in Fluid mechanics, the Condensed-matter physics, and so on. Whereas some technological applications are the storage in silos, metallic-alloy processing, petroleum industry, mineral processes, solid propellants, concrete, soils, biologic systems, transportation, etc. Despite lot of information can be found for the case of spherical collections, both monodisperse or polydisperse, still the particle packing is an open question for the cases of nonspherical particle geometry especially for the case of nonconvex shapes.

The random particle packing phenomenon is firstly presented from a purely mathematical perspective. Herein, different particle packing concepts are introduced: the particle

packing randomness, the packing fraction (Random Loose Packing and Random Close Packing fractions), the packing mechanical contacts, etc.

Subsequently, several experimental packing examples in literature are collected in order to highlight the influence of the protocol, particle geometry and hydrodynamic conditions on the packing fraction. Additionally, some packing fraction characterizing techniques are also introduced.

Finally, a brief literature review of the available packing modeling techniques is considered. They are classified in geometrical and dynamic techniques. In the dynamic techniques we focus on the Discrete Element Method (DEM) which is a numerical discipline that considers the dynamics of each particle and also the interparticle interactions for large granular systems. Several literature examples of DEM are presented. Additionally, we also include several examples of CFD-DEM, which is the coupling between the particle dynamics and the fluid dynamics.

1.2 Equiaxed grain packing in solidification

There is a need to better understand the microscopic phenomena in solidification to improve the quality of the cast product. In this section the phenomenon of equiaxed grain sedimentation and packing is presented as well as the importance of this phenomenon in the solidification context, i.e. how this phenomenon is related to the macrosegregation defect in the industrial casting.

Firstly, the phenomenon of equiaxed grain packing is introduced via the solidification of transparent alloys. These experiments have been commonly used in the solidification research for the phenomenological visualization and comprehension. Subsequently, the concept of packing fraction or packing limit is related to the concept of macrosegregation, particularly for the direct chill casting of aluminum and static ingot steel casting. Finally, several equiaxed grain packing structures of metallic alloys are shown.

1.2.1 Analog experiments: transparent alloys

In solidification, analog experiments are commonly employed, e.g. transparent alloys. This is the case of the experimental work carried out in the 1960s by *K. A. Jackson* and *J. D. Hunt* (see Refs. [Jackson and Hunt, 1965, Jackson et al., 1966]). By means of ammonium chloride-water solutions, $NH_4Cl - H_2O$, they show the phenomenon of equiaxed grain formation, recirculation due to the thermo-solutal melt convection, sedimentation and finally, the grain packing. In Fig. 1.1, the equiaxed grains coming from the upper part of the mold sediment due to the solid-liquid density difference, forming an agglomeration of grains in mechanical equilibrium at the bottom. This agglomeration of grains is the so-called grain packing. The zoomed image lets us visualize how the packed structure looks like. Like in a bad *Tetris* game, the approaching grains pose over the previously packed particles leaving some porosity among them. This phenomenon is mainly ruled by the minimization of the granular system gravitational potential energy coupled with the mechanical constraints that each grain imposes to its neighboring grains.

According to these authors, several mechanisms contribute to the formation of the equiaxed dendritic grains in solidification:

- Detachment from columnar region: the dendritic remelting at the columnar region on the vertical and top walls of the mold coupled with the melt convection feed the melt with equiaxed grains that keep on growing, recirculating, sedimenting and packing.
- Undercooling nucleation: when the superheated melt is poured in the cooled mold, a great amount of grains is nucleated in the melt. Subsequently, the crystal remelting and the effect of the melt convection can contribute to multiply the amount of grains. Finally, they grow, circulate, sediment and pack.

The phenomenon of formation and packing of equiaxed grains continue until the end of the solidification process. The Fig. 1.2 shows the solidification at an intermediate instant:

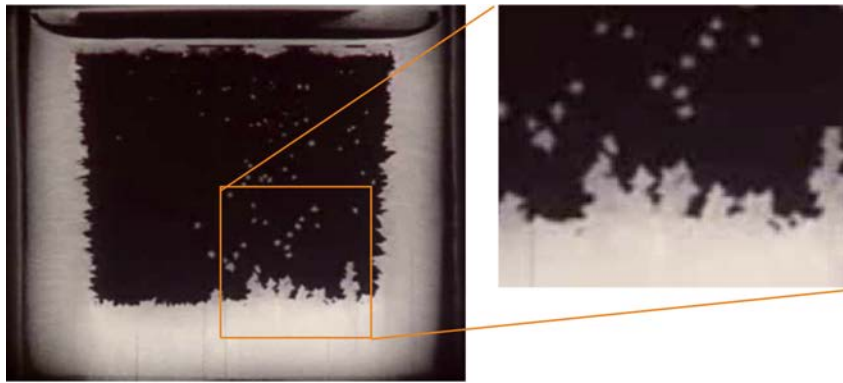


Figure 1.1: Visualization of the equiaxed dendritic grain packing by means of ammonium chloride-water solution (beginning of the movie). Image from the video "Equiaxed zone formation in castings and explanation based on dendritic remelting". K. A. Jackson and J. D. Hunt, Bell Telephone Laboratories. The size of the mold is approximately $51 \times 51 \times 6$ mm.

the columnar dendritic grains horizontally advance from the vertical mold walls whereas the largest part of the solidification domain is filled up with the sedimenting equiaxed dendritic grains. Likewise, the sedimentation is coupled with the grain growth: a grain size polydispersity is expected since those grains with a longer *residence* time in the melt before packing get larger.

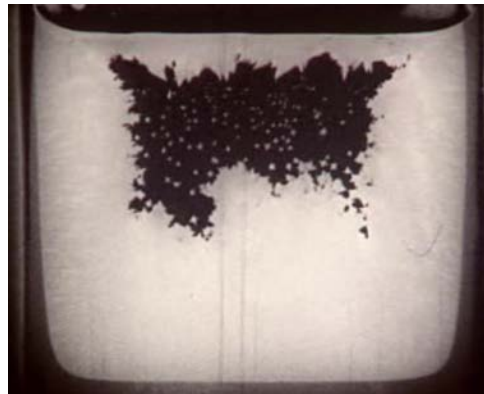


Figure 1.2: Visualization of the equiaxed dendritic grain packing by means of ammonium chloride-water solution, $t = 26s$ (actual speed). Image from the video "Equiaxed zone formation in castings and explanation based on dendritic remelting". K. A. Jackson and J. D. Hunt, Bell Telephone Laboratories. The size of the mold is approximately $51 \times 51 \times 6$ mm.

Furthermore, to complete this section of transparent alloys, the thesis work of *B. Appolaire* and *S. Gerardin* is presented (see Refs. [Appolaire et al., 1999, Gerardin et al., 2001]). It consists of the sedimentation of a single equiaxed dendritic grain in isothermal melt by means of $NH_4Cl - H_2O$ solution. It is possible to visualize the equiaxed dendritic shape of

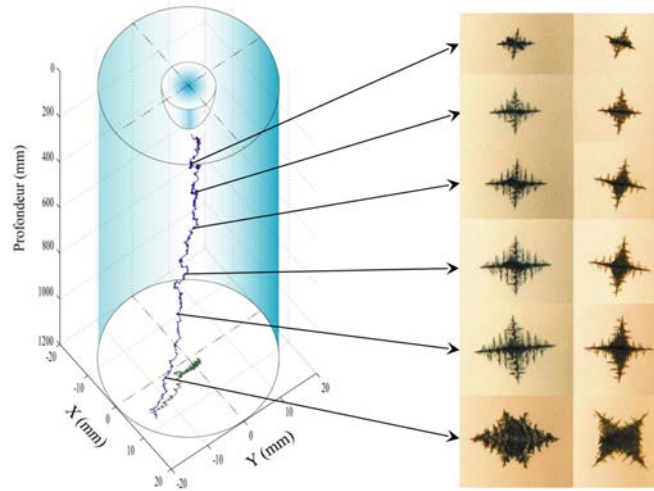


Figure 1.3: Left: Trajectory example of a $NH_4Cl - H_2O$ crystal. Right: Photographic montage representing The morphological evolution of a $NH_4Cl - H_2O$ crystal. Ref. [Gerardin et al., 2001].

a single grain as well as its growth evolution (see Fig. 1.3). Additionally, this thesis work permits to observe the trajectory of one grain proving that the geometry is not perfectly equiaxed since there are some deviations in the horizontal plane. In Chaps. 3 and ?? an envelope model of the equiaxed dendrite is used.

1.2.2 Solidification background

After presenting the phenomenon of packing by means of the transparent alloys, some fundamental concepts of solidification are introduced. In industrial scale solidification, some macroscopic phenomena such as the melt natural convection, heat transfer, equiaxed grain transport, solute transport, shrinkage are coupled with microscopic phenomena such as the grain nucleation, grain growth or grain fragmentation. Thereby, to comprehend the macrosegregation in industrial-scale cast products all previous phenomena must be considered.

According to Ref. [Dantzig and Rappaz, 2009] the macrosegregation is the *solute composition inhomogeneities at the macroscopic scale of the casting which is a undesirable phenomenon*. The macroscopic non-uniformity contributes to a non-uniformity in mechanical properties of the cast product that can even be more prominent in case the product undergoes a heat treatment afterwards. Macrosegregation cannot be solved by the solute diffusion in a heat treatment hence this phenomenon must be prevented as much as possible during solidification.

The macrosegregation is the result of the microsegregation, i.e. the solute solubility is normally lower in the solid phase than in the melt, and the transport of the solute in a macroscopic scale. In this way, at some regions of the cast product positive macrosegre-

gation exists which average composition is higher than the nominal composition and at other regions, negative macrosegregation which composition is lower than the nominal.

Generally, four different solute transport mechanisms contribute to macrosegregation. In Ref. [Dantzig and Rappaz, 2009] these mechanisms are sorted out as:

- Shrinkage: liquid is suctioned at the columnar region if the solid formed downstream the solidification interface is denser ($\mathbf{v}_l = -\beta\mathbf{v}^*$ where \mathbf{v}_l is the liquid velocity, $\beta = \frac{\rho_s - \rho_l}{\rho_l}$ the shrinkage coefficient and \mathbf{v}^* is the solidification interface velocity).
- Nature or forced convection (magnetic field, pouring, stirring or rotation): the melt flow transports solute if $\mathbf{v}_l \cdot \nabla c_l \neq 0$, where c_l is the solute concentration in liquid.
- Grain movement: equiaxed grains have different composition than melt. When they relatively move with respect the melt driving by solid-liquid density difference then they contribute to macrosegregation $\mathbf{v}_s \neq \mathbf{v}_l, \mathbf{v}_s \neq \mathbf{0}$, where \mathbf{v}_s is the solid velocity.
- Deformation of the mushy solid: due to compression or traction on the mushy solid, the melt can be expelled or suctioned $\nabla \cdot \mathbf{v}_s \neq 0$.

Two main solidification structures can be distinguished: columnar and equiaxed. The characteristic morphology of the columnar dendritic grains is that of the schematic representation in Fig.1.4 (left) with the principal branches normally aligned with the thermal gradient direction. And secondly, the equiaxed grains which have approximately the same growth evolution in every axis in Fig. 1.3 and Fig. 1.4 (right).

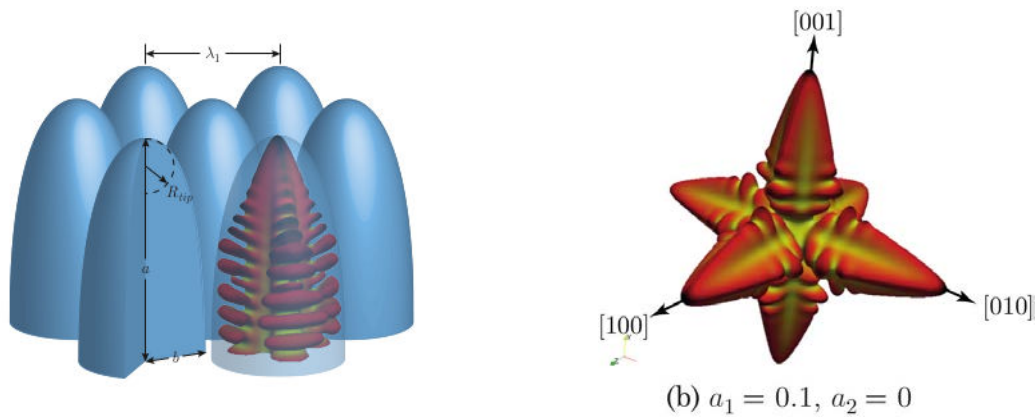


Figure 1.4: Left: Scheme of columnar dendritic grains. Right: Equiaxed dendrite simulation example. Ref. [Dantzig and Rappaz, 2009].

In our case of interest, the equiaxed dendritic morphology is characterized by six principal branches growing along the $\langle 100 \rangle$ crystal directions which sphericity is approximately in the interval 0.40 – 0.90, Ref. [Souhar et al., 2016]. Subsequently, a secondary set of arms

grow from the principal ones, and this phenomenon is repeated with a tertiary set of branches grown from the secondary and so on, as a fractal-like geometry. On the other hand, a globular-like equiaxed morphology is much similar to the spherical shape with sphericity tending to the unity.

Additionally, it is important to consider that the equiaxed grains can also present anisotropy, e.g. due to the melt convection or the influence of other grains. Finally, the concept of polydispersity for a set of equiaxed grains is important as well, since the grain size can be considerably different from one grain to others. One reason of grain size polydispersity is the different residence time of the grains in the melt due to the melt convection.

1.2.3 Why is the grain motion and packing important?

The grain motion and packing have an influence on the heat transfer in the solidification process, on the grain structure (size, morphology, columnar-to-equiaxed transition), on the permeability of the mushy zone (likewise influencing the macrosegregation, porosity, hot tearing, etc.).

Herein, two industrial examples are presented in order to illustrate the main transport mechanisms (among them the grain motion): the direct chill (DC) casting of aluminum alloy ingots and the steel static ingot casting.

DC casting is a vertical semi-continuous technology where the liquid is poured from top to a mold cavity and a moving bottom continuously extracts the solidified ingot. Water is sprayed directly to the solidified ingot skin for cooling and extracts most of the heat. In Fig. 1.5, the main mechanisms contributing to the macrosegregation formation in this technique are schematically shown: thermal and solutal natural convection of the melt, equiaxed grain motion and shrinkage flow. According to the Ref. [Založnik et al., 2011a] the equiaxed free-floating grain movement and the shrinkage are responsible of the negative segregation at the center of the ingot and the positive segregation at the outer part of the ingot, being more important the effect of the shrinkage. On the other hand, the melt natural convection decreases the negative segregation at the center and decreases the positive segregation at the outer part, damping the segregation effect of the grain movement and shrinkage.

Additionally, it is important to highlight the two possible regimes depending on the solid phase behavior at the mushy zone, that is that zone where solid and liquid phases coexist:

- Slurry flow: solid equiaxed grains move freely in the melt. They can be totally dragged by the melt or have a relative velocity with respect to the melt (brown zone in scheme). This regime is possible when the solid fraction is lower than a threshold fraction so-called packing fraction or packing limit, g_s^{pack} .
- Porous flow: once the solid fraction is equal or higher than g_s^{pack} , the grains cannot move and they remain jammed. They form a porous structure (green zone in scheme)

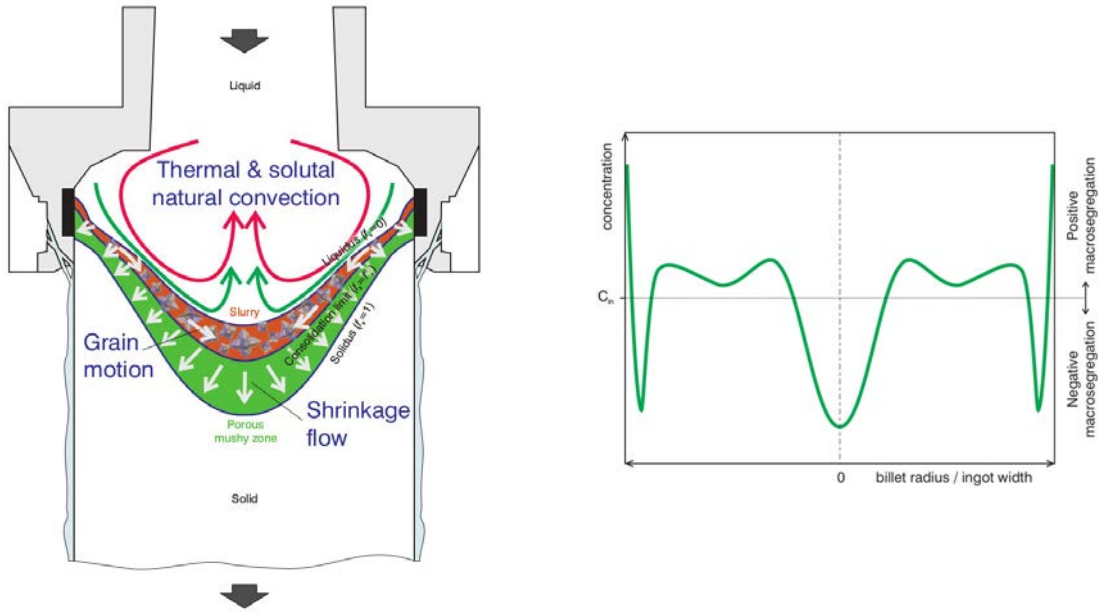


Figure 1.5: Left: Scheme of the various transport mechanisms causing macrosegregation in aluminum alloy DC casting. Right: scheme of common concentration of alloying elements in a transverse cross-section of a DC cast ingot. Ref. [Založnik et al., 2011a]. The negative macrosegregation at the center of the ingot is caused by the grain motion and shrinkage flow (likewise related to the grain packing through the permeability of the grain packed bed).

which permeability is related to the local solid fraction ($\geq g_s^{pack}$). The melt flow cross this porous structure feeding the shrinkage.

In this way, the packing limit, g_s^{pack} in solidification can be understood as the particle packing fraction in Granular Materials, ϕ_s^{pack} , i. e. the ratio between the solid volume and the overall occupied volume when the particles are in mechanically stable equilibrium. The concept of packing is extended in detail in Sec. 1.3 from a Granular Materials perspective.

Besides, it is important to differ between the packing fraction or packing limit and the coherency point in solidification. More precisely, the packing fraction is the fraction corresponding to the phenomenon of grain packing just after sedimentation, that is, the grains are just packed. They form a jammed grain bed where each grain is constrained by its neighbors but there is no solid attachment among them. On the other hand, at the dendritic coherency point the grains are no longer individual elements but they become attached forming a coherent network (see Ref. [Djurdjevic et al., 2012]).

Modeling is a fundamental approach to comprehend the solidification process, the defect formation and the parameter sensibility. For instance, in macrosegregation modeling, the packing limit is an input parameter that is unknown. These models usually implement the packing limit though the *envelope packing limit*, g_{env}^{pack} , since it is generally considered

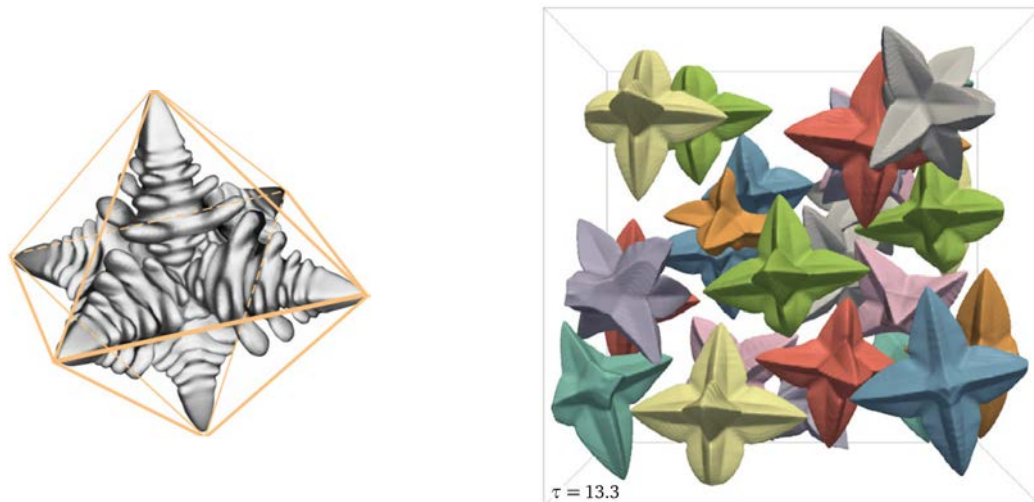


Figure 1.6: Left: scheme of equiaxed dendritic grain circumscribed by a simplified octahedral envelope, Ref. [Appolaire et al., 2008]. Right: realistic dendritic envelopes, understood as the virtual surface that wraps the tips of the secondary arms of the dendritic grain, Ref. [Souhar et al., 2016].

Table 1.1: Envelope packing limit, g_{env}^{pack} , employed in Al macrosegregation models.

Ref.	Model application	alloy	Grain geo.	g_{env}^{pack}
[Vreeman et al., 2000]	DC casting	Al-4.5% Cu, Al-6.0% Mg	sphere (globular)	[0, 30%]
[Založnik et al., 2011a]	DC casting	Al 7449	sphere (globular)	30%
[Wang et al., 2005]	ingot casting	Al-4Cu	sphere (globular)	63.7%
[Reddy and Beckermann, 1995]	DC casting	Al-4.5Cu	sphere (globular)	63.7%
[Vreeman and Krane, 2002]	DC casting	Al-6Cu	sphere (globular)	[20, 25]%
[Heyvaert et al., 2017]	DC casting	Al-6Cu	octahedron	20%

an envelope around the equiaxed dendritic grain. Moreover, these envelopes are simple geometrical shapes such as the sphere or octahedron. In Fig. 1.6 (left), it is schematically shown an equiaxed dendritic grain with principal and secondary ramifications as well as an octahedral envelope attached to it. Additionally, in Fig. 1.6 (right) a realistic dendritic envelope is also shown. In this case, the envelope is formed by joining the tips of the secondary arms of the dendritic grain. Finally, g_{env}^{pack} is the ratio between the envelope volume and the overall occupied volume. Little is known about this input parameter in solidification modeling where a great disagreement among the modeling authors exists. Table 1.1 collects the parameter g_{env}^{pack} chosen by several authors in the modeling of aluminum casting.

The sensibility of the packing limit is studied in Ref. [Heyvaert et al., 2017]. Herein the experiments carried out in Ref. [Vreeman and Krane, 2002] are numerically modeled. Subsequently, the sump shape is compared between experimental and numerical results. Different values for the envelope packing fraction are used obtaining the best fitting be-

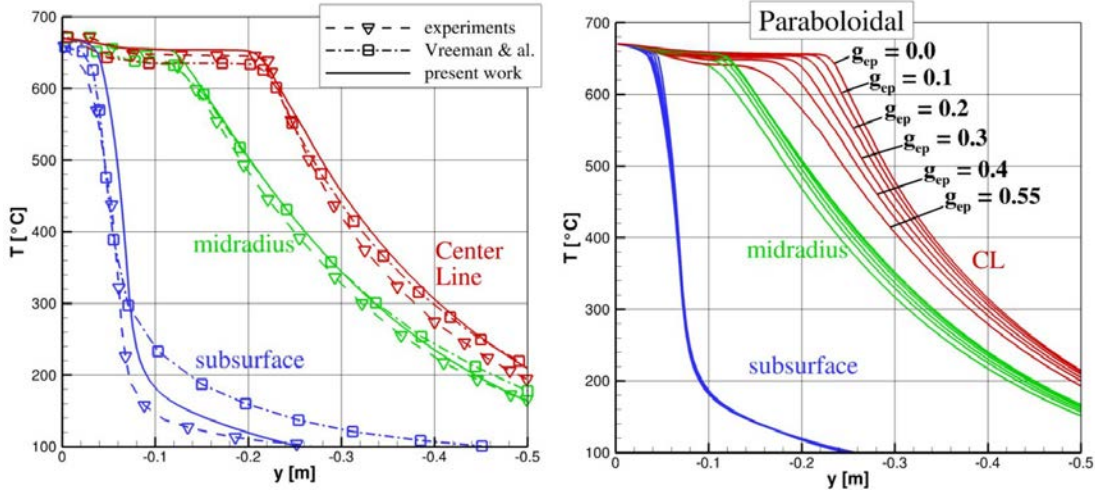


Figure 1.7: Comparison of measured and computed vertical temperature profiles at three different radius in the ingot (subsurface in blue, midradius in green and centerline in red). Left: comparison of simulations with globular grains (paraboloidal tip model of growth) and $g_{env}^{pack} = 20\%$ with experiments and with simulations of Ref. [Vreeman and Krane, 2002]. Right: influence of g_{env}^{pack} on the temperature profiles for globular grain morphology. Both graphs are taken from Ref. [Heyvaert et al., 2017].

tween experiments and simulation for an envelope fraction of 20%. According to this author, the heat transfer and macrosegregation in the billets are very sensitive to the packing parameter. In Fig. 1.7 (left) a comparison between experimental and numerical temperature profiles are shown for an envelope packing fraction of 20%. Whereas Fig. 1.7 (right) shows the high sensitivity of the temperature profile at the center of the ingot on function of the packing fraction. In this case a paraboloidal grain growth model oriented to a globular grain morphology is used.

In Fig. 1.8 (left) the experimental packing fraction and complete solid isopleths (g_{ep} and $g_s = 1$, respectively) are shown in magenta and compared to those numerically obtained in Ref. [Heyvaert et al., 2017] with packing fraction of 20%. Whereas in Fig. 1.8 (right), the numerical characteristic lengths of the sump $L1$ and $L2$ are compared to the experimental (taken as reference) and their relative errors represented as a function of the envelope packing fraction. For both lengths the best fitting is found for approximately 20%.

In general, there is a great dispersion of the packing fraction limit among the authors in case of the direct chill casting technique. Some authors use low values of packing ($\approx 20\%$) whereas others use larger values ($\approx 64\%$ which is the random close packing for a monodisperse noncohesive dry sphere collection as later described in Sec. 1.3). Several factors could decrease the solid packing fraction such as the grain morphology, the fluid presence or the cohesive forces among the grains.

In this way, assuming that the lower packing fractions are physically logic since the best

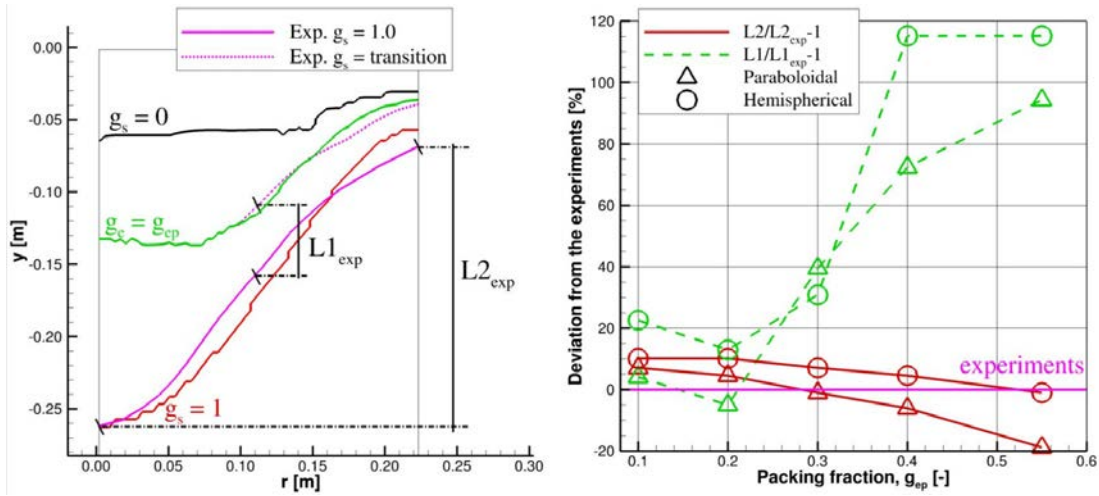


Figure 1.8: Left: Comparison of the sump shape obtained with the paraboloidal tip growth model and packing fraction of 20% to the experimental sump shape. Right: Relative error of the lengths $L1$ and $L2$ as a function of the packing fraction, shown for simulations with both tip models. Both graphs are taken from Ref. [Heyvaert et al., 2017].

fitting with experiments is found for a 20% in Ref. [Heyvaert et al., 2017], several questions arise:

- Why is the packing fraction much lower than the random close packing of dry spheres ($\approx 64\%$)?
- How influential are the equiaxed grain morphology, the polydispersity of the grain size, the fluid presence or the cohesive forces on the packing fraction?

After presenting the DC casting, the static ingot casting is briefly introduced explaining the different mechanisms of macrosegregation and understanding the role of the grain sedimentation and packing phenomena in it. Though majority of steel production is carried out by continuous casting, high added value products such as the nuclear vessels are fabricated by static ingot casting. Since the macroscopic chemical uniformity is highly desired for these demanding products, the prediction of the macrosegregation becomes fundamental.

According to Ref. [Combeau et al., 2009] the mechanics of macrosegregation for the particular case of static solidification are similar to those previously presented: shrinkage, melt convection and equiaxed grain sedimentation. Besides, it is shown the importance of the morphology of the moving grains on macrosegregation: globular grain sedimentation increases the negative segregation at the bottom of the ingot since more solid phase (solute depleted) is transported in case of globular morphology (see Fig. 1.9) than in case of dendritic grains.

Additionally, we schematically show a common solidification structure in a steel ingot in Fig. 1.10 (left). Three different regions can be distinguished as a function of the grain morphology:

- Dendritic equiaxed grain at the ingot upper central part
- Globular equiaxed grains at the ingot lower central part
- Columnar dendritic grains nearby mold vertical walls

Differing from the aluminum DC casting where only equiaxed grains are present, in static steel ingot solidification both columnar and equiaxed are present with the columnar-to-equiaxed transition, CET. Moreover, both equiaxed globular and equiaxed grains are present due to the different solidification conditions along the domain: for a large undercooling, a larger growth velocity of the principal arm tips with respect to the growth velocity of the solid-liquid interface is expected, i.e. dendritic grains whereas globular grains are expected, otherwise.

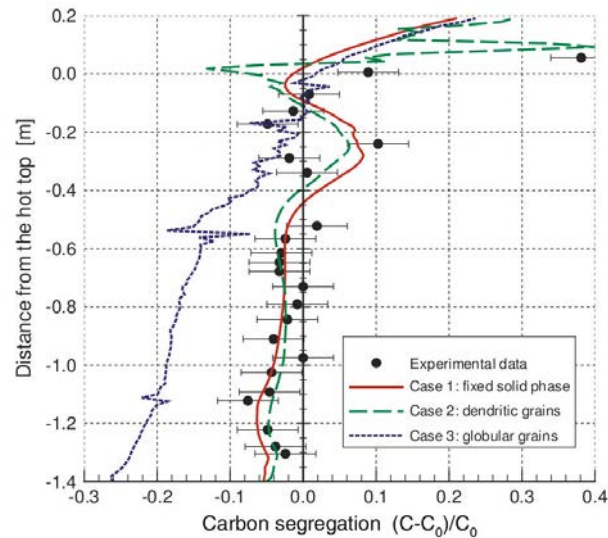


Figure 1.9: Segregation ratio in carbon along the centerline of the ingot; experimental and model results, Ref. [Combeau et al., 2009].

In Fig. 1.10 (right), we present several different regions are distinguished in the cast ingot according to its macrosegregation.

- Positive segregation (+): hop-top segregation, A-segregates, V-segregates and inverse segregation.
- Negative segregation (-): base and banding segregation. The negative base segregation can be due to packing.

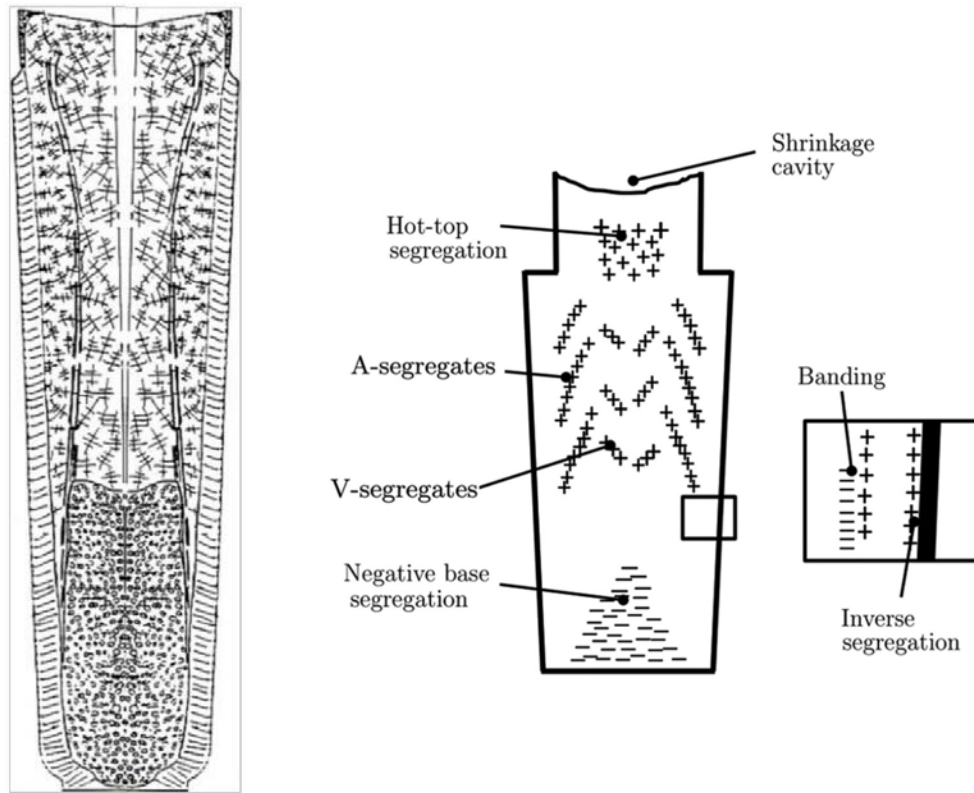


Figure 1.10: Left: map of structures and morphologies of a 6.2-ton steel ingot casted by Ascométal Ref. [Mazet, 1995]. Right: schematic of the different types of macrosegregation that can be found in large ingots. Positive segregation is denoted by (+) symbols and negative by (-) Ref. [Pickering, 2013].

In Refs. [Combeau et al., 2009, Leriche, 2015] an envelope packing limit of 40% is used as input parameter in macrosegregation modeling for both globular and dendritic equiaxed grains since this envelope packing fraction provides the best fit with experiments.

1.2.4 Experimental observation of metallic mushy zone

In Fig. 1.11 is shown a typical network formed by six-principal-arm equiaxed dendrite packing in metallic alloys (see Ref. [Steinbach, 2013]). The authors state to have approximately a 20% of solid fraction in the region where the photo is taken. In order to take the photo the interdendritic melt is sucked by a vacuum chamber. In Ref. [Suzuki and Taniguchi, 1981] this experimental technique of interdendritic melt extraction is well-described. In this second reference, the authors state to have measured solid fraction values in the interval of 26 – 32% for different low-alloy steels.

Recently, the real-time X-ray radiography technique has gained importance for the observation of solidification phenomena such as the growth of the columnar dendritic grains or the nucleation, growth, sedimentation, packing and rearrangement of equiaxed grains.

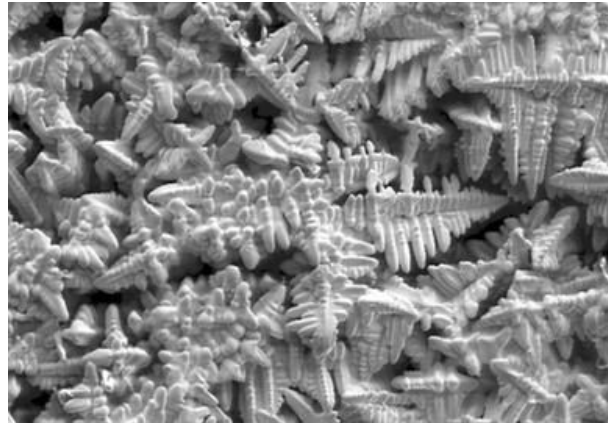


Figure 1.11: Packed equiaxed dendritic grains of metallic alloy forming a network. Ref. [Steinbach, 2013].

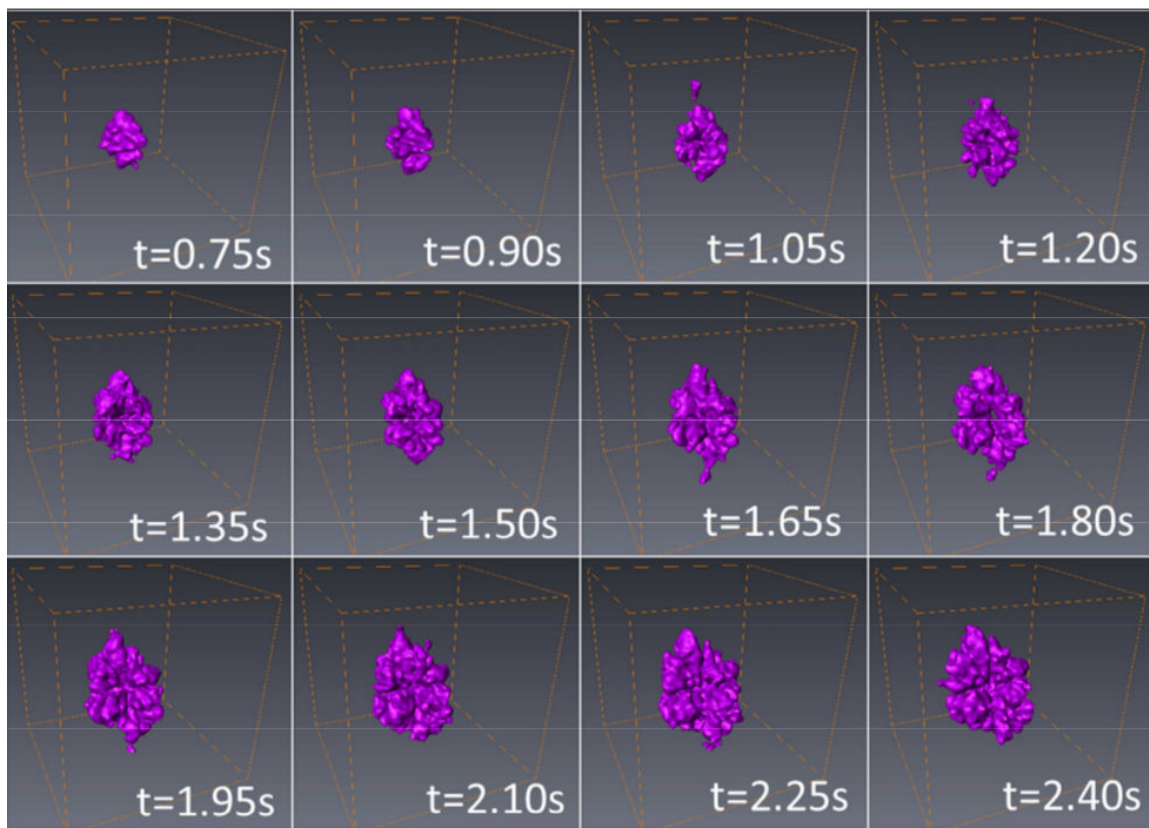


Figure 1.12: Morphological evolution of one $Al - 20\% \text{ wt } Cu$ dendrite during the first three seconds of solidification, Ref. [Salvo et al., 2012].

Thereby, the morphology of the equiaxed grains can be characterized as a function of the alloying elements or the solidification parameters. Nevertheless, this technique has limitations in the sample size (usually the order of several millimeters) so the recipient wall influence must be considered.

Herein some X-ray radiography examples of aluminum alloys are presented. In Fig. 1.12 the morphological evolution of one dendrite during the first three seconds of solidification is shown evolution of two equiaxed dendritic grains close to the packing is shown (Ref. [Salvo et al., 2012]). A second example of use of real-time X-ray tomography is that of Fig. 1.13 showing the morphology of Al-Cu growing dendrites.

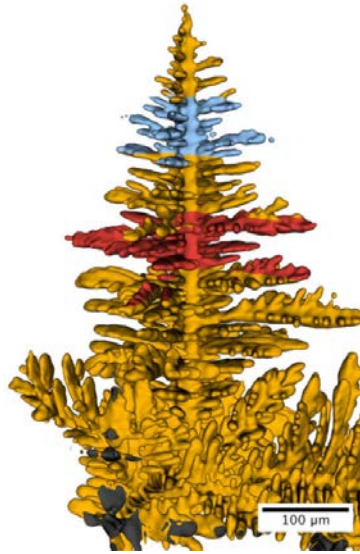


Figure 1.13: Morphology of a nearly free-growing dendrite of $Al - 24\% \text{ wt } Cu$ alloy. Ref. [Gibbs et al., 2015].

1.2.5 Dendritic grain growth

The morphology and size of the dendritic grains evolve from their nucleation until their packing. Herein we introduce the *mesoscopic* modeling of equiaxed dendritic grains of a binary alloy, Ref. [Souhar et al., 2016], in order to better comprehend how the grain envelope grows. The envelope is a virtual surface that wraps the tips of the secondary arms. In this section, we exclusively present the growth phenomenon, neglecting the grain morphology evolution due to remelting. The dendritic grain growth is a consequence of the diffusion and convection of the heat and the solute as well as of the capillary phenomena.

The principal idea of this model is that of applying a model of dendrite tip growth to an amount of points of the envelope to compute their growth velocity and in this way the evolution of the envelope. Neglecting the thermal and capillary undercooling, the dendrite tip growth is governed by the solutal field forehead the tip. The solute is rejected from the solid to liquid in the phase transformation and then its diffuses in the liquid.

More precisely, the tip velocity can be related with the supersaturation dimensionless parameter, Ω_∞ , which is defined as $\Omega_\infty = (C_l^* - C_\infty)/(C_l^*(1 - k_p))$ with C_l^* , C_∞ and k_p the solute concentration at the tip, the solute far from the tip and the partition coefficient, respectively. Thereby, a higher supersaturation provokes a higher tip velocity.

In Fig. 1.14 we show the evolution of the morphology and size of 27 dendritic grains for a low grain density (low ratio of grains per volume unit). The solute rejection increases the solute concentration among the grains. In this way, the closer the grains are, the lower the supersaturation is (lower growth driving force) and consequently the lower the tip velocity is. Besides, the grains can develop preferential growth directions in those directions where there is a higher supersaturation.

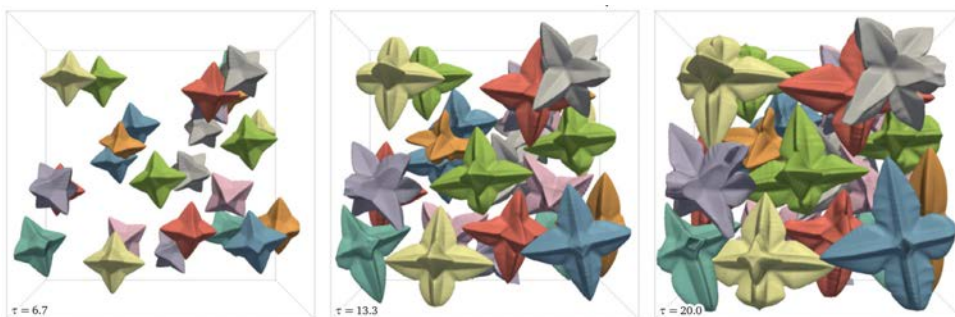


Figure 1.14: Isothermal growth of 27 dendritic grains randomly positioned and oriented with an initial supersaturation of $\Omega_{\infty_0} = 0.05$. Image from Ref. [Souhar et al., 2016].

In Fig. 1.15 the mean sphericity of the dendritic grains is shown as a function of time. Four different parametric cases are presented: from high grain density to one single grain in the domain (free growth). For a high grain density, the sphericity evolves from 1 to approximately 0.90 whereas for the free growth, the sphericity decreases down to 0.4.

1.2.6 Conclusion of the solidification review

To sum up the phenomenon of interest in this thesis, a scheme of equiaxed dendrite grain packing in 2D is shown, Ref. [Leriche, 2015]. The domain is split up in two sub-zones: free-floating grain ($g_{env} < g_{env}^{pack}$) and packed grains ($g_{env} \geq g_{env}^{pack}$). Though in this 2D scheme the grain packing phenomenon seems straightforward, in 3D the dendritic principal branches interlace forming a complex network as previously seeing in Fig. 1.11. Little is known about this grain packing limit in solidification.

The main characteristics to consider in the solidification equiaxed grain packing are:

- 3D packing
- Complex nonspherical particle morphology
- Randomness in orientation and approaching positions of the grain

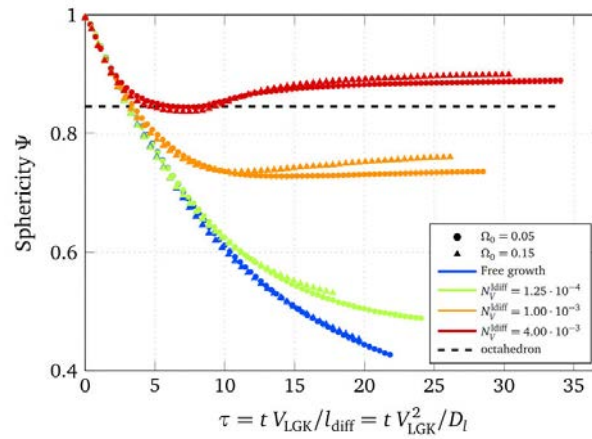


Figure 1.15: Evolution of the mean sphericity of the dendritic grain envelopes over dimensionless time. Image from Ref. [Souhar et al., 2016].

- Viscous fluid presence with a low density difference between the grains and the fluid
- Grain size and morphology polydispersity
- Evolution of the grain size and morphology: grain growth

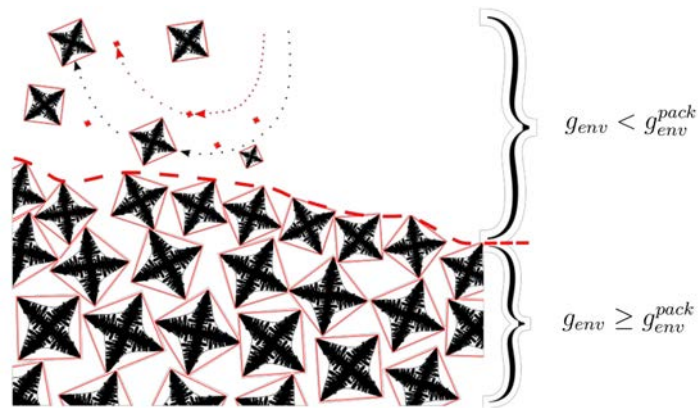


Figure 1.16: Schematic representation in 2D of equiaxed dendritic grain packing phenomenon. A squared envelope is circumscribing each grain. Figure from Ref. [Leriche, 2015].

1.3 Particle packing

Historically, the particle packing has been a fascinating problem to mathematicians and physicists. Thereby, some of the main concerns have been those of discovering the minimal space that a given collection of particles is able to fill up, for both ordered and random arrangements.

Understanding the packing structures has been the interest of plenty scientists such as Johannes Kepler, Isaac Newton, Carl Friedrich Gauss, David Hilbert or more recently, J. D. Bernal and Thomas Hales (see Refs. [Berthier, 2011, Desmond and Weeks, 2009, Torquato and Stillinger, 2010]). Some of their progress has been:

- Kepler conjecture: in 1611 Kepler stated that the face cubic centered (FCC) lattice pattern was that with highest packing fraction for a collection of monodisperse spheres filling the space, with a packing fraction of $\pi/\sqrt{18} \approx 0.74$.
- Newton published that the largest kissing number is equal to 12 in three-dimension space for spheres.
- Gauss: in 1831, he published a partial solution to prove that Kepler conjecture is the densest Bravais lattice.
- Hilbert: in 1900, he included Kepler conjecture as one of the twenty three unsolved problems of mathematics.
- Bernal: in the 1960s he introduced a new interpretation of liquid structures: *homogeneous assembly, consistent but irregular and not containing crystalline regions, or holes*.
- In 1998, Thomas Hales computationally verified the Kepler conjecture with a 99 % certainty.

1.3.1 Fundamental concepts

Herein, some essential mathematical definitions of the particle packings are presented. The rigorous mathematical definition of particle packing itself is not straightforward. According to Ref. [Torquato and Stillinger, 2010], a packing is *a large collection of nonoverlapping particles in either a finite-sized container or in d -dimensional Euclidean space \mathbb{R}^d* .

Particle packings can be jammed or unjammed. *Jammed packings are those particle configurations in which each particle is in contact with its nearest neighbors in such a way that mechanical stability of a specific type is conferred to the packing. A packing is locally jammed when each particle of the packing is trapped by its neighbors*, Ref. [Torquato and Stillinger, 2010].

At this point it is important to define what the randomness is in particle packing. According to Ref. [Donev, 2006] the terms *disordered*, *random*, *amorphous* and *glassy* are

synonyms. On the other hand, the term *ordered* is equivalent to *crystalline*. A scale must be introduced for the randomness measurement in packings by means of an *order metric* where the value 1 matches with the ordered situation (i.e. centroids of the particles are located in a lattice and their orientation is identical), meanwhile, the value 0 matches with the totally disordered case. Many different order metrics exist. Bond order parameters are usually used for the detection of local crystalline arrangements (see Refs. [Torquato et al., 2000], [Mickel et al., 2013]). In case of nonspherical particles, the evaluation of the particle orientation randomness can be carried out by means of an orientational order parameter, e.g. ellipsoids (see Ref. [Delaney et al., 2011]).

An essential parameter to characterize particle packings is the *packing fraction*. To this point, we focus on the average packing fraction which is the ratio between total particle volume and total volume occupied by the particles. The local packing fraction will be later presented in detail. In this vein, for the case of jammed packings, which is the relation between randomness and average packing fraction? An answer to this question is provided in Ref. [Torquato and Stillinger, 2010]: there is no clear relation between randomness and average packing fraction, there are lots of accessible combinations for these two quantities. The achieved combination depends on the protocol used to form the packing and on the particle characteristics.

These accessible combinations are schematically illustrated in the white region of Fig. 1.17 (with the inaccessible combinations in gray). Likewise, in the accessible region there are two sub-regions: jammed structures where each particle of the structure is jammed (limited by the border containing the points A , B and MRJ) and the unjammed structures (otherwise). The point A represents the lowest average packing fraction of a jammed system. At this point the order is higher than other points of the jammed system, i.e. the condition of lowest average fraction requires some specific order. Besides, the jammed system reaches the maximum average packing fraction at point B , when the order metric parameter reaches the value 1. In the case of monodisperse spheres this point is FCC or HCP. Finally, the MRJ point, i.e. Maximally Random Jammed, is the state that maximizes the randomness out of all the infinite possible jammed states.

After having introduced the concepts of particle packing, jamming and order, we discuss the concepts of random close packing (RCP) and random loose packing (RLP) which are widely used in the field of Granular Media.

According to the commonly accepted definition, RCP is a random jammed state which has the maximum packing fraction. But how random the packing is? As previously explained, randomness is not defined by an unique value but by a continuous order metrics. The terms of random and close packing are antagonistic (see Ref. [Torquato and Stillinger, 2010] and Fig. 1.17), i.e. the higher the average packing fraction, the lower the randomness of the system.

From a practical point of view, the RCP is a jammed state with the maximum packing fraction while maintaining certain randomness (avoiding any ordered particle zones in the packing). It depends on the packing protocol (i.e. the method to produce the particle

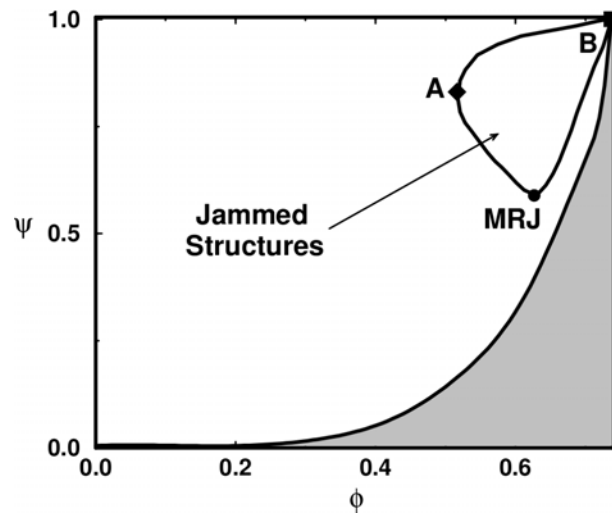


Figure 1.17: Scheme of order metric parameter, Ψ , as a function of the average packing fraction, ϕ , for case of hard monodisperse spheres for case of collectively jammed packing stability situation. Accessible jammed (each of the particles forming the jammed structure is jammed) and unjammed combinations are illustrated as well as the inaccessible combinations (gray region). Three points are distinguished: A) lowest average packing fraction; B) highest average packing fraction (ordered packing); and MRJ which is the Maximal Random Jammed packing. Schematic figure from Ref. [Torquato et al., 2000].

packing) and particle collection under use (e.g. the geometry or the frictional characteristics of the particle surface). Among the different random packing experimental protocols the *vertically shaking* of noncohesive particles with low friction is commonly used to obtain RCP (see Refs. [Scott and Kilgour, 1969, Nowak et al., 1998]). By this protocol, the formation of locally ordered regions near the vessel walls is common, increasing the packing fraction with reduction of randomness.

On the other hand, the commonly accepted definition of random loose packing, RLP, is that of a jammed state able to provide the lowest packing fraction for a given collection of noncohesive particles. However, according to Ref. [Torquato and Stillinger, 2010] there is a unique combination (point A in Fig. 1.17) to get the lowest packing fraction of the jammed system, likewise to obtain this point a certain order is required. Hence, the traditional RLP is not universal but depends on the used protocol and the characteristics of the particle collection. A common experimental protocol to obtain relatively low average packing fractions for a collection of noncohesive particles is fluidization with high inter-particle friction (see Refs. [Onoda and Liniger, 1990, Jerkins et al., 2008, Schröter et al., 2005, Aste et al., 2007, Delaney et al., 2010]).

In Table 1.2 we compare different important concepts related to monodisperse collections of hard disks and hard spheres. Firstly, we show that 2D packings are much denser than 3D packings. Secondly, we show some ordered arrangements, which are some of the Bravais crystallographic packings in 3D (see Ref. [Pickard, 2010]). Thirdly, we show the

Table 1.2: Packings of monodisperse hard disks (2D) and hard spheres (3D).

Order	Arrangement	Packing fraction	Contacts	Equilibrium
ordered	Honeycomb circle packing (2D)	$\pi/\sqrt{12} \approx 90.7\%$	6	jammed (hyperstatic)
random	RCP in 2D	$\approx 80.6\%$	4 (frictionless)	jammed (isostatic)
random	RLP in 2D	$\approx 77.5\%$	3 (∞ friction)	jammed (isostatic)
ordered	FCC / HCP	$\pi/\sqrt{18} \approx 74\%$	12	jammed (hyperstatic)
ordered	BCC	$\pi\sqrt{3}/8 \approx 68\%$	8	jammed (hyperstatic)
ordered	Simple Cubic	$\pi/6 \approx 52.4\%$	6	jammed (isostatic)
random	RCP in 3D	$\approx 64\%$	6 (frictionless)	jammed (isostatic)
random	RLP in 3D	$\approx 54\%$	4 (∞ friction)	jammed (isostatic)

number of mechanical contacts, Z , related to the spatial dimension of packing, d , and the static stability. According to Ref. [Papanikolaou et al., 2013], the monodisperse sphere packings can be related to their static stability:

- Case of frictionless spheres: isostatic ($Z = 2d$), hyperstatic ($Z \geq 2d$) or hypostatic ($Z \leq 2d$).
- Case of infinite friction spheres: isostatic ($Z = d + 1$), hyperstatic ($Z \geq d + 1$) or hypostatic ($Z \leq d + 1$).

The case of random configurations of disks and spheres were estimated by a Statistical Mechanics procedures (see Ref. [Meyer et al., 2010] and Ref. [Song et al., 2008], respectively). In case of RCP they assume frictionless particles (then $Z = 2d$, isostatic equilibrium), whereas, in case of RLP they assume infinite interparticle friction (then $Z = d+1$, isostatic equilibrium).

In Fig. 1.18 the concept of order and random packings are shown for monodisperse spheres. Two dense ordered planes are unintentionally formed over a wet flat frictionless wall (see blue circle). The particle centers follow a pattern that in this case is the densest packing (FCC or HCP). A third stacked plane is needed to determine if the packing is FCC or HCP. Additionally, we show some particles which are randomly jammed within the red circle.

The Voronoi tessellation provides a helpful tool to compute the *local packing fraction*. In this text, the local packing fraction for a specific particle is the ratio between the particle volume and the total volume occupied by only this particle. This total volume is unique and defined by means of Voronoi tessellation as the closes space that surrounds this particle. This mesh is widely used in the field of Granular Media (see Refs. [Rycroft, 2009, Aste and Di Matteo, 2008]).

1.3.2 Dry and fluidized packings of spheres

Historically, large efforts both experimentally and numerically have been done to understand the particle packings. However the vast majority of the work is focused on the dry

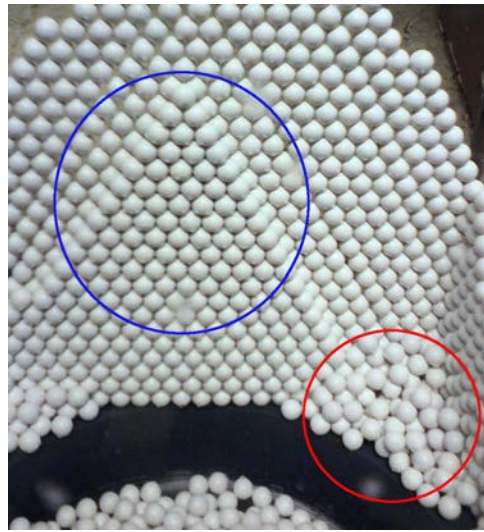


Figure 1.18: Monodisperse hard spheres: ordered FCC/HCP (blue circle) and random arrangements (red circle). The zone in the blue circle is formed by two stacked planes with the configuration FCC/HCP which is the densest ordered configuration. It is needed a third stacked plane to determine if FCC or HCP. Whereas the zone in the red circle there is a disordered packing.

packing of noncohesive monodisperse spheres.

Herein, the dry sphere packings are firstly introduced and subsequently this text focuses on the fluidized packings. For both dry and fluidized packings, experimental results, numerical results, packing protocols and packing properties are discussed.

Dry sphere packings

By means of the dry sphere packings, lots of packing characteristics have been traditionally studied such as the number of contacts, the packing order, the vessel wall effect on the packing, the effect of the diameter polydispersity on packing, the interparticle friction effect on packing, etc. In this section some of them are explained.

Some experimental examples of dry hard noncohesive monodisperse sphere packings are collected in Table 1.3. We include the particle and vessel materials and sizes, number of particles used in these packings, used protocol and packing fraction obtained. These examples serve as a reference for our experimental designing in Chap. 3.

According to these literature references, the material of the spheres is commonly plastic or glass whereas in case of the vessel, plastic. Different vessel to sphere diameter ratios, D/d , have been used: from 10 up to 34. The packing fraction depends on the protocol of packing, that is, how the particles are introduced in a vessel (commonly cylindrical). In dry packings, the most common protocol families are: *pouring* and *vertical shaking*. The vertical shaking is generally used to obtain the RCP configuration and to study the

transition of the granular system from randomness to order (see Ref. [Nowak et al., 1998]). On the other hand, by pouring the packings are formed with a packing fraction lower than RCP.

According to Table 1.3 denser packings form by quickly particle pouring in the vessel than for those formed by careful pouring. In Ref. [Delaney et al., 2010] different pouring protocols are compared for the same monodisperse sphere collection and vessel (see Table 1.3 for details of the sphere collection and vessel), obtaining packing fractions from approximately 0.60 up to 0.64:

- a) pouring the particles to the container while a stick is placed in the middle of it. After pouring the stick is removed ($\phi_s^{pack} = 0.596$).
- b) quick pouring ($\phi_s^{pack} = 0.626$).
- c) quick pouring and then wall tapping ($\phi_s^{pack} = 0.630$).
- d) quick pouring, wall tapping and compressing the particles from above ($\phi_s^{pack} = 0.640$).

Table 1.3: Hard sphere dry monodisperse packings.

Ref.	Particles	Vessel	Protocol	ϕ [%]
	acrylic	acrylic		
[Auwerda et al., 2010]	$d = 12.7mm$ $N_{pt} = 5457$	$D/d = 18$	careful poured	60.5
	acrylic	acrylic		
[Delaney et al., 2010]	$d = 1.6mm$ $N_{pt} = 35000$	$D/d = 34$	quickly poured	62.6
	soda-lime glass	pyrex	vertically-shaken (30Hz)	up to 65.8
[Nowak et al., 1998]	$d = 2mm$	$D/d \approx 10$	(up to 7g acceleration)	

The vessel-to-particle diameter ratio, D/d , have an effect on the random packing consisting of the decrement of the average packing fraction due to the vessel wall effect: higher average packing fractions are obtained for higher D/d (see Ref. [Mueller, 1993]).

In Ref. [Mueller, 1992] a correlation between the local fraction along the radius coordinate is given in Eq. (1.1) with corresponding coefficients in Eqs. (1.2) and (1.3). This correlation is used to compute the effect of the vertical and bottom walls of the vessel on the average packing fraction (see Fig. 1.19). A larger D/d ratio and/or a larger H/d ratio is a lower wall effect on the average packing fraction.

$$\phi\left(\frac{r}{d}\right) = \left(0.635 - \frac{0.22}{D/d}\right) \left(1 - J_o(a(r/d)) e^{-b\left(\frac{r}{d}\right)}\right), \text{ for } D/d \geq 2.02 \quad (1.1)$$

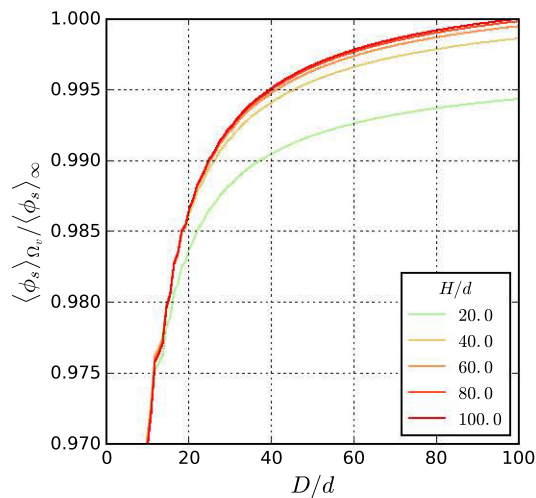


Figure 1.19: Recipient wall effect on the average packing fraction according to Ref. [Mueller, 1992].

$$a = \begin{cases} 7.45 - \frac{3.15}{D/d}, & \text{for } 2.02 \leq D/d \leq 13.0 \\ 7.45 - \frac{11.25}{D/d}, & \text{for } D/d > 13.0 \end{cases} \quad (1.2)$$

$$b = 0.315 - \frac{0.725}{D/d} \quad (1.3)$$

where D , d and r are the recipient diameter, particle diameter and radial position coordinate. J_0 is the Bessel function of first kind of order 0 to model the packing fraction oscillations.

In Ref. [Faure et al., 2009] the effect of the recipient wall on the local packing fraction as a function of the distance from the wall is shown for monodisperse spheres and nonspherical particles (see Fig. 1.20). A similar wall effect on the packing fraction (oscillatory behavior of the packing fraction with the distance from wall) is shown for the different numerical packings with a maximum effect of approximately 5 equivalent diameters for all geometries. In this way, the correlation aforementioned (Eq. 1.1) is used for both spheres and nonspherical particles in this text.

Additionally, the friction among spheres plays an important role in dry packings. The higher the friction is, the looser is the packing, maintaining the pouring protocol and sphere characteristics invariable. Herein some numerical results that show the influence of the friction are presented in Table 1.4: a correlation among the average solid packing fraction, the contact number and the friction coefficient is provided for monodisperse spheres (simulation results).

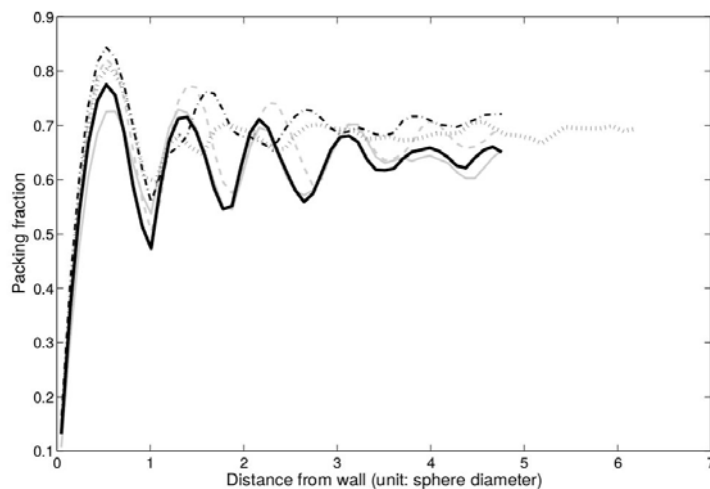


Figure 1.20: Radial packing fraction as a function of the dimensionless distance from wall for spherical and nonspherical particles (see Ref. [Faure et al., 2009]). The nonspherical particles consist of two equal spheres (of diameters d) which centers are separated a certain distance lower than d .

Table 1.4: Influence of frictional contact on average packing fraction and contact number for monodisperse spheres, Ref. [Silbert, 2010].

μ_{fr}	ϕ_s^{pack}	Z^{pack}
0.0	0.639	5.96
0.1	0.614	5.17
0.2	0.595	4.60
0.5	0.574	4.22
1.0	0.556	3.98
10.0	0.544	3.88

The effect of the particle size polydispersity is presented for spheres. According to Ref. [Desmond and Weeks, 2014], in the case of a binary distribution of hard spheres which radii ratio tends to infinity, the RCP can reach up to 0.88. The smallest spheres fill up the empty volume among the largest spheres which are already packed at monodisperse RCP. Additionally, in this same reference a correlation between the RCP and the sphere radius distribution is provided:

$$\phi_s^{RCP} = 0.634 + 0.0658 \delta_p + 0.0857 S_p \delta_p^2 \quad (1.4)$$

where δ_p is the radius polydispersity defined as the standard deviation divided by the mean radius and S_p is the skewness of the radius distribution.

In case of nonspherical particles, we add the effect of size polydispersity and *shape polydispersity* on the packing fraction for pentagons (2D convex particle packing) from

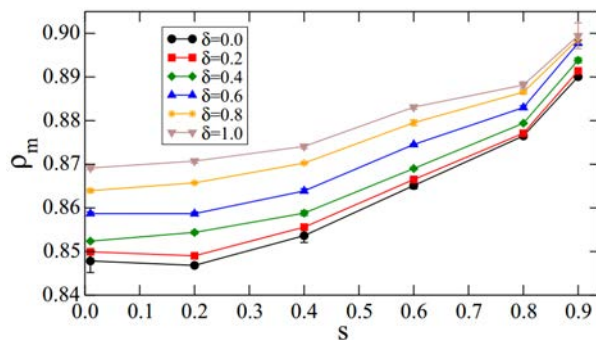


Figure 1.21: Packing fraction of pentagons (2D convex geometry) as a function of size span s for different values of shape polydispersity δ . Image from Ref. [Nguyen et al., 2014].

Ref. [Nguyen et al., 2014]. The authors of this reference defined a dimensionless normalized parameter of polydispersity, called size span, as $s = (d_{max} - d_{min}) / (d_{max} + d_{min})$ where d_{max} and d_{min} are the largest and smallest diameters (diameter of the pentagon circumscribing circumference) in the granular system, respectively. They defined the shape polydispersity, δ , as a dimensionless normalized parameter with $\delta = 0$ for regular pentagons and $0 < \delta < 1$ for the irregular pentagons, increasing the grade of irregularity with δ .

In this way, the authors found that the packings are denser for a larger size polydispersity and/or for a larger shape polydispersity (see Fig. 1.21).

Fluidized sphere packings

As previously presented, the commonly accepted definition of RLP is the random state with the lowest average packing fraction, avoiding any order region in the packing. Nonetheless, this concept is not as straightforward as this definition since the RLP depends on the packing protocol and the particle characteristics. Besides, the randomness and average packing fraction are competitors since some order in the system can decrease average packing fraction, Ref. [Torquato and Stillinger, 2010].

The parameters involved in the sedimentation inside a liquid, i.e. solid-liquid density ratio, interparticle friction or liquid viscosity play a key role in the final static configuration. In Refs. [Jenkins et al., 2008], [Schröter et al., 2005], [Aste et al., 2007] and [Delaney et al., 2010] an experimental particle fluidization and sedimentation protocol is carried out in order to inquire about the influence of previously cited parameters on the packing. The protocol is identical in all four references. It consists of the following steps:

- 1) Initially, the collection of particles is packed in a vertical vessel filled up with liquid.

Table 1.5: Monodisperse hard sphere packings by fluidization protocol.

Ref.	Particles	Vessel	Liquid	Flow rate [ml/s]	ϕ [%]
[Jerkins et al., 2008]	glass $d \in [96, 322]\mu m$	polycarbonate $D \in [40, 133]d$	solution of: water + sodium polytungstate $\frac{\rho_s}{\rho_f} \in (1.04, 2.48)$	[2, 50]	[55, 58]
[Schröter et al., 2005]	glass $d = 250\mu m$	glass (square) side: $96d$	water $\frac{\rho_s}{\rho_f} \approx 2.5$	[20, 60]	[58, 61]
[Aste et al., 2007]	glass $d = 250\mu m$	glass $D = 51d$	water $\frac{\rho_s}{\rho_f} \approx 2.5$	-	[56, 60]
[Delaney et al., 2010]	glass $d = 250\mu m$	polycarbonate $D = 51d$	water $\frac{\rho_s}{\rho_f} \approx 2.5$	-	[56, 60]

- 2) A liquid flow is injected upwards from the bottom of the vessel resulting in the fluidization and expansion of the particle system along the vessel height.
- 3) Eventually, a steady state is achieved when particles do not expand anymore.
- 4) At that point, the liquid injection from bottom is switched off and the sphere collection sediments forming a packing over the bottom of the vessel. According to Ref. [Jerkins et al., 2008], a higher flow rate results in a more expanded bed, longer sedimentation time of the system, and lower average packing fraction. Besides, according to this author, a higher sedimentation kinetic energy of the particles implies a higher average packing fraction.

In Table 1.5 we collect the most important information of each of these four experiments: sphere properties (material and size), vessel properties (material, shape and diameter), used liquid, solid-liquid density ratio, flow rates and average packing fraction intervals obtained. Some useful conclusions for our experiment design (see Chap. 3) are presented in Ref. [Jerkins et al., 2008]:

- The lowest RLP for monodisperse spheres is reported to be approximately 0.55.
- The average packing fraction of the four references is between 55% and 61%. In the fluidization protocol the packing fraction depends on the flow rate, particle size, interparticle or particle-recipient friction.
- Flow rate effect on packing fraction: the higher the flow rate, the more expanded the fluidized sphere bed, longer sedimentation time and looser packing.

- Friction effect among spheres on the packing fraction: the higher the friction, the looser the packing. However, for monodisperse spheres this difference between smooth and roughness particles is about 2% of the ϕ_s^{pack} value.
- Density different, $\rho_s - \rho_f$, effect on the packing fraction: the lower the density difference, the looser the packing for both smooth and rough monodisperse spheres.

On the other hand, a dimensionless parameter relating the packing and the hydrodynamic conditions is more suitable than the dimensional variables previously presented. In Ref. [Farrell et al., 2010] the *Stokes number*, which is the ratio between the particle inertia and viscous dissipation, is experimentally proved to be the dimensionless parameter governing the packing phenomenon of monodisperse noncohesive spheres in fluid. Several collections of acrylic (more frictional) and steel (less frictional) monodisperse spheres are sequentially packed in different fluids. The packing results are firstly plotted as a function of the parameter S (which is the Stokes number without the Reynolds correction on the particle drag) showing an useful relation between the packing fraction and this parameter, Fig. 1.22 (a). A similar behavior of the packing fraction is found when plotted against the Reynolds number. However, there is no function between the packing fraction and $1 - \rho_f/\rho_s$.

This reference defines a threshold, S_{th} , in such a way that under this threshold the RLP is achieved. For the acrylic monodisperse spheres (more frictional) they found $S_{th} \approx 5$ and for the steel monodisperse spheres (less frictional) they found $S_{th} \approx 0.1$. A similar sigmoidal correlation between the packing fraction and the S is found for both acrylic and steel collections. Looser packings are found with a higher interparticle friction. The most viscous liquid can relatively decrease the packing fraction up to a 7% in case of the lower frictional collection whereas up to a 4% in case of the higher frictional collection.

In Fig. 1.23, the authors show the packing fraction as a function of the inverse Stokes number, where the Stokes number is computed by means of the measured sedimentation velocity of the spheres. The packing fraction changes abruptly with the Stokes number. Once the Stokes number is lower than a certain threshold the packing fraction is stable and corresponds to the RLP. They show a threshold Stokes value of approximately 10. Moreover, also the restitution coefficient of the settling particle collision with the packed bed is given, with a null value when the Stokes is lower than the Stokes threshold. This result of the restitution coefficient also agrees with Ref. [Izard et al., 2014].

A lower RLP in Ref. [Farrell et al., 2010] is found than that of Ref. [Jerkins et al., 2008]. However, due to the setup configuration in Ref. [Farrell et al., 2010], an important influence of the recipient wall effect on the packing fraction is expected but no correction is provided from the authors. In this way, we consider 0.55 the lowest RLP, Ref. [Jerkins et al., 2008].

Finally, the influence of the cohesive forces (van der Waals forces) on the packing by a sedimentation in fluid protocol is also considered, Ref. [Dong et al., 2012]. Thus, the

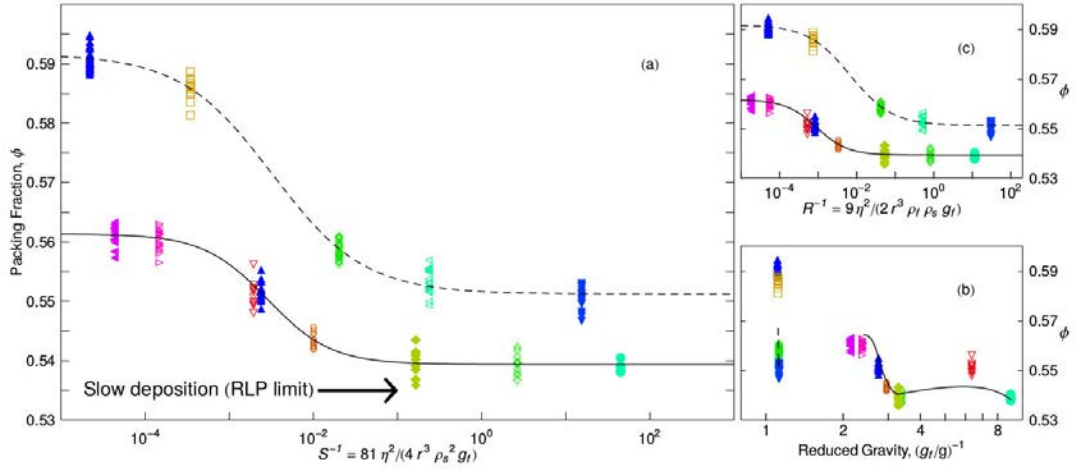


Figure 1.22: Average packing fraction, ϕ , as a function of: a) the inverse theoretical Stokes number, S^{-1} , assuming the Stokes terminal velocity in the particle sedimentation; b) the inverse Reynolds number, R^{-1} , assuming the Stokes terminal velocity in the particle sedimentation; c) the inverse of $(1 - \rho_f/\rho_s)$ (figures from Ref. [Farrell et al., 2010]). Solid line corresponds to the steel spheres (higher friction) and dashed lines to the acrylic smooth spheres.

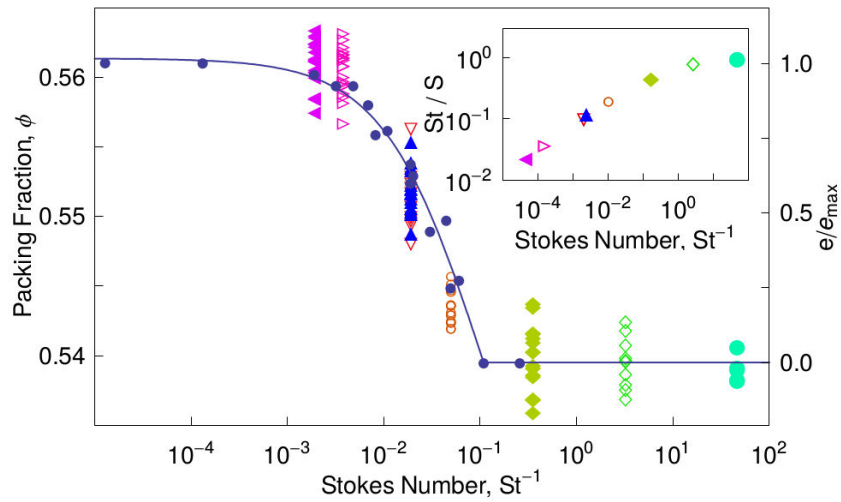


Figure 1.23: Average packing fraction, ϕ , and restitution parameter, e/e_{max} , as a function of the inverse of the Stokes number, St^{-1} . The correlation between S and St is also given.

interparticle cohesion forces contribute to loose the packing via the reduction of particle motion since there is a limitation of the rearrangement during the packing. This reference proposes a correlation between the average packing fraction, ϕ_s^{pack} , and the dimensionless ratio between the cohesion forces and driving force of the packing, χ , $\phi_s^{pack} = \phi_{s_o}^{pack} (1 - e^{-\alpha \chi^\beta})$, where χ is given by Eq. 1.5 and the constant parameters of the correlation $\phi_{s_o}^{pack}$, α and β are 0.616, -2.78 and -0.195 , respectively. Besides, this expression is valid for a wide range of cases: sphere diameter of $d \in [5, 1000]\mu m$, Hamaker constant of $A \in [10^{-23}, 10^{-19}]J$, solid-fluid density ratio of $\rho_s/\rho_f \in [1.02, 4.9]$ with a fixed $\rho_s = 2450kg/m^3$ and fluid dynamic viscosity of $\mu_f \in [10^{-6}, 10^{-1}]Pa.s$.

$$\chi = \frac{F_{coh}}{F_{drive}} = \frac{A d/(12h_{min}^2)}{\rho_s(\pi/6)d^3 \left[(1 - \rho_f/\rho_s)g_o + k \frac{v_{imp}}{\Delta t_{imp}} \right]} \quad (1.5)$$

The van der Waals cohesion forces among the spheres are modeled as $F_{coh} = Ad/(12h_{min}^2)$ where A is the Hamaker constant and $h_{min} = 1nm$. The packing driving force, F_{drive} , is composed by two terms: the contribution of the weight-bouyancy difference (apparent weight) and the *impact induced* force where v_{imp} is the impact velocity which is the velocity of the spheres previous to packing and Δt_{imp} is the impact time given by:

$$\Delta t_{imp} = \left(\frac{d}{(1 - \rho_f/\rho_s)g_o} \right)^{1/2} \quad (1.6)$$

According to this reference, the presence of the van der Waals coherent forces dramatically influences the packing. In Fig. 1.24 (left) we show χ as a function of the sphere diameter, d , for six combinations of the parameters A and v_{imp} . For the considered input intervals, χ ranges from $o(10^{-3})$ up to $o(10^6)$. In this case, larger importance of the coherent forces is found with lower d , higher A and lower v_{imp} . In Fig. 1.24 (right) we show the packing fraction corresponding for each parametric case. A strong influence of the van der waals coherent forces is found for $\chi > 10^{-1}$, dramatically loosing the packing.

1.3.3 Arbitrary geometry particle packing

The vast majority of packing work in literature is focused on spherical particle packing: theoretical, numerical and experimental work abording different topics such as the influence of the presence of fluid, of the interparticle friction, of the cohesion forces, of the size polydispersity, the mechanical stability, etc. Herein we present some work about non-spherical particle packing, with an emphasis in those morphologies similar to the equiaxed dendritic envelopes.

In [Jiao et al., 2009] the densest known ordered packings of superballs (both convex and nonconvex equiaxed particles) are analytically studied. The equiaxed particle geometry is analytically given by Eq. 1.7. A single parameter, p , defines the particle shape (see particle examples in Fig. 1.25). The different equiaxed particle cases are:

- $p \geq 0.5$, convex particle

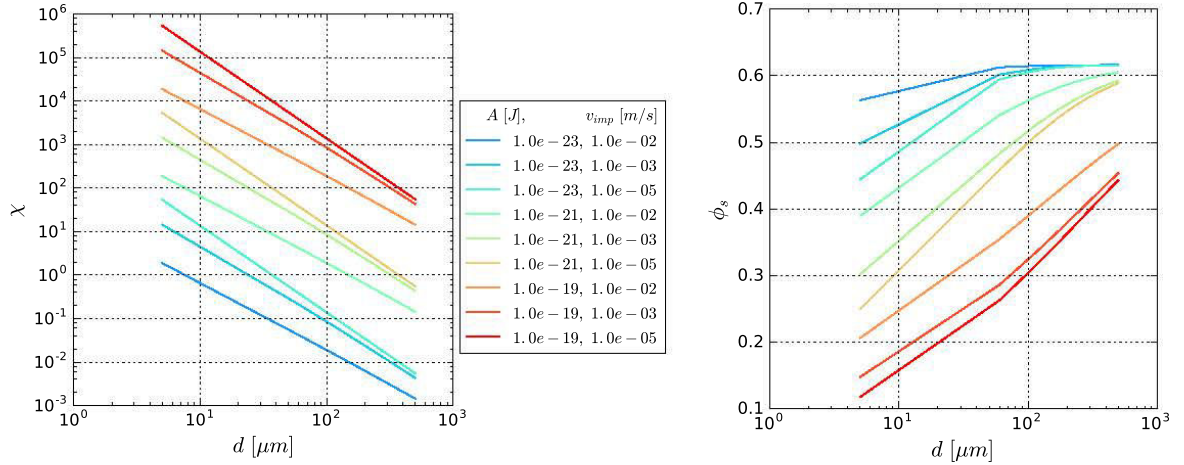


Figure 1.24: Effect of the van der Waals (coherent forces) on the packing fraction for packing of monodisperse spheres in viscous fluid. The plots are carried out with the correlations of Ref. [Dong et al., 2012].

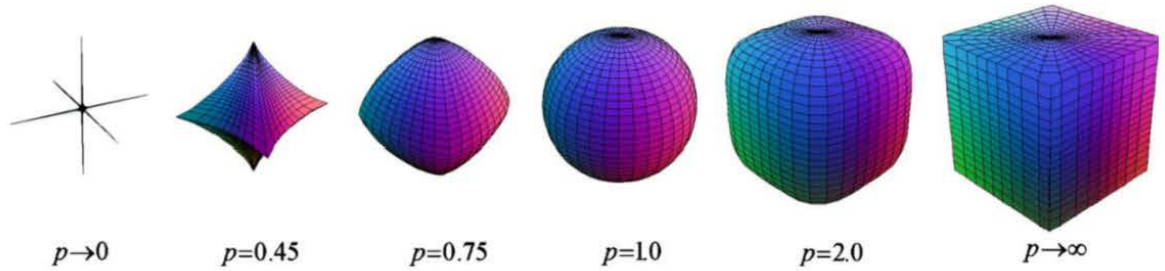


Figure 1.25: Convex and nonconvex 3-dimensional particles given by Eq. (1.7), Ref. [Jiao et al., 2009].

- $0 \leq p < 0.5$, nonconvex particle
- $p = 1$, sphere
- $p = 0.5$, regular octahedron
- $p \rightarrow \infty$, regular cube
- $p \rightarrow 0$, three-dimensional cross (hexapod)

$$|x|^{2p} + |y|^{2p} + |z|^{2p} \leq 1 \quad (1.7)$$

In Fig. 1.26 the maximum fraction of ordered packings of nonconvex and convex particles (in left and right, respectively) is shown. We firstly focus on the nonconvex morphology

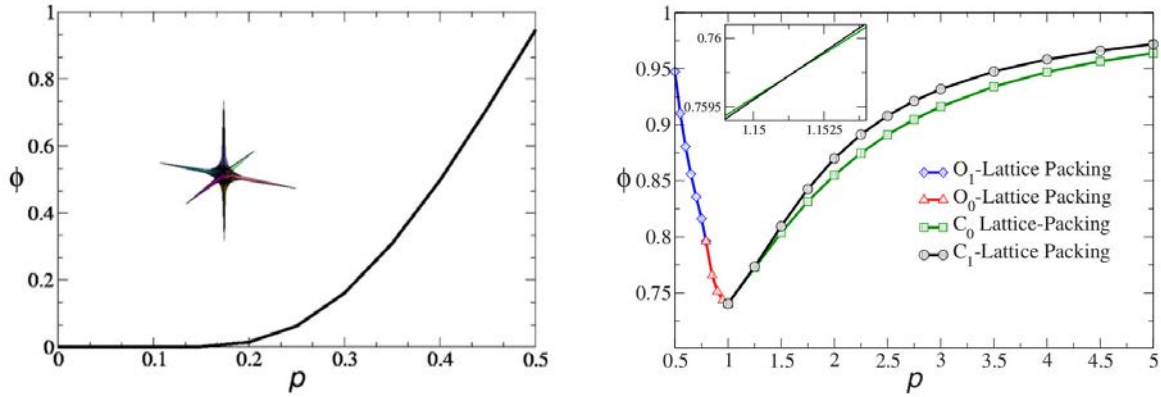


Figure 1.26: Average packing fraction as a function of the shape parameter, p . Left: nonconvex superballs. Right: convex superballs. The particles are ordered in specific lattices to obtain the densest packings (figures from Ref. [Jiao et al., 2009]).

which is the characteristic of the dendrites (considering the dendritic envelope as a virtual surface that wraps the dendritic grain by the tip of the secondary arms, see Fig. 1.6). In this way, for the shape interval of $0.4 \leq p < 0.5$, a maximum ordered packing fraction interval of $0.5 \leq \phi_s^{pack} < 0.95$ is associated, with ϕ_s^{pack} increasing monotonically with p in this interval. The local maximum $(p, \phi_s^{pack}) = (0.5, 0.95)$ corresponds to the regular octahedral geometry. Additionally, for the globular grain morphology we consider the interval $0.5 \leq p \leq 1.0$ with a maximum packing fraction monotonically decreasing from 0.95 to 0.74 which is the FCC/HCP value.

Subsequently, the experimental random packing of the Platonic Solids by means of different dry and fluidized protocols is included, Ref. [Baker and Kudrolli, 2010]. The Platonic Solids are five regular convex polyhedrons composed by: tetrahedron, cube, octahedron, dodecahedron and icosahedron. In this reference, the authors investigate the role of four packing protocols (dry careful pouring, dry pouring + hand shaken, dry pouring + mechanically shaken and fluidization protocol) on the average packing fraction.

The comparison of the different values of ϕ_s^{pack} according to geometry and protocol is collected in Table 1.6. For all Platonic Solids similar behavior of ϕ_s^{pack} with the protocol is observed: 1) in the dry protocols, denser packings are obtained with more intensively shaking and 2) the fluidization packings are the loosest (from 5% up to a 10% looser than the dry careful packings). Slightly higher packing fractions are obtained for the cube.

A numerical example of nonconvex particle random packing is included, Ref. [Malinuskaya et al., 2009]. Among all different nonconvex geometries investigated in this reference (the major part are very spiky with different number of branches), one set of them resemble the dendrite-like morphology in metal alloy solidification with six principal arms in the $\langle 100 \rangle$ directions (see the example of Fig. 1.27). The random packing is numerically created by a sequential deposition in the presence of gravity, i.e. the particles

Table 1.6: Random packing of Platonic Solids with four different packing protocols, Ref. [Baker and Kudrolli, 2010].

Solid	Careful pouring	Hand Shaken	Mechan. Shaken	Fluidization
Tetrahedron	0.54	0.62	0.64	0.51
Cube	0.57	0.66	0.67	0.54
Octahedron	0.57	0.62	0.64	0.52
Dodecahedron	0.56	0.60	0.63	0.51
Icosahedron	0.53	0.57	0.59	0.50

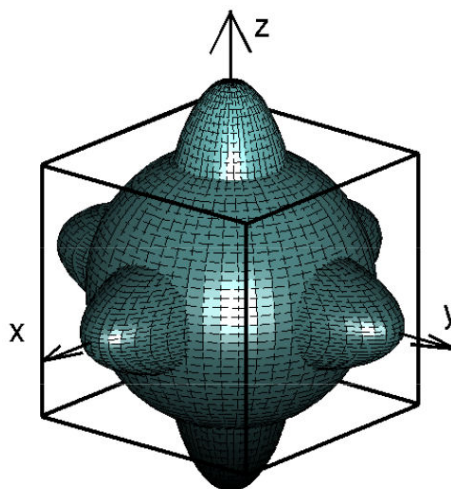


Figure 1.27: Nonconvex particles based on a central sphere (which radius is R_{sph}) and three revolution ellipsoids (which major semiaxis is R_3 and minor semiaxes are $R_{12} = R_1 = R_2$). The geometrical ratios between the constituent elements are $R_3/R_{sph} = 1.5$ and $R_{12}/R_{sph} = 0.5$. Figure from Ref. [Malinouskaya et al., 2009].

are packed one by one minimizing their potential over the previously packed particle bed. The particles are frictionless and no fluid effect is accounted.

We focus on the six-branch geometries which packing fractions, ϕ_s^{pack} , are shown in Table 1.7 as a function of the geometrical ratios between their constituent elements (R_3/R_{sph} and R_{12}/R_{sph}), including their sphericity, Ψ , in brackets. Among the 9 cases in this table, the $R_{12}/R_{sph} = 1.0$ with $R_3/R_{sph} = 1.5$ ($\Psi = 0.95$) and $R_3/R_{sph} = 3.0$ ($\Psi = 0.72$) are thought to be the most representative for the solidification packing, with ϕ_s^{pack} equal to 58% and 39%, respectively.

Only after understanding the general properties of packing, we present the isostaticity and the particle contacts for the case of nonspherical geometry, without any revolution axis. So, how many contacting neighbours does a nonspherical geometry particle (without any revolution axis) have in a random packing? This type of particle has 6 degrees of freedom (d_f) in 3-dimensional space: 3 translational and 3 orientational and since no revolution

Table 1.7: Random packing fraction, ϕ_s^{pack} , of six-branch dendrite-like particles composed by a central sphere of radius R_{sph} and three revolution ellipsoids of major semiaxis R_3 and minor semiaxes $R_{12} = R_1 = R_2$ (see morphology in Fig. 1.27). The shape sphericity, Ψ , appears in brackets.

Ratios		R_3/R_{sph}	
R_{12}/R_{sph}	1.5	3.0	5.0
1.00	0.58 (0.95)	0.39 (0.72)	0.23 (0.57)
0.50	0.52 (0.86)	0.22 (0.57)	0.10 (0.45)
0.25	0.48 (0.90)	0.16 (0.60)	0.08 (0.43)

axis are present, the 6 degrees of freedom are important in packing. Thereby, the particle needs 6 linearly-independent constraints to be isostatic. These constraints are provided by other surrounding particles which are equally constrained by others and so on. In this way, the particles are both constrained and constraining in granular media, hence, each particle has $2d_f$ constraints for the isostatic condition, i.e. 12 constraints for the arbitrary geometry without revolution axes (see Refs. [Donev et al., 2006] and [Delaney et al., 2011]).

In case of revolution axes, the number of constraints to reach isostaticity is $2(d_f - n_{rev})$, where d_f is 6 in 3 dimensions and n_{rev} is the number of revolution axes in the particle geometry. Thereby for the spherical geometry (3 revolution axes), 6 constraints are needed for isostaticity in the packing and for the revolution ellipsoidal geometry (1 revolution axis), 10 constraints.

Once it is known the number of constraints for an isostatic packing, it is important to understand that constraints are not equivalent to mechanical contacts. From a geometrically point of view, different contact cases exist:

- point-point frictionless contact: equivalent to 1 translational constraint, i.e. 1 constraint.
- edge-face frictionless contact: equivalent to 1 translational and 1 rotational constraints, i.e. 2 constraints.
- face-face frictionless contact: equivalent to 1 translational and 2 rotational constraints, i.e. 3 constraints.

In case of frictional contact, each mechanical contact could activate tangential constraints (static friction), thus, less contacts are needed to reach isostaticity. Finally the number of contacts is not equivalent to the contacting neighbours in case of nonconvex particles (dendrite-like) since a pair of them could have more than one point-point contact.

In [Jaoshvili et al., 2010], the authors experimentally investigate the random packings of tetrahedrons. They obtain 6.3 ± 0.5 contacting neighbours and 12 ± 1.6 total constraints, which is possible since 86% of particles have at least one face-face contact, determining

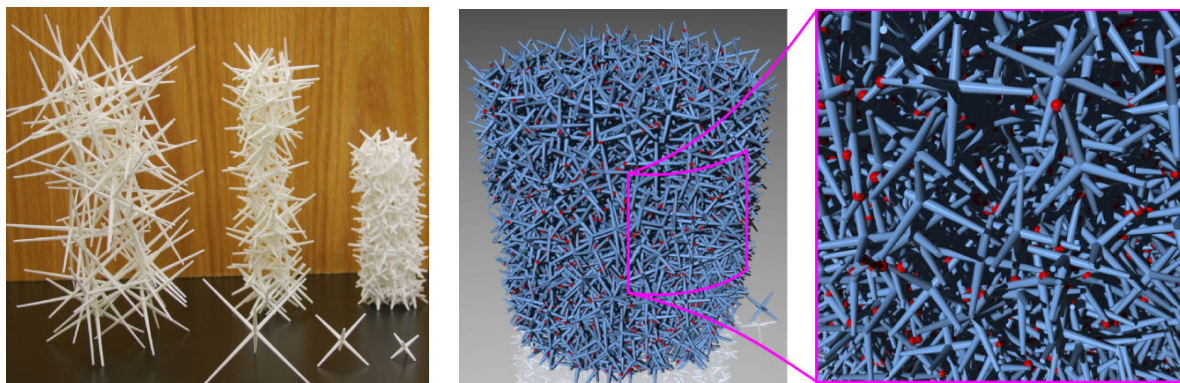


Figure 1.28: Hexapods packings from Ref. [Barés et al., 2017]. Left: packings with three different collections according to the arm size. Center and Right: X-ray tomography reconstruction of a packing of hexapods which arm size is smallest.

Table 1.8: Average solid packing fraction and average contacts for hexapods, Ref. [Barés et al., 2017].

Type	ϕ_s	Z
25 mm non-vibrated	14%	6.58
25 mm vibrated	16%	7.13
50 mm non-vibrated	5.6%	9.18

that the system is under isostatic conditions (12 constraints in case of tetrahedrons). The packing protocol consists of partially pour the tetrahedron collection in the container, manually shaking and pouring the rest of the particles.

To end this section, a recent investigation about the packing stability of *hexapods* is also added, Ref. [Barés et al., 2017]. The hexapods are 3D particles formed by three orthogonal arms, equivalently to the principal arms of the equiaxed dendritic grains (see Fig. 1.28 left). These nonconvex particles are characterized by having a repose angle of even up to 90° due to the high entanglement between arms.

In this reference, the contacts between particles and packing fraction is experimentally investigated. Two hexapod monodisperse collections, manufactured by 3D printing of polyamide, are packed by means of sequential deposition in a cylindrical recipient: 1) 25 mm-arm hexapods (of volume 175 mm^3) and 2) 50 mm-arm hexapods (of volume 350 mm^3). Besides, for the smallest hexapods, a second protocol is carried out: horizontal vibration of the recipient after pouring.

Table 1.8 shows the average results of solid packing fraction and average number of contacts. In this way, very low solid packing fractions are found but the structures are very stable. The higher the number of contacts is, the more stable are the packings.

The last interested results added are the contact position along the arm length, Fig. 1.29.

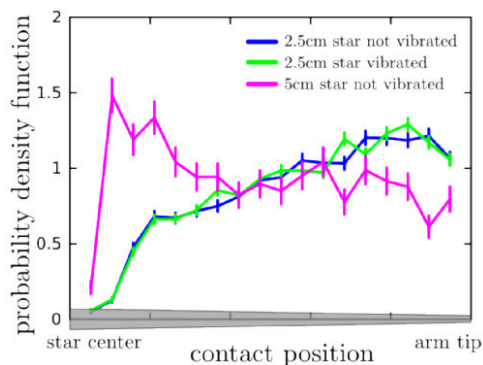


Figure 1.29: Distribution density of the contact position along the arm length of the hexapods packings from Ref. [Barés et al., 2017].

For the shorter arm hexapods, more contacts are concentrated close to the tips. However, for the longer arm hexapods, a higher concentration of contacts is shown close to the center of the particle.

1.3.4 Experimental characterization techniques for packings

Plenty different techniques are used in literature to characterize packed systems. Some of these techniques enable a high description of the system such as the particle-center position and orientation, e.g. X-ray tomography, whereas simpler ones provide system information such as the average packing fraction, e.g. packing height.

Magnetic Resonance Imaging (MRI)

This technique is one of the most sophisticated to characterize packed media. It reconstructs the 3D structure of the packed bed (see Refs. [Jaoshvili et al., 2010, Man et al., 2005]). In Fig. 1.30 (left) a slice from a tetrahedral packed bed in a cylindrical container is obtained by this technique.

Vertical beam gamma-ray scanning

A gamma-ray beam vertically crosses the packed bed from the upper surface of the packing to the bottom of the container, Ref. [Auwerda et al., 2010]. At the bottom there is a sensor which measures the beam intensity and later it is compared to its intensity upwards at the top. Thereby, a relation between the intensity loss and the height-averaged packing fraction at a certain (x, y) coordinates of the horizontal plane is established in Eq. 1.8 where H is the height of the packed bed and $L_s < H$ is the length of solid particles in H . This device enables to estimate the wall effect of the recipient vertical walls on the packing fraction.

$$\langle \phi_s \rangle_H(x, y) = \frac{1}{H} \int_{z=0}^{z=H} \phi(x, y, z) dz = \frac{L_s(x, y)}{H} \quad (1.8)$$

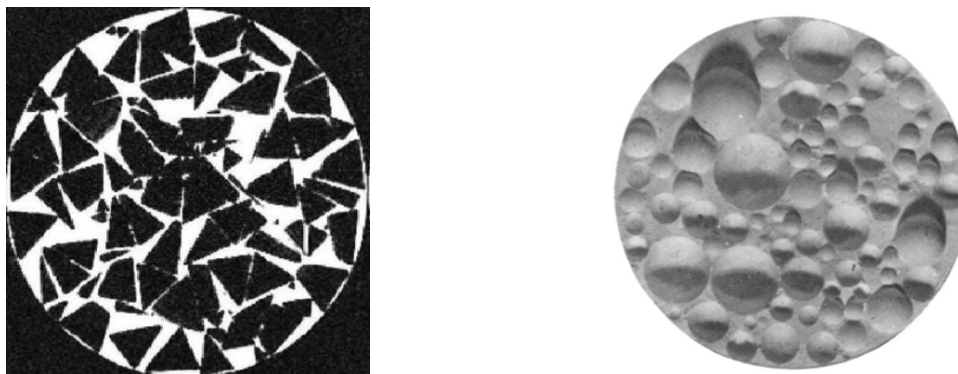


Figure 1.30: Left: A slice from MRI scan of tetrahedral monodisperse particles in a cylindrical container, Ref. [Jaoshvili et al., 2010]. Right: a slice of a polydisperse spherical (logarithmic normal diameter distribution) packing in cylindrical container by the paraffin technique, Ref. [Higuti, 1961].

X-ray tomography

By means of X-ray tomography the position of each particle center is determined. The material of the solid particles must be transparent to the X-ray. Two photographs in the planes $x - z$ and $y - z$ (with z the vertical axis) enable the obtainment of the center coordinates of each sphere in the 3D domain, Ref. [Mueller, 1993]. Besides in Ref. [Barés et al., 2017] this characterizing method is used for nonspherical nonconvex particles to determine the position of their center, orientation and number of contacts.

Furthermore, the combination of tomography and numerical tools such as DEM permits to model and obtain properties which are not directly accessible such as the contact number or the contact force. In [Delaney et al., 2010] the authors, after producing the desirable packing, use the output of tomography as input in a DEM model. Thereby, they are able to obtain the contact point and normal and frictional contact forces.

Solidifying paraffin

The void space between particles is filled up with molten paraffin and then this substance solidifies. The solid formed by particles and the solidified paraffin is drawn from the vessel. Then, the cylindrical body is sliced parallel to the bottom face. The particles at the chopping section are removed leaving dimples at the sliced surface, Ref. [Higuti, 1961]. With this technique it is possible to visualize the packing cross-section shown in Fig. 1.30 (right) and to obtain the packing fraction averaged along the slice cross-section at a certain height, z , (see Eq. 1.9 where A_s is the solid area in the slice cross-section Σ).

$$\langle \phi_s \rangle_{\Sigma}(z) = \frac{1}{\Sigma} \int_{\Sigma} \phi(x, y, z) d\Sigma = \frac{A_s(z)}{\Sigma} \quad (1.9)$$

Electrical tomography

The electrical tomography family includes the capacitance tomography, ECT, the electromagnetic tomography, EMT, and the electrical resistance tomography, ERT. The principle of these techniques is relating the solid packing fraction and some electrical parameter such as capacitance, impedance and inductance for ECT, ERT and EMT, respectively. Depending on the technique, a collection of capacitive plates, electrodes or coils is set at the vertical walls of the typical cylindrical container. The selection of the technique depends upon the materials involved in the sample and the continuity of the solid or fluid phase in the packing, Refs. [Nowak et al., 1998, Villarruel et al., 2000, Mahmoud et al., 2008]. With this technique, the packing fraction averaged along the volume formed by two parallel slice cross-sections separated by ΔH_c at a certain height is obtained (see Eq. 1.10). ΔH_c is the *thickness* of the slice where the sensors capture the solid volume.

$$\langle \phi_s \rangle_{\Sigma, \Delta H_c}(z) = \frac{1}{\Delta H_c \Sigma} \int_{h=z-\Delta H_c/2}^{h=z+\Delta H_c/2} \int_{\Sigma} \phi(x, y, h) d\Sigma dh = \frac{V_s(z)}{\Delta H_c \Sigma} \quad (1.10)$$

Volume-height: cylindrical container

In case of dry packed beds, this technique provides the packing fraction as a function of the system height, averaged along the cross-section (see Eq. 1.9). With a constant section along the height, the void space between the solid particles is filled up with a liquid. By the continuous measurement of the injected liquid volume and the reached height in the packed system the packing distribution fraction along vertical axis is obtained. The quality of this measurement depends on the influence of the *wall effect* of the vertical walls on the packing Refs. [Higuti, 1961, Kolonko et al., 2010, Nowak et al., 1998, Villarruel et al., 2000]. However, we cannot use this technique for particle packings in fluid.

1.3.5 Conclusion of the particle packing review

According to this particle packing review, we expect that the random equiaxed grain packing in solidification is a loose packing with values close to the random loose packing (RLP). In this way, a packing limit in the interval from 55% to 61% is expected for monodisperse spherical grains (fluidized monodisperse spherical packing, Refs. [Jerkins et al., 2008, Schröter et al., 2005, Aste et al., 2007, Delaney et al., 2010]).

The effect of the nonspherical geometry has an important effect on the packing fraction. In case of fluidized octahedral monodisperse grains, the packing fraction is approximately 52%, Ref. [Baker and Kudrolli, 2010]. For the equiaxed dendritic grains in solidification with six principal arms in the $\langle 100 \rangle$ directions, the packing limit is expected to dramatically decrease with respect to the spheres. According to the spiky particles composed by three ellipsoids forming the $\langle 100 \rangle$ directions with a central sphere in Ref. [Malinouskaya et al., 2009], the packing fraction decreases down to approximately 10% for the most spiky geometry.

Moreover, in case of cohesive monodisperse packings of spheres, much looser packings are obtained. The packing fractions can decrease down to 10%, Ref. [Dong et al., 2012].

The effect of the hydrodynamic conditions on the packing fraction is governed by one dimensionless parameter which is the Stokes number of the grains approaching to the packed grain bed, Ref. [Farrell et al., 2010], at least in case of sequential deposition. When the Stokes number of the approaching particles is lower than a certain threshold value, the packing achieves its loosest configuration (RLP), then, the influence of the hydrodynamic approaching conditions is negligible under the threshold Stokes value which depends on the interparticle friction: the Stokes threshold ranges from approximately 0.1 and 5 for low and high interparticle friction.

Lower influence of the interparticle friction and polydispersity on the packing fraction is found for the spherical collections. The higher the interparticle friction is, the looser is the packed system with a decrement of a relatively 8% with respect to the frictionless packing fraction, Ref. [Silbert, 2010]. In case of polydispersity of spheres or pentagons (2D convex particles), the larger the size polydispersity is, the denser the packing, Refs. [Desmond and Weeks, 2014, Nguyen et al., 2014].

1.4 Numerical techniques for packing modeling

There are two main groups of numerical techniques for packing modeling:

- Geometrical methods: the physics of the packing problem is not taken into consideration. They do not provide information about the packing dynamics since these algorithms do not follow physical laws. Examples: the *Monte Carlo rejection method* and *expanding system method*.

According to Ref. [Auwerda et al., 2010], the Monte Carlo rejection method consists of the initial creation of a random point cloud in the domain, typically 10^5 times the number of spheres. Hence, the vessel is filled up with spheres from bottom to top. Sphere centers are checked at diverse random points (rejected) until there is no overlapping with other spheres. The expanding system algorithm consists of the initial set of the sphere centers randomly distributed in the domain. Afterwards, the size of the sphere is progressively increased. If there is contact among spheres, they rearrange to avoid overlappings.

- Dynamics methods. Two methods of packing generation are discussed:
 - 1) Lubachevsky-Stillinger algorithm (LSA) and 2) the Discrete Element Method (DEM). The LSA was created to understand the properties of matter (Condensed Matter Physics) such as the amorphous solids [Lubachevsky and Stillinger, 1990]. Based on Molecular Dynamics, the initial infinitesimal spheres are located at random position with random velocities. Besides, their diameter is increased linearly with time. In this way, the particle collision frequency is progressively increasing until a top threshold. At this point, the system is jammed and the simulation is stopped. Depending on the sphere growth, different jammed configurations are possible. The interparticle collisions are elastic without permitted overlapping.

The DEM permits to model the dynamics of a large amount of particles: the dynamics of the granular media, the interparticle contact forces are described by different types of contact models related to the interparticle overlapping. The dynamics of each particle is calculated from the force and momentum balance. Additionally, other interactions can be accounted: particle-recipient contact, hydrodynamic forces on the particles, electro-magnetic forces on the particles, etc. The DEM will be presented in detail in Chap. 4.

In Ref. [Auwerda et al., 2010] the Monte Carlo rejection method, expanding system method and DEM are compared. They are used to generate a dry monodisperse sphere packing to reproduce the physical packing by gravity deposition in a dry cylindrical vessel. For this deposition protocol, the DEM and expanding system method numerical techniques provide similar results than the experiments. They give accurate predictions of the wall-effect and the average solid packing fraction (60.10%, 60.28% and 60.47% for the DEM, expanding method and experimental results, respectively). The Monte Carlo rejection method obtains a lower average packing fraction of 54.68%.

There is an example of application of LSA to hard monodisperse spheres in Ref. [Torquato et al., 2000]. Herein 500 particles are randomly pack in a cubic periodic domain with an

initial average solid fraction of 0.30. Different growth rates lead to different final arrangements. The average packing fraction is inversely proportional to the particle growth rate: 1) rapid growth forms very random packing since the system does not have sufficient time for rearrangement; 2) low growth leads to higher packing fractions losing randomness; 3) infinitesimal growth rate produces ordered arrangements. Due to the random character of the method, the authors repeat each simulation 27 times to mean.

In this thesis, we have selected the DEM technique to model the equiaxed grain sedimentation and packing phenomenon since we are interested in describing the particle dynamics of each grain and the interactions among them (see Chap. 4). Plenty of information can be found in literature about DEM since this numerical technique is broadly used in a large range of domains, such as the Mineral processing, Chemical Engineering or Geophysics.

In Table 1.9, we firstly collect some pure DEM references that include examples of dry spherical and nonspherical packing or strategies to model the dendritic and globular grain morphologies. Two examples of spherical and nonspherical particle sedimentation and packing that account the fluid dissipation on the particles by a simple drag approach are also included herein (afterwards the CFD-DEM coupled approach is also introduced). By these references, we better understand important questions for packing such as the domain size relative to the particle size or the particle collection size in packing modeling.

Table 1.9: Discrete Element Method examples.

Ref.	Geometry	Phenomenon	N_{pt}
[Delaney et al., 2010]	Monodisperse spheres	Dry packing by deposition	7000
[Auwerda et al., 2010]	Monodisperse spheres	Dry packing by deposition	5500
[Dong et al., 2012]	Monodisperse spheres	Packing in liquid by sedimentation (fluid accounted by a drag model)	3500
[Delaney et al., 2011]	Monodisperse ellipsoids	Packing in liquid by sedimentation (fluid accounted by a drag model)	500
[Pasha et al., 2016]	Nonspherical (clumped spheres)	Dry rotary batch seed coater	1250
[Wachs et al., 2012b]	Nonspherical (Convex geometries)	Dry packing by deposition Dry horizontal rotating drum	250 3000
[Yuan et al., 2012]	Equiaxed 2D dendrites polydisperse geometries	Mushy-zone mechanics	225

Two publications are chosen as a reference of monodisperse particle packing in liquid by sedimentation due to the straightforward approach to model the dissipation effect of the fluid on the particles (spherical and ellipsoidal geometries in Refs. [Dong et al., 2012]

and [Delaney et al., 2011], respectively). In both publications, the simulation domain is a rectangular box (see Fig. 1.31) with vertical periodic boundaries in order to reduce the wall effect on the average packing fraction. The particles pose over a horizontal rigid wall. The initial particle position and orientations are random with null linear and angular particle velocities. In sphere case the cross section is $15d \times 15d$ with d the sphere diameter, whereas, in the ellipsoidal case the cross-section is $25d_{eq} \times 25d_{eq}$ with d_{eq} the equivalent diameter of the ellipsoid. A collection of 500 ellipsoids is used in [Delaney et al., 2011] for the packing.

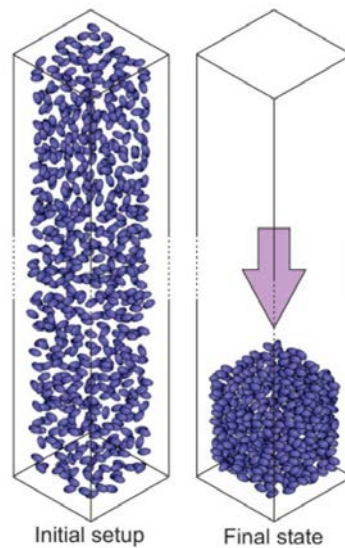


Figure 1.31: Particle sedimentation and packing in viscous liquid: rectangular box domain with vertical periodic boundaries. Initially the particles are spread along the whole domain with random positions and orientations. Figure from Ref. [Delaney et al., 2011].

Among the different strategies to represent the nonspherical grain geometry and to tackle the contact detection (see the reviewal publication about CFD-DEM Ref. [Zhong et al., 2016]), the surface discretization by spherical elements with the *clumped logic* for the contact detection is chosen. As later explained in detail in Chap. 4, this strategy is selected since it facilitates to have an arbitrary grain geometry logic in the solver making the contact detection easier. Two publications based on the clumped logic (Refs. [Yuan et al., 2012] and [Pasha et al., 2016]) are selected as references to model the nonspherical dendritic and globular morphology of our grains. In [Yuan et al., 2012], 2D dendritic envelopes are discretized by means of polydisperse circles, Fig. 1.33 (left) whereas in Ref. [Pasha et al., 2016] the volume of the nonspherical grain geometry is modeled by means of polydisperse spheres, Fig. 1.33 (right).

CFD-DEM approaches are used to solve both the fluid and particle motion in particle-laden flows. We classify the CFD-DEM work in two families:

- *Averaged Navier-Stokes* coupled with DEM: this is the most extended CFD-DEM

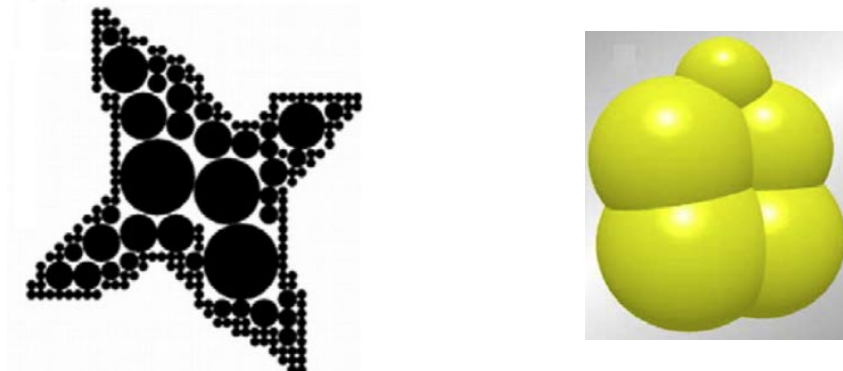


Figure 1.32: Left: 2D dendritic envelope morphology by 160 clumped polydisperse spheres (image from Ref. [Yuan et al., 2012]). Right: 3D globular morphology by 5 clumped polydisperse spheres (image from Ref. [Pasha et al., 2016]).

approach. The effect of the fluid on the particles (bouyancy, drag or lift) is implemented by means of models accounting the multiparticle, nonspherical and Reynolds effects. On the other hand, the influence of the particles on the fluid is accounted for example by means of the locally averaged Navier-Stokes equations where the properties of the lagragian particles are averaged in the Eulerian mesh. In this approach, the particle characteristic size is commonly much smaller than the fluid mesh size.

By this CFD-DEM coupling approach, a large amount of particles can be modeled. Specially, in case of spheres (see Refs. [Zhao and Shan, 2013, Afkhami et al., 2015, Liu et al., 2013, Wu et al., 2014]), modeling up to $o(10^7)$ spheres in Ref. [Sun and Xiao, 2016] with efficient parallelization techniques.

- *Immersed* full-coupling CFD-DEM: the fluid flow is disturbed by the presence of the particles, in this way, the flow is solved considering the boundaries that the immersed particles provide. The fluid flow can be precisely computed around the immersed particles even for complex morphologies. The fluid mesh size must be considerably smaller than the particle characteristic size, increasing the computational cost. As examples of fluid-particle coupling techniques we include: the adaptive meshing methods, Ref. [García et al., 2011], or the Immersed Boundary Method, Ref. [Peskin, 2002].

Scarse work is done in the domain of large collections of 3D nonspherical moving particles immersed in a fluid. The work for 3D nonspherical solids is basically focused on the computation of the fluid flow around a fix 3D nonspherical particle. Very complex morphologies can be modeled, see Fig. 1.34 (left). In Fig. 1.34 (right), the phenomenon of avalanche is modeled by means of 250 monodisperse spheres where the fluid-solid coupling is carried out with the Immersed Boundary Method.

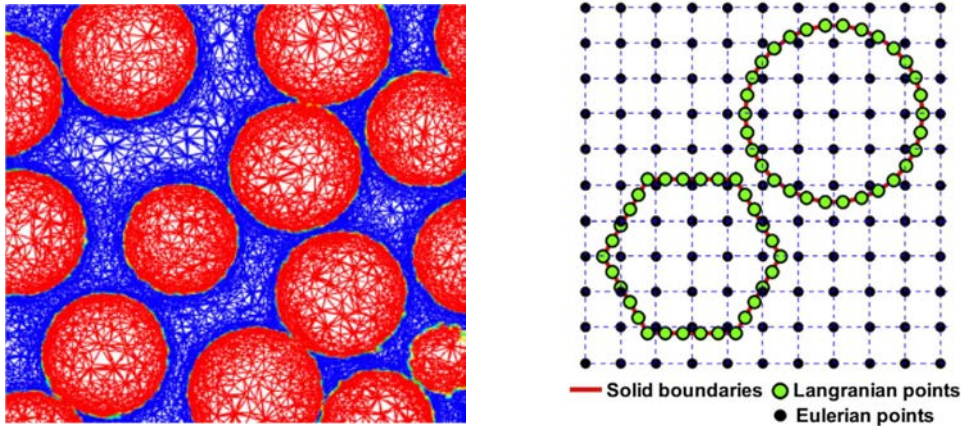


Figure 1.33: Left: example of adaptive meshing method. In this case, the fluid-solid coupling is solved by a two-phase adaptive finite element method. The solid particles are a second fluid, so Navier-Stokes equations are also solved at the solid regions. Image from Ref. [García et al., 2011]. Right: schematic representation of the solid boundaries and fluid points with the Immersed Boundary Method. The Navier-Stokes fluid equations are solved in both fluid and solid regions by the Lattice Boltzmann Method. Image from Ref. [Fu et al., 2017].

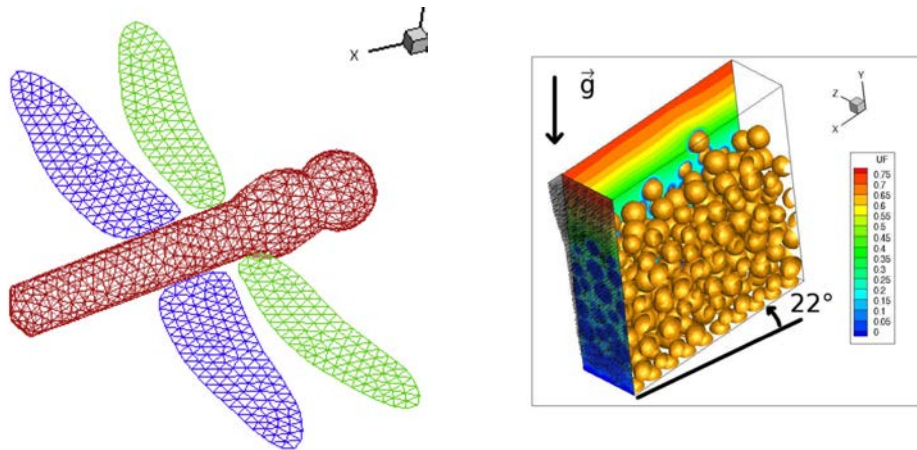


Figure 1.34: Left: in Ref. [Wang et al., 2014], the fluid flow is computed around 3D nonspherical complex geometry solids. The fluid motion around the particles is solved by means of the Lattice Boltzmann Method and the Immersed Boundary Method technique. Right: 3D avalanche phenomenon with 250 spheres. The Immersed Boundary Method is used to fluid-solid coupling. Image from Ref. [Izard et al., 2013].

1.4.1 Conclusion of the numerical techniques review

According to this review of the numerical techniques to model the particle packing phenomenon, the packings can be formed by both geometrical and dynamic algorithms. The geometrical algorithms are much simpler to develop than the physical algorithms. They can be useful to provide preliminary packing results or to reproduce packings which are valid for certain asymptotic physical situations (see Sec. 4.2).

On the other hand, with a dynamic method, more specifically by a Discrete Element Method, we can simulate the phenomenon of sedimentation and packing of equiaxed dendritic grains, including the interparticle contact of the nonspherical grains, interparticle frictional contact or the fluid influence on the packing grains.

There are three different strategies to model the influence of the fluid on the grains. Thereby, classifying them from higher to lower difficulty level:

- *Immersed* full-coupling CFD-DEM: this is the simulation approach that provides a better description of the physics of the actual phenomenon, solving the fluid flow around the moving bodies. However, the development from scratch of this model for a large number of nonspherical grains (several hundred grains) is not affordable in a three-year experimental-numerical thesis. Our own experience in this approach shows us that the computational time of this type of simulations can be the order of several months, even parallelized. In this way, this approach is abandoned for our thesis.
- *Soft* full-coupling CFD-DEM: this strategy is focused for a large amount of particles (specially monodisperse spheres). The solution depends on the models used to describe the fluid-grain interactions (buoyancy, drag, lift, etc) including the nonspherical, multigrain and Reynolds effects. For the dendritic grains this strategy requires an experimental calibration. Despite the important required development (DEM for nonspherical grains and CFD), the fluid-grain interaction models must be experimentally calibrated. In this way, this model is not affordable in a three-year experimental-numerical thesis.
- DEM including the fluid dissipation effect on the grains, Ref. [Delaney et al., 2011]. In this approach the fluid flow is not solved. The kinetic energy of the packing grains is dissipated by means of models of the fluid-solid interaction (drag, lift, etc). As in the previous strategy, this method requires of an experimental calibration to reproduce the packing dynamics. This approach is the most suitable for a three-year experimental-numerical thesis.

Second Part

Theoretical, experimental and modeling
analysis

Introduction

As previously presented in Sec. 1.2.1, the grain packing phenomenon in solidification is coupled to many other phenomena. Thereby, several assumptions are taken into consideration along next theoretical, experimental and numerical chapters (Chaps. 2, 3 and 4, respectively) in order to decouple the grain packing from the rest of phenomena in solidification. We summarize these assumptions in several points:

- We focused on the mesoscopic scale of the grain packing phenomenon, i.e. we investigate a domain of a size of several grains (the order of 10 grains). For grains of size ranging from $100 \mu m$ up to $1 cm$, this domain has a volume in the interval from $1 mm^3$ up to $10^3 cm^3$.
- We consider an equiaxed grain morphology simplification, neglecting the secondary-arms, by means of the idea of envelope which is a virtual surface wrapping the dendrite branches.
- The transport of energy is neglected: athermal models are considered.
- The transport of solute is neglected.

In Chap. 2, we develop a theoretical model of the grain dynamics in case of sequential particle packing. The objective of this chapter is to show the most important hydrodynamic dimensionless parameters governing this phenomenon: the *Stokes* and *Archimedes* numbers. These parameters are considered in Chaps. 3 and 4 to create a hydrodynamic similarity between the grain packing in the actual casting processes and our experimental and simulated packings. In this chapter we account for the possible grain growth previous to packing.

Chapter 3 is based on an experimental model that scales up the grain packing phenomenon. It consists on a sedimentation vertical column of size of $1 m$. With this model we visualize the packing phenomenon and we measure the average packing fraction under different hydrodynamic conditions and for two different monodisperse particle collections characterized by a spherical and dendritic morphologies. We neglect the dendritic growth: the grains have a fixed morphology.

The experimental investigation is completed with a numerical modeling chapter, Chap. 4. Herein, a wide range of effects on the packing fraction and packing dynamics are investigated: grain morphology, friction between grains, cohesion between grains, grain size polydispersity, and so on.

Finally, the results from Chaps. 3 and 4 are applied to solidification in Chap. 5. Herein, we propose a correlation between the packing fraction of equiaxed grains and the packing conditions: geometry of the grains and hydrodynamic conditions. Additionally, we also propose a correlation between the characteristic size of the packing phenomenon as a function of the packing conditions of grain geometry and hydrodynamic conditions.

Chapter 2

Single grain approaching a packed grain bed: theoretical analysis

2.1 Introduction

Solidification is an essential process in materials science, characterized by its complexity to be modeled: grain nucleation, microsegregation, grain growth, thermo-solutal convection, solid phase sedimentation, dendritic granular rheology, etc. In the mushy zone there are two typical flow regimes: 1) Slurry flow, where both solid and liquid phases move. The solid crystals freely move both settling and dragged by the melt flow. 2) Porous medium, where solid phase becomes a sponge-like medium in which melt can still flow. As previously introduced in Chap. 1.2.1, the packing fraction front separates both behaviors. The formation of the packing mainly depends on the morphology and on the hydrodynamic conditions of the approaching grains to packing.

Understanding the *close-to-packing dynamics* of the solid grains is fundamental to comprehend the influence of the hydrodynamics of settling on the packing. In this theoretical chapter, we focus on the dynamics of a single particle approaching and reaching mechanically stable equilibrium over a packed particle bed. This corresponds to particle packing by sequential deposition. In this vein, only the particle motion perpendicular to the packed particle bed is studied, not considering the tangential component.

Two phases are identified: 1) approaching phase; 2) rearrangement phase. During the approaching phase, the particle immersed in the viscous fluid, dissipates its initial kinetic energy. In this phase, the packed particle bed is modeled with an impermeable flat wall. Additionally, once the particle poses over the packed particle bed, the rearrangement phase begins. After this first contact, the particle moves to a more mechanically stable position.

The forces on the particle that we include in the analysis are: the fluid viscous dissipation (drag and lubrication), which is fundamental to the approaching phase, the apparent weight and the melt flow dragging the particle. The apparent weight and melt flow act as driving force for particle motion. Moreover, the effect of the grain growth on the particle

motion is also analyzed.

Once the single-particle dynamics is modeled, a dimensional analysis is carried out to determine the fundamental dimensionless parameters governing this phenomenon: the Stokes and the Archimedes numbers. Finally, the order of magnitude of these parameters for equiaxed grains in steel and aluminum castings are determined.

2.2 Approaching phase

Firstly, the approaching phase is modeled. A solid particle is perpendicularly approaching a bed formed by previously-packed particles. This moving particle has a known initial velocity and it is initially located *relatively far* from the packed particle bed, in order to initially neglect the fluid lubrication effect. This situation is schematically illustrated for spheres in Fig. 2.1.

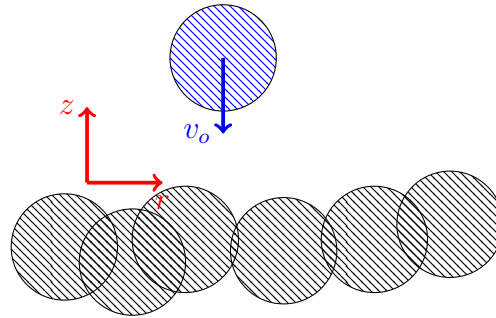


Figure 2.1: Schematic 2D sketch of a sphere approaching a previously-packed sphere-bed. The coordinates $\{r, z\}$ represent the tangential and perpendicular to packed front directions, respectively.

The model of the dynamics of the approaching particle is built based on next statements:

- Incompressible Newtonian viscous fluid.
- Rigid particles: particle deformations are neglected.
- Equivalent spheres: any particle of arbitrary geometry is characterized by its equivalent diameter, d_{eq} . We treat these particles as spheres with identical volume, identical inertia.
- Basset non-steady force is neglected due to the low accelerations.
- Rotational energy is neglected with respect to the translational energy of the particle.
- Steady flow, v_{flow} in the \hat{e}_z direction: we include a component of flow perpendicular to the packing front in order to represent the *shrinkage flow* in the mushy zone.
- The particle can grow with a known growth rate.

- We neglect cohesion forces between particle and packed particle bed.
- Particle bouncing is not considered: if the *Stokes* dimensionless number for the particle approach is lower than the critical value of rebound ($St_c \approx 10$ [Izard et al., 2014]), the restitution coefficient is null.
- The particle drag tensor is spherical.
- Semi-infinite domain for the fluid region is considered.
- The hydrodynamic interaction between the moving particle and the previously packed particle bed is modeled by means of a the lubrication force on a sphere approaching a wall. From now on, the term *wall* is employed to refer to the top surface that the packed particles form.

We describe the particle dynamics by means of the Eq. 2.1 and its appropriate initial conditions:

$$\frac{d}{dt}(\rho_{pt}V_{pt}\mathbf{v}_{pt}) = \mathbf{F}_g + \mathbf{F}_d + \mathbf{F}_{wall} + \mathbf{F}_a + \mathbf{F}_{flow} \quad (2.1)$$

- $\rho_{pt}V_{pt}\mathbf{v}_{pt}$: particle momentum. V_{pt} is the particle volume.
- \mathbf{F}_g : particle apparent weight z -component.
- \mathbf{F}_d : drag force with null flow.
- \mathbf{F}_{wall} : hydrodynamic force resulting from the particle-wall interaction.
- \mathbf{F}_a : non-steady force due to the inertia of the fluid surrounding the solid particle (added mass).
- \mathbf{F}_{flow} : force due to a vertical fluid convection component. In solidification a shrinkage flow perpendicular to the packed particle bed is common (see scheme in Fig. 1.5.)

In order to model each of the forces involved in the particle motion, we present models for the drag force, particle-wall lubrication force and particle growth.

2.2.1 Drag force

The drag force is the result of the relative motion between particle and fluid, which can be written as:

$$F_{drag} = \frac{1}{2}C_d\rho_f S_{ref}v_{pt,f}^2 \quad (2.2)$$

Where C_d is the drag coefficient, S_{ref} is the projected surface to the motion direction or cross-section, ρ_f is the fluid density and $v_{pt,f}$ is the velocity of the particle with respect to the fluid.

Assuming the particular case of *Stokes regime*, where the Reynolds number is low, $Re = (\rho_f d_{eq} v_{pt,f}) / \mu_f \ll 1$, the previous drag coefficient becomes $C_d = \frac{24 f_{geo}}{Re}$. Thereby, the Eq. 2.2 is rewritten as Eq. 2.3, Ref. [Leith, 1987].

$$F_{drag} = 3\pi \mu_f d_{eq} v_{pt,f} f_{geo} \quad (2.3)$$

The new coefficient f_{geo} is the so-called the dynamic shape factor and it exclusively depends on the geometrical shape of the particle. For the spherical geometry $f_{geo} = 1$ whereas for nonspherical geometry $f_{geo} > 1$. According to Ref. [Leith, 1987], for the case of prisms with three axes of symmetry (convex particles), the dynamic shape factor basically depends on the $d_{S_{ref}}/d_{eq}$ (see Eq. 2.4), where $d_{S_{ref}}$ is the equivalent diameter of the projected surface in case of the non-spherical object.

$$f_{geo} \approx 0.357 + 0.684 \frac{d_{S_{ref}}}{d_{eq}} \quad (2.4)$$

We use the previous expression to evaluate the geometrical shape factor of dendrites, assuming that it can give a useful approximation in case of dendrites. Using the experimental dendrite model of Chap. 3 where $\frac{d_{S_{ref}}}{d_{eq}} \approx 1.48$, we obtain $f_{geo} \approx 1.37$. Thereby, the drag force is slightly increased with respect to that of the spherical geometry.

2.2.2 Particle-wall lubrication force

When a rigid particle approaches to a smooth infinite impermeable plane within an incompressible fluid, the fluid located between the particle and the wall undergoes an overpressure (squeezing). This overpressure balances the viscous and inertial effects of the fluid between particle and wall which must be removed from the particle trajectory.

A preliminary model of lubrication is the classical *Lubrication Theory*, Ref. [Lecoq et al., 2004] (see Reynolds equation, Eq. 2.5). The corresponding hypothesis of this model are given by Eqs. 2.6, 2.7 and 2.8, where h_l is the lubrication film thickness, p is the fluid pressure in the film.

$$\frac{\partial h_l}{\partial t} = \frac{1}{12\mu_f r} \left(\frac{\partial}{\partial r} \left(r h_l^3 \frac{\partial p}{\partial r} \right) \right) \quad (2.5)$$

$$\frac{h_l}{d} \ll 1 \quad (2.6)$$

$$Re \frac{h_l}{d} = \frac{\rho_f v h_l}{\mu_f} \ll 1 \quad (2.7)$$

$$\frac{\partial p}{\partial z} \approx 0 \quad (2.8)$$

Integrating the pressure over the particle surface provides the so-called *lubrication force*. In case of a sphere the lubrication force is given by Eq. (2.9), Ref. [Lecoq et al., 2004].

$$F_{wall} = 6\pi\mu_f \left(\frac{d}{2}\right)^2 \frac{dh_l/dt}{h_l} \quad (2.9)$$

This force is inversely proportional to the gap between particle and wall and directly proportional to the approaching velocity. By means of this model, the time to contact tends to infinite (the so-called *Stokes Paradox*) since the lubrication force monotonously increases with the decrement of the gap. The wall roughness, wall permeability or compressibility of the fluid limit the top value of the lubrication force, and consequently providing a finite time of contact.

Moreover, we have also considered the case of a smooth rigid sphere approaching to a second identical sphere along the line which joins the centers of both spheres (see Ref. [Davis et al., 1986]), obtaining the same result for the lubrication force as that of Eq. 2.9, where the gap is the minimum distance between both spheres.

Other lubrication models which add corrective terms to the lubrication force of Eq. 2.9 for spherical geometry are available in literature. For instance:

- Brenner, Ref. [Brenner, 1961]: this model considers the influence of the wall effect either relatively near to the wall and further from it. See Eqs. 2.10, 2.11 and 2.12).

$$F_{wall_{Br}} = 6\pi\mu_f \left(\frac{d}{2}\right)^2 \frac{dh_l/dt}{h_l} \lambda_{Br} \quad (2.10)$$

$$\lambda_{Br} = -1 + \frac{4}{3} \sinh \alpha_{Br} \sum_{n=1}^{\infty} \frac{n(n+1)}{(2n-1)(2n+3)} \left(\frac{2 \sinh(2n+1)\alpha_{Br} + (2n+1) \sinh 2\alpha_{Br}}{4 \sinh^2(n+1/2)\alpha_{Br} - (2n+1)^2 \sinh^2 \alpha_{Br}} - 1 \right) \quad (2.11)$$

$$\alpha_{Br} = \cosh^{-1} \left(1 + \frac{h_l}{d/2} \right) \quad (2.12)$$

- Cox and Brenner, Ref. [Cox and Brenner, 1967]: the first-order inertial influence is considered via a corrective term that is function of the particle Reynolds number (see Eq. 2.14). The hypothesis in Eq. 2.6 is considered.

$$F_{wall_{CoxBr}} = 6\pi\mu_f \left(\frac{d}{2}\right)^2 \frac{dh_l/dt}{h_l} \lambda_{CoxBr} \quad (2.13)$$

$$\lambda_{CoxBr} = 1 - \frac{1}{5} \left(1 + \frac{Re}{2} \right) \left(\frac{h_l}{d/2} \right) \ln \left(\frac{h_l}{d/2} \right) \quad (2.14)$$

The corrective terms to the lubrication force of Brenner, λ_{Br} , and Cox and Brenner, $\lambda_{CoxBr}(Re)$ are shown in Fig. 2.2 as a function of the dimensionless layer thickness h_l/d_{eq} .

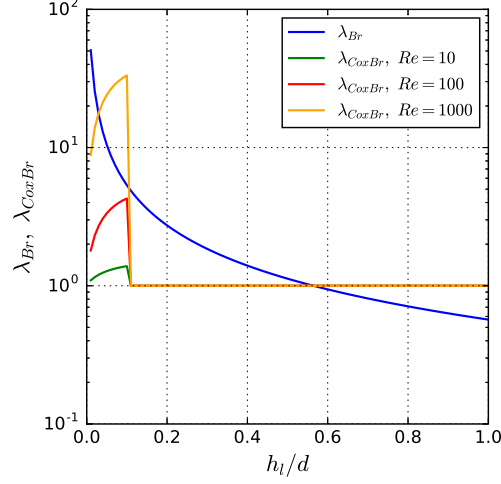


Figure 2.2: Corrective terms to the lubrication force of Brenner, λ_{Br} , and Cox and Brenner, λ_{CoxBr} .

We define the dimensionless parameter λ_{wall} already introduced in Eq. 2.17 as the ratio between the particle-wall lubrication force and the Stokes drag force:

$$\lambda_{wall} = \frac{F_{wall}}{F_d} \quad (2.15)$$

2.2.3 Particle growth

A simple time-evolution of the equivalent diameter of the approaching particle is presented (see Eq. 2.16). The constant couple of parameters (K_{gr}, n) are defined as $K_{gr} > 0$ and $n \geq 1$ for particle diameter growth. No diameter reduction is considered $K_{gr} < 0$.

$$d_{eq}^n(t) = d_{eq_0}^n + |K_{gr}| t \quad (2.16)$$

Considering a linear evolution of the grain with time, $n = 1$, we can identify $|K_{gr}|$ with dd_{eq}/dt . According to the simulations of aluminum DC casting (see Appx. A.1) dd_{eq}/dt has values up to $10^{-2} \mu m/s$.

2.2.4 Particle motion equation

The Eq. 2.1 is rewritten in Eq. 2.17 using the models previously explained and the reference frame of Fig. 2.1. This frame is defined by the base \mathcal{A} : $\{\hat{e}_r, \hat{e}_\beta, \hat{e}_z\}$ with $\hat{e}_\beta = \hat{e}_z \times \hat{e}_r$. Its origin is in the point of the first contact of the particle with the packed bed.

The terms of this equation are purposely ordered as the *harmonic oscillator* equation: where the first term of the left hand is inertia of the particle and fluid (added mass), the second term is the viscous dissipation (in absense of fluid flow), and the right hand side is the driving force of the particle's motion due to the apparent weight and fluid flow dragging it, Eq. 2.18. A stiffness term does not appear in this phenomenon.

The initial conditions of position and velocity are given in Eqs. 2.19 and 2.20, respectively.

$$\left(\rho_{pt} V_{pt} + \rho_f \frac{V_{pt}}{2} \right) \frac{d^2 z}{dt^2} + \left(\mu_f \frac{d_{eq}}{2} 6\pi f_{geo} (1 + \lambda_{wall}) + \rho_{pt} \frac{dV_{pt}}{dt} \right) \frac{dz}{dt} = \sum F_{drive} \quad (2.17)$$

$$\sum F_{drive} = -\Delta \rho g_o \cos(\alpha_{inc}) V_{pt} + \mu_f \frac{d_{eq}}{2} 6\pi f_{geo} v_{flow} \quad (2.18)$$

$$z(t = 0) = z_o \gg d_{eq} \quad (2.19)$$

$$\frac{dz}{dt}(t = 0) = v_o \quad (2.20)$$

The *gap distance*, z , is the vertical distance between the top of packed bed and the equivalent sphere. The position of the particle center of mass is given by:

$$z_c = z + \frac{d_{eq}}{2} \quad (2.21)$$

The growth model must be incorporated through the particle volume terms V_{pt} and dV_{pt}/dt .

In case the packed particle bed is not horizontal, only the particle motion component that is perpendicular to the packed particle bed is considered. The projection of the volumetric force \mathbf{g}_o is considered: $-g_o \cos(\alpha_{inc}) \hat{e}_z$, where α_{inc} is simply the angle of the inclined bed plane with respect to the horizontal plane. α_{inc} is assumed to be lower than the maximum stability angle. This critical angle depends on the particle geometry and interparticle friction. In case of monodisperse spheres it ranges from approximately 10 to 50° as a function of friction, Ref. [Sánchez and Scheeres, 2016]. In case of hexapods, the stability angle can even reach 90°, Ref. [Barés et al., 2017].

2.2.5 Dimensionless analysis

The objective of this section is to determine the dimensionless parameters governing the particle approaching phase of the packing phenomenon. We scale the equation of the particle approaching dynamics, Eq. 2.17, using the following characteristic scales of time, length and mass (Eqs. 2.22, 2.23 and 2.24, respectively). The grain motion time is used as the characteristic time.

$$t_{ch} = \frac{d_{eqo}}{v_o} \quad (2.22)$$

$$l_{ch} = d_{eqo} \quad (2.23)$$

$$m_{ch} = \rho_{pt} d_{eqo}^3 \quad (2.24)$$

where d_{eqo} and v_o are the initial particle equivalent diameter and the initial perpendicular-to-wall velocity, respectively. As characteristic time, we select the time needed by a particle to move over a distance of d_{eqo} with the initial velocity, v_o . Thereby, Eqs. 2.25, 2.26, 2.27, 2.28 and 2.29 for dimensionless time, particle position, velocity, acceleration, and equivalent diameter are obtained, respectively.

$$t^* = \frac{t}{d_{eqo}/v_o} \quad (2.25)$$

$$z^* = \frac{z}{d_{eqo}} \quad (2.26)$$

$$dz^*/dt^* = \frac{dz/dt}{v_o} \quad (2.27)$$

$$d^2z^*/dt^{*2} = \frac{d^2z/dt^2}{v_o^2/d_{eqo}} \quad (2.28)$$

$$d_{eqo}^* = \frac{d_{eq}}{d_{eqo}} \quad (2.29)$$

where (*) refers to the dimensionless variables. Eq. 2.17 is rewritten as Eq. 2.30.

$$[A] \frac{d^2z^*}{dt^{*2}} + [B] \frac{dz^*}{dt^*} = -[C] \quad (2.30)$$

$$[A] = \frac{\pi}{6} \left(1 + \frac{1}{2} \frac{\rho_f}{\rho_{pt}} \right) \rho_{pt} d_{eqo}^2 v_o^2 (d_{eq}^*)^3 \quad (2.31)$$

$$[B] = 3\pi f_{geo} \mu_f d_{eqo} v_o d_{eq}^* (1 + \lambda_{wall}(z^*)) + \frac{\pi}{2} \rho_{pt} d_{eqo}^2 v_o^2 d_{eq}^* \frac{dd_{eq}^*}{dt^*} \quad (2.32)$$

$$[C] = \frac{\pi}{6} (1 - \lambda_{flow}) \left(1 - \frac{\rho_f}{\rho_{pt}} \right) \rho_{pt} g_o \cos(\alpha_{inc}) d_{eqo}^3 (d_{eq}^*)^3 \quad (2.33)$$

where the dimensionless parameter λ_{flow} considers the convection flow perpendicular to the wall, defined in Eq. 2.34, where $v_{\Delta\rho}$ is simply the terminal velocity in the absence of any convection flow which is given by $v_{\Delta\rho} = \frac{\Delta\rho g_o \cos(\alpha_{inc}) d_{eq}^2}{18 f_{geo} \mu_f}$.

$$\lambda_{flow} = \frac{v_{flow}}{|v_{\Delta\rho}|} \quad (2.34)$$

Assuming that only approaching is possible, this previous parameter is in the range $-\infty < \lambda_{flow} < 1$. With $\lambda_{flow} = 1$ the apparent weight and the fluid flow forces are balanced and the particle has no motion. Nevertheless, for the shrinkage flow in solidification we consider the values $\lambda_{flow} < 0$.

A dimensionless parameter, Γ , is defined to compare the importance of the growth with respect to the particle motion. We define it as the ratio between the *growth characteristic time* and *motion characteristic time* (see Eq. 2.35).

$$\Gamma = \frac{t_{chgr}}{t_{ch}} \quad (2.35)$$

where t_{chgr} is the time needed for a particle to grow from d_{eqo} to $2d_{eqo}$. With the model of growth of Eq. 2.16, Γ is rewritten in Eq. 2.36.

$$\Gamma = \frac{d_{eqo}^{n-1}(2^n - 1)v_o}{|K_{gr}|} \quad (2.36)$$

Additionally, with the used growth law the terms $d_{eq}^*(t^*)$ and $\frac{d}{dt^*}d_{eq}^*(t^*)$ are rewritten as:

$$d_{eq}^*(t^*) = \left(1 + \frac{2^n - 1}{\Gamma} t^*\right)^{1/n} \quad (2.37)$$

$$\frac{d}{dt^*}d_{eq}^*(t^*) = \frac{2^n - 1}{n\Gamma} (d_{eq}^*(t^*))^{1-n} \quad (2.38)$$

In this way, a single dimensionless parameter governs the particle growth with respect to the approaching motion, Γ . Three different cases are distinguished:

$$\Gamma = \begin{cases} \gg 1, & \text{Growth is negligible compared to approaching motion.} \\ \approx 1, & \text{Growth and approaching motion are coupled.} \\ \ll 1, & \text{Approaching motion is negligible compared to growth.} \end{cases} \quad (2.39)$$

The terms [B] and [C] are compared with respect to the term [A] in Eqs. 2.40 and 2.41:

$$\frac{[B]}{[A]} = \frac{2}{\tilde{S}t} (d_{eq}^*)^{-2} \left(1 + \frac{d_{eq}^*}{2z^*}\right) + 3 \left(1 + \frac{\rho_f}{2\rho_{pt}}\right)^{-1} (d_{eq}^*)^{-1} \frac{dd_{eq}^*}{dt^*} \quad (2.40)$$

$$\frac{[C]}{[A]} = (1 - \lambda_{flow}) \left(\frac{1 - \frac{\rho_f}{\rho_{pt}}}{1 + \frac{1}{2}\frac{\rho_f}{\rho_{pt}}}\right) \frac{d_{eqo}}{v_o^2} g_o \cos(\alpha_{inc}) \quad (2.41)$$

Where the dimensionless number $\tilde{S}t$ is the Stokes number, Eq. 2.42. We retain the fluid inertia term which becomes important in the particular case of similar solid and liquid

density, Ref. [Harada et al., 2000]. This number computes the ratio between particle inertia and viscous dissipation. The conventional Stokes number does not include the fluid inertia. We have also included the geometrical drag factor of non-spherical grains in the Stokes number.

$$\tilde{St} = \left(\frac{1}{f_{geo}} \right) \left(1 + \frac{1}{2} \frac{\rho_f}{\rho_{pt}} \right) \left(\frac{\rho_{pt} v_o d_{eq_o}}{9\mu_f} \right) \quad (2.42)$$

Furthermore, it is known that the initial velocity v_o is the result of gravity effect $g_o \cos \alpha_{inc}$ and fluid convection v_{flow} or simply the sedimentation velocity of an *equivalent gravity* ($\tilde{g}_o = g_o \cos \alpha_{inc} (1 - \lambda_{flow})$) defined in Eq. 2.43.

$$v_o = \frac{\Delta \rho d_{eq_o}^2 \tilde{g}_o}{18 f_{geo} \mu_f} \quad (2.43)$$

Finally isolating \tilde{g}_o from Eq. 2.43 and injecting in Eq. 2.41, it is found out that $\frac{[C]}{[A]} = \frac{2}{\tilde{St}}$.

Hence, we rewrite the Eq. 2.30 in Eq. 2.44 as a function of dimensionless parameters.

$$\begin{aligned} \frac{d^2 z^*}{dt^{*2}} + \left\{ \frac{2}{\tilde{St}} \left(1 + \frac{2^n - 1}{\Gamma} t^* \right)^{-2/n} \left[1 + \frac{1}{2z^*} \left(1 + \frac{2^n - 1}{\Gamma} t^* \right)^{1/n} \right] \right\} \frac{dz^*}{dt^*} + \\ + \left\{ \frac{3}{1 + \frac{1}{2} \frac{\rho_{pt}}{\rho_f}} \frac{2^n - 1}{n\Gamma} \left(1 + \frac{2^n - 1}{\Gamma} t^* \right)^{-1} \right\} \frac{dz^*}{dt^*} = -\frac{2}{\tilde{St}} \end{aligned} \quad (2.44)$$

with the initial conditions:

$$z^*(t^* = 0) = z_o^* > 1 \quad (2.45)$$

$$\frac{dz^*}{dt^*}(t^* = 0) = v_o^* = -1 \quad (2.46)$$

In case of growthless single particle approaching to a packed particle bed (packing by sequential deposition protocol), we assume a $\Gamma \gg 1$, and the Eq. 2.44 is simplified:

$$\frac{d^2 z^*}{dt^{*2}} + \frac{2}{\tilde{St}} \left(1 + \frac{1}{2z^*} \right) \frac{dz^*}{dt^*} = -\frac{2}{\tilde{St}} \quad (2.47)$$

In this way, a single dimensionless parameter (Stokes number) governs this phenomenon. If the Stokes number is the only parameter that governs the particle settling, we can assume that it is also the only parameter that is needed to describe the influence of the presence of a viscous fluid on the final packing fraction. This theoretical result is in accordance with the experimental analysis of Ref. [Farrell et al., 2010] that have shown

that the influence of the fluid on the packing fraction is given by the particle Stokes number.

The Eq. 2.44 is numerically integrated considering the corrective term of *Brenner*, $\lambda_{wall_{Br}}$ and the Reynolds correction of *Cox and Brenner*, $\lambda_{wall_{CoxBr}}$ (both included in Sec. 2.2.2). The solutions z^* vs t^* , dz^*/dt^* vs t^* and d_{eq}^* vs t^* for three growth regimes are shown in Figs. 2.3 (top) growthless, $\Gamma = 10^5$; (center) moderate growth, $\Gamma = 10$ and (bottom) faster growth, $\Gamma = 1$. All integrations are carried out with a dimensionless time step of $\Delta t^* = 10^{-4}$. Besides, z_o^* is 6 for comparison with the experimental results in Chap. 3. A coefficient $n = 2$ is considered for the growth. For the growthless regime, a velocity break condition is implemented ($v_{break}^*/v_o^* = 0.1$ %) in order to avoid the Stokes paradox, i.e. an infinite time to touch the wall.

In the slow growth situation, the lower the St number is, the smoother is the $z^* - t^*$ curve. Likewise, the $v^* - t^*$ curve tends to a sigmoidal and *Heaviside* shape for low St and high St , respectively. A growing particle can accelerate due to an increase of apparent weight with respect to the dissipation forces, Fig. 2.3 (center). Additionally, the break condition is achieved much earlier in growth. Finally, the St number is not influential to the single particle approaching behavior when $St < 1$ in the slow growth condition.

According to [Harada et al., 2000] there are different situations for the kinetic energy dissipation of the particle, which are only function of Stokes parameter. When this parameter is lower than an experimental threshold value of $St \approx 10$ the particle rebound is not possible and the kinetic energy is dissipated by the viscous forces at the lubrication layer. If Stokes parameter is larger than this value but lower than a value of $St \approx 1000$, the particle will rebound, the coefficient of restitution, ϵ , being a function of Stokes parameter and of mechanical properties of the system particle-wall, that is, part of the initial kinetic energy will be dissipated at the lubrication layer and part at the particle-to-wall contact. Finally, for larger Stokes numbers the lubrication film does not affect the coefficient of restitution. This situation is known as *dry collision*.

2.3 Rearrangement phase: single particle model

Secondly, the rearrangement phase is qualitatively analyzed in order to obtain the dimensionless numbers governing it. Herein, we assume that a rigid particle is posed over the packed particle bed without kinetic energy (see scheme in Fig. 2.4). All kinetic energy has been dissipated during the approaching stage. Due to the apparent weight the particle tends to a more mechanically stable position, lower potential energy.

The phenomenon is modeled for the case of negligible particle growth, $\Gamma \gg 1$. Only the direction \hat{e}_z is considered. In this way, the particle center evolves to a lower more stable position following Eq. 2.48 with an initial condition of $dz/dt(t = 0) = 0$.

$$\left(\rho_{pt} V_{pt} + \frac{\rho_f}{2} V_{pt} \right) \frac{d^2 z}{dt^2} = -\Delta \rho g_o V_{pt} + D \mu_f \frac{d_{eq}}{2} \frac{dz}{dt} \quad (2.48)$$

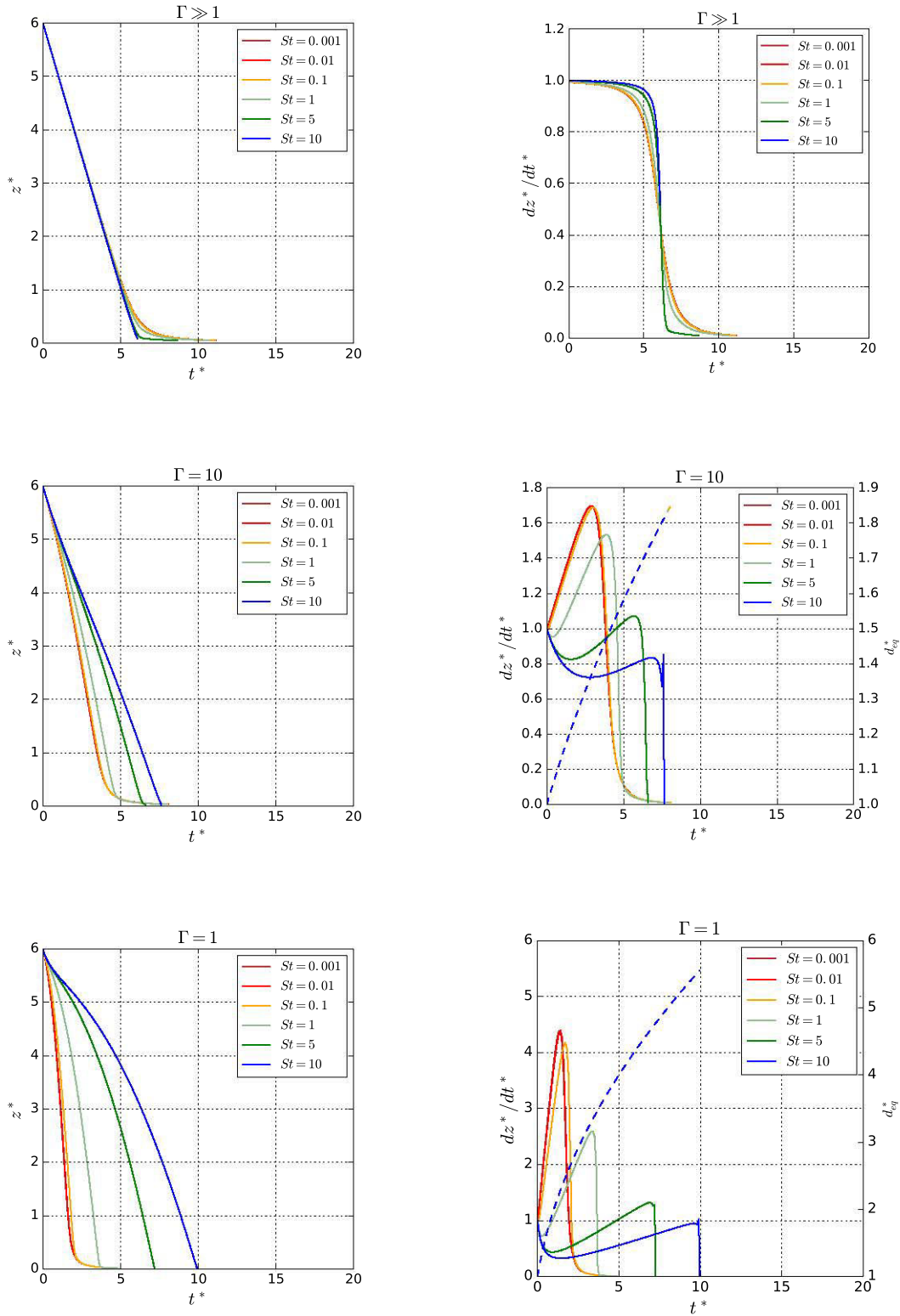


Figure 2.3: Approaching of a single particle to a flat smooth wall (Eq. 2.44). Left: gap between the initial equivalent sphere and the wall. Right: vertical component of the particle velocity and dimensionless diameter (dashed). Top: growthless; center: moderate growth $\Gamma = 10$; bottom: faster growth, $\Gamma = 1$. Parametric study for $St \in [10^{-3}, 10]$.

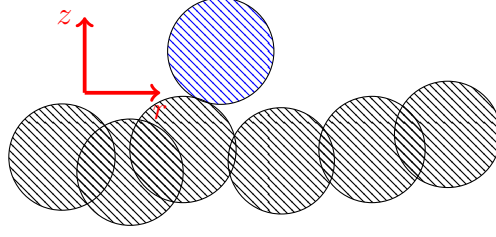


Figure 2.4: Schematic 2D sketch of the beginning of the rearrangement phase. The coordinates $\{r, z\}$ represent the perpendicular and anti-parallel to gravity, respectively.

The damping coefficient D includes two effects: 1) the viscous fluid dissipation, 2) the dissipative contacts with other particles, assuming a viscous fluid layer at the contact between two solid particles. The approaching phase is mainly governed by the initial particle velocity whereas in this second phase the apparent weight is the driving force for rearrangement.

2.3.1 Dimensionless analysis

We scale the equation of the particle rearrangement, Eq. 2.48, using the following characteristic values of time and length, Eqs. 2.49 and 2.50. The diffusion time is used as the characteristic time. We obtain Eq. 2.51, where Ar is the *Archimedes* number, $Ar = \frac{\rho_f \Delta \rho g_0 d_{eq}^3}{\mu_f^2}$.

$$t_{ch} = \frac{d_{eq}^2}{\mu_f / \rho_f} \quad (2.49)$$

$$l_{ch} = d_{eq} \quad (2.50)$$

$$\frac{1}{Ar} \frac{d^2 z^*}{dt^{*2}} = -1 + \frac{3D}{\pi} \frac{1}{Ar} \frac{dz^*}{dt^*} \quad (2.51)$$

Only one dimensionless parameter, Ar , governs the dynamics of the rearrangement phase. The higher Ar is, the higher is the acceleration of the particle and then the quicker is the rearrangement dynamics.

In this way, the phenomenon of particle packing is expected to be composed by two phases, at least for the situation of low relative growth $\Gamma \gg 1$. In the first phase the particles with an initial velocity, which is the result of the apparent weight and liquid convection, travel toward the packed particle bed. This phase is ruled by the *Stokes* number and a dimensionless growth parameter, Γ , which relates the characteristic growth time and characteristic approaching time. On the other hand, we expect that for situations of relatively low growth, the particles experience a rearrangement after approaching until obtaining more favorable mechanical stability. This second phenomenon is governed by the *Archimedes* number. In situations with an important particle growth, the rearrangement is not expected to play a fundamental role since the particle achieve a jamming state

by growth: the translation and orientation particle rearrangement is determined by the constraints among the particles which are continuously growing.

Once the hydrodynamic dimensionless numbers governing the packing phenomenon are presented, they are understood in the Solidification context: specifically in the solidification of metallic alloys: aluminum and steel. Thereby, the order of magnitude of the hydrodynamic dimensionless numbers is computed, which is fundamental to build the similarity in the packing experience setup (see Chap. 3).

2.4 Application to casting processes

Firstly, the grain settling phenomenon in aluminum and steel solidification is analyzed in the situation of quiescent melt. In Fig. 2.5 the trajectory of an equiaxed grain in a Al-Zn alloy in DC casting is simulated. Equivalent results are computed for steel ingot casting shown in Fig. 2.6. The characteristic physical parameters are collected in Table 2.1. Since the grain size plays a fundamental role when the phenomenon is analyzed dimensionally ($v_{set} \propto d_{eq}^2$, $St \propto d_{eq}^3$ and $Ar \propto d_{eq}^3$), a parametric study is carried out with respect to the grain size.

For the compared cases of aluminum and steel similar settling velocities and Stokes number are obtained for the same particle size (see Table 2.2). The values in Al are slightly higher since the ratio between shrinkage coefficient, $\beta = \rho_s/\rho_l - 1$, and kinetic viscosity is higher in aluminum than in steel $(\beta/\nu)_{Al} > (\beta/\nu)_{Steel}$.

Table 2.1: Input data for aluminum and steel grain settling in quiescent fluid.

Case	Reference	ρ_f [kg/m^3]	ρ_s/ρ_f	μ_f [$mPas$]
AA7449 (Al-Zn)	[Založnik et al., 2011a]	2519	1.057	1.28
Fe-1.01%wt.C	[Leriche, 2015]	7060	1.048	4.20

Table 2.2: Settling velocity and Stokes number for aluminum and steel spherical grain settling in quiescent fluid as a function of grain size.

d [μm]	50	100	200	500	1000
$v_{set,Al}$ [mm/s]	0.16	0.62	2.49	15.55	62.21
$St_{set,Al}$	$1.7 \cdot 10^{-3}$	$1.4 \cdot 10^{-2}$	$1.1 \cdot 10^{-1}$	1.7	14.0
$v_{set,Steel}$ [mm/s]	0.11	0.44	1.76	11.00	43.97
$St_{set,Steel}$	$1.2 \cdot 10^{-3}$	$0.96 \cdot 10^{-2}$	$0.77 \cdot 10^{-1}$	1.20	9.6

Subsequently, a parametric study of the influence of the grain equivalent diameter and melt kinematic viscosity on the steady-state settling velocity (far from the packing front) is carried out with a fixed solid-liquid density ratio of $\rho_s/\rho_l = 1.05$. A kinematic viscosity ranging from 0.5 to 2.0 mm^2/s and a grain size up to 500 μm are considered, Fig. 2.7 (left). Sedimentation velocities up to 10 mm/s are found.

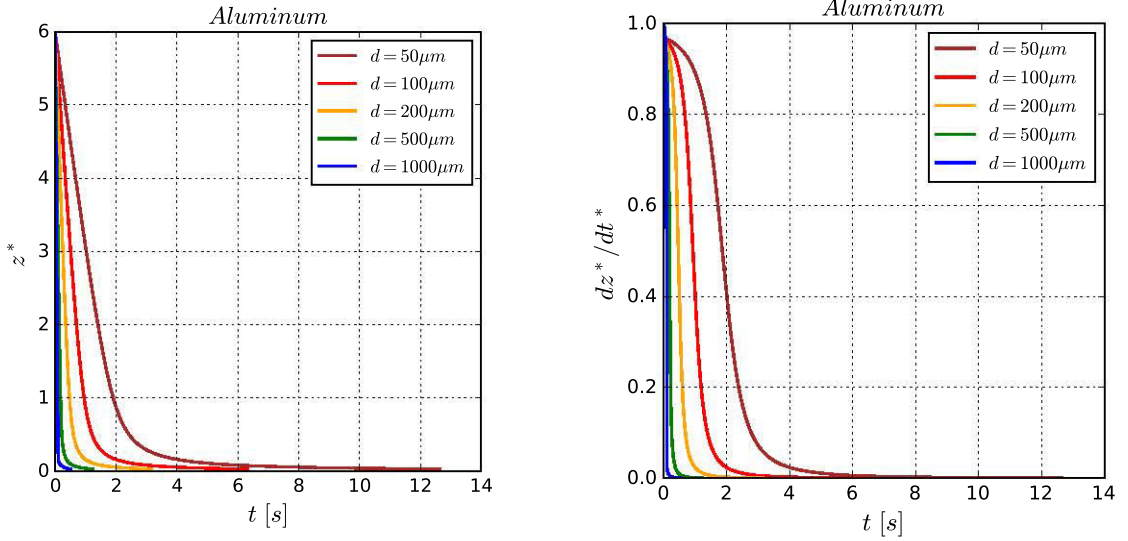


Figure 2.5: Spherical grain approaching to an impermeable smooth wall: influence of grain size for aluminum. The Brenner lubrication model and Brenner-Cox Reynolds influence are considered. Input data is collected in Table 2.1. Left: particle position. Right: vertical velocity of the particle. The analyzed sizes are d_{eq} : 50, 100, 200, 500 and 1000 μm .

Additionally considering the grains dragged by a melt flow with a velocity in the interval from 0.1 up to 100 mm/s , the solid grain Stokes number ranges from 10^{-3} up to 500, Fig. 2.7 (right). In this graph the curves are computed with a fixed melt kinematic viscosity and solid-liquid density ratio of 1.0 mm^2/s and 1.05, respectively.

The previous result is very general. We use the values from simulations of aluminum and solid casting processes in order to quantify the Stokes number more precisely. In case of aluminum DC casting (see Appx. A.1), a grain size of $d_{eq} \approx 80 \mu m$ and a grain velocity component perpendicular to the packing front of $o(10^{-6}) m/s$ is assumed at the packing front iso-pleth ($g_s = 0.3$ in this simulation). In this situation, the Stokes number is $o(10^{-4})$ which is much lower than the threshold of $St = 10$, then nil values of the restitution coefficient are expected.

On the other hand, in case of static steel ingot solification, values of the Stokes number up to $St \approx 10^2$ are expected (assuming grain velocities which order of magnitude is 10 cm/s and grain size with an order of magnitude of 1 cm , see Ref. [Leriche, 2015]).

Secondly, the importance of the growth phenomenon is evaluated. We assume a linear growth model with $n = 1$ and $K_{gr} = \frac{dd_{eq}}{dt}$. So we consider $\Gamma = v_{s\perp} / \frac{dd_{eq}}{dt}$ where $v_{s\perp}$ is the component of the grain velocity perpendicular to the packing front.

In case of DC casting of aluminum (see Appx. A.1), the dimensionless growth parameter, Γ , is obtained from numerical simulations of the casting process. It is evaluated at the packing front ($g_s = 0.3$ iso-pleth in the simulations) at two positions, assuming a grain

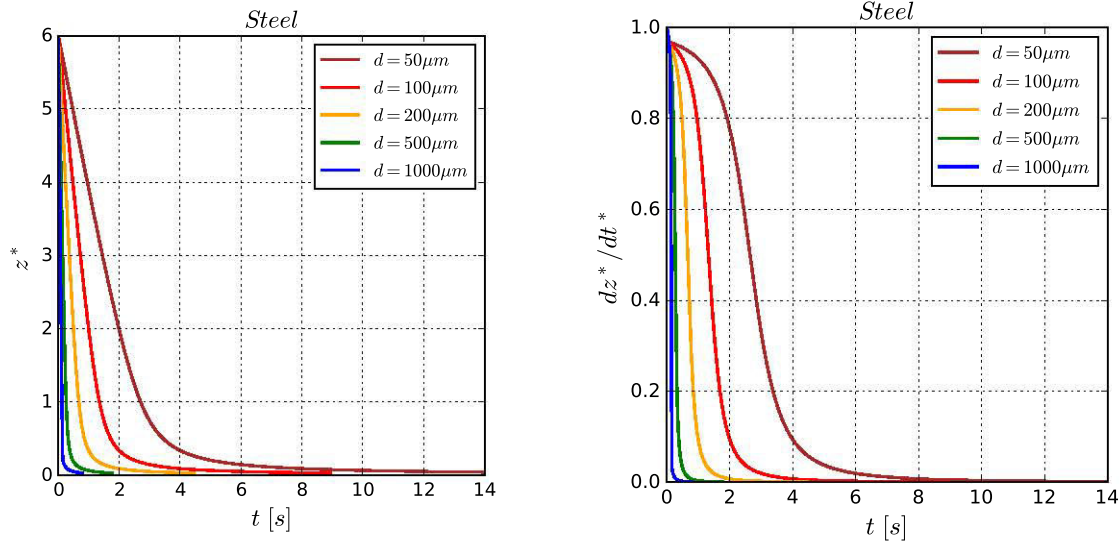


Figure 2.6: Spherical grain approaching to an impermeable smooth wall: influence of grain size for steel. The Brenner lubrication model and Brenner-Cox Reynolds influence are considered. Input data is collected in Table 2.1. Left: particle position. Right: vertical velocity of the particle. The analyzed sizes are d_{eq} : 50, 100, 200, 500 and 1000 μm .

velocity component perpendicular to the packing front of $o(10^{-6})$ m/s:

- 1) Ingot center line (horizontal packed grain bed): $\Gamma = o(10^{-6})/o(10^{-10}) \gg 1$.
- 2) Ingot quarter-thickness (inclined packed grain bed): $\Gamma = o(10^{-6})/o(10^{-8}) \gg 1$.

We consider negligible the influence of growth on packing for aluminum DC casting due to the low growth rates. However, static grains could also be present in case of absence of grain motion. In this situation, the packing is achieved by growth, $\Gamma \ll 1$.

Subsequently, the characteristic Archimedes number in aluminum DC casting is computed as a function of the equiaxed grain size and melt kinematic viscosity in Fig. 2.8. The Archimedes ranges in the interval $Ar \in [10^{-3}, 300]$. According to the simulations in Appx. A.1, at the packing zone, iso-pleth of $g_s = 0.30$, an Archimedes number of $o(1)$ is expected. In static steel ingot casting with grains of 1 cm, the Archimedes is expected to be much higher than in aluminum, $Ar = o(10^6)$.

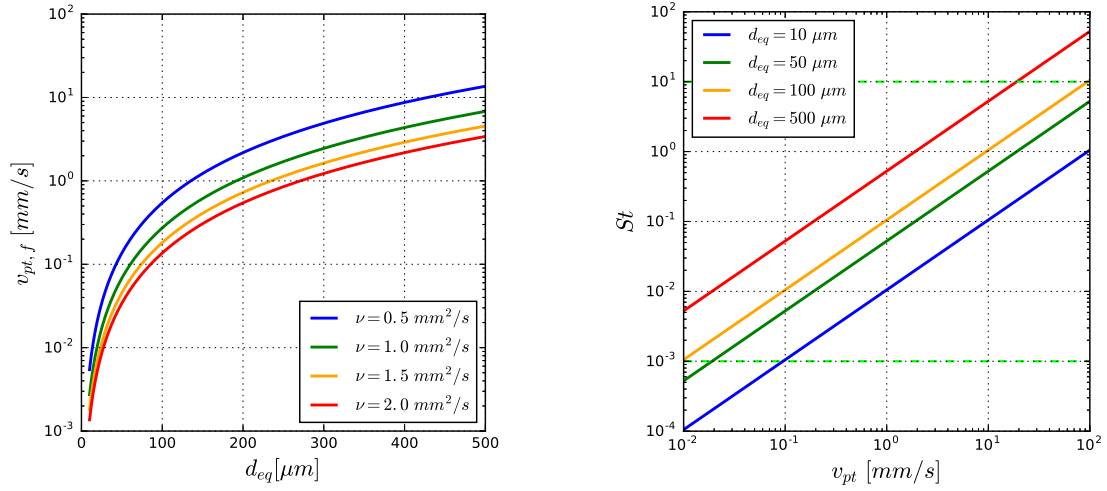


Figure 2.7: Left: grain sedimentation velocity in quiescent fluid as a function of the particle equivalent diameter. A density ratio of $\rho_s/\rho_l = 1.05$ and a kinematic viscosity of 0.5, 1.0, 1.5 and 2.0 mm^2/s are assumed. Right: grain Stokes number as a function of the grain velocity respect to the packing front. Grain equivalent diameters in the interval $[10, 500] \mu\text{m}$ are considered. A density ratio of $\rho_s/\rho_l = 1.05$ and kinematic viscosity of $\nu = 1.0 \text{ mm}^2/\text{s}$ are considered.

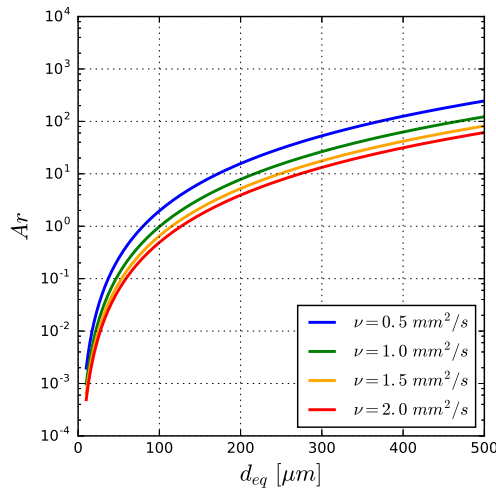


Figure 2.8: Archimedes number as a function of equivalent equiaxed grain diameter and melt kinematic viscosity.

2.5 Theoretical conclusions

In this chapter the dimensionless hydrodynamic parameters governing the equiaxed grain packing in solidification are investigated. In this vein, the phenomenon is studied by means of a single particle traveling toward a wall (sequential particle packing). This wall represents the packed grain bed, i.e, the packing front. Only the evolution of the particle perpendicular to the wall gap is investigated.

Two phases of the motion of the particle traveling toward the packed particle bed are identified: 1) approaching phase with the *Stokes number*, St , as hydrodynamic number governing this phase. Additionally, in order to include the importance of the particle growth in this phase, a dimensionless parameter, Γ , is defined. 2) Rearrangement phase with *Archimedes*, Ar , governing it. In case of growth, the parameter Γ must be also considered.

The St , Γ and Ar characteristic values in casting are computed, basically for the DC casting of aluminum. A low Stokes number is found for aluminum, $o(10^{-4})$. Values of Stokes number up to 10^2 can be expected in case of static steel ingot solidification.

The growth parameter, Γ , is computed for DC casting of aluminum. Only situations of $\Gamma \gg 1$ are assumed due to the low values of growth rate.

Finally, Archimedes values of $o(1)$ and $o(10^6)$ are expected for aluminum DC casting and static steel casting processes, respectively.

Chapter 3

Experimental analysis

3.1 Introduction

How do equiaxed grains pack in solidification? In the solidification literature review (see Sec. 1.2.1), two methods to visualize the equiaxed grain packing in solidification are presented: transparent alloys and X-ray tomography of metallic alloys. Nevertheless, in these methods the equiaxed grain sedimentation and packing is strongly coupled with the grain growth, making difficult to isolate the packing phenomenon.

Herein, an experimental model is developed to exclusively reproduce the equiaxed grain sedimentation and packing with hydrodynamic similarity with the actual packing phenomenon in solidification. Thereby, with this experiment the sedimentation and packing is isolated from other solidification phenomena, e.g. the grain growth or the melt convection. The objective of this experiment is to visualize the formation of the grain packed bed as well as measuring the grain packing fraction as a function of the grain morphology and hydrodynamic conditions of the packing.

The main stages in the experimental analysis are:

- Conception of the experimental setup from scratch.
- Selection of solid particles and liquid in order to reproduce the hydrodynamic similarity with the actual solidification phenomenon.
- Conception of the packing protocols.
- Analysis of the average packing fraction as a function of the grain morphology and sedimentation hydrodynamic conditions: development of the average solid packing fraction measurement technique.
- Analysis of the grain packing dynamics as a function of the grain morphology: development of a particle tracking technique.

Lots of questions are initially considered for the experimental conception. Some of these questions are the experimental configuration, the suitable setup-to-particle dimensions,

the hydrodynamic similarity parameters which are possible to reproduce, the number of grains or the equiaxed grain morphologies to use.

3.2 Setup conception

The experimental setup is composed by two 1000 *mm* long concentric columns made of transparent acrylic, Fig. 3.1 (left) and Appx. B.1 for more detail, and integrated in a metallic structure that serves of support.

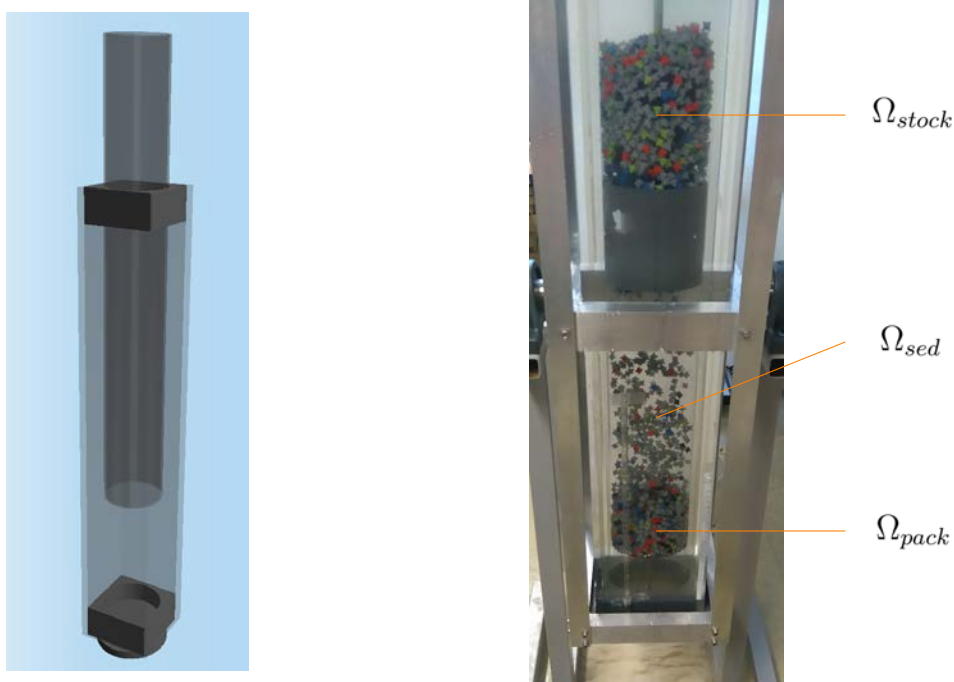


Figure 3.1: Left: Schematic representation of the double acrylic column device. Right: Experimental setup during dendritic sedimentation and packing. Three regions are distinguished according to the particle regime. Bottom: the particles are packed occupying a volume Ω_{pack} . Center: the particles are sedimenting in the volume Ω_{sed} . Top: the particles are stocked (packed) occupying the volume Ω_{stock} .

During particle sedimentation and packing the axial direction of the columns is aligned with gravity. The inner column is cylindrical with 120 *mm* internal diameter whereas the wider column has a squared cross-section which internal side is 160 *mm*. The fluid fills up the volume located inside the cylindrical column as well as the remaining volume between the two columns. This double-wall configuration is projected in order to avoid the optical horizontal deformation of the observed particles due to the curved surface refraction and different refraction index of air and the used liquid, Ref. [Pedrotti, 2012]. Moreover, both columns are perfectly sealed, being the cylindrical column the only accessible via a screw cap. In this way, liquid leaks are avoided as well as the liquid contact with the atmosphere.

The particles are only allowed to move along the interior of the cylindrical column. Likewise, the cylindrical column is divided in two sub-volumes (an upper and a lower of approximately 400 and 600 *mm* long, respectively) by means of an injection gate. The whole device volume is filled up by the particle solid volume and liquid, avoiding the presence of air.

Initially, the injection gate is closed blocking the access to the lower sub-volume, Fig. 3.2 (left), in this way, the collection of particles is located at the upper sub-volume in stable equilibrium over the injector. In this situation, the liquid is quiescent filling up the whole lower sub-volume and also the space left by the particles at the upper sub-volume.

Once the injection gate is opened, Fig. 3.2 (right), a particle flow passes to the lower sub-volume, where it expands (occupying the whole cross-section) and finally packs over a bottom horizontal grid. Fig. 3.1 (right) shows the experimental setup when the steady regime is already reached. At the lower sub-volume two zones are clearly distinguished: at bottom the particles are already packed in mechanically stable equilibrium occupying a volume Ω_{pack} and a second zone where the particles are sedimenting occupying a volume Ω_{sed} . Meanwhile, there is a liquid flow upwards whose rate is equivalent to that of the particles. The third zone is formed by the particles over the injector in the upper sub-volume, Ω_{stock} .

According to Ref. [de Moraes Franklin and de Andrade, 2015] the particle discharge rate of silos immersed in fluid does not depend on the height of the stocked particle bed due to the so-called *Janssen effect*, Ref. [Sperl, 2006].

When all particles reach the mechanical stable regime and the data measurements are carried out, this experimental device permits to easily reset the granular system to the initial conditions. The metallic structure can turn 180° about a horizontal rotation axis that approximately passes through the column center of mass. In this vein, particles do the opposite way. Once, they are in the initial sub-volume, the column is turned 180° to its initial configuration.

3.3 Particle selection

Two collections of monodisperse noncohesive hard particles are used: spheres and equiaxed dendritic grains. The monodisperse spherical collection is necessary in order to compare the packing results with those of the literature review (see Sec. 1.3.2) and validate the experimental setup, the packing protocol and the measurement technique of the packing fraction. Additionally, the spherical collection can be considered an approximation to the globular equiaxed grain morphology.

On the other hand, the packing of a monodisperse equiaxed dendritic particle collection is a novelty in both the Solidification and Granular Material disciplines. In Solidification little is known about the dendritic grain packing and in the case of Granular Material there is scarce experimental work done about nonconvex particle packing.

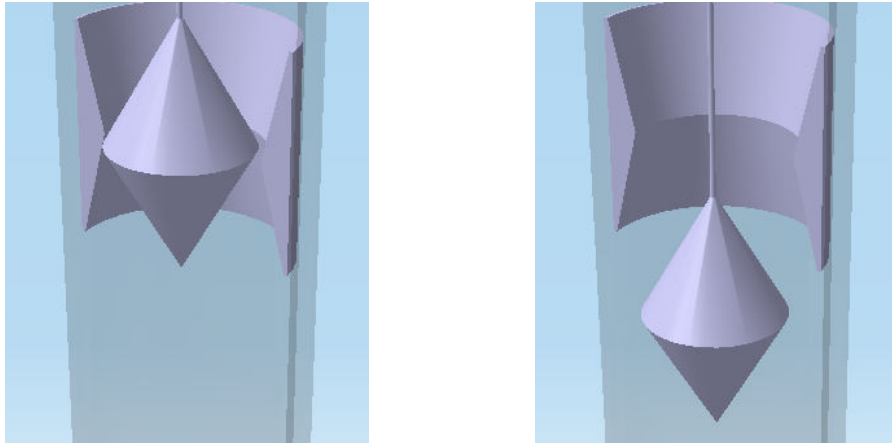


Figure 3.2: Schematic representation of the grain injector: close (left) and open (right). The front half of the cylindrical column is removed to visualize the injector.

The dendritic particle geometrical model is based on the actual dendritic shape (see Fig. 1.3) but important simplifications are considered. Firstly, an equiaxed dendritic grain geometry including secondary arms is proposed for the experimental analysis in this thesis (see Fig. 3.3) however this geometrical complexity have some disadvantages such as the fabrication price or the fragility.

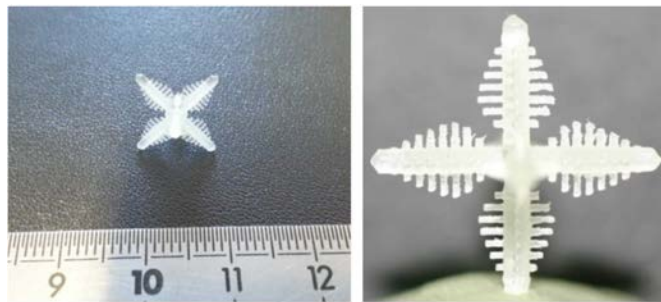


Figure 3.3: Equiaxed dendritic grain prototype including secondary arms made by additive manufacturing.

An equiaxed dendritic grain model based on the idea of the dendritic envelope which is a virtual surface wrapping the dendrite secondary arms is used, Fig. 3.4 (left). The envelope prototype is thought to provide similar packing configurations than those prototypes that include secondary arms.

A great number of dendritic grain envelopes must be fabricated, then due to budget reasons, a strong geometrical simplification is considered: the nonconvex envelope is basically composed by a central cube and six quadrilateral pyramids of 45° apex-angle which base is attached to each of the cube faces, Fig. 3.4 (left). We geometrically define the dendrite widest length, l_c , as the length of the line joining two pyramid apexes, passing through

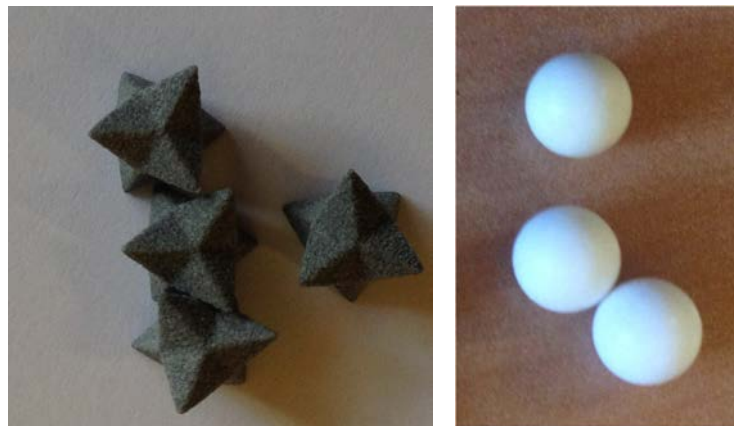


Figure 3.4: Left: monodisperse equiaxed dendritic grain envelopes by additive manufacturing. (Apex-angle, θ , of 45° and widest length, l_c , of $12.59 \pm 0.22 \text{ mm}$). Right: monodisperse spheres of $5.92 \pm 0.05 \text{ mm}$ of diameter.

the center of the particle. In the context of solidification, this l_c is twice the dendrite arm length. The envelope geometrical characteristics are analyzed in detail in Chap. 4. Among them, the prototype sphericity, Ψ , and the ratio between the widest length and the particle equivalent diameter, l_c/d_{eq} . In this experimental dendrite prototype, $\Psi \approx 0.70$ and $l_c/d_{eq} \approx 1.83$.

The set of spheres is composed by approximately 12200 white particles, Fig. 3.4 (right) the material of which is based on cornstarch. The sphere size is chosen to have a great container-to-particle diameter ratio ($D/d = 20$) in order to have a low effect of the container wall on the average packing fraction. This effect is quantified to loose the average packing fraction less than a 2%, by integration of the radial packing fraction correlation in Ref. [Mueller, 1992] along the container, which is shown in Fig. 1.19.

The equiaxed dendritic collection is formed by approximately 4400 particles created by additive manufacturing. An innovative material based on quasicrystal-polymer composites, Ref. [Kenzari et al., 2014], is used to reduce the particle porosity, i.e. decreasing the permeability, to avoid fluid absorption and consequently, the particle density variation.

The resulting bulk density of the composite material is $\rho_s = 1484 \pm 17 \text{ kg/m}^3$ measured by means of a pycnometer according to the protocol in [ASTM, 2000]. A sample of 30 nonconvex particles are randomly chosen for mass measurement in a precision balance obtaining a mass of $0.3541 \pm 0.0357 \text{ g}$ with a level of confidence of 95%. The equivalent diameter, d_{eq} , is $7.70 \pm 0.31 \text{ mm}$ and the widest characteristic particle length, l_c , is $12.59 \pm 0.22 \text{ mm}$. An interparticle dry friction coefficient of approximately 0.50 is considered obtained by tribometer testing (see Appx. B.2).

The density of the spherical collection is chosen to be as similar as possible to that of the dendrites, $\rho_s = 1391 \pm 6 \text{ kg/m}^3$ measured by the pycnometer protocol in Ref. [ASTM, 2000]) and a mass of $0.1532 \pm 0.0074 \text{ g}$ with a level of confidence of 95%. The d_{eq} is

5.92 ± 0.05 mm.

3.4 Fluid selection

The *Stokes number*, i.e. the inertia-to-dissipation ratio of those particles approaching to the packed bed, plays an important role in the formation of the packings as aforementioned in Chaps. 1 and 2. In solidification of aluminum by DC casting, the Stokes number can be as low as 10^{-4} . In case of static steel ingot, the Stokes number can reach values of $o(10^2)$. The fluid section criterion is based on the reproduction of the hydrodynamic conditions by hydrodynamic similarity with the packing in the casting processes: Stokes and Archimedes numbers. Additionally, in the experimental analysis, we maintain a low solid-liquid relative density ratio, $(\rho_s - \rho_f)/\rho_s$, similar to that of the metallic alloys.

Hence, four different fluids are selected to reproduce a large Stokes interval. Herein the fluid requirements, which are classified by importance, are summarized:

- Transparent fluids.
- Nontoxic fluids.
- Fluids with a density and a viscosity (ρ_f and μ_f , respectively) enable to reproduce, as far as possible, the solidification *Stokes* interval ($St \in [10^{-4}, 10^2]$). In this way, the hydrodynamic similarity of the approaching phase is reproduced.
- Fluids that enables to reproduce, as far as possible, the solidification *Archimedes* interval ($Ar \in [10^{-3}, 10^6]$). In this way, the hydrodynamic similarity of the rearrangement phase is reproduced.

Thereby, three liquids are selected: **glycerol**, a **glycerol-water solution** and **water** to reproduce the solidification Stokes interval. Additionally, the particle packing is also carried out in **air** (high Stokes) for comparison with the dry packing protocols in literature.

3.4.1 Glycerol

A 99.5% glycerol solution is chosen as a working liquid with a density and a dynamic viscosity are approximately $\rho_f = 1261.9 \text{ kg/m}^3$ and $\mu_f = 1.18 \text{ Pa.s}$, respectively, according to Ref. [Cheng, 2008] for a liquid temperature of approximately 21° which is measured by means of a thermocouple. In Table 3.1 the main sedimentation hydrodynamic parameters according to the solid and liquid characteristics are given: density ratio and theoretical Stokes number (see more details in Appx. B.3). In this vein, with glycerol as working liquid a Stokes of order 10^{-3} is obtained with a solid-liquid density ratio very similar to that of the metallic alloys. On the other hand, Archimedes values in the interval $Ar \in (10^{-1}, 1)$ are possible with glycerol. This protocol is suitable to reproduce low values of the Stokes number of the packing in aluminum DC casting.

Table 3.1: Sedimentation parameters in glycerol

Parameter	Spheres	Dendrites
$(\rho_s - \rho_f)/\rho_s$	0.09	0.15
St	$1.2 \cdot 10^{-3}$	$5.0 \cdot 10^{-3}$

Table 3.2: Sedimentation parameters in glycerol-water solution

Parameter	Spheres	Dendrites
$(\rho_s - \rho_f)/\rho_s$	0.16	0.20
St	0.5	1.68

3.4.2 Glycerol-water solution

A glycerol-water solution (approximately 22.3% of water) is chosen as a working liquid with a density and a dynamic viscosity are approximately $\rho_f = 1201.3 \pm 24.3 \text{ kg/m}^3$ and $\mu_f = 0.0504 \pm 1.4 \text{ Pa.s}$, respectively. The dynamic viscosity is measured by means of a falling-ball viscosimeter. With this value of viscosity and a fluid temperature of approximately 26° which is measured by means of a thermocouple, we use the data in Ref. [Cheng, 2008] to obtain the water volume fraction of the solution and the solution density. In Table 3.2, the main sedimentation hydrodynamic parameters according to the solid and liquid characteristics are given: density ratio and theoretical Stokes number (see more details in Appx. B.3).

3.4.3 Water

By means of packing in water ($\rho_f = 998 \text{ kg/m}^3$ and $\mu_f = 10^{-3} \text{ Pa.s}$ at the working temperature of approximately 21°) the obtained Stokes is the order of 10^2 with a solid-liquid relative difference density of approximately 30% (see Table 3.3 where the main hydrodynamic dimensionless sedimentation parameters are provided. See Appx. B.3 for more details). Archimedes values of the order of $Ar = o(10^6)$ are obtained with water. This protocol is suitable to reproduce the grain packing in the static steel ingot casting.

We provide the theoretical range of the Stokes and Archimedes numbers as a function of glycerol-water solutions. Fig. 3.5 (left) shows the theoretical Stokes sedimentation number resulting of a solid-liquid density ratio of ρ_s/ρ_f and kinetic viscosity of the fluid of ν in case of spheres of 6 mm diameter. The blue dashed circle indicates the *glycerol protocol* for our particle characteristic density ($\rho_s/\rho_f \approx 1.10$ and $\nu = o(10^{-3}) \text{ m}^2/\text{s}$) whereas the red dash circle indicates the *water protocol* for our particle characteristic density ($\rho_s/\rho_f \approx 1.35$

Table 3.3: Sedimentation parameters in water

Parameter	Spheres	Dendrites
$(\rho_s - \rho_f)/\rho_s$	0.28	0.33
St	198	368

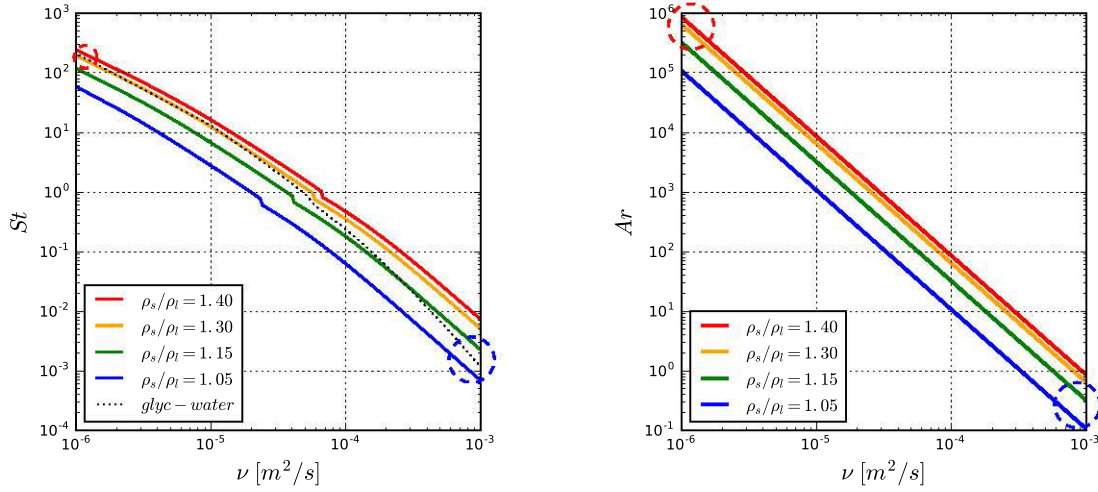


Figure 3.5: Left: sphere theoretical sedimentation Stokes number, St , as a function of the fluid kinematic viscosity, ν , for four solid-to-liquid density ratios (from 1.05 to 1.40). Right: Ar , as a function of the fluid kinematic viscosity, ν , for four solid-to-liquid density ratios (from 1.05 to 1.40). The blue dashed and red dashed circles represent the glycerol and water protocols, respectively. The black dashed line in left corresponds to glycerol-water solutions.

and $\nu = o(10^{-6}) \text{ m}^2/\text{s}$. The dashed black line joining the pure glycerol and pure water protocols is the result of glycerol-water solutions (see Appx. B.3 for more details). Fig. 3.5 (right) shows the Archimedes number as a function of the kinematic viscosity.

3.4.4 Air (dry packing)

With air, $\rho_f = 1.2 \text{ kg/m}^3$ and $\mu_f = o(10^{-5}) \text{ Pa.s}$ at temperature of approximately 21° , the Stokes number is the order of 10^5 and a solid-fluid density ratio of approximately 1.

3.5 Average packing fraction

Each of the particle sets (monodisperse spheres and dendrites) are sedimented and packed in the four different working fluids over a flat plane: a total of 8 experiments, that is, each collection packs for $St = o[10^{-3}, 1, 10^2, 10^5]$.

The challenge in this section is that of measuring the *average solid volumetric packing fraction* of the granular system, $\langle \phi_s \rangle_{\Omega_{pack}}$, as a function of the *Stokes number* for both spherical and dendritic geometries.

We firstly present the average packing fraction measuring technique exclusively developed for this thesis: *volume reconstruction technique* and secondly, we present the obtained results: highlighting the influence of the geometry and Stokes number on the packing fraction.



Figure 3.6: Upper surface of the equiaxed dendritic packed bed: Left) convex surface with dry protocol. Right) flat surface with glycerol protocol.

3.5.1 Volume reconstruction technique

Among the experimental techniques to determine the mean packing fraction, the simplest is to obtain the total volume of the packed bed by measuring its height from images (see Refs. [Jerkins et al., 2008, Baker and Kudrolli, 2010, Higuti, 1961, Schröter et al., 2005]). A vertical cylindrical vessel sufficiently large to reduce the effect of walls on the packing fraction was used.

In this thesis, this technique is employed to obtain the average solid packing fraction, $\langle \phi_s \rangle_{\Omega_{pack}}$, computed by the ratio between the granular system solid volume and granular total volume, $\langle \phi_s \rangle_{\Omega_{pack}} = V_s / V_{\Omega_{pack}}$. The solid volume, V_s , is obtained from the mass and the solid density measured by pycnometer ($V_s = m_s / \rho_s$). On the other hand, $V_{\Omega_{pack}}$ is estimated by reconstruction of the volume from a 2D image for each packing (see Fig. 3.6 as an example for the case of nonconvex dendritic particles in dry (left) and glycerol (right) protocols). The reconstruction technique is detailed in Appx. B.4.

According to Fig. 1.19, the packing fraction in an infinitely wide cylindrical domain ($D/d \rightarrow \infty$) is between 1.4% and 1.7% larger than the measured packing fraction for our monodisperse spherical collection ($D/d \approx 20$). Since the difference is very low, the packing results of the next section are not corrected.

3.5.2 Influence of geometry and hydrodynamic conditions on the packing fraction

The experimentally measured packing fractions are shown in Fig. 3.7 plotted as a function of the parameter S (where S is the particle Stokes number in the approaching to packing assuming Stokes terminal velocity of sedimentation which is only function of the particle and fluid properties: d , ρ_s , ρ_f and μ_f . $S = \rho_s^2 g_o (1 - \rho_f / \rho_s) d_{eq}^3 / (162 \mu_f^2)$).

For sedimentation and packing in glycerol of the spherical and dendritic particle collections a $\langle \bar{\phi}_s \rangle_{\Omega_{pack}}$ of $57.5 \pm 0.8\%$ and $39.7 \pm 0.6\%$ are found, respectively whereas a slightly denser packing is obtained for the glycerol-water protocol. The mean packing fractions are obtained from repeating the packings 10 times for both spheres and dendrites with

glycerol and glycerol-water protocols. Whereas, for the packing in water $\langle \bar{\phi}_s \rangle_{\Omega_{pack}}$ of $61.7 \pm 2.5\%$ and $43.1 \pm 1.5\%$ are obtained for spheres and dendrites, respectively. Finally a much denser packing is obtained for the dry protocol being $\langle \bar{\phi}_s \rangle_{\Omega_{pack}}$ of $62.8 \pm 1.13\%$ and $46.8 \pm 1.9\%$ for spheres and dendrites, respectively (see Fig. 3.7 where the sphere results have green circular markers and dendrites have blue triangles). The mean packing fractions with dry and water protocols are obtained from repeating 30 times the packing experiment for each collection.

The grain morphology has the largest influence on the packing fraction: the dendritic shape packs looser than the spherical shape. Specifically, the dendritic packing fraction is a 31%, 30% and 25% relatively looser than the sphere packing fraction with glycerol, water and dry protocols, respectively.

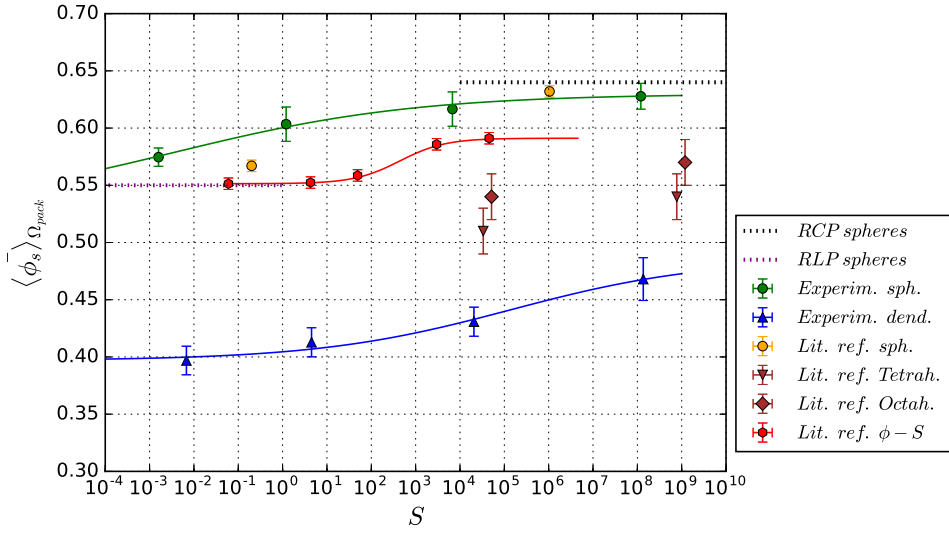


Figure 3.7: Average solid packing fraction, $\langle \bar{\phi}_s \rangle_{\Omega_{pack}}$, as a function of the dimensionless parameter $S = \rho_s^2 g_o (1 - \rho_f / \rho_s) d_{eq}^3 / (162 \mu_f^2)$, for spheres (green) and nonconvex dendritic grains (blue). The sphere ϕ_{RCP} and ϕ_{RLP} are included in dotted black and purple lines, respectively. The new results are compared with data from literature: Orange) sphere packing: 56.7% for water fluidized [Jerkins et al., 2008] (with the lowest fluidization flow rate) and 63.2% for faster dry pouring protocol [Delaney et al., 2010]. Brown) fluidized in water and simply poured packing of tetrahedrons and octahedrons [Baker and Kudrolli, 2010]. Red) the steel monodisperse sphere packings from Ref. [Farrell et al., 2010] by sequential deposition are also added.

The hydrodynamic conditions have a much less important influence on the packing fraction than the particle geometry. A similar influence of the dimensionless parameter S on the packing fraction is observed for both the spherical and the nonconvex dendritic particles: looser packings for lower S . For the low S packing protocol (glycerol), spheres and dendrites pack a 8% and 15% relatively looser than by the dry protocol. Hence, the

lower S , the softer the particle approaching is since a higher amount of the granular kinetic energy is dissipated through the fluid viscous dissipation. The results of steel (low interparticle friction) monodisperse spheres packing by sequential deposition from Ref. [Farrell et al., 2010] are also included in red. The packings from this reference are looser since they are affected by an important wall effect. We fit our results and those from Ref. [Farrell et al., 2010] with the sigmoidal model describe in Appx. B.5.

The average packing fraction the of monodisperse sphere packings in glycerol, glycerol-water solution, water and dry remain between the RLP and RCP asymptotes. The packing of our sphere collection in glycerol is a 3% relatively denser than the loosest experimentally obtained packing, Ref. [Jerkins et al., 2008], which is 0.55. On the other hand, the dry protocol for spheres provides similar results as that of fast pouring from literature (e.g., those of faster dry pouring protocol in Ref. [Delaney et al., 2010]).

The nonconvex dendrite-like particles are found to pack much looser for fluidized and dry protocols than Platonic Bodies (convex geometries). Particularly when compare to tetrahedron and octahedron packings, the obtained $\langle \bar{\phi}_s \rangle_{\Omega_{pack}}$ are between 15% and 23% relatively lower for dendrites.

The mean packing fraction and its error are computed from a n_{exp} sample for each of the 8 experimental tests (particle collection and packing protocol). In this way, dry and water packings are repeated $n_{exp} = 30$ and glycerol and glycerol-water packings $n_{exp} = 10$, since a much regular upper surface of the packing is found. See Appx. B.4 for a detailed description of method for the mean and error packing fraction obtaining.

In Fig. 3.8 our experimental results are also plotted as a function of the Stokes number which is computed as indicated in Appx. B.3. Assuming the same sigmoidal model previously used to fit the correlation of the packing fraction with St , we obtain:

- **Spherical grains** ($\Psi = 1$):

$$\langle \bar{\phi}_s \rangle_{\Omega_{pack}} = 50.3 + 12.8 \left\{ 1 + e^{-0.376(\log_{10}(St)+3.56)} \right\}^{-1} \quad [\%] \quad (3.1)$$

- **Dendritic equiaxed grains** ($\Psi = 0.70$):

$$\langle \bar{\phi}_s \rangle_{\Omega_{pack}} = 39.2 + 12.0 \left\{ 1 + e^{-0.464(\log_{10}(St)-4.06)} \right\}^{-1} \quad [\%] \quad (3.2)$$

In this way, we conclude that the grain geometry is the most important influence for the packing fraction in solidification. A lower influence of the hydrodynamic conditions is found for the considered protocols.

3.6 Packing dynamics: Lagrangian description

In this text the *packing dynamics* is understood as the evolution of the granular system from the sedimentation to packing and it is investigated by means of the glycerol protocol

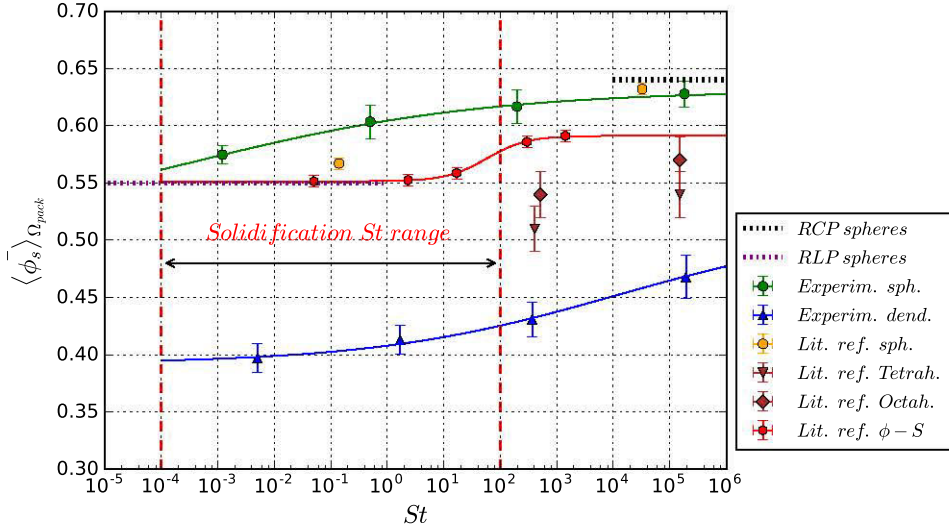


Figure 3.8: Average solid packing fraction, $\langle \bar{\phi}_s \rangle_{\Omega_{pack}}$, as a function of the theoretical Stokes dimensionless parameter $St = \rho_s d_{eq} v_s / (9\mu_f)$ (see Appx. B.3) for spheres (green) and nonconvex dendritic grains (blue). The sphere ϕ_{RCP} and ϕ_{RLP} are included in dotted black and purple lines, respectively. Our results are compared with literature. The literature results included are: Orange) sphere packing: 56.7% for water fluidized [Jerkins et al., 2008] (with the lowest fluidization flow rate) and 63.2% for faster dry pouring protocol [Delaney et al., 2010]. Brown) fluidized in water and simply poured packing of tetrahedrons and octahedrons [Baker and Kudrolli, 2010]. Red) the steel monodisperse sphere packings from Ref. [Farrell et al., 2010] by sequential deposition are also added.

($St \ll 1$) since it is not feasible to us for higher Stokes due to the high velocities. The multi-particle system settles due to the apparent weight. The mean velocity of the settling particles is given by:

$$\bar{\mathbf{v}}_s^{sed}(t) = \frac{\sum_{i=1}^{n_{\Omega_{sed}}(t)} \mathbf{v}_i^{sed}(t)}{n_{\Omega_{sed}}(t)} \quad (3.3)$$

where $n_{\Omega_{sed}}(t)$ are the particles contained in Ω_{sed} at an instant t .

Though individually a particle could undergo sedimentation velocity oscillations, the sedimentation mean velocity oscillations with time are thought to be negligible due to the large number of particles in Ω_{sed} in steady regime.

The sedimentation and packing of the sphere and dendritic particle collections in glycerol are shown in Figs. 3.9 and 3.10. In Fig. 3.9 (left), a settling sphere (green-marked) is approaching to packing. At this instant, the particle is still far from the *packing front* (orange). After a certain time (114s in this specific case) the particle packs, Fig. 3.9 (right). While the particle is approaching to packing, the packing front (which is the

virtual surface that results from joining the center of those particles that have just packed) is moving upwards. Equivalently for dendrites, the Figs. 3.10 (left) and (right) show a settling dendrite (green-marked) approaching to packing and the same dendrite already packed, respectively (42s later).

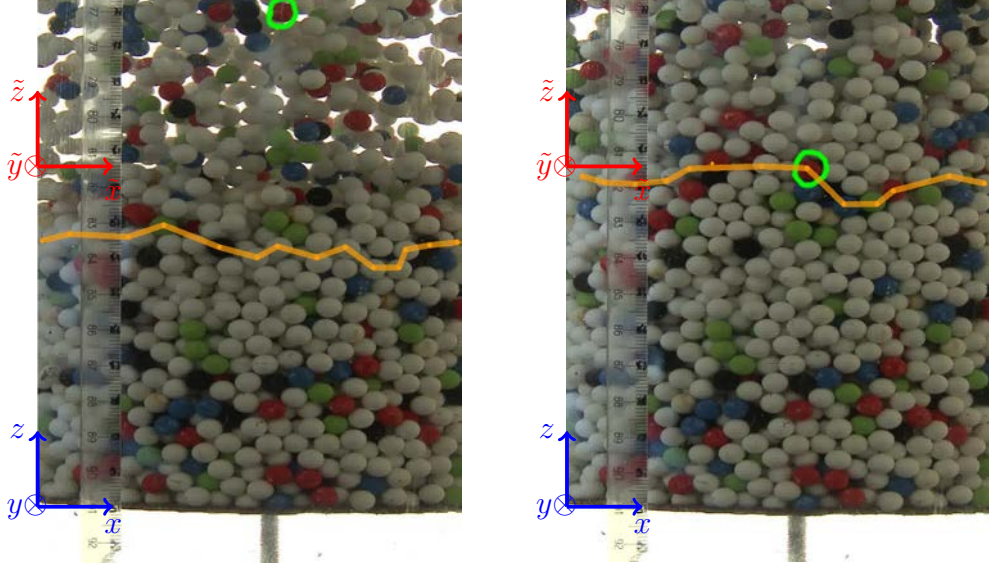


Figure 3.9: Example of spherical particle tracking in glycerol. The position of the particle marked by a green circle is tracked from an initial instant (left) until the final packed instant, 114s later (right). 30% of the granular system is painted to ease the tracking. The packing front is schematically shown in orange. The fixed-to-vessel global reference frame $\{x, y, z\}$ is shown in blue and the fixed-to-vessel particle reference frame $\{\tilde{x}, \tilde{y}, \tilde{z}\}$ with its origin vertical position located at the particle vertical packing position is shown in red.

We track n_{track} particles from the sedimentation regime until packing. For each tracked particle, i , we are interested to identify the instant when it begins to decelerate, $t_{i,0}$, from their initial sedimentation velocity, \mathbf{v}^{sed} , and the instant when the packing is achieved, $t_{i,pack}$. These two instants ($t_{i,0}$ and $t_{i,pack}$) are defined as:

- $t_{i,0}$: begining of deceleration (approaching to packing):

$$\begin{cases} \left| \frac{d\mathbf{x}_i}{dt} \right| = v_i^{sed}, & \text{if } t \leq t_{i,0}. \\ \left| \frac{d\mathbf{x}_i}{dt} \right| < v_i^{sed}, & \text{if } t > t_{i,0}. \end{cases} \quad (3.4)$$

- $t_{i,pack}$: begining of packing:

$$\begin{cases} \left| \frac{d\mathbf{x}_i}{dt} \right| > 0, & \text{if } t < t_{i,pack}. \\ \left| \frac{d\mathbf{x}_i}{dt} \right| = 0, & \text{if } t \geq t_{i,pack}. \end{cases} \quad (3.5)$$

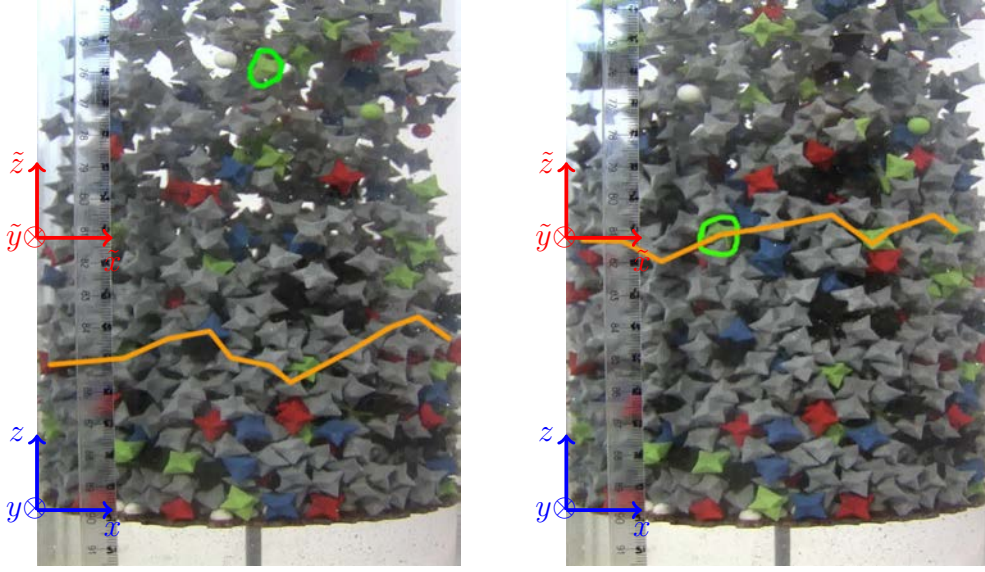


Figure 3.10: Example of dendritic particle tracking in glycerol. The position of the particle marked by a green circle is tracked from an initial instant (left) until the final packed instant, 42s later (right) 30% of the granular system is painted to ease the tracking. The packing front is schematically shown in orange. The fixed-to-vessel global reference frame $\{x, y, z\}$ is shown in blue and the fixed-to-vessel particle reference frame $\{\tilde{x}, \tilde{y}, \tilde{z}\}$ with its origin vertical position located at the particle vertical packing position is shown in red.

In this chapter, we define the transition time, $\Delta t_{i,trL}$, in Eq. 5.11 and the Lagrangian transition length, $L_{i,trL}$, in Eq. 5.12, by means of the particle velocity, i.e. the beginning of the transition is given by the instant when the particle begins to decelerate and the end of the transition is given by the instant when the particle deceleration finishes and the mechanical equilibrium is achieved. In Chap. 4, we investigate the time evolution of the local solid fraction in the Lagrangian description (associated to the particle) and the time evolution of the contacting neighbors that a particle has. In this way, we will improve the criterion to define the transition by means of the simulation results. We will define the beginning of the transition with the instant when the local solid fraction begins to increase with respect to the initial sedimentation local solid fraction, since it is previous to the beginning of the particle deceleration. Additionally, we will identify the end of transition with the instant when the number of contacting neighbors finishes to increase and remains constant, since this happens after the particle deceleration finishes.

$$\Delta t_{i,trL} = t_{i,pack} - t_{i,0} \quad (3.6)$$

$$L_{i,trL} = |\mathbf{x}_i(t_{i,pack}) - \mathbf{x}_i(t_{i,0})| \quad (3.7)$$

We use $n_{track} + 1$ reference frames to track each particle system:

- A fixed-to-vessel global reference frame (see blue reference frame in Figs. 3.9 and 3.10): common for all tracked particles.
- A fixed-to-vessel particle reference frame (see red reference frame in Figs. 3.9 and 3.10): each tracked particle has its own particle reference frame with its origin's vertical coordinate at the vertical coordinate of the particle's final position.

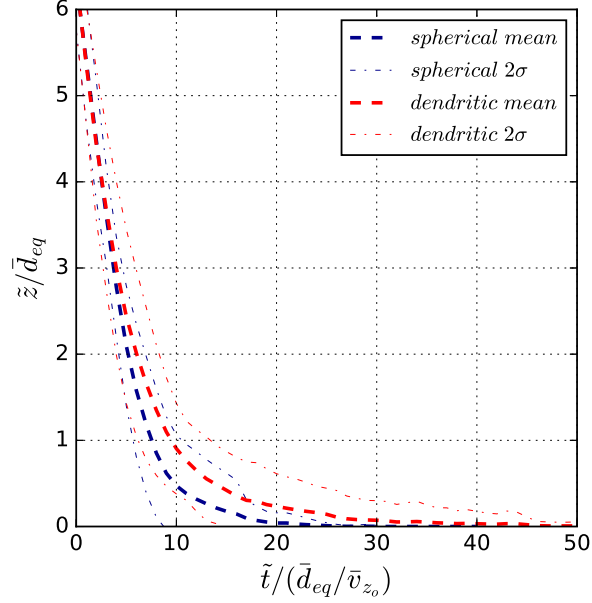


Figure 3.11: Dimensionless vertical coordinate, \tilde{z}/\bar{d}_{eq} , as a function of dimensionless time, $\tilde{t}/(\bar{d}_{eq}/\bar{v}_{z_o})$ for spherical (blue) and nonconvex dendritic grains (red). The mean 10-particle trajectory is shown for each geometry as well as the envelope formed by the values in a level of confidence of 95% ($-2\sigma, +2\sigma$).

Experimentally, the characterization of the particle trajectory until packing is carried out by tracking of a sample of 10 particles for each particle collection (spheres and dendrites). Tracking is carried out by analysis of images taken with a fixed HD video camera. Over 30% of the system particles are painted in four colors in order to facilitate the tracking.

With this technique, the projected trajectory of the tracked grains is obtained in a global reference frame fixed to the vessel $\{x(t_n), z(t_n)\}$ with an acquisition frequency of $1Hz$ ($t_n = n\Delta t_a$ with $n \in \mathbb{Z}^*$ and $\Delta t_a = 1s$). The measurement of the coordinate perpendicular to observation plane, y , is not possible. A particle is considered in mechanically stable equilibrium (packed) when its position has not observable modifications during $5s$. Afterwards, we translate the tracked particle trajectory from global to its own reference frame ($\tilde{z}(t) = z(t) - z_{pack}$, see the global and particle reference frames in Fig. 3.9). Additionally, only the particle trajectory segment given by $0 \leq \tilde{z} \leq 6 \bar{d}_{eq}$ is kept, translating the time origin for each particle in order to have $\tilde{z}(\tilde{t} = 0) = 6 \bar{d}_{eq}$.

Subsequently, all results are given in dimensionless physical variables to compare both granular collections. We define $\tilde{\mathbf{x}}/\bar{d}_{eq}$ and $\tilde{t}/(\bar{d}_{eq}/\bar{v}_{z_o})$ as the dimensionless position and dimensionless time, respectively, where \bar{v}_{z_o} is the mean vertical velocity at $\tilde{z} = 6\bar{d}_{eq}$, and \bar{d}_{eq} is the particle mean equivalent diameter. For each tracked particle, v_{z_o} is obtained by the derivation of the vertical coordinate at $\tilde{t} = 0$ via the central difference scheme (see Eq. 3.8).

$$v_{z_o} = \frac{\tilde{z}(\tilde{t} = \Delta t_a) - \tilde{z}(\tilde{t} = -\Delta t_a)}{2\Delta t_a} \quad (3.8)$$

Firstly, the evolution of the vertical coordinate over time is shown in Fig. 3.11 for spheres and dendrites. The mean vertical trajectory dramatically changes its behavior in the last $2\bar{d}_{eq}$ before the mechanically stable position. This phenomenon occurs due to the importance of the fluid lubrication forces. Similar vertical trajectory behavior is shown in Ref. [Dong et al., 2012] for numerical sedimentation of spheres with $St = o(1)$.

Assuming the mean Lagrangian transition length, \bar{L}_{trL} , of approximately $6\bar{d}_{eq}$ for both geometries (later numerically shown in Chap. 4), the dendritic packing dynamics is slower than that of the spheres for the same Stokes. A mean transition time ($\bar{\Delta}t_{trL}$) of $24.95\bar{d}_{eq}/\bar{v}_{z_o}$ and $46.01\bar{d}_{eq}/\bar{v}_{z_o}$ for spheres and nonconvex grains, respectively, is computed from the mean trajectories considering the packing when $\tilde{z} = 0.01\bar{d}_{eq}$.

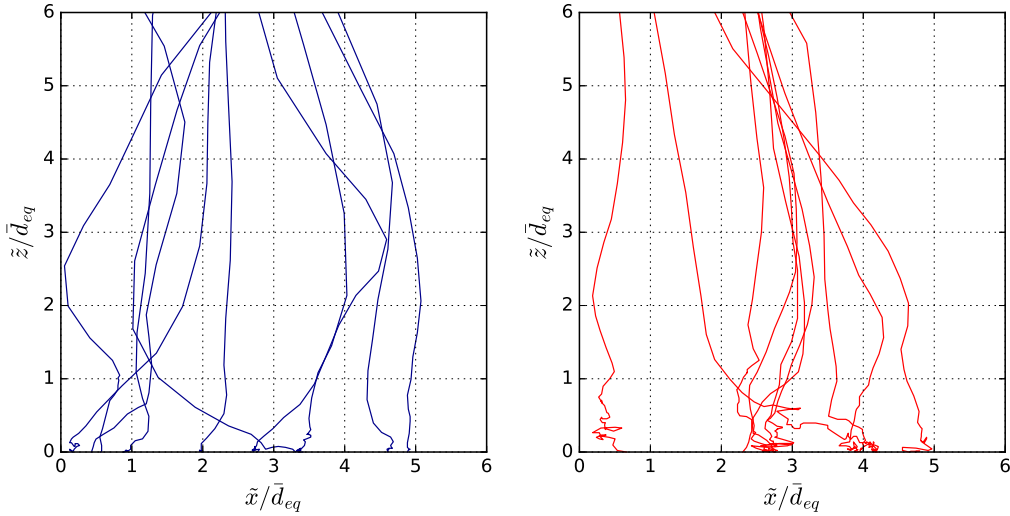


Figure 3.12: Dimensionless projected trajectory $\{\tilde{x}/\bar{d}_{eq}, \tilde{z}/\bar{d}_{eq}\}$ for spheres (blue) and nonconvex dendritic grains (red). 10 particle trajectories are shown for each geometry.

Figure 3.12 shows the dimensionless projected trajectory of the tracked grains $\{\tilde{x}/\bar{d}_{eq}, \tilde{z}/\bar{d}_{eq}\}$ for $0 \leq \tilde{z}/\bar{d}_{eq} \leq 6$. At the zone $0 \leq \tilde{z}/\bar{d}_{eq} \leq 1$, some horizontal oscillations are presented for the nonconvex particles, differing from the spherical. We think that this phenomenon is a consequence of the orientational rearrangement of the nonspherical particles, that is,

both translational and orientational rearrangement are activated until the packing position is reached in case of dendrites, whereas, mainly the translational rearrangement is active in case of spheres.

The absolute horizontal displacement (or horizontal path length), l_x , is computed by a central difference scheme from the horizontal projected coordinate:

$$l_x(\tilde{t}_n) = \frac{1}{2} \sum_{i=0}^n |\tilde{x}(\tilde{t}_{i+1}) - \tilde{x}(\tilde{t}_{i-1})| \quad (3.9)$$

In Fig. 3.13 we show the mean horizontal path length as a function of the vertical coordinate. A similar mean behavior is found for both spheres and nonconvex grains for most of the mean trajectory, although the dendritic shows an important horizontal displacement very close to packing (as previously seen with the horizontal oscillations). We show that both spheres and dendrites have a mean horizontal path displacement of about a third of the vertical displacement for the region close to packing.

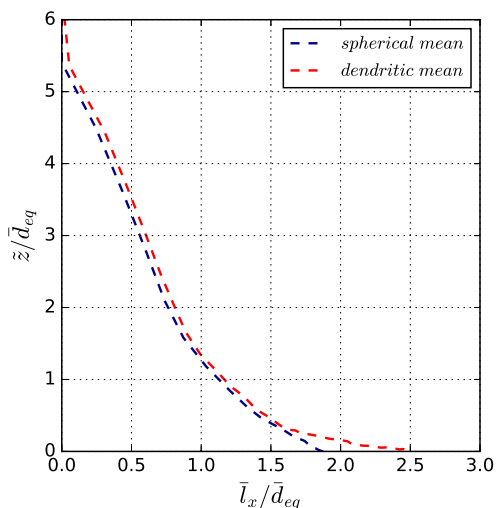


Figure 3.13: Dimensionless mean horizontal path displacement, \bar{l}_x/\bar{d}_{eq} , as a function of the dimensionless vertical coordinate, \tilde{z}/\bar{d}_{eq} , for spheres (blue) and nonconvex dendritic grains (red).

3.7 Conclusions of the experimental analysis

- The packing phenomenon of spherical and nonconvex dendritic grains in the context of metal alloy solidification is investigated from two points of view: 1) packing, i.e. final mechanically stable equilibrium and 2) packing dynamics, i.e. the transition of the granular system from the sedimentation to packing regimes. For this, a design of an experimental setup is developed from *scratch*, reproducing the solid grain sedimentation and packing in metal alloy solidification by hydrodynamic similarity. The packing of two monodisperse collections of spheres (reproducing the spherical envelopes in solidification) and nonconvex dendritic particles (reproducing the dendritic envelopes in solidification) are packed by four protocols (packing in glycerol, in a glycerol-water solution, in water and in air) to reproduce different packing hydrodynamic conditions. The glycerol protocol is more suitable for the packing phenomenon of aluminum DC casting whereas the water protocol, for static steel ingot casting.
- An experimental technique to obtain the packing fraction of spherical and non-spherical nonconvex equiaxed particles under different hydrodynamic conditions is developed for this thesis. It consists of the reconstruction of the total volume occupied by the granular system via 2D profiles from lateral photos of the packing.
- The geometrical influence is found to be more important than the hydrodynamic packing conditions since a 30% looser packings are found for the nonconvex dendritic grains for all hydrodynamic conditions studied.
- We show the average packing fraction results as a function of the Stokes number. The lower the Stokes, the looser is the packing. For the considered Stokes interval between $o(10^{-3})$ and $o(10^5)$, the monodisperse spheres pack in an interval between 57.5% and 62.8% and the monodisperse dendrites between 39.7% and 46.8%.
- Regarding the packing dynamics, an experimental methodology to investigate the transition from the sedimentation regime to packing in a low Stokes hydrodynamic condition of $St = o(10^{-3})$ (glycerol protocol) is developed for this thesis.
- The particle tracking for the two particle collections (spheres and dendrites) is carried out for the glycerol protocol. From the experimental tracking the xz -projected particle trajectory is obtained as a function of time, concluding that the dimensionless transition time, $\bar{\Delta}t_{trL}^*$, is much longer for the dendritic geometry.

Chapter 4

Packing modeling

4.1 Introduction

The possibility to numerically simulate the packing of equiaxed dendrite grains with the appropriate conditions to reproduce the packing in solidification becomes a personal desire from the first thesis day. The experimental analysis, previously presented in Chap. 3, is tedious and limited to two monodisperse noncohesive particle collections: spheres and dendrites. Moreover, the fundamental disadvantage is the limited accessible granular information.

Although the average solid fraction is experimentally obtained in the mechanically stable equilibrium (packing), the majority of the information cannot be determined, e.g. the mechanical contacts, contacting neighbors, local solid packing fraction, packing orientation or the vessel wall effect on the packing. Moreover, quantitative observations of the settling regime and of the transition to packing are extremely limited. Only the trajectories of a few grains can be measured. Grain fractions, collisions, collective interactions, etc, cannot be determined quantitatively in the experiments.

Thereby, the numerical modeling of the dynamics of the granular system, integrating the dynamics of each single particle composing the system, seems to be an optimal solution to obtain detailed information on the grain ensemble. The main difficulties of this model are the description of the nonconvex dendritic particles and accounting for the effect of the fluid presence on a large ensemble of particles. A Discrete Element Method (DEM) solver for arbitrary geometry that specifically addresses these issues is developed from *scratch*.

In this chapter, two models are introduced in the chronological order they were developed: 1) a geometrical model; 2) a dynamics model (DEM). The purpose of the geometrical model is to obtain a preliminar result of the effect of the grain morphology on the packing by means of a simple algorithm. Besides, with this model we understand the direct interactions between two solid particles, which is fundamental for the development of the dynamics model. This geometrical solver is based on the idea that when a particle, traveling toward an already packed particle cluster, touches any of the particles composing the cluster it gets stuck to them. Once it is stuck there is no possibility of translation or

orientation rearrangements.

Subsequently, the DEM solver is presented. The model is validated by the packing fraction of the experiments and then used to investigate the packing of a larger variety of grain shapes and a larger range of parameters. The influence of other properties of the particles (friction, polydispersity) and of the packing (wall effects) on the packing fraction is also estimated. Additionally, we investigate the packing dynamics (transition to packing) with this tool. The time evolution of several variables such as the local solid fraction, particle contacts, contacting neighbors, particle orientation and particle velocity are presented in both Lagrangian and Eulerian descriptions. 3D images and 2D slices of the granular media are also presented for visualization.

This model is based on straightforward ideas from Flight Mechanics and Linear Vibrations disciplines. It solves the dynamics of each particle (translation and rotation), the mechanical contacts among them (also frictional), and fluid interactions on the particles by drag, buoyancy and lubrication. It does not solve the dynamics of the fluid among the particles.

4.2 Geometrical packing model

4.2.1 Description

Low inertia to dissipation hydrodynamic conditions are frequent in grain packing during casting processes, see Chap. 2. We develop a geometrical particle packing algorithm in order to reproduce the limit physical situation of packing with an infinitively low inertia-to-dissipation approaching and an infinitively slow rearrangement, $St \rightarrow 0$ and $Ar \rightarrow 0$, respectively. Under these conditions, we assume that an approaching particle gets stuck to the packing front once the particle touches it, avoiding the rearrangement.

With this algorithm we investigate the influence of the geometry on the packing fraction and contacting neighbors for these conditions. The algorithm creates a first particle with a random orientation (see the *K. Shoemaker algorithm*, Ref. [Shoemaker, 1985] for a isotropic random orientation of a 3D particle) at the origin of the global reference frame. The next particles are sequentially added with random orientation to form a packed cluster. Each particle is born at a random point of an external sphere (center at origin), larger than the packed particle cluster. It approaches along a random direction to the packed particle cluster. Finally, once the approaching particle touches a particle from the cluster, it remains stuck to the cluster without rearrangement.

Another limit situation of interest for this algorithm is the situation where the cohesion forces among particles is much more important than the apparent weight, which is given by $\chi = F_{coh}/F_{drive} \gg 1$ (see Sec. 1.3). The approaching particle gets stuck to the packed particle cluster without rearrangement due to the strong cohesive forces. According to Ref. [Dong et al., 2012] the larger the cohesion forces, the looser the packing shown for monodisperse spheres.

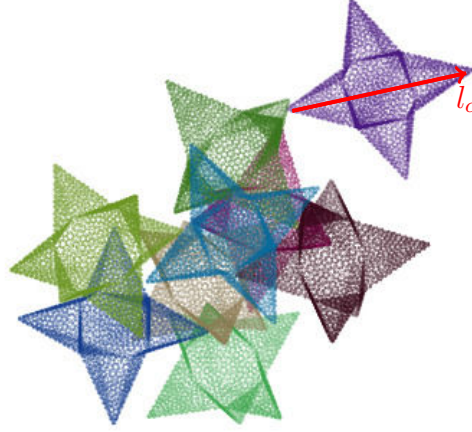


Figure 4.1: Geometrically packed 10-particle cluster. The particles consist of a dendrite-like envelope formed by six quadrilateral pyramids with a central cube. The characteristic particle size, l_c , is also shown in red.

Fig. 4.1 illustrates a 10-particle cluster formed by this geometrical algorithm. The purple particle, which was the last particle added to the cluster stopped in the position shown in the figure. In this figure the chosen geometry is that of a dendritic envelope formed by a central cube and six quadrilateral pyramids with an apex angle of 45° .

The *contact detection* is based on the *bisection method* to accelerate the contact detection. The surface of the nonspherical particles is described by a large number of markers. In this algorithm over 10^4 markers per particle are used to provide an accurate description of the dendritic envelope. The i and j particles enter in contact when the distance between only one pair of markers (one from i and another from j particles) is smaller than a certain tolerance:

$$\|\mathbf{r}_{i,l} - \mathbf{r}_{j,m}\| < \epsilon \quad (4.1)$$

where $\mathbf{r}_{i,l}$ and $\mathbf{r}_{j,m}$ are the position vectors of the marker l (on particle i) and the marker m (on particle j), respectively. ϵ is the contact tolerance, which is commonly set to 1% of the nonspherical characteristic particle size, l_c (see Fig. 4.1).

We can define a counter of the number of pairs of markers (markers that belong to two particles i and j) that fulfill the tolerance criterion as $S_{il,jm}$. In case that only a pair of markers (one from i and another from j) satisfies the this criterion: $S_{il,jm} = 1$. When more than a pair of markers satisfies the criterion, $S_{il,jm} > 1$, we do not consider contact but an excessive overlap between particles i and j . Finally, if $S_{il,jm} = 0$, no pair fulfills the tolerance criterion. See the algorithm flowchart to obtain the packing position of the particle $i > 1$ in Appx. C.1.

An efficient strategy to compute the counter $S_{ij,lm}$ between the approaching particle i and

the $i - 1$ already packed particles, where $1 < j < i - 1$, is developed. We introduce the concept of *sphere of influence* for the approaching particle. In this way, we do not simply compare marker by marker. We filter those particles that are contained in the sphere of influence of the particle i . Normally we use a sphere of influence of radius slightly larger than l_c (for a monodisperse collection of particles).

Thanks to this geometrical algorithm, we get a better understanding of the strategies to manage the contact between nonspherical particles. This knowledge is applied in the development of a Discrete Element Method solver for arbitrary geometry particles.

4.2.2 Sphere and dendrite packings

By means of the aforementioned geometrical algorithm, a collection of 20000 monodisperse spheres and a collection of 20000 monodisperse dendrites (apex angle of 45° , $\Psi = 0.7$) are packed around a point. Fig. 4.2 shows a 3D view of both packings: spheres and dendrites on the left and on the right, respectively.

In Fig. 4.3 the local solid packing fraction, ϕ , and the number of particle contacts, Z , are shown as a function of the dimensionless cluster radius, $r_{cluster}/d_{eq}$, where d_{eq} is the equivalent diameter of a particle. For both spheres and dendrites three regions are observed: the core of the cluster, an intermediate region and the external particle layers of the cluster. We consider the intermediate region to compare the solid packing fraction and the contacts. In case of the spheres, the region of interest ranges from 5 to 15 d_{eq} whereas for dendrites from 5 to 20 d_{eq} . For spheres we consider an average packing fraction of approximately 0.27 whereas for dendrites 0.15 with approximately 2.1 contacts for both geometries.

Additionally, it is interesting to qualitatively comprehend what the packed granular system looks like when it is sliced by a plane. Thereby, it is possible to compare the simulated packings with the grains (dendritic contours) of the metallic alloy microstructure. Hence, Fig. 4.4 shows an arbitrary *plane slice* (plane containing the cluster origin) of both the sphere and dendritic packings, left and right, respectively.

In case of spheres, the fraction obtained by this geometrical algorithm, 0.27, is much lower than that of the the random loose packing (approximately 0.55). In case of dendrites, this fraction, 0.15, is also much lower than the experimental packing fraction obtained in glycerol (approximately 0.40). In this way, when the particle translational or rotational rearrangements are not allowed, the packing fraction dramatically decreases.

We also compare this monodisperse sphere packing fraction with the DEM simulation of cohesive monodisperse spheres in Ref. [Dong et al., 2012] where the packing fraction varied from 0.64 down to 0.10 depending on the ratio between cohesive forces and the apparent weight. In this reference, a solid packing fraction of 0.27 is obtained when the cohesive forces are about 10^3 times larger than the apparent weight.

Finally, we can also compare the geometrical packing fractions obtained by this geometri-

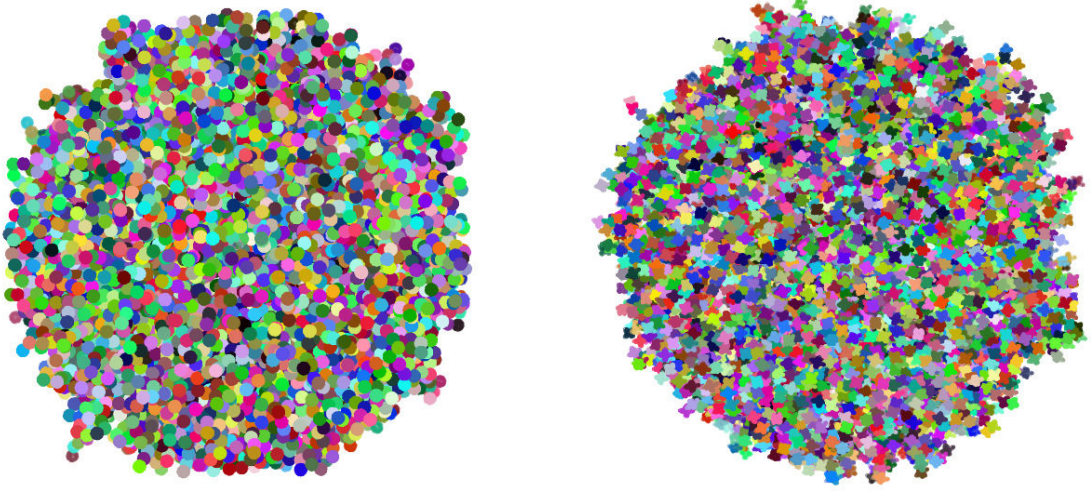


Figure 4.2: 3D view of spherical (left) and dendritic (right) geometrical packings of monodisperse particles around an initial point. Both of them are formed by 20000 randomly oriented particles and sent to the cluster from a random direction.

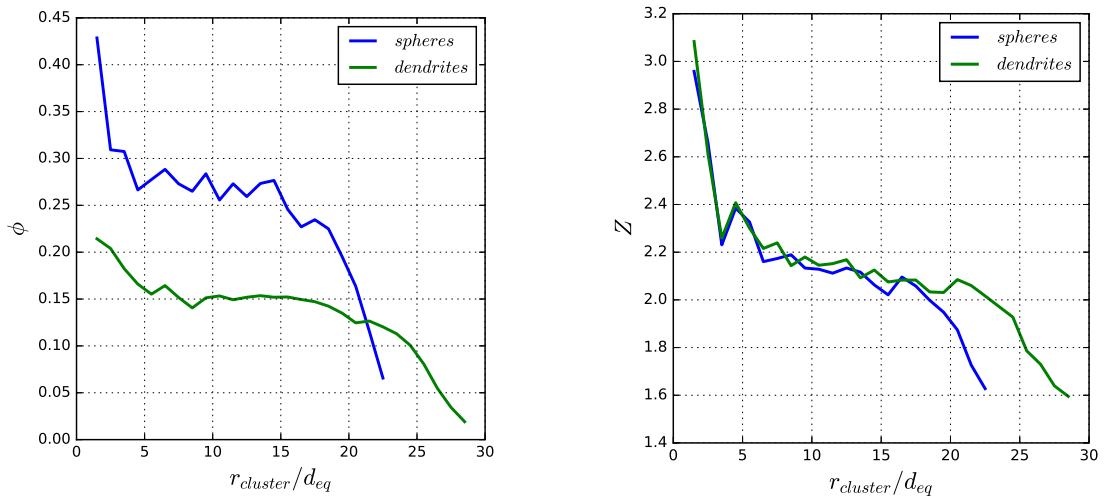


Figure 4.3: Left: local solid packing fraction, ϕ , as a function of the dimensionless cluster radius, $r_{cluster}/d_{eq}$, for packings of monodisperse spheres and dendrites about a central point. ϕ is computed with a radial discretization $\Delta r_{cluster}/d_{eq} = 1$. Right: number of contacts, Z , as a function of $r_{cluster}/d_{eq}$. Z is computed with a radial discretization of $\Delta r_{cluster}/d_{eq} = 1$.

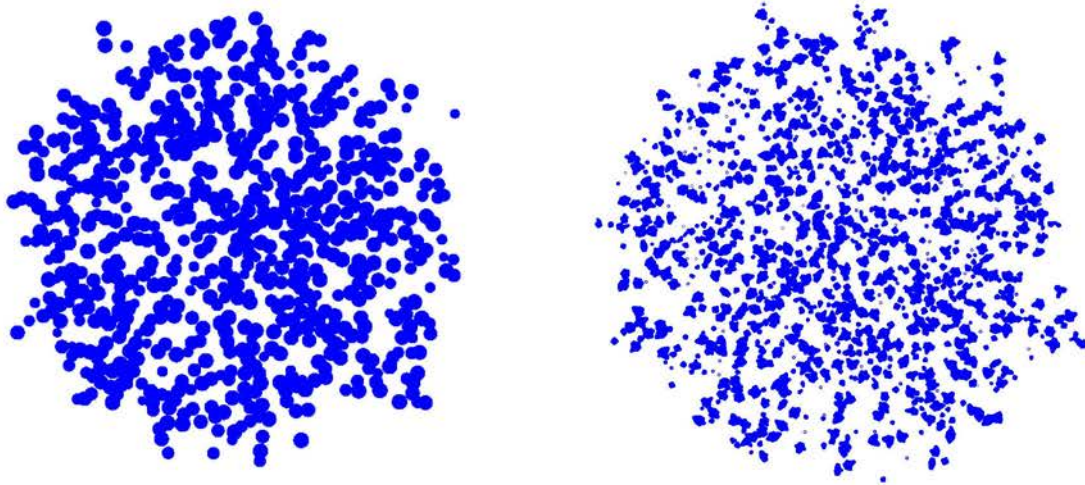


Figure 4.4: Plane slicing of the packings of spheres (left) and dendrites (right) about an initial point. Both of them are formed by 20000 particles which are randomly orientated and sent to cluster along a random direction.

cal algorithm, ranging from 0.15 to 0.27, with the packing fraction used by Ref. [Heyvaert et al., 2017] in modeling of DC casting of an Al alloy. [Heyvaert et al., 2017] have shown that the best fit of the simulations to the experimental measurements of temperature and macrosegregation is obtained with packing fractions of 0.20. The grain morphology was globular. Our simulations of geometrical packings indicate that such packing fractions correspond to a very loose unjammed configuration. Such packings can be obtained if the cohesive forces are extremely high and thus seem to loose for equiaxed grains in solidification.

4.3 Discrete Element Method

4.3.1 Motivation

The development of a numerical tool able to reproduce the grain packings in solidification is essential to understand the phenomenon of packing as well as the influence of the principal parameters. Generally, the higher amount of particles that a packing is composed by, the less disturbing effects are included (such as those inserted by the boundary conditions). In this vein, the challenge of the modeling of the packing in solidification is summarized in next points:

- Maximizing the number of equiaxed dendritic grains.
- Maximizing the detail of the dendritic envelope shape.
- Developing a realistic packing protocol that includes the fluid effect on the grains, interparticle friction or grain size polydispersity.
- Minimizing the computational cost. The numerical model must be conceived with strategies that accelerate the computation such as the parallelization or strategies that reduce the domain size such as the periodic boundary conditions.
- Reasonable development time of the numerical tool.

In this way, the numerical tool that we present is a compromise between the aforementioned points with special attention to the last point. In the context of a three-year numerical-experimental thesis, special care must be taken in the development time of the numerical tools. A pure Discrete Element Method is proposed without solving the fluid dynamics. Nevertheless, the fluid effect on the grains is carefully modeled by drag and lubrication models. This numerical tool is based on the integration of the motion of each of the particles composing the granular system. The interparticle interaction model uses a sophisticated algorithm for the detection of contacts between grains.

4.3.2 Rigid body dynamics

Two reference frames are considered to project the tensorial variables, of 1^{st} and 2^{nd} ranks:

- Inertial frame \mathcal{I} : global reference frame, common for all the particles of the system.
- Body frame \mathcal{B} : attached to the solid particle. Each particle has its own body frame. Its origin is located in the center of mass of each particle. The orientation of the particle with respect to its body reference frame is arbitrary. However, it is preferable to work with the principal axes of inertia since the inertia tensor is diagonal when projected on them, see Fig. 4.5 (left).

The conservation of linear and angular momentum are individually computed for each particle i of the granular system:

$$\frac{d}{dt}(m\mathbf{v}) = \mathbf{F}_{tot} \quad (4.2)$$

$$\frac{d}{dt}(\mathbf{I}_G\omega) = \mathbf{M}_{G,tot} \quad (4.3)$$

where m , \mathbf{v} and \mathbf{F}_{tot} are the particle mass, the velocity of the particle's center of mass and the sum of all external forces applied to the particle's center of mass. \mathbf{I}_G , ω and $\mathbf{M}_{G,tot}$ are the particle inertia tensor about the center of mass, the particle angular velocity and the sum of all external moments applied to the particle about the center of mass, respectively. In Eq. (4.2), the mass is intentionally included in the time-derivative to account for the possible particle mass time-evolution, e.g. particle growth.

The linear momentum balance, Eq. (4.2), is projected in \mathcal{I} , see Eq. (4.5), whereas the angular momentum balance, Eq. (4.3), is projected in \mathcal{B} to maintain the particle inertia tensor constant over time, see Eq. (4.7). Moreover, the necessary kinematic relations are added for closure: Eq. (4.4) for the relation between particle position and linear velocity, and the Eq. (4.6) for the relation between orientation and angular velocity. In case of time-dependent particle-geometry due to growth, the variation of particle inertia is given by Eqs. (4.8) and (4.9).

$$\frac{d\mathbf{r}_{ir}}{dt} = \mathbf{v}_{ir} \quad (4.4)$$

$$\frac{d\mathbf{v}_{ir}}{dt} = m^{-1}(\mathbf{F}_{tot,ir} - \frac{dm}{dt}\mathbf{v}_{ir}) \quad (4.5)$$

$$\frac{d\hat{q}}{dt} = \frac{1}{2}\hat{q} \diamond \hat{\omega}_b \quad (4.6)$$

$$\frac{d\omega_b}{dt} = \mathbf{I}_{G,b}^{-1}(\mathbf{M}_{G,tot,b} - \omega_b \times (\mathbf{I}_{G,b}\omega_b)) \quad (4.7)$$

$$m = f_m(t) \quad (4.8)$$

$$\mathbf{I}_{G,b} = \mathbf{f}_I(t) \quad (4.9)$$

Indices ir and b mean *projected in inertial reference* and *projected in body reference*, respectively. In Eq. (4.4) \mathbf{r} is the position vector of the particle center of mass. In Eq. (4.6) \hat{q} is the particle quaternion which describes the orientation of the body reference frame with respect to the inertial frame, $\hat{\omega} = [0, \omega]$ is the quaternion of the angular velocity vector and \diamond is the *Grassmann product* (see Ref. [Zhao and van Wachem, 2013]) or simply product between two quaternions. The term $-\omega_b \times (\mathbf{I}_{G,b}\omega_b)$ in Eq. (4.7) is an inertial or fictitious moment, a consequence of *Coriolis Theorem* since the body frame is non-inertial.

Thereby, the obtained system of equations, from Eq. (4.4) to Eq. (4.9), is a first-order ordinary differential vectorial equation of rank 13 containing 13 scalar dependent variables to describe the motion of one single particle. Moreover, to completely describe the physical problem, the corresponding initial conditions for the 13 variables must be provided.

Quaternions are chosen for orientation description to avoid the singularities of the rotation matrix when using Euler's angles, also known as gimbal lock.

4.3.3 Particle geometry discretization

To provide an arbitrary geometry character to the DEM model, we decide to discretize the particles by means of *extra spheres*. Despite there are certain geometries which can be analytically described (e.g. superballs, see Sec. 1.3.3).

This algorithm is designed to support two different geometrical discretization strategies:

- Surface discretization: basically focused on an accurate surface description of the particle geometry. The inner part of the geometry is free of extra spheres to increase the computational efficiency of the algorithm. Nonetheless, the particle inertial properties do consider the inner volume, Fig. 4.5 (left). To determine the positions of the extra spheres, we compute a triangular mesh at the surface of a rescaled smaller geometry via the mesh generator `gmsh` (see Ref. [Geuzaine and Remacle, 2009]).
- Volume discretization or classical clump logic (see an example of this discretization in Ref. [Pasha et al., 2016]): a set of extra spheres is used to create the whole volume of the particle, Fig. 4.5 (right). In case of spherical particle shape, it is obvious that a single extra sphere composes the particle.

4.3.4 Contact model

The *contact* between the particle i and the particle j exist if at least one extra sphere of the particle i is overlapping one or several extra spheres of the particle j . The contact force is the consequence of the overlap, only computed if there is overlap.

In this vein, $\Omega_{i,l}$ and $\Omega_{j,m}$ are the volumetric regions occupied, at a certain time, by the extra sphere l belonging to the particle i and the extra sphere m belonging to particle j , respectively. The contact force that the particle i receives from the particle j is $\mathbf{F}_{cont_{i,j}}$. Likewise, $\mathbf{M}_{cont_{i,j}}$ is the moment that the particle i receives from the particle j due to the contact. Without loss of generality, since $\mathbf{F}_{cont_{j,i}} = -\mathbf{F}_{cont_{i,j}}$ and $\mathbf{M}_{cont_{j,i}} = -\mathbf{M}_{cont_{i,j}}$, the model description is focused on the particle i from now on.

The contact force and moment are written in Eqs. (4.10) and (4.11), respectively.

$$\mathbf{F}_{cont_{i,j}} = \sum_{l=1}^{N_{sph,i}} \sum_{m=1}^{N_{sph,j}} \mathbf{F}_{il,jm} \lambda_{l,m} \quad (4.10)$$

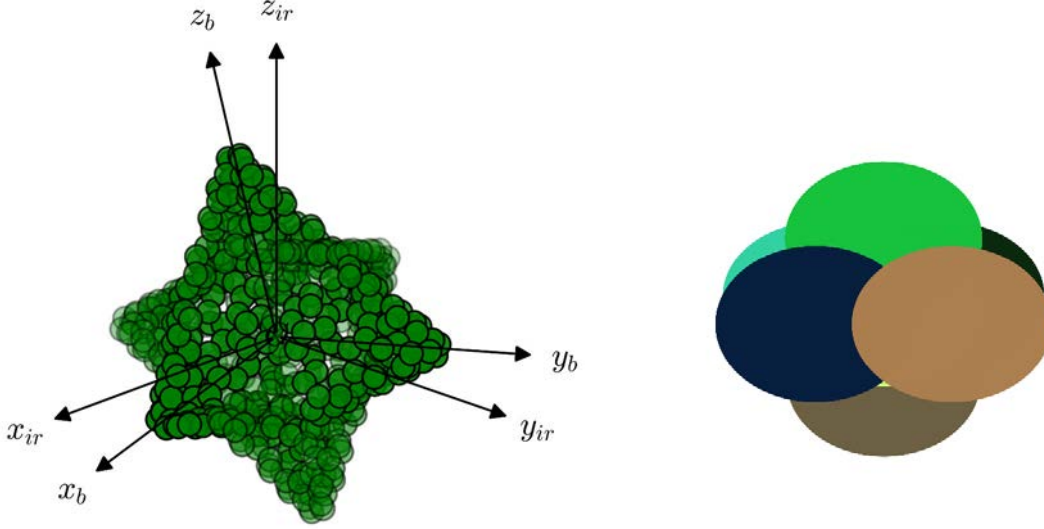


Figure 4.5: Left: surface discretization of a dendritic envelope where 527 extra spheres are used to define the particle surface $l_c/d_{xsph} \approx 20$. The extra spheres are internally tangential to the envelope virtual surface. The body frame \mathcal{B} is shown as well as an inertial frame with parallel axes than \mathcal{I} but whose origin is located at the particle's center of mass. Right: volume discretization of a globular grain with six extra spheres, $l_c/d_{xsph} \approx 1.8$. l_c and d_{xsph} are the largest particle length and the diameter of the extra sphere.

$$\mathbf{M}_{cont_{i,j}} = \sum_{l=1}^{N_{xsph,i}} \sum_{m=1}^{N_{xsph,j}} (\mathbf{r}_{cont_{lm}} - \mathbf{r}_i) \times \mathbf{F}_{il,jm} \lambda_{l,m} \quad (4.11)$$

$$\lambda_{l,m} = \begin{cases} 1, & \text{if } \Omega_{i,l} \cap \Omega_{j,m} \neq \emptyset. \\ 0, & \text{otherwise.} \end{cases} \quad (4.12)$$

where $N_{xsph,i}$ and $N_{xsph,j}$ are the number of extra spheres of the particle i and the particle j , respectively. $\mathbf{F}_{il,jm}$ is the force that the extra sphere m belonging to the particle j transmits to the extra sphere l that belongs to particle i . $\mathbf{r}_{cont_{lm}}$ is the position vector of the *contact point* between the extra spheres l and m , whereas, \mathbf{r}_i is the position vector of the center of mass of the particle i . Finally $\lambda_{l,m}$ is a binary operator to compute the sum of extra sphere forces if there is overlap, defined by Eq. (4.12).

The overlap, δ , is defined as $\delta = (d_{il} + d_{jm})/2 - \|\mathbf{r}_{il} - \mathbf{r}_{jm}\|$ where d_{il} and d_{jm} are the diameters of the extra spheres l and m , respectively; \mathbf{r}_{il} and \mathbf{r}_{jm} are the positions of the center of both extra spheres. As a consequence, the overlap is limited by both upper and lower limits: $0 < \delta < (d_{il} + d_{jm})/2$. Besides, an upper limit of extra sphere overlap can be defined, $0 < \delta < \delta_{max} < (d_{il} + d_{jm})/2$, to avoid excessive overlaps.

$\mathbf{F}_{il,jm}$ is projected in a normal-tangential-binormal base, \mathcal{C} , $\{\mathbf{e}_n, \mathbf{e}_t, \mathbf{e}_b\}$ with the origin in

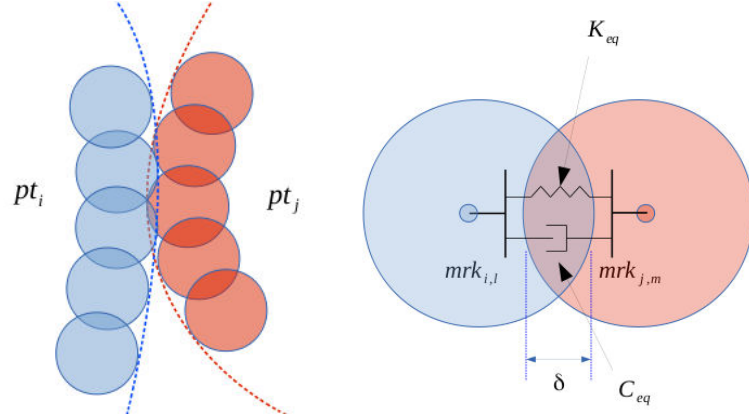


Figure 4.6: Left: particle i (in blue) and particle j (in red), which are superficially discretized by means of extra spheres, have a contact. Right: overlap between a extra sphere, l , from the particle i and another extra sphere, m , from the particle j . The Kelvin-Voigt (spring-dashpot) model for the normal component of the contact force between both extra spheres is shown schematically. K_{eq} and C_{eq} are the equivalent stiffness and damping coefficients, respectively.

$\mathbf{r}_{cont_{lm}}$. This base is associated to the particle i since the normal direction goes out from this particle (see Eq. (4.13)).

$$\mathbf{e}_{n_i} = \frac{\mathbf{r}_{jm} - \mathbf{r}_{il}}{\|\mathbf{r}_{jm} - \mathbf{r}_{il}\|} \quad (4.13)$$

Hence, the contact point between the extra spheres l and m is defined as: $\mathbf{r}_{cont_{lm}} = \mathbf{r}_{il} + (d_{il} - \delta/2) \mathbf{e}_{n_i}$. To define the tangential direction of the base, some kinematic concepts are introduced. Note that the contact point, which is a geometrical point, belongs both to the particle i and particle j . Thereby, the velocity of this point at both particles i and j is computed (see Eqs. (4.14) and (4.15), respectively). Moreover, the relative velocity of contact point at m with respect to l is computed (see Eq. (4.16)).

$$\mathbf{v}_{cont_{il}} = \mathbf{v}_i + \omega_i \times ((\mathbf{r}_{il} - \mathbf{r}_i) + (d_{il} - \delta/2)\mathbf{e}_{n_i}) \quad (4.14)$$

$$\mathbf{v}_{cont_{jm}} = \mathbf{v}_j + \omega_j \times ((\mathbf{r}_{jm} - \mathbf{r}_j) - (d_{jm} - \delta/2)\mathbf{e}_{n_i}) \quad (4.15)$$

$$\Delta \mathbf{v}_{cont_{m,l}} = \mathbf{v}_{cont_{jm}} - \mathbf{v}_{cont_{il}} \quad (4.16)$$

The previous relative velocity is projected in the normal direction of \mathcal{C} in Eq. (4.17). Besides, the *tangential component* of the relative velocity is also computed, in Eq. (4.18), which will provide the tangential direction of \mathcal{C} .

$$\Delta \mathbf{v}_{cont_{m,l}}^n = \dot{\delta} \mathbf{e}_{n_i} = \Delta \mathbf{v}_{cont_{m,l}} \cdot \mathbf{e}_{n_i} \quad (4.17)$$

$$\Delta \mathbf{v}_{cont_{m,l}}^t = \Delta \mathbf{v}_{cont_{m,l}} - \Delta \mathbf{v}_{cont_{m,l}}^n \quad (4.18)$$

Finally, it is possible to compute the tangential and binormal directions (see Eqs. (4.19) and (4.20)). By means of this definition of tangential direction, \mathcal{C} is only unique if $\Delta \mathbf{v}_{cont_{m,l}}^t \neq \mathbf{0}$. Otherwise, there is a singularity since there are infinite possibilities to define the tangential and binormal directions.

$$\mathbf{e}_{t_i} = \frac{\Delta \mathbf{v}_{cont_{m,l}}^t}{\|\Delta \mathbf{v}_{cont_{m,l}}^t\|} \quad (4.19)$$

$$\mathbf{e}_{b_i} = \mathbf{e}_{n_i} \times \mathbf{e}_{t_i} \quad (4.20)$$

After obtaining \mathcal{C} , $\{\mathbf{e}_n, \mathbf{e}_t, \mathbf{e}_b\}$, the force $\mathbf{F}_{il,jm}$ is computed by means of modeling each of its components in this base (see from Eq. (4.21) to Eq. (4.24)).

$$\mathbf{F}_{il,jm} = F_{il,jm}^n \mathbf{e}_{n_i} + F_{il,jm}^t \mathbf{e}_{t_i} + F_{il,jm}^b \mathbf{e}_{b_i} \quad (4.21)$$

$$F_{il,jm}^n = f_K(\delta) + f_C(\dot{\delta}) \quad (4.22)$$

$$F_{il,jm}^t = \begin{cases} \mu_{fr,s} F_{il,jm}^n \left(\frac{\Delta \mathbf{v}_{cont_{m,l}}^t}{v_{th}} \right), & \text{if static: } \|\mathbf{v}_{cont_{m,l}}^t\| \leq v_{th} . \\ \mu_{fr,d} F_{il,jm}^n, & \text{if dynamic: } \|\mathbf{v}_{cont_{m,l}}^t\| > v_{th}. \end{cases} \quad (4.23)$$

$$F_{il,jm}^b = 0 \quad (4.24)$$

The normal force is the sum of the stiffness and the damping effects: we set them in *parallel* (see Eq. (4.22)). f_K and f_C are functions which depend on δ and $\dot{\delta}$, respectively. Different models can be used for f_K and f_C . The simplest is a linear elastic spring for the stiffness element and a linear viscous damper for the dissipation, this is the so-called *Kelvin-Voigt* model (see Eq. (4.25)). This linear model of the contact normal component permits to use the *superposition* principle for the addition of all contact forces at the extra spheres in case of arbitrary particle geometry.

$$F_{il,jm}^n = K_{eq} \delta + C_{eq} \dot{\delta} \quad (4.25)$$

Assuming this linear model, the *equivalent stiffness coefficient*, K_{eq} , and *equivalent damping coefficient*, C_{eq} , are straightforward to obtain by solving the *one and a half degrees of freedom* system with the *Linear Vibration Theory* (see Eqs. (4.26) and (4.27)).

$$K_{eq} = \frac{K_i K_j}{K_i + K_j} \quad (4.26)$$

$$C_{eq} = \frac{C_i C_j}{C_i + C_j} \quad (4.27)$$

where K_i and K_j are the linear stiffness of the particles i and j , respectively. In the same way, C_i and C_j are the linear viscous damping coefficients of the particles i and j , respectively.

Moreover, we add the tangential friction at the contact. Specifically, we use a friction model based on the Coulomb friction model (see Eq. (4.23)) but with the possibility to have different coefficients for static or dynamic situations, $\mu_{fr,s}$ and $\mu_{fr,d}$, respectively. A threshold velocity, v_{th} , is defined to switch between the quasi-static and dynamic state (see Ref. [O'Reilly, 2013]). The main objective of this strategy is to avoid the numerical instabilities of a simple Coulomb friction model.

The component of the contact force along the binormal direction is not considered for our application.

4.3.5 Fluid model

In this numerical model, we developed a cleverly simplified, yet rather accurate model that is computationally much cheaper than a directly coupled CFD-DEM model. In this way, we can simulate larger domains, more nonspherical particles, longer times and perform more extensive parameter studies. The main objective is to accurately describe the influence of the fluid on the particle packing. A simplified model of the fluid is presented accounting for some effects of the presence of fluid on the particles:

- Dissipative effects: the fluid is described as a dissipative quiescent medium where the particles dissipate their kinetic energy. The dissipative effects are split in two terms:
 - Drag model: force and moment.
 - Lubrication model: a pressure is exerted by the fluid squeezed out of the fluid layers between the solid particles. This phenomenon is mathematically understood as a non-linear viscous damping for every couple of neighboring particles.
- Fluid buoyancy

Drag model: force and moment

Assuming incompressible Newtonian fluid, low Reynolds regime and the steady situation of the fluid flow the *Stokes flow* is used to model the force and momentum of drag. Herein the inertial, \mathcal{I} , and body, \mathcal{B} , frames are recovered. Moreover, a new reference frame is needed, \mathcal{B}^* which is a non-inertial reference frame whose origin is also located at the particle center of mass, as \mathcal{B} , however, its axes are not attached to the particle but they remain parallel to \mathcal{I} 's axes.

The equations of the fluid flow around the particle in \mathcal{B}^* reference frame (*Stokes flow*) are:

$$\nabla \cdot \mathbf{v}_f = 0 \quad (4.28)$$

$$\nabla p_f + \mu_f \nabla \times (\nabla \times \mathbf{v}_f) = 0 \quad (4.29)$$

with the boundary conditions at the particle contour, $C(\mathbf{x}, t) = 0$, and the infinity, defined in Eqs. (4.30) and (4.31), respectively.

$$\mathbf{v}_f = \boldsymbol{\omega} \times \mathbf{x} \text{ in } C(\mathbf{x}, t) = 0 \quad (4.30)$$

$$\mathbf{v}_f \rightarrow v_f \mathbf{e}_f - \mathbf{v}_{pt_{in}} \text{ when } |\mathbf{x}| \rightarrow \infty \quad (4.31)$$

The force and moment that the particle receives from the Stokes flow, previously described by Eqs. 4.28 and 4.29, are:

$$\mathbf{F}_d = -\mu_f \frac{d_{eq}}{2} \left\{ \mathbf{A}_G \mathbf{v}_{pt-f} + \frac{d_{eq}}{2} \mathbf{B}_G \boldsymbol{\omega}_{pt-f} \right\} \quad (4.32)$$

$$\mathbf{M}_{G,d} = -\mu_f \left(\frac{d_{eq}}{2} \right)^2 \left\{ \mathbf{C}_G \mathbf{v}_{pt-f} + \frac{d_{eq}}{2} \mathbf{D}_G \boldsymbol{\omega}_{pt-f} \right\} \quad (4.33)$$

where \mathbf{F}_d and $\mathbf{M}_{G,d}$ are the drag force and the drag moment of the fluid on the particle, respectively. \mathbf{v}_{pt-f} , $\boldsymbol{\omega}_{pt-f}$ are the linear and angular particle velocity with respect to the fluid, respectively. In case of arbitrary particle geometry, the tensors \mathbf{A} , \mathbf{B} , \mathbf{C} and \mathbf{D} are not constant when they are projected in \mathcal{B}^* , since particle can rotate. On the other hand, if the force and moment are projected in body frame, \mathcal{B} , these tensors are constant and they depend on the particle geometry exclusively.

In case of equiaxed geometry and assuming the principal branches, $\langle 100 \rangle$, as body axes, we assume $\mathbf{A}_{G,b}$ and $\mathbf{D}_{G,b}$ as spherical tensors, where $\mathbf{A}_{G,b} = A \mathbf{1}$, $\mathbf{D}_{G,b} = D \mathbf{1}$, and $\mathbf{1}$ is the unit tensor of rank 2. On the other hand, $\mathbf{B}_{G,b}$ and $\mathbf{C}_{G,b}$ are null tensors. In case of spheres, A and D are: 6π and 8π , respectively.

Lubrication model

The lubrication forces are modeled to account for the transmission of forces between two neighboring particles through the viscous fluid. Mathematically, the lubrication forces are distance interactions among the neighboring particles which consist of a non-linear dash-pot. The calculation of lubrication forces requires a solution of the Reynolds lubrication equations between two particles. Analytical solutions exist only for simple geometries, such as for pair interactions of spheres of equal size Ref. [Frankel and Acrivos, 1967], but not for complex shaped particles, such as dendrites. We therefore use the monodisperse sphere lubrication model provided by Ref. [Frankel and Acrivos, 1967], modified by calibration coefficients:

$$\mathbf{F}_{lub,ij,n} = \lambda_{lub} \frac{3}{8} \pi \mu_f \frac{d_{eq}^2}{h} \Delta \mathbf{v}_{ij} \mathbf{e}_{n_{ij}} \quad (4.34)$$

$$\mathbf{F}_{lub,ij,t} = \lambda_{lub} \frac{\pi}{2} \mu_f d_{eq} \left\{ \left(1 + \frac{h}{d_{eq}} \right) \ln \left(1 + \frac{d_{eq}}{h} \right) - 1 \right\} \Delta \mathbf{v}_{ij} \mathbf{e}_{t_{ij}} \quad (4.35)$$

where $F_{lub,ij,n}$ and $F_{lub,ij,t}$ are the normal and tangential lubrication forces, respectively, applied on the particle i due to the particle j . d_{eq} is the equivalent diameter of the monodisperse collection. We add a scalar coefficient λ_{lub} to the original model where $\lambda_{lub} = 1$. This coefficient will be experimentally calibrated ($\lambda_{lub} > 1$) in order to reproduce the packing dynamics (see Sec. 4.4.2). According to the original model, the gap between two spheres is computed by Eq. 4.36. However, we modify this equation and we add a lubrication length, d_{lub} , instead of the equivalent particle diameter. The reason for this is that the lubrication effect between nonspherical particles is characterized by a distance different from the equivalent diameter. For dendrites we expect that $d_{eq} < d_{lub} < l_c$, where l_c is twice the primary arm length. The lubrication length is later calibrated by experiments (see Sec. 4.4.2). The parameters λ_{lub} and d_{lub} are expected to account for the nonspherical shape of the particles.

$$h = \|\mathbf{r}_j - \mathbf{r}_i\| - 2d_{eq} \quad (4.36)$$

$$h = \|\mathbf{r}_j - \mathbf{r}_i\| - 2d_{lub} \quad (4.37)$$

The variables $\Delta \mathbf{v}_{ij}$, $\mathbf{e}_{n_{ij}}$ and $\mathbf{e}_{t_{ij}}$ are described from Eq. (4.38) to Eq. (4.40).

$$\Delta \mathbf{v}_{ij} = \mathbf{v}_j - \mathbf{v}_i \quad (4.38)$$

$$\mathbf{e}_{n_{ij}} = \frac{\mathbf{r}_j - \mathbf{r}_i}{\|\mathbf{r}_j - \mathbf{r}_i\|} \quad (4.39)$$

$$\mathbf{e}_{t_{ij}} = \frac{\Delta \mathbf{v}_{ij} - (\Delta \mathbf{v}_{ij} \mathbf{e}_{n_{ij}}) \mathbf{e}_{n_{ij}}}{\|\Delta \mathbf{v}_{ij} - (\Delta \mathbf{v}_{ij} \mathbf{e}_{n_{ij}}) \mathbf{e}_{n_{ij}}\|} \quad (4.40)$$

Finally, two last parameters are needed to close the lubrication model: the radius of the *lubrication influence sphere*, R_{lub} , and the minimum gap to cut off the increment of the lubrication force, avoiding the so-called *Stokes paradox*, h_{min} . Then, if $h < h_{min}$ the lubrication force takes the value of the lubrication force that corresponds to the gap h_{min} . The influence of R_{lub} is investigated in Sec. 4.4.2 for values ranges from $1.5 l_c$ up to $2.5 l_c$. On the other hand, the minimum gap is fixed for all simulations: $h_{min} = 0.01 d_{eq}$.

Buoyancy

The fluid buoyancy is given by:

$$\mathbf{F}_{buoy} = -\rho_f \left(\frac{\pi}{6} d_{eq}^3 \right) \mathbf{a}_o, \quad (4.41)$$

where $\mathbf{a}_o = \mathbf{g}_o + \mathbf{a}_{ni}$, and \mathbf{a}_{ni} is a non-inertial acceleration.

4.3.6 Initial conditions

The initial position, velocity and angular velocity (vectors) and orientation (quaternion) must be provided for each particle as initial conditions:

$$\mathbf{r}_i(t = 0) = \mathbf{r}_{i_o} \quad (4.42)$$

$$\mathring{q}_i(t = 0) = \mathring{q}_{i_o} \quad (4.43)$$

$$\mathbf{v}_i(t = 0) = \mathbf{v}_{i_o} \quad (4.44)$$

$$\omega_i(t = 0) = \omega_{i_o} \quad (4.45)$$

The Random Sequential Addition (RSA) algorithm is used to initialize the positions of the particle centers. It basically consists of a random particle addition within the simulation domain ensuring that they do not overlap with the previously added particles (see Appx. C.2 for the details).

The initial particle orientations are uniformly random by means of the *K. Shoemaker algorithm*, Ref. [Shoemaker, 1985]. See Appx. C.3 for an explanation of the algorithm.

4.3.7 Particle-boundary interaction

The developed algorithm supports *rigid walls*, *semi-rigid walls* and *periodic boundaries* in a rectangular prism simulation domain. We define:

- Rigid and semi-rigid walls. Equally to the interparticle contact, the wall transmits a force on the particle, in case there is a contact between a particle and domain wall (rigid or semi-rigid). The particle-wall contact at time t is defined in Eq. 4.46.

$$\Omega_{il}(t) \cap \partial\Omega(t) \neq \emptyset \quad (4.46)$$

where the $\Omega_{il}(t)$ is the space region occupied by the extra sphere l of the particle i . The time-dependence of the domain contour $\partial\Omega(t)$ is intentionally added since our algorithm supports the motion of the wall domain.

The particle-wall contact is defined in an equivalent way than that of the interparticle contact (from Eq. 4.14 to Eq. 4.27). The only difference is that of the normal direction of the contact reference frame: in case of the particle-wall contact, the normal direction corresponds to the normal direction to the wall at the contact point.

- Rigid walls: the *equivalent particle-wall stiffness* must ensure that any overlap between an extra sphere and wall is lower than the maximum allowed overlap.

- Semi-rigid walls: in this case the *equivalent particle-wall stiffness* is reduced in order to: 1) increase the integration time step (see Appx. C.4) and 2) reduce the vessel wall effect on the packing. The particles can partially cross the domain contour (wall), but it is ensure that the center of mass of the particles do not cross the contour.
- Periodic boundary: in particle packing simulations, the wall effect on the packing structure can be reduced by using periodic boundary conditions. Smaller simulation domains can then be used. In our arbitry-geometry algorithm, the periodic boundary is implemented as follows:

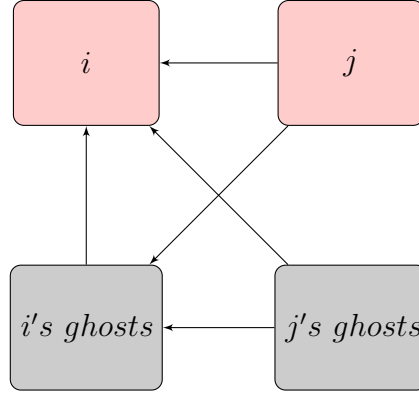


Figure 4.7: Without periodicity the particle i only receives forces and moments from the particle j . In case of periodicity, it is needed to include the ghost parts. Hence, i can receive contact forces from j 's ghosts. Additionally, the i also receives forces and moments from j and j 's ghosts through its ghost parts (i 's ghosts).

- When a particle center leaves the domain through a wall then the particle center enters though the periodic side. Without loss of generality, this concept is explained using x -direction in eqs. (4.47) and (4.48). The domain walls in the x direction are located at $x = 0$ and $x = L_x$ in the next explanation.

$$\text{if } \mathbf{r}_i \cdot \mathbf{e}_x > L_x \Rightarrow (\mathbf{r}_i \cdot \mathbf{e}_x)_{new} = \mathbf{r}_i \cdot \mathbf{e}_x - L_x \quad (4.47)$$

$$\text{if } \mathbf{r}_i \cdot \mathbf{e}_x < 0 \Rightarrow (\mathbf{r}_i \cdot \mathbf{e}_x)_{new} = L_x - |\mathbf{r}_i \cdot \mathbf{e}_x| \quad (4.48)$$

- Interparticle contact force: for particles that are partially split by a periodic domain boundary, the particle parts outside the domain are incorporated at their corresponding periodic positions, these new parts are called *ghosts*. A particle can have at most three *ghost parts*, if it is located at a corner of the rectangular prism domain in case of threefold domain periodicity. It is important to highlight that the particle i can receive contact forces from another particle j , as well as, from j 's ghost parts. Finally, i could receive forces through its ghost parts (i 's ghosts) from the particle j , as well as, from j 's ghost parts. The possible interactions are schematically shown in Fig. 4.7.

4.3.8 Contact detection

The main difficulty of the contact detection between nonspherical particles is to design an efficient algorithm to compute the binary operator, $\lambda_{l,m}$, (previously defined in see Sec. 4.3.4). For that, we use the knowledge acquire from the geometrical algorithm (see Sec. 4.2).

In this way, each particle i has its stored neighbors. The neighbors of the particle i are those particles inside the *influence sphere* of i . The center of the influence sphere is the particle center of mass and the radius of the influence sphere of i is slightly larger than $(l_{c_i} + l_{c_{max}})/2$, where l_{c_i} is the size l_c of particle i and $l_{c_{max}}$ is the largest l_c of the particle collection in case of polydispersity. We avoid to compute the neighbors of i for every time step since it can be computationally expensive. Instead of this, we update its neighbors every certain time steps (e.g. every $o(10^2)$ for some of our sedimentation and packing simulations). In case of periodic boundary conditions, we must consider the ghost parts as neighbors.

We introduce a second level filters for the contact detection between the extra spheres of the particle i and the extra spheres of its neighbors. We define the circumscribed sphere of the particle i of radius $R_{flt_i} = l_{c_i}$, and equivalently for the particle j , $R_{flt_j} = l_{c_j}$. In this way, we only operate between the extra spheres of the particle i that are contained in the circumscribed sphere of j and the extra spheres of the particle j that are contained in the circumscribed sphere of i , considerably reducing the number of operations per time step.

4.4 DEM simulations

A packing depends on the particle characteristics (e.g. geometry, material, surface, etc) and the packing protocol, as previously shown in Sec. 1.3. In this section, two different simulation protocols are designed to investigate the characteristics of the particle mechanical stable equilibrium (packing) as well as the packing dynamics. The common idea in all protocols is that of maximizing the simulation detail (maximizing the number of grains and maximizing the detail of the dendritic envelope shape) with attention to the computational cost. The developed protocols are:

- A) Low weight protocol. This protocol is designed for the packing hydrodynamic conditions of low inertia-to-dissipation, that is, for Stokes numbers lower than approximately 10 since the restitution coefficient upon contact is nil Ref. [Izard et al., 2014]. The grains are packed with a very small vertical acceleration ($a = 10^{-5}g_0$). The drag or lubrication models are not used in this protocol. The objective is to decrease as much as possible the computational cost of the simulations. In absence of an important weight, the packed particles are not loaded with the weight of the upper particles. The numerical stiffness of the particles is chosen following the collision criterion in Appx. C.4.
- B) Fluid effect protocol. In this protocol the grains are packed due to the apparent weight. The drag and lubrication models are used. The packed particles are loaded with the apparent weight of the pile of particles above. Higher values of the numerical stiffness of the particles are needed, then, shorter integration time step, see Appx. C.4.

4.4.1 Low weight protocol

Herein we focus on the packing hydrodynamic conditions characterized by a low inertia-to-dissipation ratio. According to Ref. [Izard et al., 2014], the grain restitution coefficient (in case of spheres) is nil if the Stokes number is lower than a threshold which is approximately 10. In this way, the logic of this first packing protocol is to pack the grains with a simple protocol able to reproduce this restitution condition, avoiding the simulation of the fluid. The apparent weight, the drag and lubrication models are not used.

A low uniform vertical acceleration, $a = 10^{-5} g_0$, is applied to the particles that simultaneously sediment and pack over the horizontal domain wall, $z = 0$. The kinetic energy of the particles is dissipated by the dashpots at the contacts. We use a *critical* viscous damping to ensure the nil restitution coefficient for the collisions. The low vertical acceleration of the protocol allows us to considerably increase the integration time step of the simulations. The choice of the numerical parameters is explained in Appx. C.4.

With this protocol, we investigate the influence of the grain geometry, the interparticle friction and the particle size polydispersity on the packing fraction. Additionally, the influence of the vessel wall and the initial conditions on the packing are also considered.

Influence of the geometry

We investigate the influence of the geometry on the packing with frictionless monodisperse particle collections. We consider two typical characteristic morphologies of the equiaxed grains: a) dendritic and b) globular (see Sec. 1.2.1). In this way, the influence of two geometrical models (dendritic and globular) on the packing is studied.

- a) Dendritic envelope model: based on a central cube with six quadrilateral pyramids which apex-angle is θ . We provide three geometrical parameters to characterize the geometry: 1) the sphericity, $\Psi(\theta)$ (see Eq. 4.49), 2) the ratio of the widest length and the equivalent diameter, $l_c/d_{eq}(\theta)$ (see Eq. 4.50) and 3) the ratio between the equivalent diameter of the principal section and the perimeter of the principal section, that we called $\eta(\theta)$. It is defined in detail in Eq. 4.51 and related to the *hydraulic diameter* of the principal section.

$$\Psi(\theta) = \sin\left(\frac{\theta}{2}\right) \left\{ \frac{\pi}{6} \left[1 + \cotan\left(\frac{\theta}{2}\right) \right]^2 \right\}^{1/3} \quad (4.49)$$

$$\frac{l_c}{d_{eq}}(\theta) = \frac{\Psi(\theta)}{\sin\left(\frac{\theta}{2}\right)} \quad (4.50)$$

$$\eta = \left(\frac{4\pi S_p}{P^2} \right)^{1/2} = \left(\frac{D_H}{P/\pi} \right)^{1/2} \quad (4.51)$$

where S_p , P and D_H are the principal section surface, the principal section perimeter and the principal section hydraulic diameter, respectively. A principal section of the particle is that section that contains two $\langle 100 \rangle$ directions. In the particular case of the dendritic envelope model, the parameter $\eta(\theta)$ is given by Eq. 4.52.

$$\eta(\theta) = \frac{\sqrt{\pi}}{2} \left\{ \sin\left(\frac{\theta}{2}\right) \left[\sin\left(\frac{\theta}{2}\right) + \cos\left(\frac{\theta}{2}\right) \right] \right\}^{1/2} \quad (4.52)$$

The Fig. 4.8 left shows the geometrical characteristics Ψ , d_{eq}/l_c and η as a function of the apex-angle, θ .

Three different dendritic shapes are generated from this dendritic geometrical model by changing the apex-angle θ :

- Dendrites of 45° of apex-angle: nonconvex (see the extra sphere discretization in Fig. 4.5 left). Moreover, it is identical to the experimental model in Fig. 3.4.
- Dendrites of 60° of apex-angle: nonconvex.
- Dendrites of 90° of apex-angle: convex, rhombic dodecahedron (Catalan Solid).

In Table 4.1 the three dendritic geometries are presented with their corresponding geometrical parameters. The simulated dendritic particles have similar inertial characteristics to those of the experiments ($\rho_s = 1400 \text{ kg/m}^3$ and $d_{eq} = 6.88 \text{ mm}$). Moreover, the number of surface extra sphere discretization, N_{xsph} , is given. This number is chosen in order to have the same d_{eq}/d_{xsph} ratio for all three geometries. Assuming that the extra spheres corresponding to the same particle do not overlap, we compute the diameter of the extra spheres as $d_{xsph} \approx (S_{pt}/N_{xsph})^{1/2}$, with S_{pt} the area of the particle surface. Using the definition of sphericity, we define the ratio $d_{eq}/d_{xsph} \approx (\Psi N_{xsph}/\pi)^{1/2}$.

We fix the stiffness to $K_{pt} = 0.1 \text{ N/m}$, which for this protocol results in a maximum overlap of $\delta_{max}/d_{eq} \approx 0.005$. It is important to highlight that in case of dendrites, up to 10 pairs of contacts between extra spheres of two particles can exist.

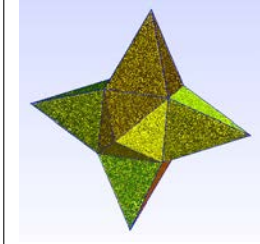
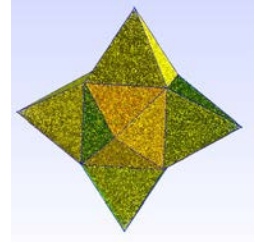
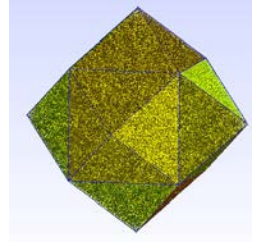
45° nonconvex	Dendrite 60°	Dendrite 90°
		
$\Psi = 0.69$	$\Psi = 0.79$	$\Psi = 0.90$
$d_{eq}/l_c = 0.57$	$d_{eq}/l_c = 0.63$	$d_{eq}/l_c = 0.78$
$\eta = 0.63$	$\eta = 0.73$	$\eta = 0.89$
$N_{xsph} = 527$	$N_{xsph} = 432$	$N_{xsph} = 383$
$d_{eq}/d_{xsph} = 10.76$	$d_{eq}/d_{xsph} = 10.42$	$d_{eq}/d_{xsph} = 10.47$

Table 4.1: Dendritic envelope models used in the DEM simulations.

- b) Globular envelope model: based on six spheres of diameter d_{xsph} (see Fig. 4.5). The center of each sphere is given by Eq. 4.53.

$$\mathbf{r}_i = \frac{\sqrt{2}}{2} \xi d_{xsph} \mathbf{e}_i, \quad i = 1, 6 \quad (4.53)$$

where \mathbf{e}_i is the unit vector of the six branch directions $\langle 100 \rangle$ and ξ is a dimensionless parameter in the interval $(0, 1)$. If $\xi = 0$ the six spheres converge in a simple spherical geometry whereas for $\xi = 1$ the maximum eccentricity of the spheres is reached. By this globular model, only six extra spheres are needed. In this case, the discretization is volumetric differing from dendritic envelopes. The geometrical parameters $\Psi(\theta)$ and $d_{eq}/l_c(\theta)$ are numerically computed whereas $\eta(\theta)$ is analytically given by Eq. 4.54.

$$\eta(\xi) = \left\{ \frac{4\pi[\xi^2 + \xi \cos(asin\xi) + asin\xi + \pi/4]}{(\pi + 4asin\xi)^2} \right\}^{1/2} \quad (4.54)$$

Fig. 4.8 (right) shows the geometrical characteristics Ψ , d_{eq}/l_c and η as a function of the parameter $1 - \xi$. With this geometrical model, three different geometries are generated with three different values of ξ :

- Globular of $\xi = 1.0$, maximum eccentricity of the centers of the extra spheres with respect to the center of mass of the grain. Ψ , d_{eq}/l_c and η are 0.65, 0.76 and 0.69, respectively.
- Globular of $\xi = 0.8$. Ψ , d_{eq}/l_c and η are 0.80, 0.82 and 0.87, respectively (see Fig. 4.5 right).
- Globular of $\xi = 0.6$. Ψ , d_{eq}/l_c and η are 0.90, 0.87 and 0.93, respectively.

The simulated globular particles have similar inertial characteristics to the experimental grains ($\rho_s = 1400 \text{ kg/m}^3$ and $d_{eq} = 6.88 \text{ mm}$). We fix a stiffness of 10 N/m , obtaining a maximum overlap of $\delta_{max}/d_{eq} \approx 0.002$.

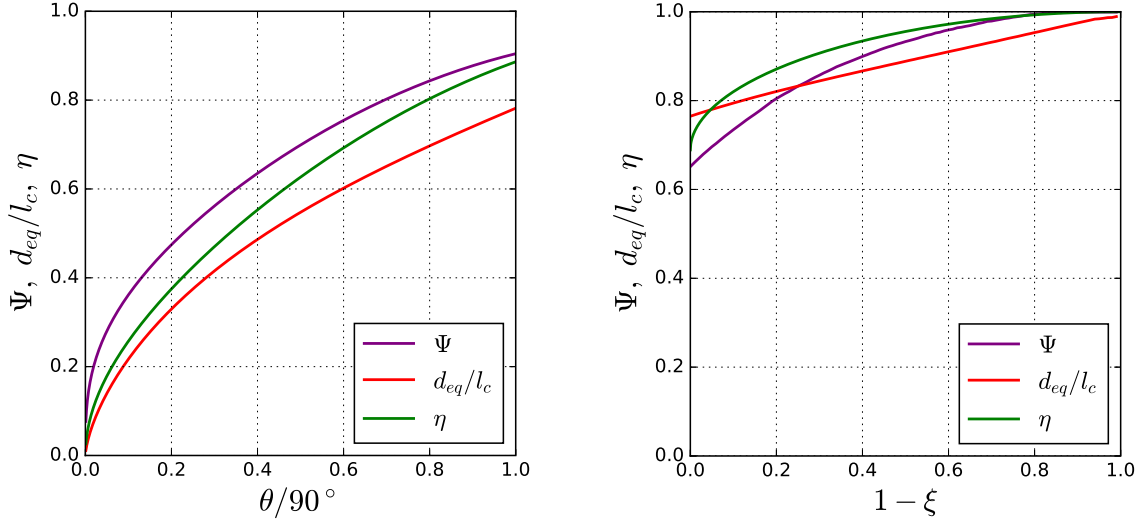


Figure 4.8: Geometrical characteristics Ψ , d_{eq}/l_c and η for Left: dendrites, as a function of apex-angle θ , and right: globular geometry, as a function of $1 - \xi$.

- c) Reference geometries: in order to compare to results available in literature, the case of a monodisperse collection of spheres (an unique central extra sphere which is the grain itself) and the case of ellipsoids of revolution with axes ratio of $1.25 : 0.8 : 0.8$ and $N_{xsph} = 380$ are added.

The sphere of $d_{xsph} = d_{eq} = 6.88 \text{ mm}$ has as geometrical parameters $\Psi = 1$, $d_{eq}/l_c = 1$ and $\eta = 1$. We fix a stiffness of 10 N/m , obtaining a maximum overlap of $\delta_{max}/d_{eq} \approx 0.002$. In case of the ellipsoidal shape, $d_{eq} = 8.0 \text{ mm}$ with $\Psi = 0.97$ and $d_{eq}/l_c = 0.80$, with a stiffness of 0.1 N/m , obtaining maximum overlap similar to the dendrites. The parameter η is not computed for the revolution ellipsoid since it is not an equiaxed geometry (it has two principal cross sections). Both collections have a $\rho_s = 1400 \text{ kg/m}^3$.

A rectangular prism domain is used for all simulations with semi-rigid walls which dimensions L_x, L_y, L_z depend on the simulation:

- Spherical: 2000 particles in a $84 \times 84 \times 1000 \text{ mm}^3$ domain with an initial low solid fraction of 4.8%.
- Dendritic and globular: 1000 particles in a $84 \times 84 \times 500 \text{ mm}^3$ domain with an initial low solid fraction of 4.8%.
- Ellipsoidal: 1000 particles in a $84 \times 84 \times 500 \text{ mm}^3$ domain with an initial low solid fraction of 7.5%.

All simulations are carried out with $\Delta t = 10^{-3} \text{ s}$, achieving the mechanically stable equilibrium for approximately 200s of simulation. Since the geometrical influence on the packing is compared, all the particle collections herein are frictionless and noncohesive.

Fig. 4.9 shows the packing of 1000 dendritic particles of 45° (upper) and 1000 globular particles (lower) with $\xi = 1.0$ with 3D and 2D postprocessings. The 2D views show the complexity of the packed granular systems when cut by a plane (vertical plane in this case).

In Appx. D the time evolutions with 3D and 2D views for the different geometries are included (see Figs. D.1, D.2, D.3, D.4, D.5 and D.6) for monodisperse spherical, 45° dendritic, 60° dendritic, 90° dendritic, $\xi = 1.0$ globular and $1.25 : 0.8 : 0.8$ ellipsoidal geometries.

Subsequently, the packings of the different geometries are shown as a function of their geometrical parameters (Ψ , d_{eq}/l_c and η). The average packing fraction, $\langle \phi_s \rangle_\Omega$, which is computed at a certain volume Ω , is obtained by means of the *Voronoi tessellation* of the granular system using *Voro++* (see Ref. [Rycroft, 2009]). Afterwards, we apply Eq. 4.55, where V_{s_i} and V_{cell_i} are the volume of the particle i and its corresponding *Voronoi cell* volume, respectively. The region Ω_A is the whole packing from wall to wall and it is defined by the intervals $[0, 84] \times [0, 84] \times [0, h] \text{ mm}^3$ where h is the lowest position of the top packing surface whereas Ω_B is a region supposed not affected by the wall effect and it is defined by $[22, 62] \times [22, 62] \times [10, 20] \text{ mm}^3$.

$$\langle \phi_s \rangle_\Omega = \frac{\sum V_{s_i}}{\sum V_{cell_i}}, \quad \forall i / \mathbf{r}_i \in \Omega \quad (4.55)$$

In the case of spheres, we obtain a value of $\langle \phi_s \rangle_{\Omega_B} = 0.643$, which corresponds to the result in Ref. [Delaney et al., 2011] for sedimentation and packing with relatively low driving force computed in DEM. A slightly looser packing fraction is obtained when the wall effect is accounted for $\langle \phi_s \rangle_{\Omega_A} = 0.618$. Besides, the results of the ellipsoids are also compared to the same literature reference [Delaney et al., 2011], obtaining a 4% looser packing in our case (see Fig. 4.10).

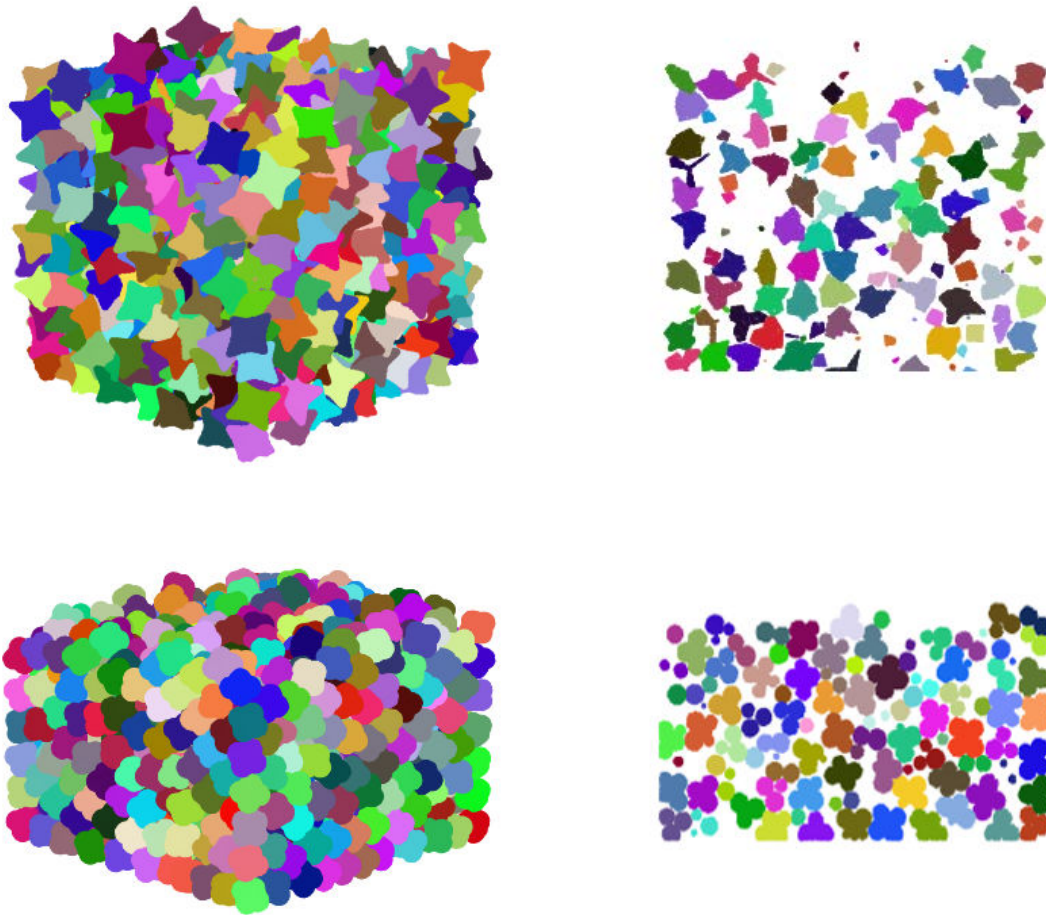


Figure 4.9: Visual post-processing of: upper: 1000 dendritic envelopes 45° packing ($\langle \phi_s \rangle_{\Omega_{pack}} \approx 0.40$) with $3D$ and $2D$ ($x = 42 \text{ mm}$) in left and right, respectively. And lower) 1000 globular envelopes $\xi = 1.0$ packing $\langle \phi_s \rangle_{\Omega_{pack}} \approx 0.60$ with $3D$ and $2D$ ($x = 42 \text{ mm}$) in left and right, respectively.

A clear influence of the sphericity, Ψ , on the packing fraction of the equiaxed dendritic grains is found: the lower the grain sphericity, the looser is the grain packing. The equiaxed dendritic envelopes with $\Psi = 0.69$ pack approximately 38% looser than spheres, see Fig. 4.10. The correlation between packing fraction and particle sphericity for six-branch particles formed by three ellipsoids from Ref. [Malinouskaya et al., 2009] is also included in Fig. 4.10. A good agreement is found between this correlation and our dendritic envelopes.

A lower influence of the sphericity is found for the globular envelope model compared to the dendritic: a higher packing fraction is obtained for the globular particles when compared to the dendrites of same sphericity. We conclude that the sphericity is not a suitable property to represent the influence of the envelope shape on the packing fraction. A function between the packing fraction and the particle geometrical shape is desired.

The vessel wall effect (the difference $\langle \phi_s \rangle_{\Omega_B} - \langle \phi_s \rangle_{\Omega_A}$) is shown to be constant with sphericity for both globular and dendritic envelopes.

Additionally, the experimental results of spheres and dendrites under low inertia-to-dissipation conditions (case of glycerol with a $St = o(10^{-3})$, see Sec. 3.5) are added for the validation of this numerical model. A good agreement between the numerical packing fraction and the experimental packing fractions of the dendritic envelope of $\theta = 45^\circ$ is achieved. In case of the spheres, a 5% relative denser packing fraction is obtained by our DEM protocol. This difference can be attributed to the importance of the interparticle friction for the sphere packing. The influence of friction is investigated in detail afterwards.

The results for spheres, equiaxed dendritic and globular geometries are shown as a function of the geometrical 2D parameter η (see Fig. 4.11). The lower η is, the looser is the packing. A similar influence of the geometrical parameter d_{eq}/l_c on the packing fraction is found for dendritic and globular envelopes.

According to the three previous correlations of the equiaxed envelope packing fraction to the geometrical envelope parameters Ψ , η and d_{eq}/l_c , the most suitable parameter is d_{eq}/l_c . Our experimental and numerical data under low inertia-to-dissipation hydrodynamic conditions is exponentially fitted using least-squares to provide a function between d_{eq}/l_c and the packing fraction:

$$\langle \phi_s \rangle_{\Omega_B} = 0.643 - 0.257 e^{2.97 - 5.31 (d_{eq}/l_c)} \quad (4.56)$$

Additionally, we also investigate the packing dynamics or time-evolution of the system. For that, the time-evolution of the solid fraction is computed in an Eulerian description, $\phi(\mathbf{x}, t)$ where \mathbf{x} is projected in a reference frame fixed to the vessel. Since the main changes of the packing fraction occur along the vertical direction ($\partial\phi/\partial x \approx \partial\phi/\partial y \ll \partial\phi/\partial z$) only the vertical profile is shown, $\phi(z, t)$ in Fig. 4.13.

The domain is vertically discretized in N_z uniform volumes, $\Omega(z_c)$, defined by their center

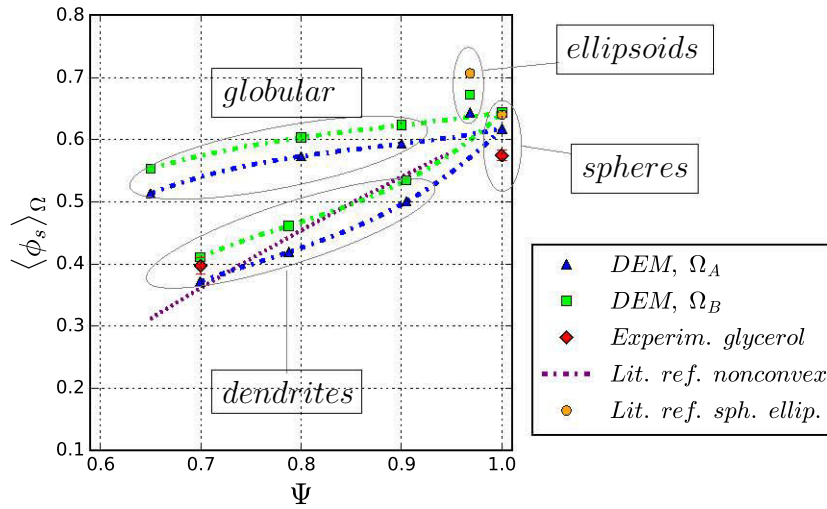


Figure 4.10: Average solid volumetric packing fraction, $\langle \phi_s \rangle_\Omega$, function of particle sphericity. $\langle \phi_s \rangle_{\Omega_A}$ (accounting for the vessel wall effect) is shown with *triangular blue extra spheres* and $\langle \phi_s \rangle_{\Omega_B}$ shown via *squared green extra spheres*. The equiaxed grain results are joined by a dashed green and blue lines, $\langle \phi_s \rangle_{\Omega_B}$ and $\langle \phi_s \rangle_{\Omega_A}$, respectively. The validation experiments (see Sec. 3.5) for 45° dendritic envelopes and spheres are shown via red rhomboid extra spheres. The numerical results from literature for spheres and ellipsoids under low gravity conditions [Delaney et al., 2011] (*Lit. ref. ellip.*) and sequential deposition under gravity of 6-branch nonconvex particles from Ref. [Malinouskaya et al., 2009] (*Lit. ref. non-convex*) are also included.

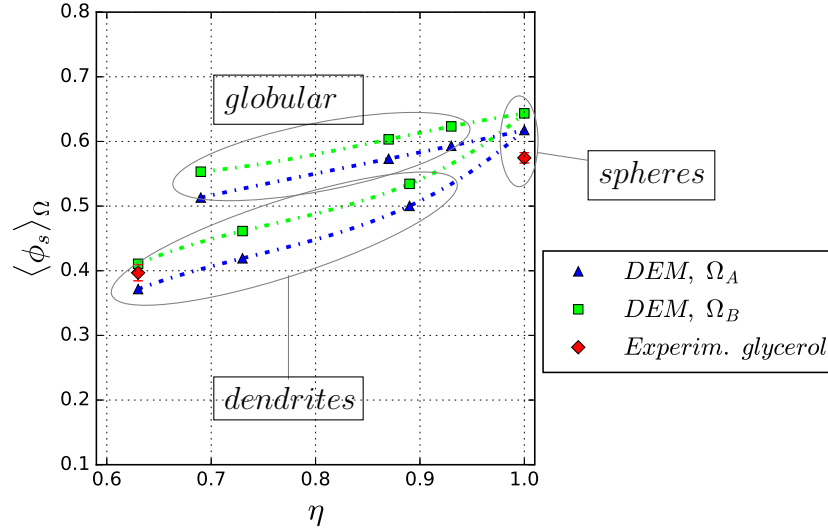


Figure 4.11: Average solid volumetric packing fraction, $\langle \phi_s \rangle_\Omega$, as a function of the geometrical parameter η . $\langle \phi_s \rangle_{\Omega_A}$ (accounting for the vessel wall effect) is shown with *triangular blue extra spheres* and $\langle \phi_s \rangle_{\Omega_B}$ shown via *squared green extra spheres*). The equiaxed grain results are joined by a dashed green and blue lines, $\langle \phi_s \rangle_{\Omega_B}$ and $\langle \phi_s \rangle_{\Omega_A}$, respectively. The validation experiments (see Sec. 3.5) for 45° dendritic envelopes and spheres are shown via red rhomboid extra spheres.

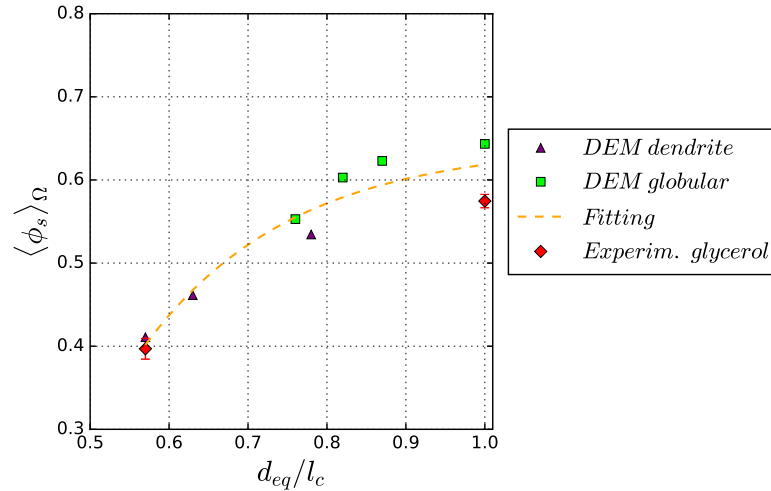


Figure 4.12: Average solid volumetric packing fraction, $\langle \phi_s \rangle_\Omega$, as a function of the geometrical parameter d_{eq}/l_c . Only numerical values without wall effect are shown ($\langle \phi_s \rangle_{\Omega_B}$). Experimental glycerol packings in red. Our DEM and experimental results are fitted by an exponential correlation (dashed orange).

vertical coordinate, z_c , and whose *north* and *south* faces are located at $z_N = z_c + \Delta z/2$ and $z_S = z_c - \Delta z/2$, respectively. Without forgetting the discrete nature of the packing, the volume thickness Δz is reduced as much as possible but avoiding any volume to be empty. Hence, $\langle \phi_s \rangle_{\Omega(z_c)}$ is computed with Eq. 4.55 for each volume and time. A $\Delta z/d_{eq} = 1$ is employed.

In this way, the vertical solid fraction profile is shown in Fig. 4.13 for the spheres, ellipsoids, dendrites and the globular shape of $\xi = 1.0$ at times: 30, 60, 90, 120, 150 and 230s.

Initially, the spherical, dendritic and globular particles are uniformly distributed in the domain with a solid fraction of $\approx 4\%$ whereas the ellipsoid initial fraction is slightly higher. The frames 30, 60 and 90s show particle feeding in the shown volume ($0 < z/d_{eq} < 12$) for all geometries. The 90s frame presents three different main regions for all the geometries: 1) particle feeding (with the initial solid fraction), 2) bottom packed bed and 3) a transition characteristic length where the solid fraction passes from initial to packing fraction. This transition profile has a sigmoidal shape with the vertical coordinate. The Eulerian transition length, L_{trE} , of these simulations ranges between 5 and 8 particle equivalent diameters.

Once in equilibrium, the packing fraction profiles are very dependent on the particle geometry: those of the spherical and globular geometries have low variations with height when compared to the others. In this way, it is thought the spherical and globular collections to have higher affinity to rearrange and compact uniformly. On the other hand, the dendritic and ellipsoidal geometries pack denser at lower layers.

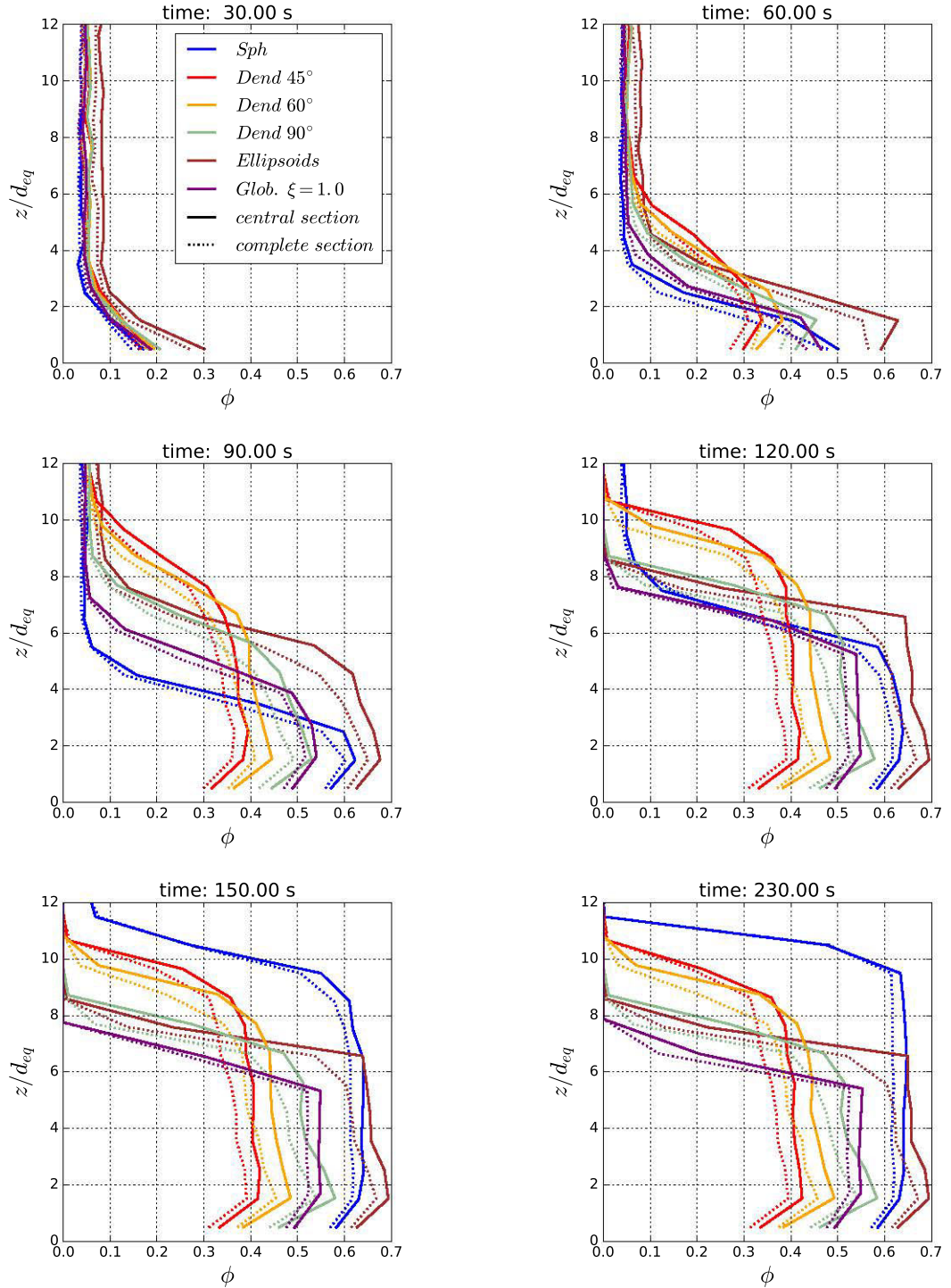


Figure 4.13: Time-evolution of the solid fraction vertical profile averaged across the section ($\phi(z, t)$) given at the instants: 30, 60, 90, 120, 150 and 230s. ϕ is computed from the Voronoi tessellation and in a vertical grid of $\Delta z/d_{eq} = 1$. For each monodisperse system (blue: spheres; purple: globular $\xi = 1.0$; red: dendrites 45° ; orange: dendrites 60° ; green: 90° ; brown: ellipsoids $1.25 : 0.8 : 0.8$) dotted lines show the averaged across the complete cross-section ($84 \times 84 \text{ mm}^2$) including the vertical recipient-wall effect whereas the solid lines show the averaged across the center of the cross-section ($40 \times 40 \text{ mm}^2$).

Influence of size polydispersity

The role of the particle size polydispersity is well-known for the case of spherical particles: higher polydispersity results in higher packing fraction. Nonetheless, in case of nonconvex geometries the role of the polydispersity is not evident. The polydispersity is defined as the ratio between standard deviation and mean value of the size distribution ($\delta_p = \sigma_p/\mu_p$), with $\mu_p = d_{eq0}$ where d_{eq0} is the particle equivalent diameter in case of monodispersity.

Herein the influence of the particle size polydispersity on the solid average packing fraction is investigated for two geometries: 1) spheres (in order to compare the DEM with the literature results) and 2) the equiaxed dendritic envelopes of apex-angle 45° . Besides, only two symmetric size polydispersity distributions are tested: uniform, \mathcal{U} , and normal, \mathcal{N} . The low weight protocol is used with frictionless noncohesive particles. Although in this section a xy periodic domain is used for both spheres and dendrites (2000 spheres in a domain of dimensions $84 \times 84 \times 1300$ mm and 400 dendrites in a domain of dimensions $54 \times 54 \times 500$ mm). We compute the average packing at the region Ω_B .

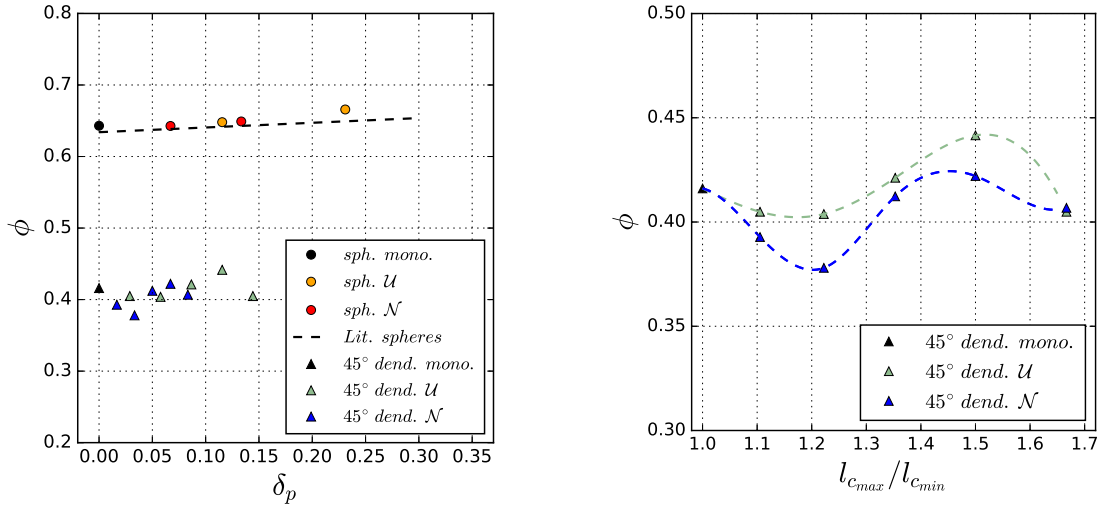


Figure 4.14: Polydisperse frictionless particle systems packed via the low weight protocol with xy periodic domain. Left: average solid packing fraction, $\langle \phi_s \rangle_{\Omega_B}$, as a function of the polydispersity, δ_p . The results of spheres with a uniform and normal distributions are in orange and red, respectively. The black dotted line corresponds to the polydisperse of spheres in literature review (see Ref. [Desmond and Weeks, 2014]). The results of 45° dendrites with uniform and normal distributions appear in green and blue triangles, respectively. Right: average solid packing fraction as a function of $l_{c_{max}}/l_{c_{min}}$ for the 45° dendrite with uniform and normal size distributions. The black circle and triangles correspond to the monodisperse sphere and monodisperse dendrites, respectively.

In Fig. 4.14 (left) the average solid packing fraction is shown as a function of the size polydispersity. In case of the spheres, the simulation results are compared to those in Ref. [Desmond and Weeks, 2014] (dotted black line), verifying that our DEM solver works

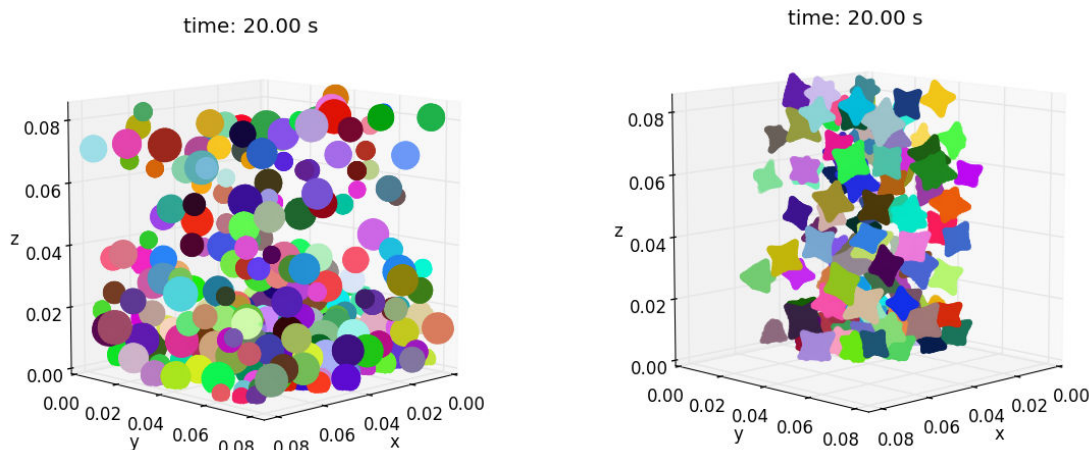


Figure 4.15: 3D views at time 20.0 seconds of dry deposition under vertical acceleration of frictionless polydisperse spheres (Left: with a uniform diameter distribution ($d_{max}/d_{min} \approx 2.33$, $\delta_p \approx 0.23$) and frictionless polydisperse dendrites (right: with a uniform distribution of characteristic length ($l_{c_{max}}/l_{c_{min}} = 1.5$, $\delta_p \approx 0.12$))

properly in case of polydisperse sphere collections (see Table 4.2 for simulation details and Fig. 4.15 left for visualization of a polydisperse sphere packing).

The dendritic polydisperse packing fraction results as a function of the polydispersity are also included in Fig. 4.14 (left). Both normal and uniform particle size simulation results present oscillations of the packing fraction with polydispersity.

The polydispersity is not a suitable parameter to organize the results of dendrites. In Fig. 4.14 (right) these results are shown as a function of the ratio between the maximum length and minimum particle size in the particle collection, $l_{c_{max}}/l_{c_{min}}$. With this new dimensionless parameter both uniform (green) and normal simulations (blue) present a similar oscillatory behavior of the packing fraction. For the investigated interval ($l_{c_{max}}/l_{c_{min}} \in [1.0, 1.67]$) both curves have a local minimum for approximately $l_{c_{max}}/l_{c_{min}} \approx 1.2$ and a local maximum at approximately $l_{c_{max}}/l_{c_{min}} \approx 1.5$.

The simulations show that the packing fraction of the polydisperse nonconvex equiaxed dendritic grains does not present a monotonous tendency with polydispersity. This result differs from the polydispersity of spheres, where a monotonous tendency of the packing fraction is obtained with polydispersity Ref. [Desmond and Weeks, 2014]. This result also differs from the polydispersity of pentagons (2D convex particles), where higher polydispersity results in a higher packing fraction Ref. [Nguyen et al., 2014].

Then we wonder if it is physically possible that the packing fraction oscillates with polydispersity. More precisely we wonder if it is possible for the packing fraction to decrease with respect to the monodisperse packing fraction with polydispersity, for low values of the polydispersity, $\delta_p \ll 1$.

To answer this question, the average solid packing fraction of a particle collection, $\phi = V_s/V_t$, is written as a function of the polydispersity, δ_p , by means of a *Maclaurin series expansion*, assuming a large collection of particles, fixed number of particles in the collection and symmetric size distribution, in Eq. 4.57. See the development in detail in Appx. C.5.

$$\frac{\phi(\delta_p)}{\phi_0} = 1 - a_{V_t} \delta_p + (3 - b_{V_t}) \delta_p^2 + o(\delta_p^3) \quad (4.57)$$

where ϕ_0 is the average packing fraction of the monodisperse collection formed by the same number of particles than the polydisperse. The solid volume of the collection is related to the polydispersity as: $V_s/V_{s_0} = 1 + 3 \delta_p^2$ and the total occupied volume of the collection is related to the polydispersity with a polynomial: $V_t/V_{t_0} = 1 + a_{V_t} \delta_p + b_{V_t} \delta_p^2$. V_{s_0} and V_{t_0} are the solid and total occupied volumes of the monodisperse collection.

In this way, several cases are possible with a small polydispersity, $0 < \delta_p \ll 1$:

$$\left\{ \begin{array}{l} 1. a_{V_t} > 0, \forall b_{V_t} \implies \frac{V_t(\delta_p)}{V_{t_0}} > 1, \frac{\phi(\delta_p)}{\phi_0} < 1. \\ 2. a_{V_t} < 0, \forall b_{V_t} \implies \frac{V_t(\delta_p)}{V_{t_0}} < 1, \frac{\phi(\delta_p)}{\phi_0} > 1. \\ 3. a_{V_t} = 0, 0 < b_{V_t} < 3 \implies \frac{V_t(\delta_p)}{V_{t_0}} > 1, \frac{\phi(\delta_p)}{\phi_0} > 1. \\ 4. a_{V_t} = 0, b_{V_t} > 3 \implies \frac{V_t(\delta_p)}{V_{t_0}} > 1, \frac{\phi(\delta_p)}{\phi_0} < 1. \\ 5. a_{V_t} = 0, b_{V_t} < 0 \implies \frac{V_t(\delta_p)}{V_{t_0}} < 1, \frac{\phi(\delta_p)}{\phi_0} > 1. \\ 6. a_{V_t} = 0, b_{V_t} = 0 \implies \frac{V_t(\delta_p)}{V_{t_0}} \approx 1, \frac{\phi(\delta_p)}{\phi_0} > 1. \end{array} \right. \quad (4.58)$$

We prove that the solid volume of the collection increases with polydispersity. In our dendrite simulations we checked, for low polydispersity, that the total occupied volume increases with polydispersity but with a decrement of the average packing fraction. This phenomenon is possible for cases 1 and 4, that is, the increment of the total occupied volume prevails over the increment of the solid volume.

However, this behavior is not monotonous with polydispersity, the tendency changes for higher polydispersity. We conclude, that the polydispersity effect on packing fraction is much more complex in case of equiaxed dendritic grains than spheres. We find the average packing fraction to have an oscillary behavior with polydispersity or the parameter $l_{c_{max}}/l_{c_{min}}$ for the studied range. Finally, we leave the polydispersity of nonconvex particles as an open question for future developments.

Table 4.2: Summary of polydispersity parameters for the sphere and dendrite simulations. The normal distribution is represented by $\mathcal{U}(d_{eq_{min}}, d_{eq_{max}})$ whereas the normal distribution $\mathcal{N}(\mu_p, \sigma_p^2)$, where $\mu_p = d_{eq_0}$ and $3\sigma_p = (d_{eq_{max}} - d_{eq_{min}})/2$. The normal tails are truncated and we consider the 99.7% central region of the normal.

Geometry	$\Delta d_{eq}/d_{eq_0}$	Distribution	$l_{c_{max}}/l_{c_{min}}$	$\delta_p = \sigma_p/d_{eq_0}$
sph	0.20	$\mathcal{U}(5.50, 8.26)$	1.5	11.5%
sph	0.20	$\mathcal{N}(6.88, 0.46^2)$	1.5	6.67%
sph	0.40	$\mathcal{U}(4.13, 9.63)$	2.33	23.09%
sph	0.40	$\mathcal{N}(6.88, 0.92^2)$	2.33	13.34%
den 45°	0.05	$\mathcal{U}(6.54, 7.22)$	1.11	2.89%
den 45°	0.05	$\mathcal{N}(6.88, 0.11^2)$	1.11	1.67%
den 45°	0.10	$\mathcal{U}(6.19, 7.57)$	1.22	5.77%
den 45°	0.10	$\mathcal{N}(6.88, 0.23^2)$	1.22	3.33%
den 45°	0.15	$\mathcal{U}(5.85, 7.91)$	1.35	8.67%
den 45°	0.15	$\mathcal{N}(6.88, 0.34^2)$	1.35	5.0%
den 45°	0.20	$\mathcal{U}(5.50, 8.26)$	1.5	11.55%
den 45°	0.20	$\mathcal{N}(6.88, 0.46^2)$	1.5	6.67%
den 45°	0.25	$\mathcal{U}(5.16, 8.6)$	1.67	14.44%
den 45°	0.25	$\mathcal{N}(6.88, 0.57^2)$	1.67	8.33%

Influence of the interparticle frictional contact

The influence of the interparticle friction on the solid packing fraction, the contacting neighbors and the mechanical contacts is investigated via the low weight protocol for two collections: the 1) monodisperse spheres and 2) monodisperse dendritic grains of 45° apex-angle. With this protocol, the friction effect on the packing is isolated from other effects, such as the fluid presence, that can act as a lubricant among the contacting grains. In Sec. 4.4.2 the effect of the frictional contact is coupled with the lubrication model.

The tangential friction model in Sec. 4.3.4 is used. A 2000-sphere collection is packed in both semi-rigid and xy periodic vessel ($84 \times 84 \times 1300 \text{ mm}^3$) whereas a 400-dendrite set is packed in a xy periodic vessel ($54 \times 54 \times 500 \text{ mm}^3$). The static and dynamic coefficients are assumed to be equal ($\mu_{fr} = \mu_s = \mu_d$) with a fixed threshold velocity of $v_{th} = 0.01 \text{ mm/s}$. A range of μ_{fr} up to 0.5 is investigated with a fixed integration time step of $\Delta t = 10^{-3} \text{ s}$.

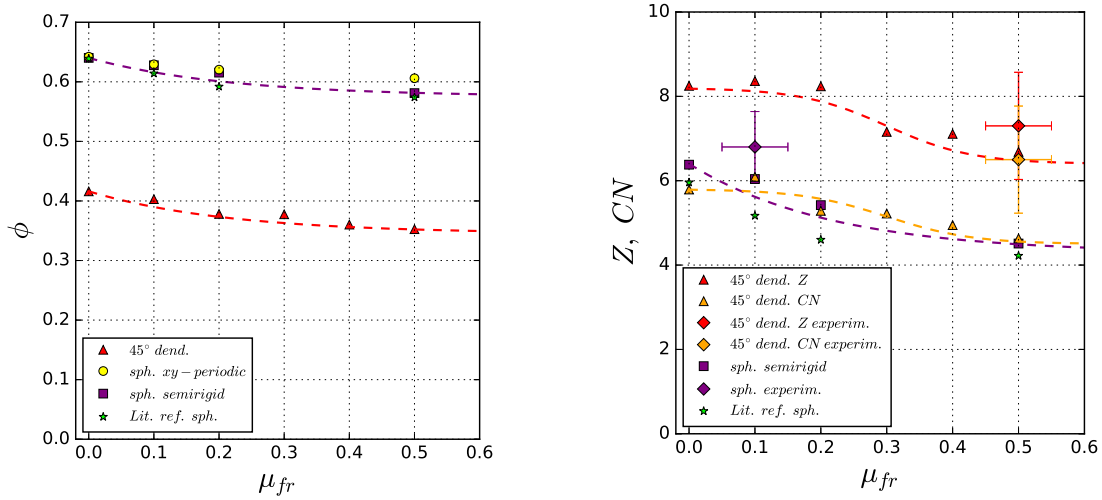


Figure 4.16: Frictional packing. Left: average packing fraction, ϕ , as a function of the friction coefficient, μ_{fr} . Sphere packing in xy periodic domain (circular yellow extra sphere), sphere packing in semi-rigid wall domain (purple square marker), 400 dendrites in xy periodic domain (red triangle marker) and literature results for monodisperse spheres (green asterisk marker) (see Ref. [Silbert, 2010]). Right: average number of mechanical contacts, Z and contacting neighbors, CN , as a function of μ_{fr} : (orange and red triangular markers, respectively for 400 dendrites in xy periodic domain; purple markers for spheres in semi-rigid domain). The experimental results of Appx. B.6 (square markers) are also included for comparison.

Firstly, the validation of the DEM solver for frictional grains is carried out by comparing our results for spheres with literature, Ref. [Silbert, 2010]. We obtain a similar tendency of the packing fraction with friction for the simulations in a domain with semi-rigid vertical walls. In case of periodic vertical walls, our packings are denser than the literature reference, Fig. 4.16 (left). Moreover, a similar tendency for the sphere mechanical contacts

to that of the reference is obtained with semirigid vertical wall simulations, Fig. 4.16 (right). In the case of the dendritic envelopes a similar $\phi - \mu_{fr}$ behavior is found to that of the spheres.

In general, the larger the friction is, the looser is the packing with an asymptotic tendency to a lower limit. In Ref. [Silbert, 2010], the saturation lower limit is found with $\mu_{fr} = 1$. We proposed an exponential law to fit by least-squares the packing fraction as a function of friction for both spheres and dendrites, $\phi(\mu_{fr}) = \phi_o - |\phi_{sat} - \phi_o| (1 - e^{-2 \ln 10 \mu_{fr}})$, where ϕ_o is the frictionless packing fraction. The sphere and dendritic saturation values of $\phi_{sat}^{sph} = 57.5\%$ and $\phi_{sat}^{den} = 35.5\%$ are obtained from the simulation, respectively.

On the other hand, we propose a similar exponential fitting model for the sphere contacts, $Z^{sph}(\mu_{fr}) = Z_o^{sph} - |Z_{sat}^{sph} - Z_o^{sph}| (1 - e^{-2 \ln 10 \mu_{fr}})$. With $Z_o^{sph} = 6.4$ and $Z_{sat}^{sph} = 4.3$, obtained from the simulations. For the contacts and contacting neighbors in case of dendrites, we propose a sigmoidal fitting:

$$CN^{den}(\mu_{fr}) = \left(\frac{CN_o + CN_f}{2} \right) + |CN_f - CN_o| \left(1 + e^{2 \ln 10 [(\mu_{fr}/\mu_{fr}^c)-1]} \right)^{-1} \quad (4.59)$$

$$Z^{den}(\mu_{fr}) = \left(\frac{Z_o + Z_f}{2} \right) + |Z_f - Z_o| \left(1 + e^{2 \ln 10 [(\mu_{fr}/\mu_{fr}^c)-1]} \right)^{-1} \quad (4.60)$$

where $CN_o = 8.2$, $CN_f = 6.4$, $Z_o = 5.8$, $Z_f = 4.5$ and $\mu_{fr}^c = 0.3$ are obtained by least-squares obtained from the simulations.

Additionally, some experimental tests specially carried out to count the number of mechanical contacts and contacting neighbors for dendrites are included in Fig. 4.16 (right) (see Appx. B.6 for details). In case of spheres, this experimental result is over 1 contact larger than the literature or DEM results. In case of dendrites, the experimental results are also larger than the DEM results, with the mechanical contacts a 9% larger. The difference for the contacting neighbors is 40%. In this way, we conclude that our DEM is able to obtain an acceptable result for the mechanical contacts however the question of multiple contacts between every couple of contacting neighbors remains an open question for improvement.

Finally, our contact results of dendrites are compared with the contact results of the hexapods in Sec. 1.3.3. In the case of the hexapods with a friction coefficient of approximately 1, an average number of contacts between 6.58 and 9.18 is found. Our results for dendrite envelopes match fairly well with the hexapods. In this way, an important result for the equiaxed grain packing in solidification is that we obtain similar number of mechanical contacts with a dendritic envelope or simply by the principal arms (hexapods).

Influence of the initial conditions

Initially, the particles are randomly distributed in the domain and randomly oriented by means of a *Random Sequential Addition* and *Shoemaker* algorithms, respectively; as described in section 4.3.6. Initial linear and angular velocities are null.

In this way, how do the initial conditions, that is, the positions (for both spherical and nonspherical particles) and orientations (in case of nonspherical particles), affect the final packing parameters such as the average solid packing fraction, average mechanical contacts and average contacting neighbors for a packing formed by a limited number of particles. In this section reference simulations for spheres and dendrites are repeated 10 times for 10 different randomly generated initial conditions.

In Table C.1 we collect the characteristic packing properties for 10 simulations of 2000 spheres (second and third columns). An average packing fraction and mechanical contacts (or equivalently contacting neighbors) of 64.11 %, and 5.73, are respectively obtained; with standard deviations relative to the average of 0.29 % and 1.96 %, respectively. Therefore, the packing fraction and contacts are slightly affected by the initial conditions for the 2000 sphere granular system.

In Table C.1 we collect the characteristic packing properties for 10 simulation of 400 dendrite (last three columns). An average packing fraction, mechanical contacts and contacting neighboring particles of 41.08 %, 8.28 and 5.71, are respectively obtained; with standard deviations relative to the average value of 1.52 %, 7.64 % and 2.83 %, respectively. Therefore, the packing fraction and contacting neighbors are slightly affected by the initial conditions for our dendritic simulations whereas the mechanical contacts are more affected.

To sum up, from these results we can define an uncertainty due to the initial conditions for our simulations. Thereby, using a level of confidence of 95% (equivalent to 2σ), we define characteristic absolute errors for spheres of: $\Delta\phi = \pm 0.38\%$ and $\Delta Z = \pm 0.22$ whereas for dendrites: $\Delta\phi = \pm 1.25\%$, $\Delta Z = \pm 1.27$ and $\Delta CN = \pm 0.32$.

4.4.2 Fluid protocol

The objective of this protocol is to simulate the experimental packings of the sphere and dendrite collections of Chap. 3. In this vein, the Discrete Element Method model complements the experimental results: we can access information on the structure of the grain ensemble that cannot be obtained experimentally, such as the local fraction, contacting neighbors, mechanical contacts or particle orientation for both the final packing or during the sedimentation.

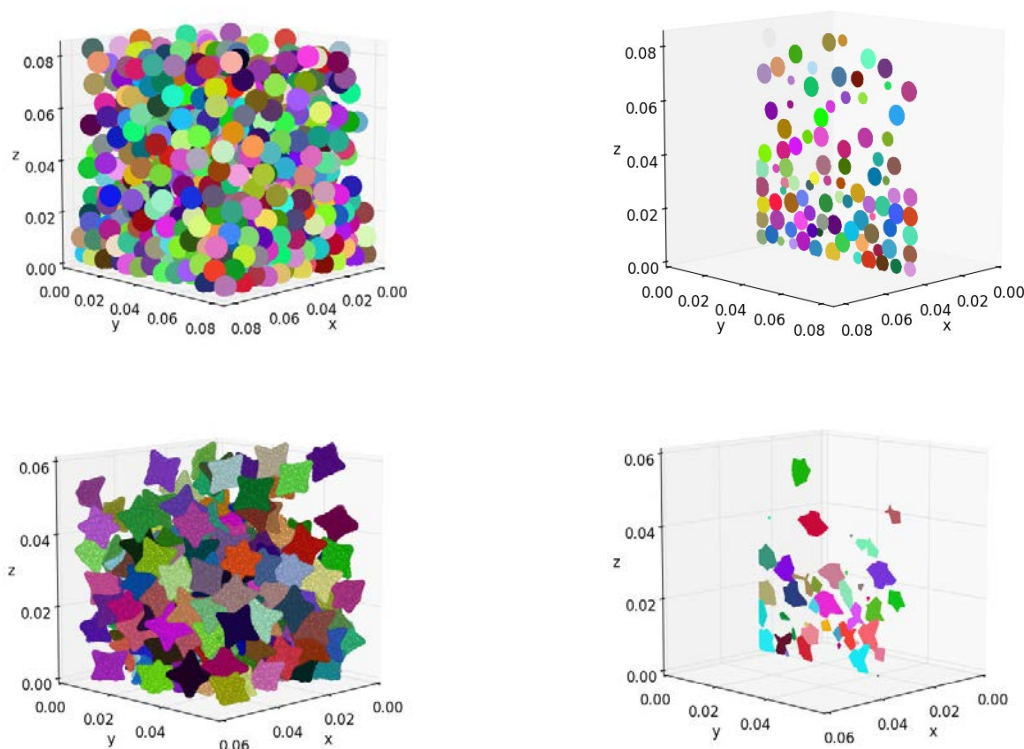


Figure 4.17: DEM simulations of the experimental spherical (top images) and dendritic (bottom images) packings in glycerol (*reference simulations*). The images on the left show a 3D frame during the packing whereas the images on the right show a 2D slice at the same instant.

In these simulations the fluid is not resolved but the fluid effect on the particles by the drag, lubrication and buoyancy is accounted for (see models in Sec. 4.3.5).

This section is divided in two parts:

- Mechanical equilibrium (packing): the influence of the lubrication model, interparticle friction (coupled with the lubrication model) and apparent weight on the packing fraction is investigated.

- Packing dynamics: we investigate the time evolution of some granular variables (local fraction, contacting neighbors, mechanical contacts or particle orientation) from sedimentation to packing in both Lagrangian and Eulerian descriptions.

Packing

The experimental sedimentation and packing of spheres and dendritic grains of 45° apex-angle in glycerol of Sec. 3.5 are simulated (see Figs. 4.17) using the drag, lubrication and buoyancy models. The simulation average packing fractions are compared to those of the experiments for validation of the *fluid protocol*. We present the details of our *reference simulations*:

- Spherical geometry: a collection of 2000 particles of $d_{eq} = 6.88 \text{ mm}$ and $\rho_s = 1400 \text{ kg/m}^3$ in a semirigid wall rectangular prism vessel of dimensions $84 \times 84 \times 300 \text{ mm}^3$ is chosen. With the initial solid fraction, $\langle \phi_s \rangle_{\Omega_{sed}}$, similar to that of the experiments (approximately 20%).
- Dendritic geometry: 400 particles of $d_{eq} = 6.88 \text{ mm}$ and $\rho_s = 1400 \text{ kg/m}^3$ in a xy periodic rectangular prism vessel of dimensions $54 \times 54 \times 500 \text{ mm}^3$ is chosen with $\langle \phi_s \rangle_{\Omega_{sed}} = 5\%$.

In both simulations, the particles are noncohesive and frictionless. The contact stiffness, the parameters of the fluid model, the apparent gravity and the integration time step are collected in Table 4.3. An identical surface discretization than that of the low weight protocol is used for the dendritic grains of 45° apex-angle. A critical damping is chosen for the normal interparticle contact to ensure that no rebound is possible. The selection criterion of the normal stiffness is based on the static overlap due to the apparent weight, differing from the low weight protocol where the overlap is almost exclusively a result of the collision. With the chosen stiffness, a maximum overlap of $\delta_{max}/d_{eq} \approx 0.003$ is computed for both spheres and dendrites, according to the expressions in Appx. C.4.

Hence, for the spheres an identical packing apparent gravity as in the experiments in glycerol is numerically simulated. Nonetheless, the dendritic packing is simulated with a $\Delta\rho/\rho_s = 5\%$ which is lower than the experimental, $\Delta\rho/\rho_s = 15\%$, in order to reduce the computational cost. For a maximum given overlap, a lower apparent weight allows a lower stiffness, then, we can use a longer integration time step. The dendrite computation cost is over 20 fold longer than that of the spheres due to the geometry complexity under equivalent protocol conditions. The fluid protocol is approximately from 10 to 20 fold slower than the low weight protocol, i.e. a computational cost for a dendrite simulation from 1 *day* with the low weight to 2 – 3 *weeks* by means of the fluid protocol.

With these simulation parameters the *Stokes* number is approximately $St = 2 \cdot 10^{-3}$ and the *Archimedes* number, $Ar = 2 \cdot 10^{-1}$ for both spheres and dendrites, which are in the order of those of the experiments in glycerol.

Table 4.3: Parameters of the DEM reference simulations.

Parameters	Spheres	Dendrites
Particle size		
d_{eq} [m]	6.88	6.88
Particle density		
ρ_s [kg/m ³]	1400	1400
Apparent gravity		
$\Delta\rho/\rho_s g_o$	$0.09g_o$	$0.05g_o$
Viscosity		
μ_f [Pa.s]	1.2	1.2
Drag		
force: A	6π	6π
moment: D	8π	8π
Lubrication		
λ_{lub}	1.0	1.0
d_{lub}/d_{eq}	1.0	1.0
R_{lub}/l_c	2.0	1.5
h_{min}/l_c	0.01	0.01
Stiffness		
K_{pt} [N/m]	100	10
Time step		
Δt [s]	$1.0 \cdot 10^{-5}$	$5.0 \cdot 10^{-5}$

Table 4.4: Numerical-experimental comparison: packing fraction in glycerol

Geometry	$\langle \phi_s \rangle_{\Omega_B}^{dem}$ [%]	$\langle \bar{\phi}_s \rangle_{\Omega_{pack}}^{exp}$ [%]	$\langle \bar{\phi}_s \rangle_{\Omega_{pack}}^{exp, \infty}$ [%]	ϵ_{ϕ_s} [%]
Spheres	59.7	57.5 ± 0.8	58.4 ± 0.8	2.2
Dendrites	36.2	39.7 ± 1.3	40.3 ± 0.8	-10.2

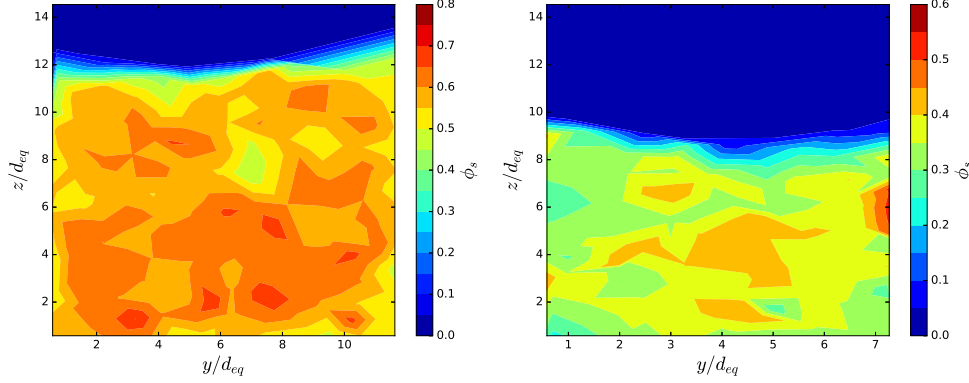


Figure 4.18: Reference simulations: local packing fraction contour map of spheres (left) and nonconvex dendritic grains (right) at the volume whose central plane is $x = 42 \text{ mm}$ and $x = 27 \text{ mm}$, for spheres and dendrites, respectively, with a l_c thickness.

The comparison between the numerical reference simulation results and the experimental results is carried out by means of the average packing fraction (see Table 4.4). The numerical averaged packing fraction computed at the region Ω_B (without wall effects) is compared with the averaged experimental packing fraction (corrected to exclude the wall effect of the cylindrical experimental recipient), $\langle \bar{\phi}_s \rangle_{\Omega_{pack}}^{exp, \infty}$ (see Sec. 1.19). Their relative difference is defined as $\epsilon_{\phi_s} = (\langle \phi_s \rangle_{\Omega_B}^{dem} - \langle \bar{\phi}_s \rangle_{\Omega_{pack}}^{exp, \infty}) / \langle \bar{\phi}_s \rangle_{\Omega_{pack}}^{exp, \infty}$.

The sphere packing relative difference is very low. The numerical packings are about a 2% denser. On the other hand, the simulation dendrite packing fraction is about a relative 10% lower than the experimental value. This lower packing fraction can be partially a consequence of the lower apparent weight employed in the simulation of dendrites. Despite the difference between the numerical and experimental values, we consider the DEM results acceptable. The fluid protocol is validated to reproduce particle packings under low Stokes conditions.

Fig. 4.18 shows the local packing fraction of these reference simulations, spheres and dendrites at left and right, respectively, at a central plane $x = x_c = 42 \text{ mm}$ of the packed block. We compute the Voronoi tessellation and we filter the particles (and their respective Voronoi cells) contained in the limits $x = x_c - l_c/2$ and $x = x_c + l_c/2$ to plot the map. In case of spheres, a denser packing is found at the lower layers, whereas, for dendrites, a denser packing is found at the central region of the packed block.

Table 4.5: Parametrical cases: sensibility of ϕ

Case	$\Delta\rho/\rho$	μ_{fr}	λ_{lub}	$\langle\phi_s\rangle_{\Omega_A}$ [%]	$\langle\phi_s\rangle_{\Omega_B}$ [%]
Spheres					
Reference (Ref.)	9%	0.0	1.0	57.2	59.7
Case 2	5%	0.0	1.0	54.3	58.1
Case 3	5%	0.3	1.0	51.0	54.8
Case 4	5%	0.5	1.0	50.3	53.6
Case 5	9%	0.0	0.0	54.4	57.9
Dendrites					
Reference (Ref.)	5%	0.0	1.0	36.0	36.2
Case 2	1%	0.0	1.0	33.9	32.9
Case 3	5%	0.3	1.0	30.9	30.2
Case 4	5%	0.5	1.0	30.8	30.5
Case 5	5%	0.0	0.0	34.6	34.7

Subsequently, the sensibility of the packing fraction to the apparent gravity ($\Delta\rho/\rho_s g_o$), interparticle friction (through μ_{fr}) and lubrication model (through λ_{lub}) are investigated. The parametric investigated cases are collected in Table 4.5, including the average packing fractions $\langle\phi_s\rangle_{\Omega_A}$ and $\langle\phi_s\rangle_{\Omega_B}$. From these results, we conclude:

- Effect of the apparent weight and the interparticle friction on the packing fraction: looser packing fractions than that of the reference case are obtained if a lower apparent gravity and/or a higher interparticle friction are applied.
- In case of spheres, the loosest averaged packing fraction is found in *Case 4* (the highest friction considered) with $\langle\phi_s\rangle_{\Omega_B} = 53.6\%$, being a 2.5% relatively lower than the experimental loosest reported value of 55.0% in Ref. [Jerkins et al., 2008]. In case of dendrites, the packing fraction decreases with the interparticle friction to approximately 30% when $\mu_{fr} \geq 0.30$.
- Effect of lubrication model: for spheres and dendrites the *Case 5* is compared to *Case Ref.* showing that a looser packing is obtained when the lubrication model is deactivated. Therefore, the lubrication forces press the packed particle bed acting as distance forces and slightly compact the packed bed increasing the average packing fraction. This means that the compacting effect of these forces acting at a distance prevails over the loosening effect of the dissipation due to lubrication.

Packing Dynamics

The DEM solver is applied to better understand the *granular packing dynamics*. In this text the concept of granular packing dynamics refers to the time evolution or transition of the granular system from a sedimentation regime to a final packing state. The main questions to answer in this section are:

- Which are the most suitable granular variables to characterize the granular system during the packing dynamics?
- How do these variables of the granular system evolve from the initial (sedimentation) to the final (packing) values?
- How influential are the particle geometry and the hydrodynamic conditions on the packing dynamics?

Our DEM is not understood as a predictive tool. This numerical tool is calibrated by means of the dynamics results from the experimental approach in Sec. 3.6. Thereby, the experimental granular information during the packing dynamics are completed with the numerically accessible variables. More precisely, the lubrication model parameters are calibrated in this section in order to numerically obtain a mean particle trajectory during the approaching phase equivalent to that observed in the experiments. Afterwards, the evolution from sedimentation to packing of granular variables such as the local fraction, contacting neighbors, particle position, particle velocity or particle orientation are computed from the numerical results and presented in both Lagrangian and Eulerian descriptions.

Our strong simplification of the fluid presents some drawbacks such as neglecting the damping effects of the upward fluid flow or the multiparticle effects on drag. The effect of these phenomena is to slow down the particle settling.

These phenomena could be incorporated to DEM by means of a more complex multiparticle drag model (see Ref. [Dong et al., 2012]). Additionally, the *continuity* equation for two phases, Eq. 4.61, must be incorporated, discretized and solved in order to obtain the fluid flow.

$$\nabla \cdot (\phi_s \mathbf{v}_s + (1 - \phi_s) \mathbf{v}_f) = 0 \quad (4.61)$$

Nonetheless, this procedure becomes tedious and it does not avoid a calibration of the drag model parameters. Thereby, we opt for a simpler idea which is avoiding any supplementary implementation to our DEM model and directly calibrate the lubrication model. In this way, the escalar coefficient λ_{lub} , lubrication length, d_{lub} , and the lubrication influence sphere, R_{lub} , (see Sec. 4.3.5) are calibrated to fit the experimental measurements of particle settling speed in glycerol.

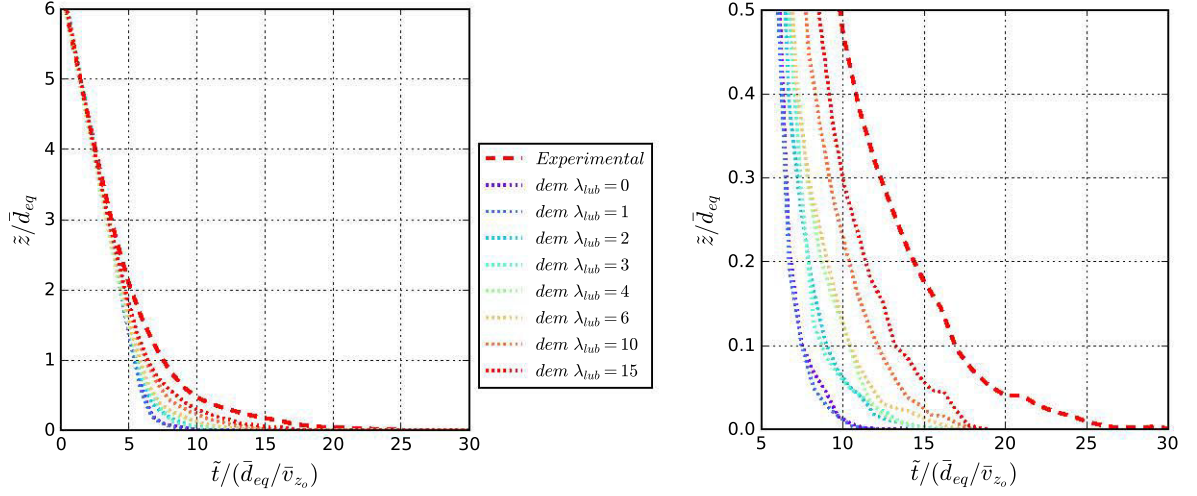


Figure 4.19: Left: sphere dimensionless 10-particle mean vertical coordinate as a function of the dimensionless time. The DEM parametric simulations for different values of λ_{lub} and the experimental results in glycerol are included. Right: zoomed figure of image on the left for a closer to packing region of $\tilde{z}/\tilde{d}_{eq} \leq 0.5$. In these simulations $d_{lub} = d$ and $R_{lub} = 2d$.

Spheres

For spheres, the influence of the lubrication parameter λ_{lub} on the granular dynamics is studied in order to calibrate the DEM model. The sphere *Reference case* (see Table 4.3) is taken as a starting point. In Fig. 4.19, the dimensionless mean vertical coordinate (mean of 10 particle trajectories measured individually) as a function of the dimensionless time, $\tilde{z}/\tilde{d}_{eq} - \tilde{t}/(\tilde{d}_{eq}/\bar{v}_{z_o})$, is shown for values of $\lambda_{lub} \in [0, 15]$ and a fixed value of $R_{lub} = 2d$. Besides, the experimental trajectory is also added. Some conclusions are drawn from this parametric study:

- A larger value of λ_{lub} implies a smoother particle approaching to packing, that is, a higher mean transition time, $\bar{\Delta}t_{trL}$.
- A value of $\lambda_{lub} = 15.0$ gives an acceptable numerical trajectory when compared to the experimental mean trajectory. For larger λ_{lub} , the convergence is not possible with the used time step of $\Delta t = 10^{-5}s$.
- The lubrication model of Sec. 4.3.5 is able to represent the dynamic behavior of the sphere packing in a viscous fluid when much higher than unit values of λ_{lub} are provided, i.e. increasing the kinetic dissipation rate.
- The packing of case $\lambda_{lub} = 0$ is governed by interparticle collisions since the lubrication forces (distance interactions among neighbors) are deactivated. In this way, the sedimentation trajectory is perturbed only at a distance of one sphere diameter

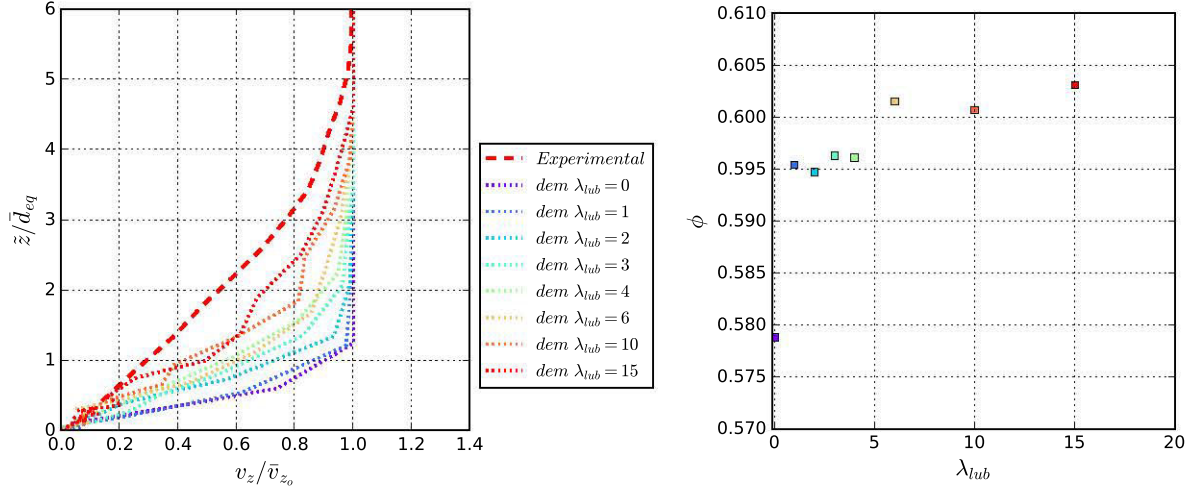


Figure 4.20: Left: mean dimensionless vertical particle velocity with the mean vertical particle coordinate for spheres. Experimental and DEM results are included. Right: influence of the parameter λ_{lub} on the packing fraction for spheres (herein $\langle \phi_s \rangle_{\Omega_B}$ is simply written as ϕ). Only DEM simulations on the right. Same legend colors are used for the left and the right graphs.

from the final position of mechanical equilibrium. In this last zone, the particles rearrange finding their final positions. It takes approximately $4(\bar{d}_{eq}/\bar{v}_{z_0})$, see the zoomed Fig. 4.19 (right) for more detail.

In Fig. 4.20 (left), the mean dimensionless vertical particle velocity is shown as a function of the mean dimensionless vertical particle coordinate, $v_z/\bar{v}_{z_0} - \bar{z}/\bar{d}_{eq}$. The mean value is computed with 10 particles for both numerical simulations and experimental results. The lower λ_{lub} is, the longer the particles maintain their sedimentation velocity. The value $\lambda_{lub} = 15$ also provides the closest behavior of that of the experiments in this plot.

Fig. 4.20 (right) shows an increment of the packing fraction with λ_{lub} . With the largest increment when the lubrication model is activated, between $\lambda_{lub} = 0$ and $\lambda_{lub} = 1$. For spheres, the compaction effect of the lubrication forces prevails over the dissipation of the particle inertia.

The experimental dimensionless results of the mean particle trajectory and its calibrated simulations by DEM are compared to the theoretical results of a single sphere approaching to a flat wall in a viscous quiescent medium (see Chap. 2) in Fig. 4.21. Surprisingly, for a low Stokes number of $o(10^{-3})$, the time evolution from sedimentation to packing of the mean vertical coordinate of a multi-particle system of spheres resembles the time evolution of the vertical coordinate of a single sphere approaching to an impermeable flat wall.

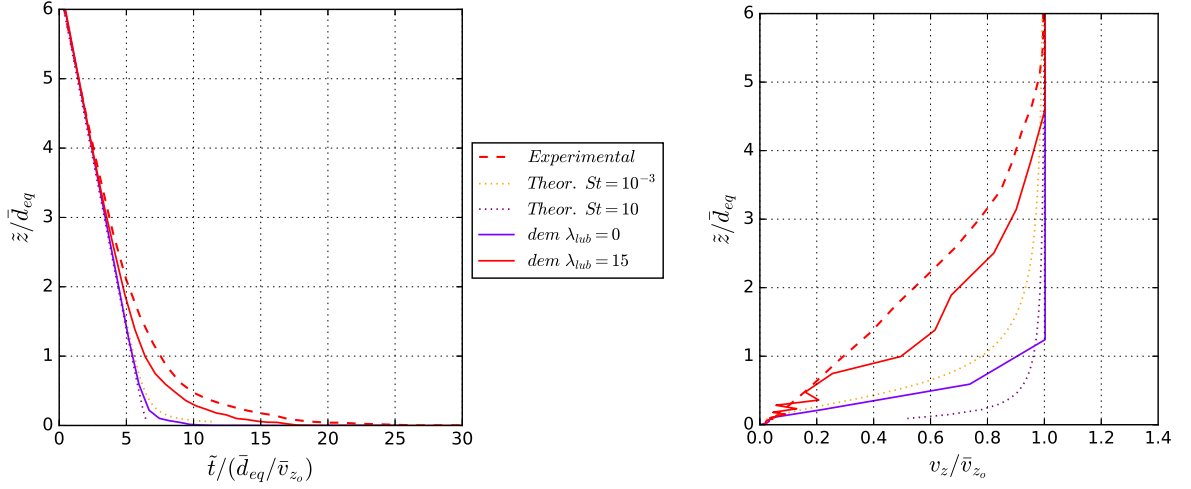


Figure 4.21: Left: dimensionless vertical coordinate as a function of dimensionless time. Right: dimensionless velocity with the dimensionless vertical coordinate. The DEM simulations with the lubrication parameter $\lambda_{lub} = 15$ and $\lambda_{lub} = 0$ are shown in both graphs. The experimental results in glycerol, $St = o(10^{-3})$ and the results of the theoretical single sphere model are also shown in both graphs.

Additionally, we assume that the time evolution of the collection of spheres also resembles that of a single sphere approaching to a wall for a Stokes number of 10. According to Ref. [Izard et al., 2013], for Stokes values higher than 10, the restitution coefficient is not nil, so the phenomenon of packing is expected to become more complex, with particle rebounding.

On the other hand, when we use the DEM model with a deactivated lubrication model, $\lambda_{lub} = 0$, we obtain a similar dimensionless time evolution of the vertical coordinate than that of the single sphere model approaching to a wall with a Stokes number of 10. With the lubrication model deactivated, the spheres begin to lose their kinetic energy when they are closer to the packing front. In this way, we use the simulation of the DEM model with the lubrication model deactivated, to obtain the time evolution of the granular system from sedimentation to packing for a Stokes number of $o(10)$.

We summarize these previous ideas as:

- The theoretical model of a single particle in Chap. 2 that includes the lubrication models of Refs. [Brenner, 1961, Cox and Brenner, 1967] can approximately describe the dimensionless approaching phase of a collection of spheres approaching to packing, for a low inertia-to-dissipation hydrodynamic condition, $St = o(10^{-3})$.
- We choose the DEM simulation with the lubrication model deactivated, $\lambda_{lub} = 0$, to reproduce the packing dynamics of the granular system for Stokes number of $St = o(10)$.

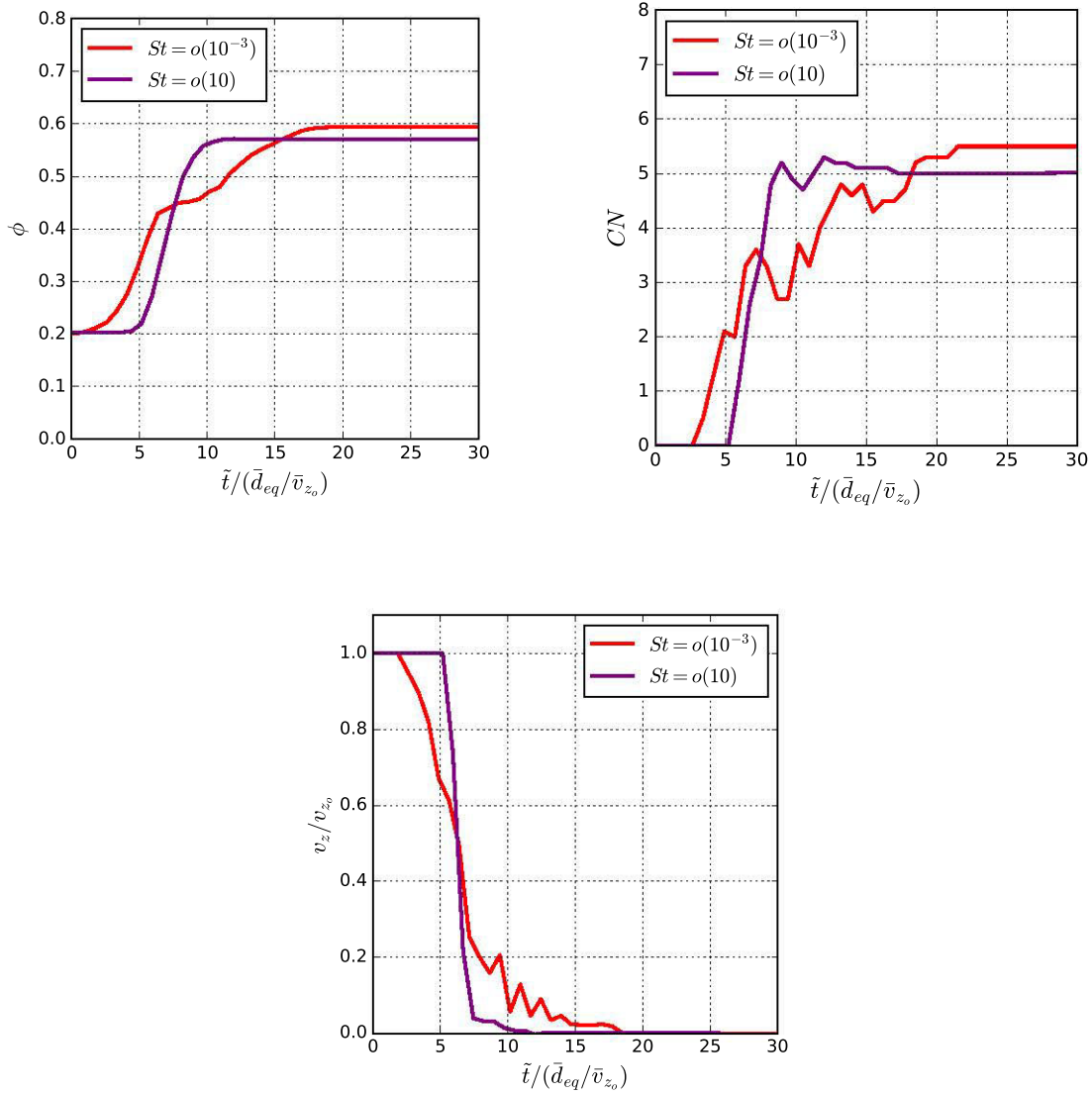


Figure 4.22: Packing dynamics of spheres in Lagrangian description. Top left: solid fraction as a function of dimensionless time; top right: contacting neighbors as a function of dimensionless time; bottom: dimensionless vertical velocity as a function of dimensionless time.

Herein we present the time evolution of some granular variables in Lagrangian and Eulerian descriptions for both situations of $St = o(10^{-3})$ and $St = o(10)$. Firstly, the evolution of a 10-particle mean solid fraction (ϕ), 10-particle mean contacting neighbors (CN), and the 10-particle mean dimensionless vertical velocity (v_z/v_{z_o}) as a function of the dimensionless time, $\tilde{t}/(\bar{d}_{eq}/\bar{v}_{z_o})$, are presented in Fig. 4.22 in a Lagrangian description. The origin of the dimensionless time corresponds to that of the Figs. 4.19 and 4.21 (left). From this analysis in a Lagrangian description, several conclusions are drawn:

- The formation of the packing is faster for the condition of Stokes number of $o(10)$ than for that of $o(10^{-3})$. We redefine the beginning and the end of the transition by means of the solid fraction and contacting neighbors, respectively. Thereby, the mean dimensionless transition time, $\bar{\Delta}t_{trL}^*$, is approximately 9 and 22 for $o(10)$ and $o(10^{-3})$ Stokes conditions, respectively.
- The mean Lagrangian transition length is shorter with higher Stokes condition. A dimensionless Lagrangian transition length, $\bar{L}_{trL}^* = \bar{L}_{trL}/d_{eq}$, of approximately 2 and 6 is found for $o(10)$ and $o(10^{-3})$ Stokes number, respectively.
- The phases of approaching and rearrangement are clearly distinguished for the $o(10^{-3})$ condition. The rearrangement phase begins at a dimensionless time of approximately 6. A lower increment rate of the mean local fraction and the mean contacting neighbors is shown for the rearrangement phase.

Secondly, in Fig. 4.23, ϕ , CN and v_z/v_{z_o} are shown as a function of the vertical dimensionless coordinate z/d_{eq} in an Eulerian description for both Stokes conditions. The reference frame is fixed to the vessel with its origin, $z/d_{eq} = 0$, set at the packing front at the consider instant. Besides, an image of the experimental sphere packing in glycerol, $St = o(10^{-3})$, is included to visualize the granular system. A dimensionless mean Eulerian transition length, $L_{trE}^* = L_{trE}/d_{eq}$, of approximately 7 is found for the Stokes condition of $o(10)$ whereas the Eulerian transition length increases up to approximately 17 for the Stokes condition of $o(10^{-3})$.

Dendrites

An equivalent procedure of calibration of the lubrication model is carried out for dendrites. However, two new difficulties consequence of the nonspherical nonconvex particle geometry have been faced:

- A second parameter of the lubrication model, $d_{lub} > 1$, must be calibrated. By means of the calibration of the λ_{lub} only (with $d_{lub} = 1$) it is not possible to fit the experimental packing dynamics of the dendritic grains.
- Computational cost: a dendrite simulation in fluid protocol needs up to 3 weeks. This is a strong limitation to calibrate the lubrication model for dendrites since a large number of simulations are required: a parametrical studied of the lubrication parameters λ_{lub} , d_{lub} and R_{lub} is desired.

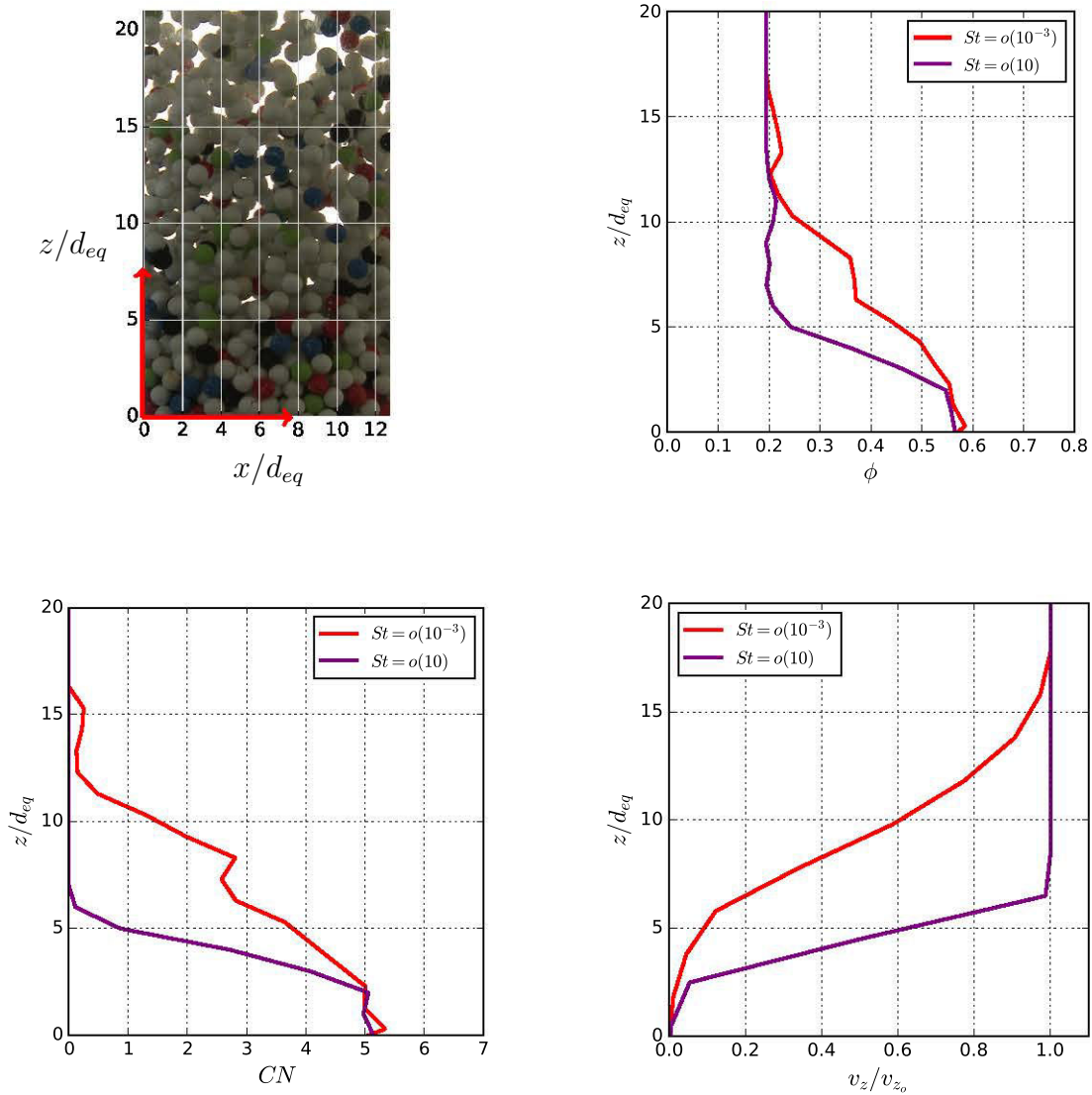


Figure 4.23: Packing dynamics of spheres in Eulerian description. Top left: experimental sedimentation in glycerol, $St = o(10^{-3})$; top right: solid fraction with the dimensionless vertical coordinate; bottom left: contacting neighbors with the dimensionless vertical coordinate; bottom right: dimensionless vertical velocity with the dimensionless vertical coordinate. The origin of the reference frame is located at the packing front for the shown instant.

Table 4.6: Packing dynamics of the dendrites: parametrical cases

Case	$\Delta\rho/\rho_s$	$\mu_f[Pa.s]$	λ_{lub}	R_{lub}/l_c	d_{lub}/d_{eq}
Case 0	5%	1.2	0	–	–
Case 1	10^{-5}	$2.4 \cdot 10^{-4}$	5.0	1.5	1.0
Case 2	10^{-5}	$2.4 \cdot 10^{-4}$	10.0	1.5	1.0
Case 3	10^{-5}	$2.4 \cdot 10^{-4}$	15.0	1.5	1.0
Case 4	10^{-5}	$2.4 \cdot 10^{-4}$	20.0	1.5	1.0
Case 5	10^{-5}	$2.4 \cdot 10^{-4}$	15.0	2.5	1.0
Case 6	10^{-5}	$2.4 \cdot 10^{-4}$	15.0	1.5	1.4

To reduce the computational cost, a hybrid protocol combining ideas from the *low weight protocol* and from the *fluid protocol* is designed. The strategy is that of decreasing the apparent gravity, i.e. $a_o = 10^{-5} g_o \ll (\Delta\rho/\rho_s)g_o$. In this way, 100 times larger time steps can be used, $\Delta t = 10^{-3}s$. Additionally, we also modified liquid viscosity to a 5000 times smaller value, $\mu_f \ll 1.2 Pa$. With these modifications we maintain the limit sedimentation velocity (grain inertia). The Stokes parameter in the numerical does not correspond to the Stokes number in the experiments. However, we calibrate the lubrication parameters to fit the numerical mean particle approaching trajectory with experiments and access to the granular information of the simulations.

In Fig. 4.24 the 10-dendrite mean dimensionless vertical coordinate is computed as a function of the dimensionless time, the simulation results are compared to the experimental results in glycerol (see Sec. 3.6). A parametrical study with different combinations of λ_{lub} , R_{lub} and d_{lub} is carried out (see Table 4.6). The *case 6*, of parameters $\lambda_{lub} = 15$, $R_{lub} = 1.5$ and $d_{lub} = 1.4$, provides the best fit.

Some conclusions are drawn from this parametrical study:

- Larger values of λ_{lub} smooth the particle approaching to packing.
- With $d_{lub}/d_{eq} = 1.4$ the distance lubrication forces act on larger distances than with $d_{lub}/d_{eq} = 1$.
- Larger values of R_{lub} smooth the particle approaching to packing. Larger R_{lub} also considerably increases the computation cost due to the higher number of interactions.

In Fig. 4.25 (left) the simulation and experimental results of the Lagrangian dimensionless vertical mean particle velocity evolution with the mean vertical particle coordinate are compared. Similar conclusions to those previously presented for the spherical packing are obtained. Additionally, the influence of the lubrication model on the average packing fraction is shown in Fig. 4.25 (right). Differing from the previous spherical results, in case of the dendrites the lubrication model and the new strategy to shorten the computational time have an important influence on the final packing fraction so special attention have

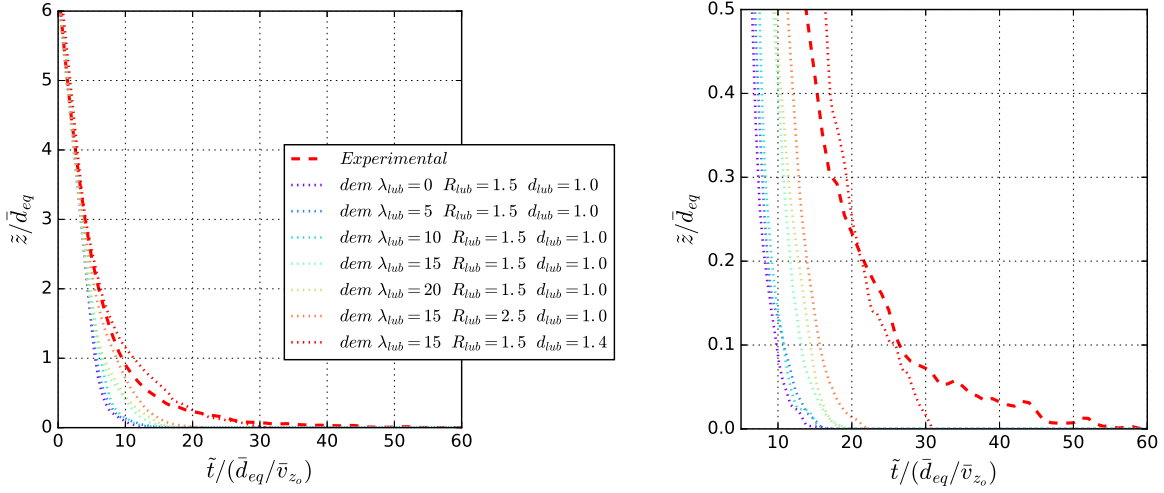


Figure 4.24: Left: dendrite dimensionless 10-particle mean vertical coordinate as a function of the dimensionless time. The DEM parametric simulations for different values of λ_{lub} , R_{lub}/d_{eq} and d_{lub}/d_{eq} are included as well as the experimental results in glycerol. Right: zoomed figure of image on the left for a closer to packing region of $\tilde{z}/\bar{d}_{eq} \leq 0.5$.

been paid to choose suitable parameters that provide an equivalent packing dynamics without dramatically influencing the packing fraction. Several conclusions are drawn:

- For those simulations with active lubrication model ($\lambda_{lub} > 0$) and $d_{lub}/d_{eq} = 1$, the average solid packing fraction decreases with λ_{lub} . This behavior is opposed to the spheres. In case of dendrites with a lubrication length equal to their equivalent diameter, $d_{lub}/d_{eq} = 1$, the dissipative effect of the lubrication forces prevails over the compaction effect of these distance forces. The lubrication forces act in a shorter distance than the distance of interaction between the dendritic arms.
- With $d_{lub}/d_{eq} = 1.4$, lubrication forces act on a longer distance than the compaction effect prevails over the compaction, similar to the spheres. The parameter combination of *case 6* not only provides an accurate packing dynamics but also maintains a similar solid packing than that of the experiments.

Subsequently, the time evolution of several granular variables are presented in Lagrangian and Eulerian descriptions during the packing dynamics. The situation of Stokes number of $o(10^{-3})$ is represented by *case 6* from Table 4.6 which is the best fit with the experimental results in glycerol. Equivalently to spheres, an approximation of the situation of Stokes number of $o(10)$ is obtained with the lubrication model deactivated, which corresponds to *case 0* from Table 4.6.

In Fig. 4.26, we show the time evolution of a 10-particle mean solid fraction, ϕ ; 10-particle mean contacting neighbors, CN ; 10-particle mean dimensionless vertical velocity, v_z/v_{z0} ; and the 10-particle mean rotation, α , in a Lagrangian description. The dimensionless time

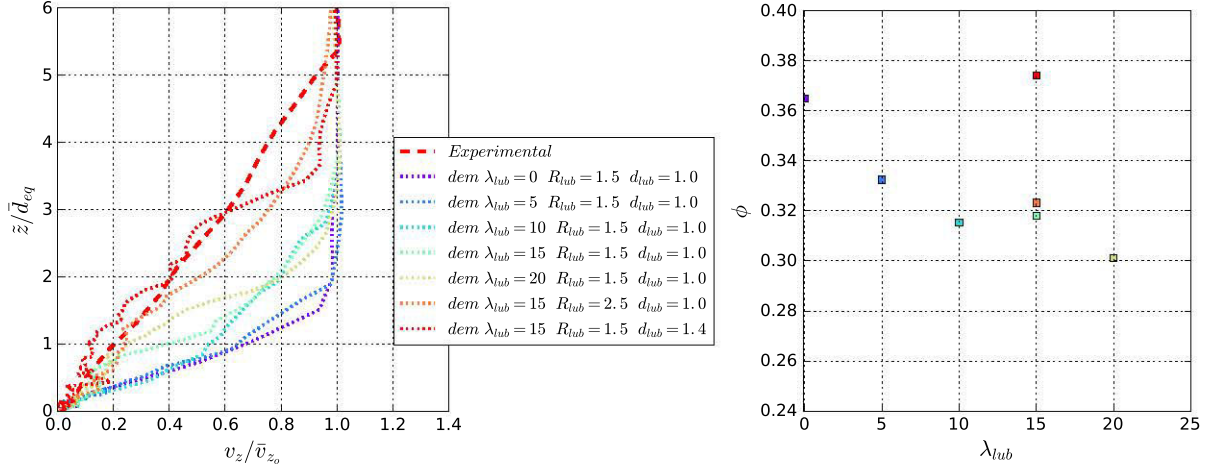


Figure 4.25: Left: mean dimensionless vertical particle velocity with the mean vertical particle coordinate. Experimental and DEM results are included. Right: influence of the parameter λ_{lub} on the average packing fraction (herein $\langle\phi_s\rangle_{\Omega_B}$ is simply written as ϕ). Only DEM simulations on the right. Same legend colors are used for the left and the right graphs.

origin corresponds to that of the Figs. 4.24. Additionally, we define the particle rotation as:

$$\alpha(\tilde{t}) = \int_{\tau=0}^{\tau=\tilde{t}} \|\omega(\tau)\| d\tau \quad (4.62)$$

From these results in a Lagrangian description we conclude:

- The variable evolutions are faster for the condition of higher Stokes number. Considering the beginning and end of the transition defined by the solid fraction and contacting neighbors, respectively, we find a dimensionless transition time, $\bar{\Delta}t_{trL}^*$, of approximately 13 for $St = o(10)$ and 32 for $St = o(10^{-3})$.
- The Lagrangian transition length is shorter with higher Stokes. A dimensionless mean Lagrangian transition length, \bar{L}_{trL}^* , of approximately 4 and 6 is found for the conditions of Stokes number of $o(10)$ and $o(10^{-3})$, respectively.
- The frictionless dendritic envelopes rotate approximately $\alpha = 45^\circ$ and $\alpha = 50^\circ$ for the conditions of $St = o(10)$ and $St = o(10^{-3})$, respectively. The cause of the rotation is the interparticle contact of the nonspherical particles. This result differs from spheres since the frictionless collection of spheres does not rotate, $\alpha^{sph} = 0^\circ$.

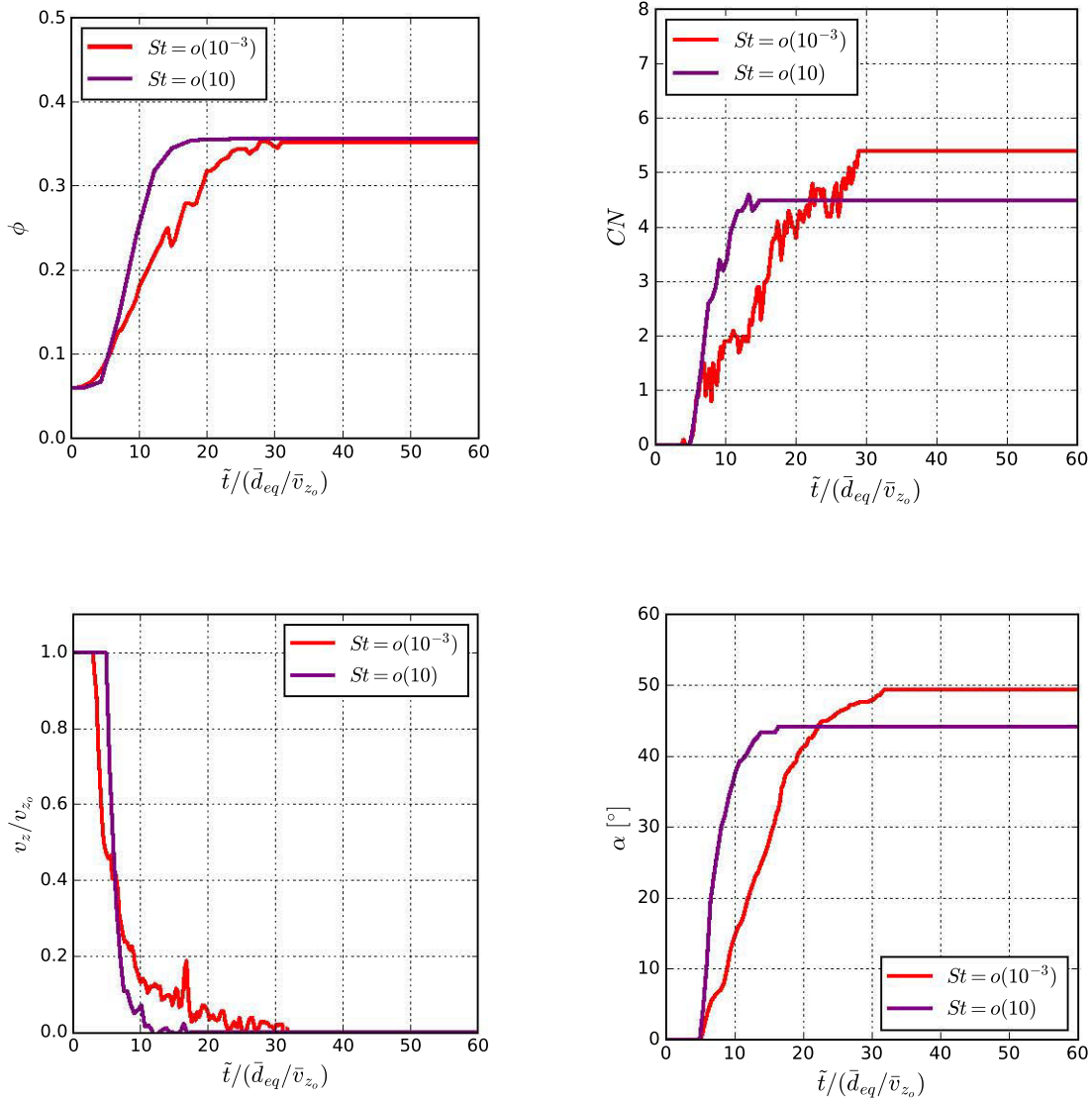


Figure 4.26: Packing dynamics of dendrites in Lagrangian description. Top left: solid fraction as a function of dimensionless time; top right: contacting neighbors as a function of dimensionless time; bottom left: dimensionless vertical velocity as a function of dimensionless time, bottom right: angular rotation as a function of dimensionless time.

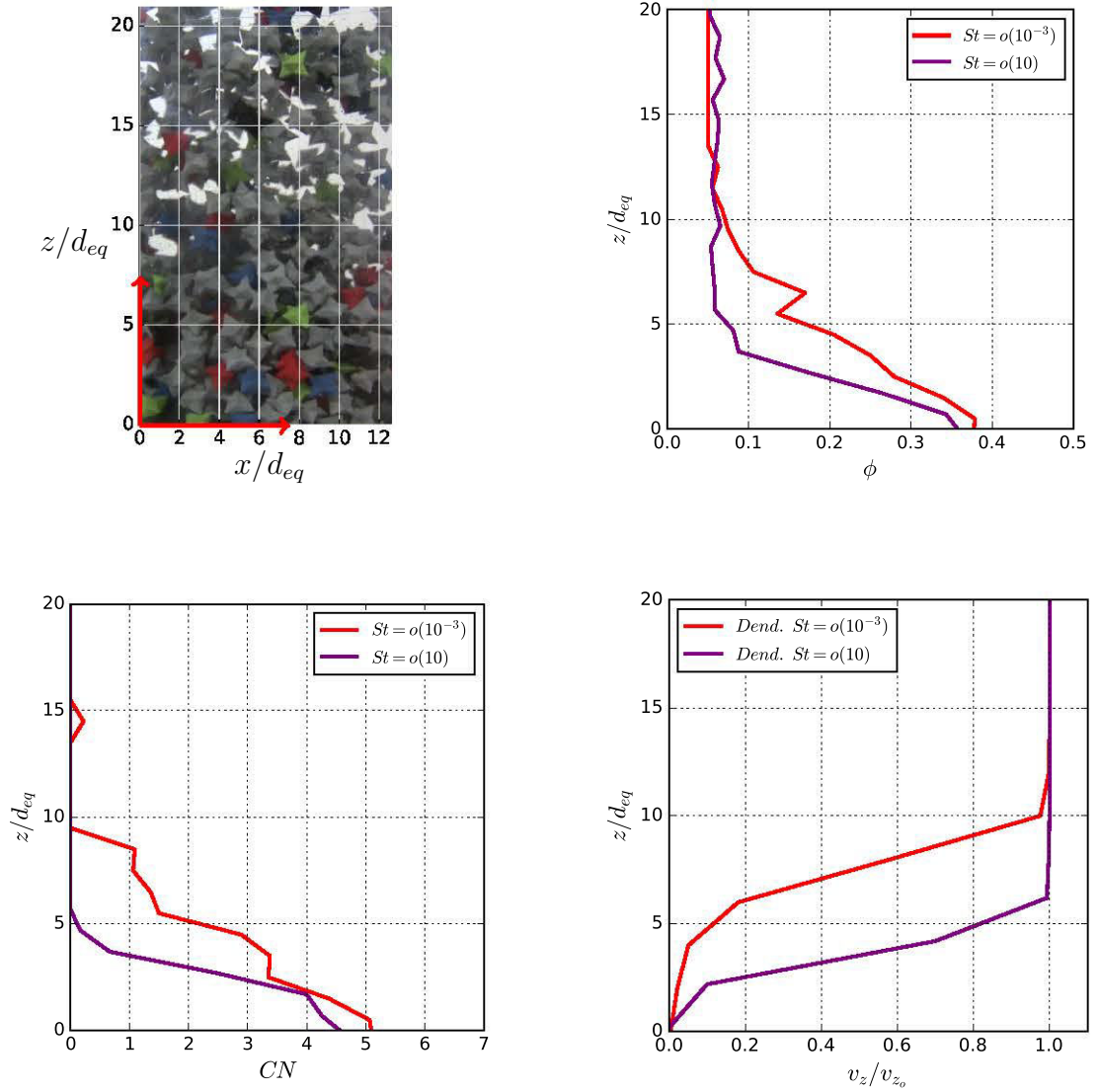


Figure 4.27: Packing dynamics of dendrites in Eulerian description. Top left: experimental sedimentation in glycerol, $St = o(10^{-3})$; top right: solid fraction with the dimensionless vertical coordinate; bottom left: contacting neighbors with the dimensionless vertical coordinate; bottom right: dimensionless vertical velocity with the dimensionless vertical coordinate. The origin of the reference frame is located at the packing front for the shown instant.

In Fig. 4.27, we show the 10-particle mean solid fraction, ϕ ; the 10-particle mean contacting neighbors, CN ; and the 10-particle mean dimensionless vertical velocity, v_z/v_{z_o} as a function of the dimensionless vertical coordinate, z/d_{eq} , in an Eulerian description for the Stokes number situations of $o(10^{-3})$ and $o(10)$. Additionally, we include an image of the experimental dendrite packing in glycerol to visualize the actual granular system. From these graphs, we conclude that the mean dimensionless Eulerian transition length, $L_{tr_E}^*$, of approximately 12 for the Stokes condition of $o(10)^{-3}$ and 6 for the condition of $o(10)$.

4.5 Modeling conclusions

- A geometrical packing numerical tool is developed from *scratch* in order to obtain a first estimate of the influence of the particle shape on the packing fraction. In this geometrical algorithm the phase of particle rearrangement is not allowed. The assumptions inherent in the geometrical model can be interpreted as: 1) zero inertia and apparent weight, and 2) perfect adherence. Packing fractions, ϕ_s^{pack} , of approximately 27% and 15% are obtained for spherical and dendritic envelope geometries, respectively. Moreover, the mechanical contacts, Z , are approximately of 2.1 for both geometries which is a very *hypostatic* situation if compared with the common packings with gravity presence (where 6 and 12 are the sphere and dendritic mechanical contacts required for isostaticity in case of frictionless contacts, respectively).
- A Discrete Element Method that allows simulations with nonspherical geometries is developed from *scratch*. We solve the particle dynamics including the interparticle contact interactions. Additionally, we developed a simplified model to account for the fluid interactions on the particles by the lubrication interactions between particles, drag and buoyancy. This model is computationally much cheaper than a directly coupled CFD-DEM model.
- A protocol based on a low apparent weight is developed to mimic the packing situations of low inertia-to-dissipation. The decrement of the apparent weight decreases the computational cost of the simulations. We investigate the influence of the geometry, the polydispersity and the interparticle friction on the packing fraction. This protocol mimics the packing conditions in glycerol with very good agreement with the experimental results for dendrites.
- We investigate the influence of the geometry on the packing for dendritic and globular equiaxed grains. The packing fraction results are shown as a function of three different geometrical parameters which are: 1) the grain sphericity, Ψ ; 2) the equivalent diameter to widest length ratio, d_{eq}/l_c ; and 3) the principal section equivalent diameter to perimeter ratio, η . Packing fraction increases with the three geometrical parameters for both dendrites and globular grains. To describe the influence of the equiaxed grain morphology on the packing fraction we proposed the parameter d_{eq}/l_c as a suitable universal geometrical parameter.
- Influence of the grain size polydispersity on the packing fraction: very good agreement is found between our simulation results and literature in case of spheres. The higher the polydispersity, δ_p , the higher is the packing fraction. In case of dendrites, which are nonconvex particles, we find that the packing fraction is not monotonous with polydispersity. This behavior is much complex than for spheres.
- The influence of the interparticle friction on the packing fraction is similar for spheres and dendrites. The higher friction is, the looser are the packings. A very good agreement we find between our simulations of spheres and literature results.

- We develop a fluid protocol including the lubrication forces between particles, drag and buoyancy in order to complement the experimental results in glycerol. We investigate the influence of the apparent weight, interparticle friction and lubrication distance forces on the packing fraction for spheres and dendrites. Additionally, we investigate the packing dynamics or transition from the sedimentation regime to packing for spheres and dendrites in glycerol. The model is calibrated with the experiments in glycerol, condition of Stokes number of the order of 10^{-3} . Additionally, we also propose an approximation of the packing dynamics for a packing condition of Stokes number of the order of 10.
- A lower apparent weight and/or a higher interparticle friction results in a looser packing for both spheres and dendrites.
- Several granular variables such as the local fraction, contacting neighbors and particle velocity are shown for spheres and dendrites in Lagrangian and Eulerian descriptions for the conditions of Stokes number of the order of 10^{-3} and 10. With these simulations we estimate two different characteristic lengths of the transition of the packing phenomenon: the Lagrangian transition length and the Eulerian transition length, and the characteristic time of the transition. Slower packing dynamics, with larger transition lengths and larger time, is expected for the condition of Stokes number of the order of 10^{-3} than for the condition of 10. Slightly slower packing dynamics, with larger transition lengths and larger time, is expected for dendrites than for spheres. The concepts of Lagrangian transition length, Eulerian transition length and transition time are recovered in Chap. 5 to apply them in solidification.

Chapter 5

Application to packing during solidification

5.1 Packing fraction correlation

In solidification, two flow regimes are possible in the mushy zone: slurry flow and porous flow, see Sec. 1.2.3. A *packing limit*, g_{env}^{pack} , is necessary as a model parameter in solidification modeling to switch from one regime to another. Depending on the flow regime, different equations of motion for the solid and different models of drag at the solid-liquid interface are used.

Herein, the objective is to provide a correlation of the packing limit that is useful for *multiphase multiscale models* of solidification, see model examples in Refs. [Založnik et al., 2011a], [Heyvaert, 2015], [Wang et al., 2005]. The correlation must account for the variation of the packing limit with time and across the macroscopic solidification domain due to the variation of the grain envelope geometry and the hydrodynamic conditions of the packing.

Thereby, with the experimental packing data from Sec. 3.5 and the simulation results from Sec. 4.4.1, we propose a correlation of the average envelope packing fraction of equiaxed dendritic grains, at a certain *representative elementary volume* which center is \mathbf{x} and a certain time t , as a function of the grain envelope geometry and hydrodynamic conditions.

We recover the results from Fig. 4.12 where the average packing fraction is shown as a function of the geometry, through the geometrical parameter d_{eq}/l_c , for low inertia-to-dissipation hydrodynamic conditions, a Stokes number of the order of 10^{-3} . Our correlation is exclusively focused on equiaxed dendritic grains, in this way, we remove the results of globular grains, see Fig. 5.1. The experimental results of spheres and dendrites in glycerol (see red rhomboid markers) and the simulation results for three types of dendritic shapes (see purple markers) are fitted with an exponential law by least-squares (see dashed green fitting):

$$g_{env_{geo, St \ll 1}}^{pack} = 0.617 - 0.220 e^{2.26 - 4.04 d_{eq}/l_c} \quad (5.1)$$

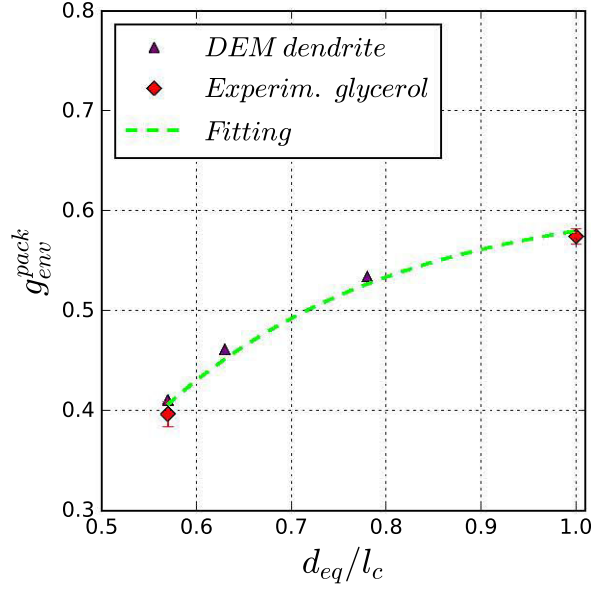


Figure 5.1: Average packing fraction, g_{env} , as a function of the geometrical parameter d_{eq}/l_c for a low Stokes number of the order of $o(10^{-3})$ ($St = 1.210^{-3}$ and 5.010^{-3} for spheres and dendrites, respectively). The DEM dendrite simulation and experimental results are fitted by an exponential correlation (dashed green).

Table 5.1: Sigmoidal $g_{env}^{pack} - St$ fitting

Particle	g_1	g_2	λ	$\log_{10}(St_c)$
Sphere	0.503	0.631	-0.376	-3.56
Dendrite	0.392	0.512	-0.464	4.06

In Fig. 5.2 we also recover the experimental results from Chap. 3 where we show the influence of the hydrodynamic conditions of the packing by the Stokes number for spheres, $d_{eq}/l_c = 1$, and dendrites of 45° of apex-angle, $d_{eq}/l_c = 0.56$. In Chap. 3 we fitted the experimental results of both spheres and dendrites by a sigmoidal law, Eq. 5.2. The parameters of these fitting are collected in Table 5.1.

$$g_{env}^{pack}(St) = g_1 + (g_2 - g_1) \left\{ 1 + e^{\lambda \log_{10}(St/St_c)} \right\}^{-1} \quad (5.2)$$

We use this previous information to build the correlation that accounts for the influence of both grain geometry and hydrodynamic conditions on the packing fraction:

$$g_{env}^{pack} \left(\frac{d_{eq}}{l_c}, St \right) = g_{env_{geo}, St \ll 1}^{pack} + g_{env_{St}}^{pack} \quad (5.3)$$

The correlation is formed by two terms. The first term describes the effect of the geometry for a low Stokes of the order of 10^{-3} . We identify this term with Eq. 5.1. The second term

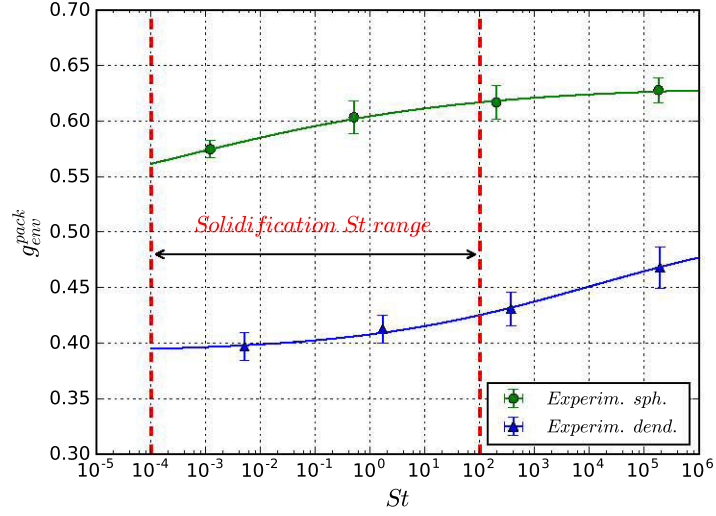


Figure 5.2: Packing fraction as a function of the Stokes number for spheres (green) and dendrites (blue).

accounts for the influence of the hydrodynamic conditions through the Stokes number. It is also a function of the geometrical parameter d_{eq}/l_c since the influence of the hydrodynamic conditions on the packing fraction is slightly different for spheres and for dendrites. The second term is given by:

$$g_{env_{St}}^{pack} = g^* + \Delta g^* \{1 + e^{\lambda^* \log_{10}(St/St_c^*)}\}^{-1} \quad (5.4)$$

We assume the functions g^* , Δg^* , λ^* and $\log_{10}(St_c^*)$ to linearly depend on the geometrical parameter d_{eq}/l_c . Then, we compute them with the parameters of spheres and dendrites in Table 5.1.

$$g^* = 0.088 - 0.143 \left(\frac{d_{eq}}{l_c} \right) \quad (5.5)$$

$$\Delta g^* = 0.110 + 0.018 \left(\frac{d_{eq}}{l_c} \right) \quad (5.6)$$

$$\lambda^* = -0.576 + 0.200 \left(\frac{d_{eq}}{l_c} \right) \quad (5.7)$$

$$\log_{10}(St_c^*) = 13.74 - 17.30 \left(\frac{d_{eq}}{l_c} \right) \quad (5.8)$$

The correlation, Eq. 5.3, is shown in Fig. 5.3. This correlation is valid for the dendrite envelopes in the range of $d_{eq}/l_c \in [0.56, 1.0]$ and $St \in [o(10^{-3}), o(10^5)]$. Additionally, in this figure we include the three profiles in which the correlation is based on.

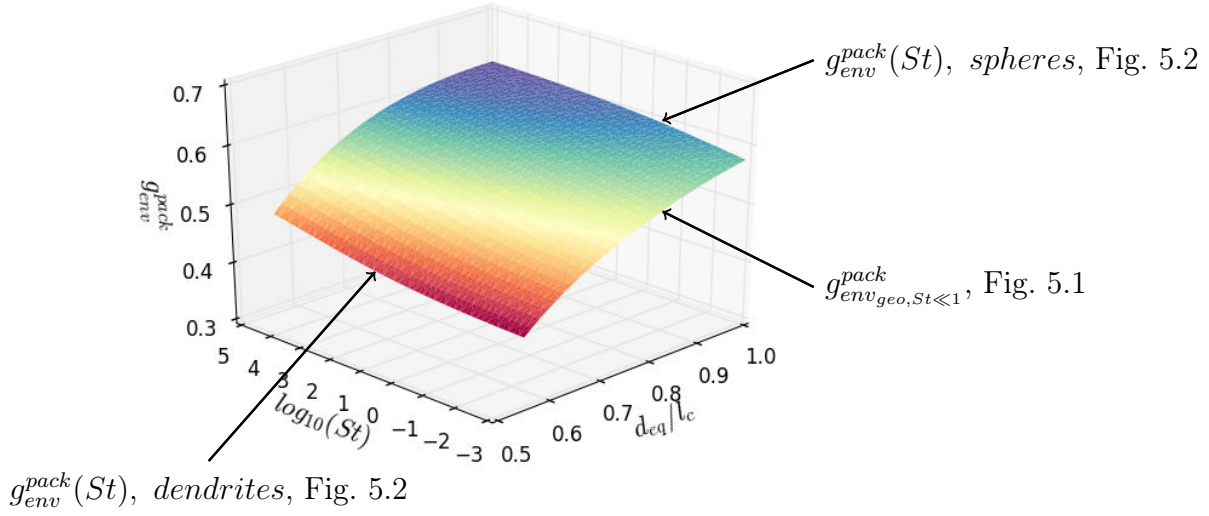


Figure 5.3: Packing fraction correlation for equiaxed dendritic grains in the range of $d_{eq}/l_c \in [0.56, 1.0]$ and $St \in [o(10^{-3}), o(10^5)]$.

The Stokes number is computed by $St = \rho_{env} d_{eq} v_{env\perp} / (9 \mu_l)$. Where the envelope density, ρ_{env} , depends on the solid density, ρ_s , melt density, ρ_l , and the volume fraction of solid in the interior of the envelope, g_{si} , $\rho_{env} / \rho_l = 1 + g_{si}(\rho_s / \rho_l - 1)$. $v_{env\perp}$ is the component of the envelope velocity perpendicular to the packing front. μ_l is the melt viscosity. d_{eq} is the equivalent diameter of the envelope. To compute the geometrical parameter it is also needed l_c which is the widest length of the dendritic envelope or twice the length of the principal arm.

5.2 Packing dynamics

We recover the figures of dedrite sedimentation in glycerol from Chap. 3 in order to explain the information of *packing dynamics* (also called transition from purely sedimentation regime to the mechanically stable equilibrium or packing) learned by the simulations in Chap. 4. After it, we apply the simulation results from Chap. 4 to solidification.

5.2.1 Lagrangian description

In the Lagrangian description we follow the grains with time. The granular variables used, such as the local fraction, the number of contacting neighbors or the particle velocity, are associated to the particles which follow a trajectory given by:

$$\mathbf{x}_i = \mathbf{x}(\mathbf{x}_i^0, t), \quad \forall i \in (1, N_{pt}) \quad (5.9)$$

With N_{pt} the number of particles forming the granular system. The trajectory of each particle i only depends on its initial position, \mathbf{x}_i^0 , and time.

In this way, the local fraction, g_{env} , the contacting neighbors, CN , and particle velocity are defined for each particle i and only depend on time:

$$\begin{cases} g_{env_i} = g_{env}(\mathbf{x}_i^0, t) \\ CN_i = CN(\mathbf{x}_i^0, t) \\ \mathbf{v}_i = \frac{d\mathbf{x}_i(t)}{dt} \end{cases} \quad (5.10)$$

According to the simulations in Chap. 4, we identify the beginning of the transition for a particle i , $t_{i,0}$, with the instant when the local fraction begins to increase since, among the variables investigated, this is the first variable that undergoes a change with respect to its initial sedimentation value. We identify the end of the transition, $t_{i,pack}$, with the instant when the number of contacting neighbors gets a steady value of packing since the number of contacting neighbors is the last variable that gets a steady value. In this way, the transition time and the Lagrangian transition length are given by:

$$\Delta t_{i,tr_L} = t_{i,pack} - t_{i,0} \quad (5.11)$$

$$L_{i,tr_L} = |\mathbf{x}_i(t_{i,pack}) - \mathbf{x}_i(t_{i,0})| \quad (5.12)$$

The Lagrangian transition length is explained by means of the Fig. 5.4. Assuming that Fig. 5.4 (left) corresponds to the beginning of the transition for the particle circled in green, $t_{i,0}$, and Fig. 5.4 (right) corresponds to the end of the transition for this particle, $t_{i,pack}$, the Lagrangian transition length, L_{i,tr_L} , corresponds to the distance that the particle travels from the instant $t_{i,0}$ to the instant $t_{i,pack}$.

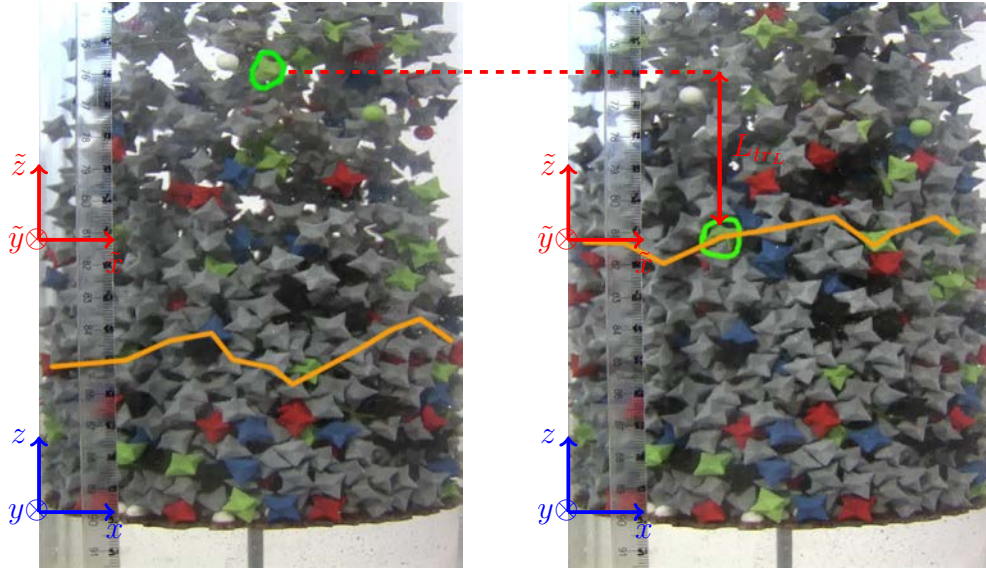


Figure 5.4: Example of dendritic particle tracking in glycerol. The position of the particle marked by a green circle is tracked from an initial instant (left) until the final packed instant, 42s later (right). In order to schematically represent the Lagrangian transition length, L_{trL} , we assume that the particle marked by a green circle at the initial instant (left) is entering to the transition zone. The packing front is schematically shown in orange. The fixed-to-vessel global reference frame $\{x, y, z\}$ is shown in blue and the fixed-to-vessel particle reference frame $\{\tilde{x}, \tilde{y}, \tilde{z}\}$ with its origin vertical position located at the particle vertical packing position is shown in red.

5.2.2 Eulerian description

In an Eulerian description we define the local fraction, number of contacting neighbors and particle velocity given by:

$$g_{env} = g_{env}(\mathbf{x}, t) \quad (5.13)$$

$$CN = CN(\mathbf{x}, t) \quad (5.14)$$

$$\mathbf{v} = \mathbf{v}(\mathbf{x}, t) \quad (5.15)$$

Now these variables are not associated to each particle i but they are given for a position in space, \mathbf{x} , and for a time, t .

We adopt a reference frame (see reference frame in green in Fig. 5.5) that moves upwards traveling with the mean packing front. We refer the vectorial variables to this reference frame. This reference frame differs from a second reference which is fixed to the recipient (see reference frame in blue in Fig. 5.5). Additionally, we assume the *steady-state* regime of the phenomenon of packing, i.e. the variables (local fraction, number of contacting

neighbors and particle velocity) on the Eulerian description and referred to the reference frame that moves with the packing front do not depend on time, $\partial/\partial t \approx 0$:

$$g_{env} = g_{env}(\mathbf{x}) \quad (5.16)$$

$$CN = CN(\mathbf{x}) \quad (5.17)$$

$$\mathbf{v} = \mathbf{v}(\mathbf{x}) \quad (5.18)$$

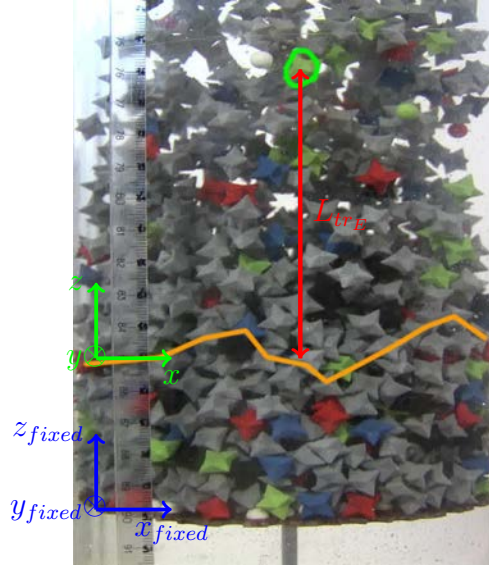


Figure 5.5: Example of dendritic particle tracking in glycerol for a given instant. In order to schematically represent the Eulerian transition length, L_{trE} , we assume that the particle marked by a green circle is entering to the transition zone. The packing front is schematically shown in orange. A reference frame moving upwards with the mean packing front is shown in green, $\{x, y, z\}$. A reference frame which is fixed to the container, $\{x_{fixed}, y_{fixed}, z_{fixed}\}$, is shown in blue.

We focus on the vertical direction, z , since the gradients of the used variables are much larger along this vertical direction than along the cross-section, $x - y$:

$$\frac{\partial g_{env}}{\partial z} \gg \frac{\partial g_{env}}{\partial x} \approx \frac{\partial g_{env}}{\partial y} \quad (5.19)$$

$$\frac{\partial CN}{\partial z} \gg \frac{\partial CN}{\partial x} \approx \frac{\partial CN}{\partial y} \quad (5.20)$$

$$\frac{\partial \mathbf{v}_z}{\partial z} \gg \frac{\partial \mathbf{v}_z}{\partial x} \approx \frac{\partial \mathbf{v}_z}{\partial y} \quad (5.21)$$

We define the Eulerian transition length, L_{trE} , as the vertical size of the region upstream the packing front where the vertical gradients of the local fraction, number of contacting neighbors and particle velocity are different than zero. The Eulerian transition length represents a different physical concept than the Lagrangian transition length. More precisely, according to the simulations of Chap. 4, the Eulerian transition length is given by two iso-pleths, $z = L_{trE}$ and $z = 0$:

- 1. Upper iso-pleth, $z = L_{trE}$:

$$\begin{cases} g_{env} = g_{env}^{sed}, & \text{if } z \geq L_{trE}. \\ g_{env} > g_{env}^{sed}, & \text{if } z < L_{trE}. \end{cases} \quad (5.22)$$

- 2. Lower iso-pleth, packing front, $z = 0$:

$$\begin{cases} CN < CN^{pack}, & \text{if } z > 0. \\ CN = CN^{pack}, & \text{if } z \leq 0. \end{cases} \quad (5.23)$$

Herein we apply the experiments and simulations results from previous chapters to solidification. In solidification *multiphase multiscale models* an Eulerian description is used. Therefore, the efforts of this section are focused on explaining the packing dynamics in an Eulerian description as a function of the geometrical (through the parameter d_{eq}/l_c), hydrodynamic conditions (through the parameter St) and the sedimentation fraction, g_{env}^{sed} .

We compute the vertical component of the velocity of the packing front with respect the reference frame fixed to the recipient (blue) by the conservation of the solid phase in the transition region:

$$v_{front_z} = \frac{g_{env}^{sed}}{g_{env}^{pack}} v_{z_{env}^{sed}} \quad (5.24)$$

We relate the Lagrangian transition length, Eulerian transition length and transition time:

$$L_{trE} \approx L_{trL} + \Delta t_{trL} v_{front_z} \quad (5.25)$$

We scale the previous equation and include the definition of the vertical component of the velocity of the packing front:

$$L_{trE}^* \approx L_{trL}^* + \left(\frac{g_{env}^{sed}}{g_{env}^{pack}} \right) \Delta t_{tr}^* \quad (5.26)$$

In Eq. 5.26 we relate the dimensionless Eulerian transition length with the dimensionless Lagrangian transition length, sedimentation fraction, packing fraction and the transition time.

The simulation results of Δt_{trL}^* and L_{trL}^* from Sec. 4.4.2 are recovered in Table 5.2. With these results, we interpolate L_{trL}^* and Δt_{trL}^* as a function of d_{eq}/l_c and St (see Eq. 5.27 and Eq. 5.28). See fitting parameters in Table 5.3.

Table 5.2: Δt_{trL}^* and L_{trL}^* results from Sec. 4.4.2.

St	d_{eq}/l_c	Δt_{trL}^*	L_{trL}^*
$o(10^{-3})$	1.0	22	6
	0.56	32	6
$o(10)$	1.0	9	2
	0.56	13	4

$$\Delta t_{trL}^*(St, d_{eq}/l_c) = a_{\Delta t} + b_{\Delta t} \log_{10} \left(\frac{St}{St_{ref}} \right) + c_{\Delta t} \left(\frac{d_{eq}}{l_c} \right) + d_{\Delta t} \left(\frac{d_{eq}}{l_c} \right) \log_{10} \left(\frac{St}{St_{ref}} \right) \quad (5.27)$$

$$L_{trL}^*(St, d_{eq}/l_c) = a_L + b_L \log_{10} \left(\frac{St}{St_{ref}} \right) + c_L \left(\frac{d_{eq}}{l_c} \right) + d_L \left(\frac{d_{eq}}{l_c} \right) \log_{10} \left(\frac{St}{St_{ref}} \right) \quad (5.28)$$

Table 5.3: Fitting parameters of Δt_{trL}^* and L_{trL}^* .

par.	a	b	c	d
Δt_{trL}^*	45.26	-8.07	-23.26	4.19
L_{trL}^*	6.0	0.19	0.0	-1.39

where $St_{ref} = 4.5 \cdot 10^{-3}$ and defined for spherical and dendrite envelopes in the interval $d_{eq}/l_c \in [0.56, 1.0]$ and $St \in [4.5 \cdot 10^{-3}, 10]$.

Finally, we use Eq. 5.26 substituting Δt_{trL}^* and L_{trL}^* by the Eqs. 5.27 and 5.28, respectively. The sedimentation envelope fraction, g_{env}^{sed} , is an input parameter. For the envelope packing fraction, g_{env}^{pack} , we use the correlation in Eq. 5.3.

Therefore, we provide an useful correlation of the characteristic size of the packing phenomenon (Eulerian transition length) as a function of the grain geometry, hydrodynamic conditions and envelope sedimentation fraction. This correlation is thought to be useful for the solidification *multiphase multiscale modeler* in order to quantify the size of the packing phenomenon. In Fig. 5.6 we show the dimensionless Eulerian transition length, L_{trE}^* , for different combinations of d_{eq}/l_c , St and g_{env}^{sed} . The lower the Stokes number is, the larger is the transition length. The higher is the sedimentation fraction, the larger is the transition length. The more dendritic the grains are, the larger is the transition length.

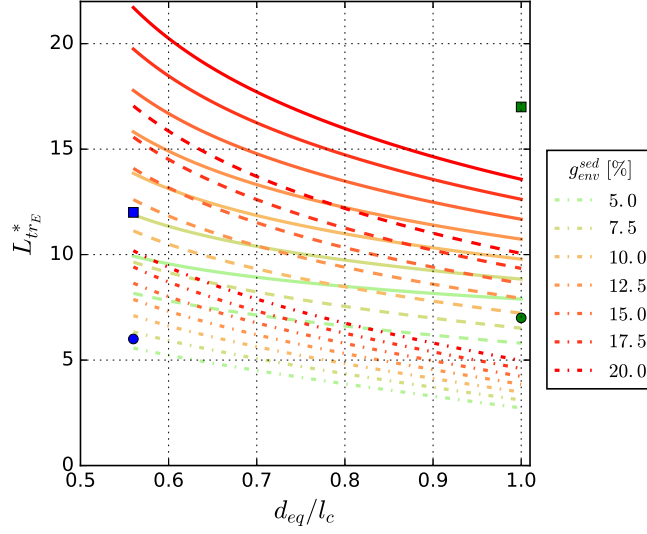


Figure 5.6: L_{trE}^* as a function of d_{eq}/l_c , St , and g_{env}^{sed} . The solid (-), dashed (- -) and dash-dot (-.) lines refer to $St = St_{ref}$, 0.1 and 10, respectively. Different colors refer to different values of g_{env}^{sed} . The L_{trE}^* obtained from the four simulations in Figs. 4.23 and 4.27 are added: spheres in green, dendrites in blue; low Stokes in squares, higher Stokes in circles.

In Fig. 5.6 we also added the Eulerian transition length, L_{trE}^* , obtained for spheres and dendrites in Figs. 4.23 and 4.27, respectively, from Chap. 4. Very similar results are obtained for the cases of dendrites, $d_{eq}/l_c = 0.56$ and $g_{env}^{sed} = 5\%$, at Stokes numbers of $o(10^{-3})$ and $o(10)$; and the case of spheres, $d_{eq}/l_c = 1.0$ and $g_{env}^{sed} = 20\%$ at Stokes number of $o(10)$. However, a relative difference of 30% is obtained between these two ways of computing L_{trE}^* for the case of spheres at Stokes of $o(10^{-3})$. The differences can be attributed to: the experimental measurement uncertainty (since the correlation in Eq. 5.26 and the simulations of Chap. 4 are based on the experimental work), the assumptions considered in the DEM simulations and in the correlations, etc.

To summarize, in this chapter we first propose a correlation of the packing fraction as a function of the grain geometry and hydrodynamic conditions in solidification. Secondly, we propose a correlation to estimate the characteristic size of the packing phenomenon in an Eulerian description. We estimated the characteristic size of the phenomenon to be between approximately 3 and 22 grain equivalent diameters.

Conclusions and perspectives

Conclusions

We investigated the phenomenon of packing of equiaxed grains in solidification. This complex phenomenon consists of the sedimentation and packing of 3D nonspherical growing grains in fluid of a similar density than the grains. The grain orientation is random and the grains are polydisperse in size and morphology.

We have shown that the most important dimensionless parameters governing the phenomenon of sequential packing in a viscous fluid are the Stokes number, St , the Archimedes number, Ar , and the growth-to-motion ratio, Γ . The Stokes number, which is the ratio between the grain inertia and viscous dissipation, governs the phase of approaching to the packing front. The higher the Stokes number is, the faster is the approaching in dimensionless terms. The Archimedes number, which is the ratio between the apparent weight and the viscous dissipative forces, governs a second phase that we called rearrangement. During this phase, the grains find their definitive position in the packing. The higher the Archimedes number is, the faster is the rearrangement in dimensionless terms. Higher values of the growth-to-motion ratio determine a low influence of the growth.

We have evaluated the previous parameters in solidification. A Stokes number in an interval between $o(10^{-4})$ and $o(10^2)$ is expected. The Archimedes number ranges from $o(1)$ to $o(10^6)$. Low influence of the grain growth, $\Gamma \geq o(10^2)$, is found for the grains that pack by motion in DC casting. We cannot discard a packing by growth for the stationary grains.

We focused on the investigation of the packing by sedimentation due to gravity, neglecting the fluid convection and the grain growth. Under these assumptions, a single parameter governs the phenomenon: the Stokes number. We study separately the packing which is the state in which all particles achieve the mechanical equilibrium, and the packing dynamics which is the transition between the pure sedimentation regime and the final packing.

We have shown that the most important influence on the packing is that of the envelope geometry. The packing fraction of dendrite grain envelopes is more than 1/3 smaller than that of spheres packing under the same hydrodynamic conditions. As the morphology of the grains changes from dendritic towards globular, the packing fraction increases. To

describe the influence of the grain morphology on the packing fraction we proposed the ratio between the equivalent diameter and the widest length, d_{eq}/l_c , as a suitable universal geometrical parameter.

The forces of adherence between grains, in case they exist, can dramatically loose the packing. Values of the packing fraction down to 0.27 and 0.15 for spheres and dendritic grains, respectively, are expected.

The influence of hydrodynamic conditions on packing in solidification processes is much smaller than the impact of the grain morphology. The influence of the fluid in which the grains settle on the final packing fraction is given by the particle Stokes number. The packing fraction clearly decreases with decreasing Stokes number, due to the lower kinetic energy with which the impacting grains can rearrange the packing. For low values of the Stokes number, the packing fraction tends to the RLP.

The influence of the friction and grain size polydispersity is much smaller than that of the grain morphology. Looser packings are found for frictional particles for both spheres and dendritic grains. Polydisperse collections of spherical grains pack denser than a monodisperse. In case of dendrites, we did not find a monotonous tendency of the packing fraction with grain size polydispersity.

We investigated the packing dynamics for low Stokes, $St = o(10^{-3})$. An approximation of the packing dynamics for higher Stokes of $o(10)$ is also proposed. Only situations of nil restitution coefficient are considered. We proposed three different parameters to characterized the packing dynamics: the transition time, Δt_{trL} , the Lagrangian transition length, L_{trL} , and Eulerian transition length, L_{trE} . The transition time refers to the time that a particle spends in the transition between sedimentation and final packing. During the transition time the particle moves a distance equal to the Lagrangian transition length. The Eulerian transition length provides the characteristic size of the packing dynamics in an Eulerian description. We conclude that the hydrodynamic conditions are more important on the packing dynamics than the grain morphology. The lower the Stokes number is, the slower the packing dynamics is, and the more dendritic the grains are, the slower the packing dynamics is.

To conclude we propose a correlation of the packing fraction of equiaxed dendritic grains with the geometrical and hydrodynamic conditions. Additionally, a second correlation is proposed to determine the characteristic size of the packing dynamics, L_{trE} . These correlations are thought to be useful for the multiphase multiscale modelers of solidification.

Perspectives

Further work should focus on three points: the influence of grain growth during the settling on packing; more complex hydrodynamical conditions that can be present in solidification processes, such as settling to an inclined packing front and in the presence of a shear flow;

and the effect of the polydispersity of dendritic grains on packing.

In the experimental or numerical approaches developed in this thesis, only the phenomenon of growthless grain packing by sedimentation is considered. A large characteristic grain growth to characteristic grain motion time ratio is considered, $\Gamma \gg 1$. An antagonistic situation of packing in metal alloy solidification is that of packing by grain growth with negligible grain sedimentation. Assuming the solid grains are dragged by the melt without sedimentation, $\mathbf{v}_s \approx \mathbf{v}_l$, the grain blocking could be achieved by growth, $\Gamma \ll 1$. We propose to computationally tackle this phenomenon by means of a *mesoscopic* approach, Ref. [Souhar et al., 2016], where the motion of the grains and the mechanical interactions between them must be also implemented.

In solidification, the grain packing over an inclined plane is common in some casting processes, e.g. aluminum direct chill casting. These conditions could lead to the avalanche granular flow before particle packing. Moreover, the thermosolutal melt convection could also introduce the presence of a shear flow over the packed grain layers. In this way, we propose this phenomenon to be experimentally investigated more advanced characterization techniques to obtain the grain motion, Ref. [Aussillous et al., 2013].

The influence of the grain size polydispersity and grain morphology polydispersity on the packing fraction remains an open question. Larger efforts in this field are required.

Résumé (long)

Introduction

Dans le contexte de la solidification, le problème de la sédimentation et de l'empilement des grains dendritiques n'est pas encore bien connu. Ces phénomènes influencent directement la qualité du produit final de solidification à travers la macroségrégation. Dans la zone pâteuse, la macroségrégation est induite par le mouvement relatif du liquide, plus riche en soluté, et du solide, plus pauvre en soluté. Les deux mécanismes de mouvement relatif sont : le mouvement des grains équiaxes et l'écoulement du liquide à travers la zone des grains empilés. La perméabilité de la zone empilée, qui dépend de sa structure est également un élément important. Il y a ainsi une relation étroite entre la dynamique de la sédimentation, l'empilement et le phénomène de macroségrégation.

La sédimentation des grains dendritiques est due à la faible différence de densité dans le cas des alliages métalliques entre les phases solide et liquide. En outre, les grains en cours de sédimentation subissent aussi l'influence de l'écoulement du liquide. Une fois les grains empilés, ils forment une structure poreuse où ils sont ordonnés aléatoirement, c'est-à-dire, que leurs positions et leurs orientations ne suivent pas une logique déterminée. De cette façon, l'empilement des grains dendritiques est un phénomène complexe du fait de sa nature aléatoire et des morphologies particulières des grains.

L'objectif de cette thèse est de comprendre le concept d'empilement ainsi que le concept de fraction d'empilement des grains dendritiques dans le contexte de la solidification des alliages métalliques. Une fois ce premier point compris, la dynamique d'empilement de grains dendritiques a été aussi discutée. Ce deuxième point est important pour déterminer le temps et la distance nécessaire pour les grains pour passer du régime de sédimentation au régime final d'empilement. Finalement, un autre objectif a été de proposer des relations simples permettant de prendre en compte dans les modèles macroscopiques l'influence de la morphologie des grains et de leurs conditions hydrodynamiques sur l'empilement et la dynamique d'empilement.

Les moyens de recherche mis en œuvre sont composés de deux volets : l'un expérimental et l'autre numérique. L'approche expérimentale consiste à faire sédimenter et empiler plusieurs collections de particules à l'intérieur d'une colonne verticale de section cylindrique. De cette façon, une fraction d'empilement expérimentale peut être déterminée. En ce qui concerne la dynamique d'empilement, la trajectoire des particules a été analysée. L'approche numérique est basée sur la méthode des Éléments Discrets (DEM). Ce type

d'approche permet de compléter le travail expérimental en accédant à des variables granulaires qui ne sont pas accessibles expérimentalement. De plus, il permet d'étudier la sensibilité de la fraction d'empilement et de la dynamique d'empilement au type de morphologie de grain, à la poly-dispersité de taille des grains, au frottement entre grains et aux propres paramètres numériques du modèle.

La thèse est composée de deux parties. Une première partie où la bibliographie existante sur le sujet de l'empilement de grains est présentée, et une deuxième partie, pour décrire le travail effectué. Cette dernière est divisée en trois chapitres abordant des aspects théoriques, expérimentaux et de modélisation.

Première partie

L'état de l'art de ce texte introduit d'abord le contexte de la solidification. Le phénomène d'empilement de particules est ensuite présenté dans le contexte des milieux granulaires. Pour conclure cette partie, une brève section sur les techniques de modélisation de l'empilement de particules de morphologie arbitraire est présentée.

Dans la solidification des alliages métalliques, les grains équiaxes nucléent dans la phase liquide, sédimentent et s'empilent aléatoirement. De cette façon, les grains équiaxes forment un réseau poreux en équilibre mécanique [Steinbach, 2013] avec une fraction volumique de solide appelée fraction d'empilement. Cette fraction d'empilement est un paramètre très important pour la modélisation de la solidification [Založnik et al., 2011a, Combeau et al., 2009] car elle sert pour commuter entre deux régimes : 1) régime de grains libres de bouger dans le liquide : possible quand la fraction de solide est plus faible que la fraction d'empilement, et 2) régime poreux où les grains sont bloqués et un écoulement de fluide entre les grains est alors possible. Ce second régime se met en place quand la fraction de solide est plus élevée que la fraction d'empilement.

La valeur de la fraction d'empilement n'est pas connue dans le domaine de la solidification. Des valeurs très différentes sont adoptées par les modélisateurs de solidification. Plusieurs exemples de la fraction d'empilement prises dans la littérature sont rapportées ici : 0.20 dans [Heyvaert et al., 2017], un intervalle entre 0.20 et 0.25 dans [Vreeman and Krane, 2002], 0.30 dans [Založnik et al., 2011a], 0.40 dans [Combeau et al., 2009, Leriche, 2015] alors qu'une valeur de 0.637 est utilisée par [Wang et al., 2005, Reddy and Beckermann, 1995]. En outre, les phénomènes de solidification (comme par exemple le transfert de chaleur ou la macroségrégation) sont très sensibles à cette valeur [Heyvaert et al., 2017]. Ainsi une compréhension de l'empilement des grains équiaxes peut conduire à une amélioration de la modélisation de la solidification.

D'un point de vue des milieux granulaires, l'empilement des particules a toujours été un problème d'intérêt pour les mathématiciens et les physiciens. Certaines de leurs principales préoccupations ont été de comprendre l'espace minimal et maximal qu'une collection de particules donnée peut remplir, pour des arrangements ordonnés et aléatoires. Dans cette thèse, nous nous sommes concentrés sur l'empilement aléatoire de particules,

c'est-à-dire que les positions et les orientations des particules ne suivent aucune logique [Berthier, 2011]. Malgré la difficulté mathématique de définir un empilement de particules aléatoire parce que le degré de hasard n'est pas unique [Torquato et al., 2000], des limites de fraction d'empilement supérieure et inférieure sont généralement acceptées. Elles sont connues sous les noms de *Random Close Packing* (RCP) et *Random Loose Packing* (RLP), respectivement.

Dans le cas de sphères indéformables non-adhérentes de taille mono-disperse, la fraction d'empilement est théoriquement comprise entre 0,536 et 0,634 [Song et al., 2008]. D'une manière expérimentale, le protocole d'empilement consistant en la fluidisation des particules dans un fluide de densité similaire est couramment choisi pour obtenir le RLP [Onoda and Liniger, 1990, Jerkins et al., 2008, Schröter et al., 2005, Aste et al., 2007, Delaney et al., 2010]. La plus faible rapportée est de $0,550 \pm 0,001$ pour les sphères non-adhérentes [Jerkins et al., 2008]. Dans le cas de sphères adhérentes, la fraction d'empilement peut considérablement diminuer [Yang et al., 2007, Tayeb et al., 2016, Dong et al., 2012]. D'autre part, un protocole d'empilement qui consiste en une agitation mécanique des particules avec un faible frottement est utilisé pour obtenir le RCP, $\approx 0,64$ [Scott and Kilgour, 1969, Nowak et al., 1998].

Ainsi, le protocole expérimentale joue un rôle fondamental dans la fraction d'empilement aléatoire. Un empilement lâche est attendu dans le cas d'un empilement aléatoire de grains dendritiques dans la solidification car les grains sont empilés dans le liquide visqueux (métal fondu) avec une faible différence relative de densité solide-liquide, $(\rho_s - \rho_l)/\rho_s$, par exemple 0,057 pour un alliage Al-Zn [Založnik et al., 2011b]. Des valeurs de la fraction d'empilement entre 0,55 et 0,61 sont rapportées dans [Jerkins et al., 2008, Schröter et al., 2005, Aste et al., 2007, Delaney et al., 2010] pour l'empilement fluidisé d'une collection de sphères mono-disperse avec une faible différence relative de densité solide-liquide.

Dans [Farrell et al., 2010], le nombre de Stokes, St , qui est le rapport entre l'inertie de la particule qui s'approche de l'empilement et la dissipation visqueuse de l'énergie cinétique, se révèle expérimentalement comme le paramètre adimensionnel qui régit le phénomène d'empilement de sphères mono-disperses par sédimentation dans un fluide. Selon cette référence, les conditions hydrodynamiques de l'empilement n'ont aucune influence sur la fraction d'empilement si le nombre de Stokes est inférieur à un certain seuil qui est d'environ 10 en cas de sphères mono-disperses avec un fort frottement. Au dessus de ce seuil, plus le Stokes est élevé, plus l'empilement est dense.

La géométrie des particules joue aussi un rôle fondamental dans la fraction d'empilement aléatoire. Certains exemples expérimentaux rapportés sont l'empilement des solides platoniques (qui sont des particules convexes) [Baker and Kudrolli, 2010]. Des fractions d'empilement de 0.48 pour le tétraèdre, de 0.54 pour le cube, de 0.52 pour l'octaèdre, de 0.51 pour le dodécaèdre et, finalement, de 0,51 pour l'icosaèdre sont obtenus avec le protocole de fluidisation. En outre, il existe une relation étroite entre la sphéricité des particules, Ψ et la limite RLP [Zou and Yu, 1996]. Les sphéroïdes, les disques, les prismes rectangulaires, les cubes, les demi-sphères, les cylindres et les sphéroïdes cônes sont expéri-

mentés, il est constaté que la fraction RLP diminue lorsque la sphéricité décroît. Dans le cas de particules équiaxes fortement non-convexes, un comportement similaire est trouvé [Malinouskaya et al., 2009], la fraction d’empilement diminuant jusqu’à environ 0,10 avec une sphéricité décroissante.

Deux philosophies de modélisation du phénomène d’empilement de particules sont présentées : 1) géométrique et 2) dynamique. Les particules sont normalement introduites aléatoirement dans un récipient et progressivement déplacées ou grandis sans suivre de lois physiques jusqu’à avoir un empilement de particules bloquées, par exemple *Monte Carlo rejection method* [Auwerda et al., 2010]. Les algorithmes dynamiques sont basés sur la résolution de lois physiques du mouvement des particules (*lois du mouvement de Newton*), par exemple la méthode DEM. Dans ce texte, nous nous concentrons sur cette méthode puisque elle permet de décrire la dynamique de systèmes de particules non-sphériques (par exemple de morphologie dendritique [Yuan et al., 2012]) aussi bien que les contacts entre particules. En outre, les interactions d’un fluide avec les particules sont relativement faciles à être incorporées à travers par exemple des modèles de traînée, lubrification, flottabilité, levage, etc [Dong et al., 2012, Delaney et al., 2011].

Dans les situations où la résolution de la dynamique des particules et aussi du fluide est désirée, les approches de couplage fluide-particules CFD-DEM sont utilisées. Nous classons le travail CFD-DEM dans deux familles : une première dans lequel la résolution du fluide est faite à une échelle plus grande que la taille des particules. De cette façon, les interactions du fluide sur les particules sont prises en compte à travers des modèles simplifiés [Sun and Xiao, 2016]. La seconde correspond au cas où l’échelle de résolution du fluide est plus petite que la taille des particules. Des méthodes de couplage fluide-particule comme par exemple la méthode de la frontière immergée [Peskin, 2002] sont alors utilisées.

Deuxième partie

Analyse théorique

Un modèle théorique de la dynamique d’une particule approchant un lit de particules déjà empilées à l’intérieur d’un fluide visqueux au repos a été développé. L’intérêt de ce modèle est d’identifier les paramètres adimensionnels les plus importants qui régissent le phénomène d’empilement des grains équiaxes dans le contexte de la solidification. En supposant des trajectoires de grains approchant perpendiculairement au front d’empilement, deux phases ont été identifiées : 1) une phase d’approche et 2) une phase de réorganisation.

La phase d’approche décrit la trajectoire du grain approchant d’une position éloignée du front d’empilement jusqu’à toucher le front d’empilement. Initialement ce grain bouge avec un régime permanent (vitesse de sédimentation constante). La présence de fluide visqueux entre le grain et le front fera ralentir le grain du fait de la force de lubrification, à

une distance relativement proche du front (plusieurs tailles du grain). Nous avons trouvé que ce phénomène de ralentissement est régi par le nombre de Stokes, St , ou rapport entre l'énergie cinétique avec laquelle le grain s'approche avant le ralentissement et la dissipation visqueuse due au fluide. De cette façon, le plus faible est le nombre de Stokes, le plus important est le ralentissement du grain. La phase de réorganisation représente le mouvement du grain après avoir été ralenti et avoir touché le front d'empilement. Ainsi, le grain cherche une position d'équilibre plus stable. Cette phase est régie par le nombre d'Archimède, Ar .

Ces notions ont été appliquées à des situations de solidification. Les nombres adimensionnels de Stokes et Archimède ont été évalués pour deux procédés différents : la coulée semi-continue d'aluminium et la coulée statique d'acier (lingots). Nous avons trouvé pour le premier procédé que le nombre de Stokes variait dans l'intervalle $10^{-4} - 10$ et Archimède dans $10^{-3} - 10^2$ pour des valeurs de taille et de vitesse de grains tirées des simulations de [Založnik et al., 2011b]. D'autre part, pour la coulée statique, le nombre de Stokes peut augmenter jusqu'à environ 10^2 et Archimède jusqu'à 10^6 avec les valeurs des simulations de [Leriche, 2015]. De cette façon, comme nous le montrerons dans l'étude expérimentale et numérique, des empilements plus lâches et avec une dynamique d'empilement plus lente sont attendus pour la coulée semi-continue d'aluminium par rapport à la coulée statique d'acier.

En conclusion, notre analyse théorique a montré que les nombres de Stokes et d'Archimède sont les nombres adimensionnels les plus importants qui régissent le phénomène de la sédimentation et l'empilement de particules à l'intérieur d'un fluide visqueux. Ce résultat est en accord avec les expériences de [Farrell et al., 2010] où l'influence des conditions hydrodynamiques sur la fraction d'empilement dépend uniquement du nombre de Stokes.

Étude expérimentale

Un montage expérimental pour reproduire le phénomène de l'empilement de grain équiaxes a été développée. L'objectif de cette expérience est d'étudier l'influence de la géométrie des grains et des conditions hydrodynamiques sur la fraction d'empilement en établissant une similitude hydrodynamique entre nos expériences et le phénomène d'empilement en solidification d'alliages métalliques à travers les nombres adimensionnels étudiés précédemment.

De cette façon, les expériences ont été réalisées pour un total de huit différentes combinaisons particule-fluide. Deux collections de particules ayant une distribution de taille mono-disperse (sphères et enveloppes de dendrite équiaxe avec un angle de sommet $\theta = 45^\circ$) ont été empilées par sédimentation dans quatre fluides différents : 1) glycérol, 2) une solution de glycérol-eau, 3) de l'eau, et 4) de l'air (empilement sec), correspondant à quatre nombres de Stokes différents pour chaque morphologie.

Le dispositif expérimental est composé de deux colonnes verticales concentriques de lon-

gueur environ 1000 mm fabriquées en acrylique transparent et intégrées dans une structure métallique servant de support. La colonne intérieure est cylindrique avec un diamètre interne de 120 mm, tandis que la colonne extérieure présente une section transversale carrée de côté interne 160 mm. La colonne cylindrique et l'espace entre les deux colonnes sont remplis avec le même fluide. Cette configuration à double paroi est conçue pour annuler la déformation optique horizontale des particules observées en raison de la réfraction sur la surface incurvée du cylindre. Les particules sont insérées dans la colonne cylindrique interne. Initialement, elles sont contenues dans la partie supérieure de la colonne, au-dessus d'une trémie, bloquées par un sas fermé. Le sas est alors ouvert et les grains traversent la trémie qui permet d'assurer un flux de grains constant [de Moraes Franklin and de Andrade, 2015]. Les grains sédimentent ensuite au fond de la colonne et s'empilent sur une grille horizontale.

La collection de sphères est composée d'environ 12200 pellets d'airsoft. La taille des sphères a été choisie pour avoir un rapport de diamètre entre la particule et la colonne relativement important ($D/d = 20$). La collection d'enveloppes dendritiques est formée par environ 4400 particules, de taille similaire à les sphères, obtenues par fabrication additive. Un matériau innovant à base de composite quasicrystal-polymère [Kenzari et al., 2014] a été utilisé pour atteindre une valeur de densité précise d'environ 1400kg/m^3 et pour éviter les porosités ouvertes qui pourraient conduire à une absorption de fluide et, par conséquent, à la variation de densité de particules.

Par ce moyen, nous avons mesuré la fraction d'empilement en fonction de la morphologie et des conditions hydrodynamiques (à travers de nombre de Stokes). Les mesures montrent que les empilements deviennent plus lâches pour un nombre de Stokes décroissant. Une tendance similaire pour l'évolution de la fraction d'empilement avec le nombre de Stokes a été trouvée par [Farrell et al., 2010] pour le dépôt séquentiel de sphères d'acier monodisperse.

Dans le cas des sphères, pour la gamme Stokes étudiée, nous trouvons que la fraction d'empilement se situe entre $0,575 \pm 0,008$ et $0,628 \pm 0,011$. Nos résultats restent entre le RLP (0.55) et le RCP (0.64). Cependant, les empilements de sphères que nous avons obtenues pour les plus faible valeurs du nombre de Stokes ($St = 1,2 \cdot 10^{-3}$ dans le glycérol) conduisent à des empilement plus dense que l'empilement expérimentalement le plus faible de 0,55 [Jerkins et al., 2008]. D'autre part, l'empilement sec des sphères fournit un résultat similaire à celui de 0,632 de [Delaney et al., 2010].

Dans le cas des dendrites dans la gamme de nombre de Stokes étudiée, nous trouvons que la fraction d'empilement se situe entre $0,397 \pm 0,012$ et $0,468 \pm 0,018$. Ainsi les empilements de dendrite sont plus lâches que les empilements de sphères pour tous les nombres de Stokes. L'influence du nombre de Stokes sur la fraction d'empilement des dendrites se révèle significative et plus important que pour les sphères. Il est également intéressant de comparer l'empilement des dendrites (non-convexes) aux empilements des solides platoniques (convexes), qui ont été étudiés par [Baker and Kudrolli, 2010]. Cette comparaison montre que les empilements de dendrites pour toute la gamme des valeurs

du nombre de Stokes explorées sont plus lâches que l’empilement le plus lâche des solides platoniques. Notamment, les dendrites conduisent à une fraction d’empilement environ 20% plus faible que les octaèdres (une forme convexe souvent utilisée pour approximer la morphologie dendritique dans la modélisation de la solidification).

Finalement, la dynamique d’empilement a été étudiée, c’est-à-dire, le ralentissement des grains d’un régime initial de sédimentation à l’empilement final. Nous avons filmé la sédimentation et l’empilement des collections de sphères et dendrites dans le glycérol (le plus bas nombre de Stokes de la gamme étudiée). À partir de cette information, nous avons obtenu la trajectoire de plusieurs particules de chaque collection. De cette façon, la longueur moyenne de la zone de ralentissement, \bar{L}_{trL} , a été calculée et aussi le temps moyen nécessaire pour traverser la zone de ralentissement, $\bar{\Delta t}_{trL}$. Nous avons détecté que les particules commencent à ralentir à une distance d’environ six diamètres équivalents avant d’arriver à leurs positions finales. Cependant, le temps de ralentissement $\bar{\Delta t}_{trL}$ est plus élevé (près du double) pour le cas de dendrites que pour les sphères.

Modélisation

Le travail expérimental décrit dans la partie précédente est fastidieux et surtout limité à deux collections mono-disperse de morphologie différente : sphérique et dendritique. De plus, le désavantage fondamental est la faible accessibilité de l’information granulaire dans les expériences. Des variables granulaires comme par exemple la fraction locale de solide, le nombre de contacts mécaniques entre particules, les nombres de particules voisines en contact ou l’évolution de l’orientation des particules sont perdues avec notre configuration expérimentale. De cette façon, il existe une forte motivation pour développer un logiciel capable de reproduire les empilements expérimentaux et permettent alors d’étudier les variables granulaires expérimentalement inaccessibles.

Une première modélisation de l’empilement des grains a été réalisée à travers un modèle géométrique. Dans ce modèle, les grains arrivent séquentiellement au niveau du front d’empilement en suivant une trajectoire de ligne droite choisie aléatoirement et avec une orientation aléatoire. Une fois qu’un grain touche le front, il s’arrête définitivement en évitant la phase de réorganisation. Une telle façon d’empiler les grains conduit à des fractions d’empilement d’environ 0,27 pour les sphères et 0,15 pour les dendritiques. Ce résultat montre que les faibles fractions d’empilements utilisées en modélisation de solidification (par exemple 0,20 de [Heyvaert et al., 2017]) correspondent à des configurations d’empilement qui sont propres à des particules ayant une forte adhérence entre elles [Dong et al., 2012]. Selon cette référence, la valeur de fraction d’empilement de 0,27 est propre d’une rapport entre les forces d’adhérence entre grains et la force motrice de l’empilement (poids apparent et la force due à l’impact) d’entre 10^3 et 10^4 .

Ensuite, un logiciel DEM permettant de prendre en compte une morphologie arbitraire de particules à été développé à partir de zéro. Cet outil résout la dynamique de chaque particule aussi bien que les interactions entre particules. Les difficultés les plus importantes

trouvées dans ce développement ont été celles de pouvoir généraliser la description du type de morphologie des grains et de développer des protocoles capables de simplifier les interactions du fluide sans résoudre la dynamique du fluide. Deux protocoles d'empilement différents ont été simulés : 1) protocole de faible poids apparent des particules; 2) protocole *fluide* où les forces de lubrification entre particules, les forces et moments de traînée et la force de flottabilité sont pris en compte

Le premier protocole est basé sur la sédimentation et l'empilement de grains avec une très faible accélération verticale ($a = 10^{-5}g_o$). Il est créé pour reproduire les empilements caractérisés par une faible valeur du nombre de Stokes ($St = o(10^{-3})$). Le fluide n'est pas directement modélisé. Au lieu de cela, un modèle de contact entre particules est utilisé pour reproduire les effets de lubrification hydrodynamique entre les particules. Ce protocole permet d'accélérer considérablement les calculs. L'effet de la morphologie sur la fraction d'empilement avec des morphologies dendritiques et globulaires, l'effet de la polydispersité de taille de particules et l'effet du frottement entre particules ont été étudiés.

Parmis les résultats les plus importants obtenus avec ce protocole, nous soulignons que le paramètre le plus pertinent pour la caractérisation de la fraction d'empilement en fonction de la morphologie équiaxe est le rapport d_{eq}/l_c , c'est-à-dire, le rapport entre le diamètre équivalent du grain et sa plus grande longueur. La classification de la fraction d'empilement est la seule qui permet d'unifier les résultats obtenus pour les morphologie de grains dendritique et globulaire et d'obtenir ainsi une loi unique de la fraction d'empilement en fonction du rapport d_{eq}/l_c . D'autres paramètres géométriques (par exemple la sphéricité) ont été aussi essayés sans résultats satisfaisants. Des résultats moins importants ont été également obtenus avec ce protocole. Ils concernent l'étude de la fraction d'empilement avec la poly-dispersité de taille des grains, l'étude de l'influence du frottement entre grains et les conditions initiales sur la fraction d'empilement.

D'autre part, dans le deuxième protocole les grains sédimentent et s'empilent à cause du poids apparent des grains, $(\rho_s - \rho_l)g_o$ avec $(\rho_s - \rho_l)/\rho_s \approx 0.05$. La force de traînée et les forces de lubrification entre grains ont été simplifiées et aussi incorporées. L'objectif de ce protocole est celui d'accéder aux variables granulaires expérimentalement inaccessibles pendant la dynamique d'empilement. De cette façon, le modèle de lubrification a été calibré jusqu'à obtenir un ralentissement similaire aux expériences en glycérol. Les variables fraction locale de solide, nombre de contacts mécaniques, nombre de grains voisins en contact, vitesse verticale et rotation des grain ont été étudiées en fonction du temps avec une description Lagrangienne et aussi en fonction de la coordonnée verticale, z , avec une description Eulérienne.

Pour conclure, nous avons appliqué ces travaux expérimentaux et de modélisation au cas de la solidification. Ainsi, nous avons pu fournir une relation universelle de la fraction d'empilement de grains équiaxes en fonction de la géométrie des grains et des conditions hydrodynamiques de l'empilement. Cette relation sera utile pour la description du phénomène d'empilement de grains équiaxes dans un modèle multi-échelle multi-physique

de solidification d'alliages métalliques. En outre, nous avons fourni une relation analytique pour estimer la taille caractéristique du phénomène d'empilement (longueur de la zone de ralentissement) en fonction de la morphologie des grains et des conditions hydrodynamiques. Cette deuxième relation pourrait être intéressante pour estimer la taille caractéristique du phénomène d'empilement dans la modélisation multi-échelle de la solidification.

Les perspectives de ce travail de thèse devraient se concentrer sur l'étude de l'influence de la croissance des grains pendant l'empilement. L'étude de l'empilement avec d'autres conditions hydrodynamiques complexes qui peuvent être présentes dans les procédés de solidification, par exemple l'empilement sur un plan incliné ou avec un écoulement de cisaillement constitue une deuxième voie importante d'investigation. Un grand effort est également nécessaire sur le sujet de la poly-dispersité des grains non-convexes.

Appendix A

Solidification modeling support

A.1 DC casting simulations

Herein, we include several outputs of an aluminum DC casting macroscopic solidification simulation (more details in Ref. [Založnik et al., 2011a]). The objective of including this simulation example is to obtain the order of magnitude of:

- Grain velocity relative to packing front: in Fig. A.1 (left) the component of the velocity of the grains perpendicular to the packing front.
- Grain growth rate, $d(d_{eq})/dt$: shown in Fig. A.1 (right).

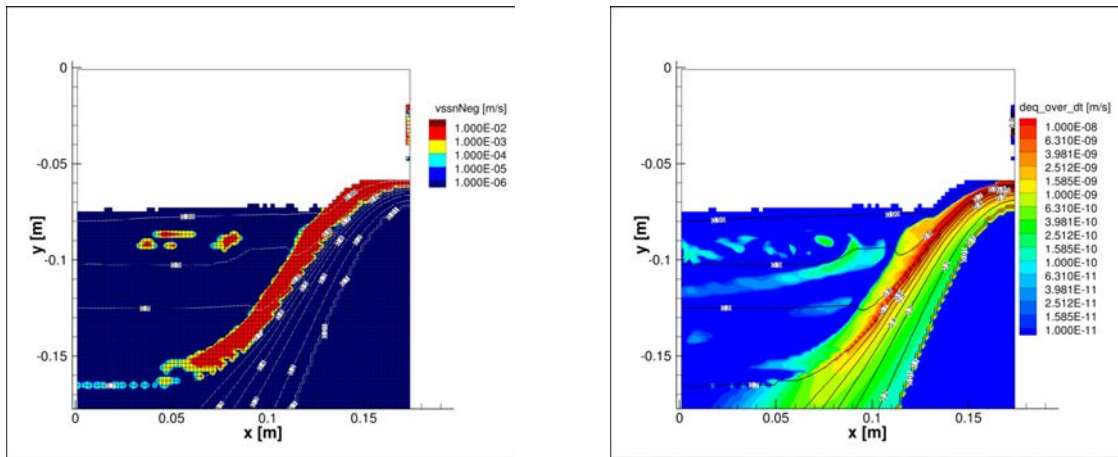


Figure A.1: Left: grain velocity relative to the packing front: magnitude of the component perpendicular to packing front. Right: grain growth rate, $d(d_{eq})/dt$.

Additionally, the grain size and grain velocity modulus relative to the packing front are included in Fig. A.2 left and right, respectively.

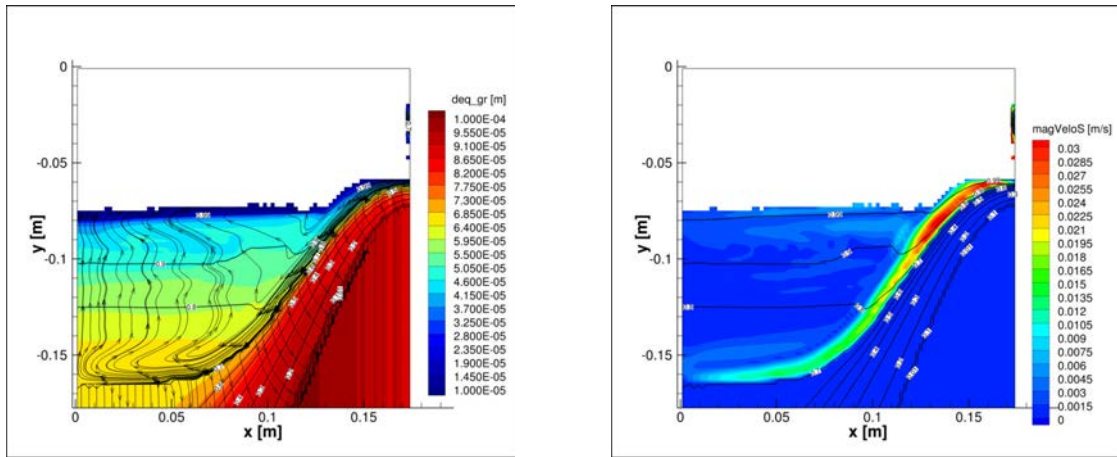


Figure A.2: Left: grain equivalent diameter. Right: magnitude of the grain velocity. Note that the velocity of the packing front in this frame is zero.

Appendix B

Experimental analysis

B.1 Sedimentation column setup

The double acrylic column is fixed to an aluminum structure which permits the column rotation about the horizontal axis passing along the column center of mass. This rotative function permits to quickly reset to the initial experiment configuration. Two photos are included to show the rotation function (see the sedimentation configuration in Fig. B.1 left and an image of the column while rotating in B.1 right).

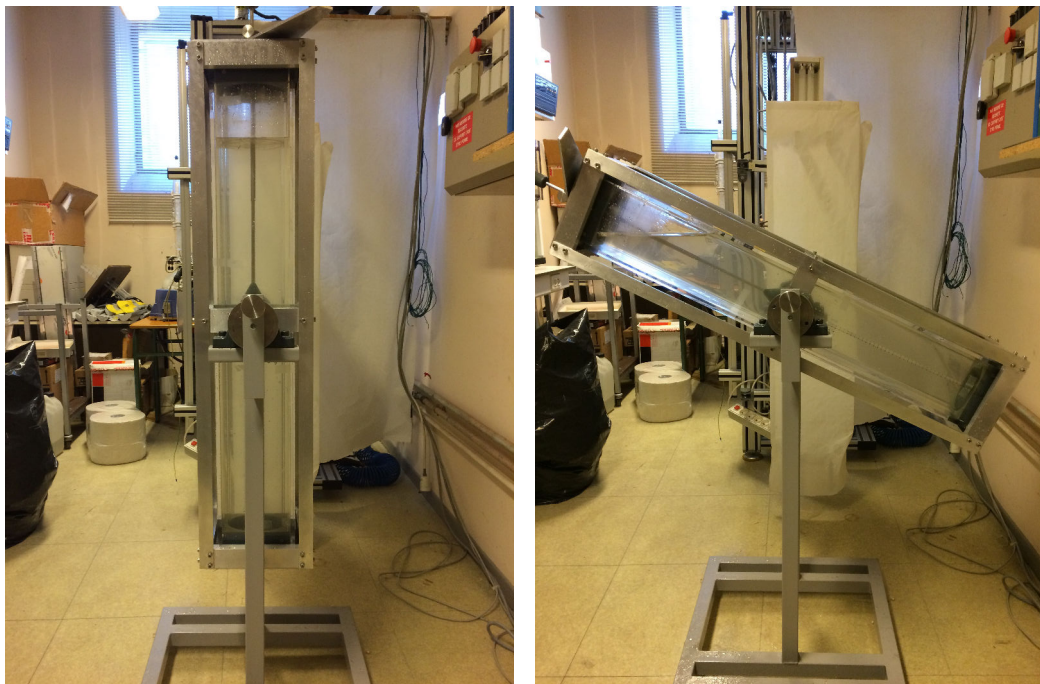


Figure B.1: Rotation function of the sedimentation column. Left) vertical sedimentation configuration. Right) the column permits to reverse the granular system to the initial stocked configuration by means of a horizontal rotation axis with an amplitude of rotation of 180°

Additionally, the drafting sketches of the main double column parts (cylindrical column, squared cross-section column, screw cap and injection system) are included showing the dimensions.

D

C

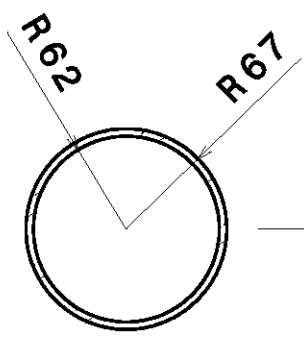
B

A

4

4

1000



3

3

2

2

1

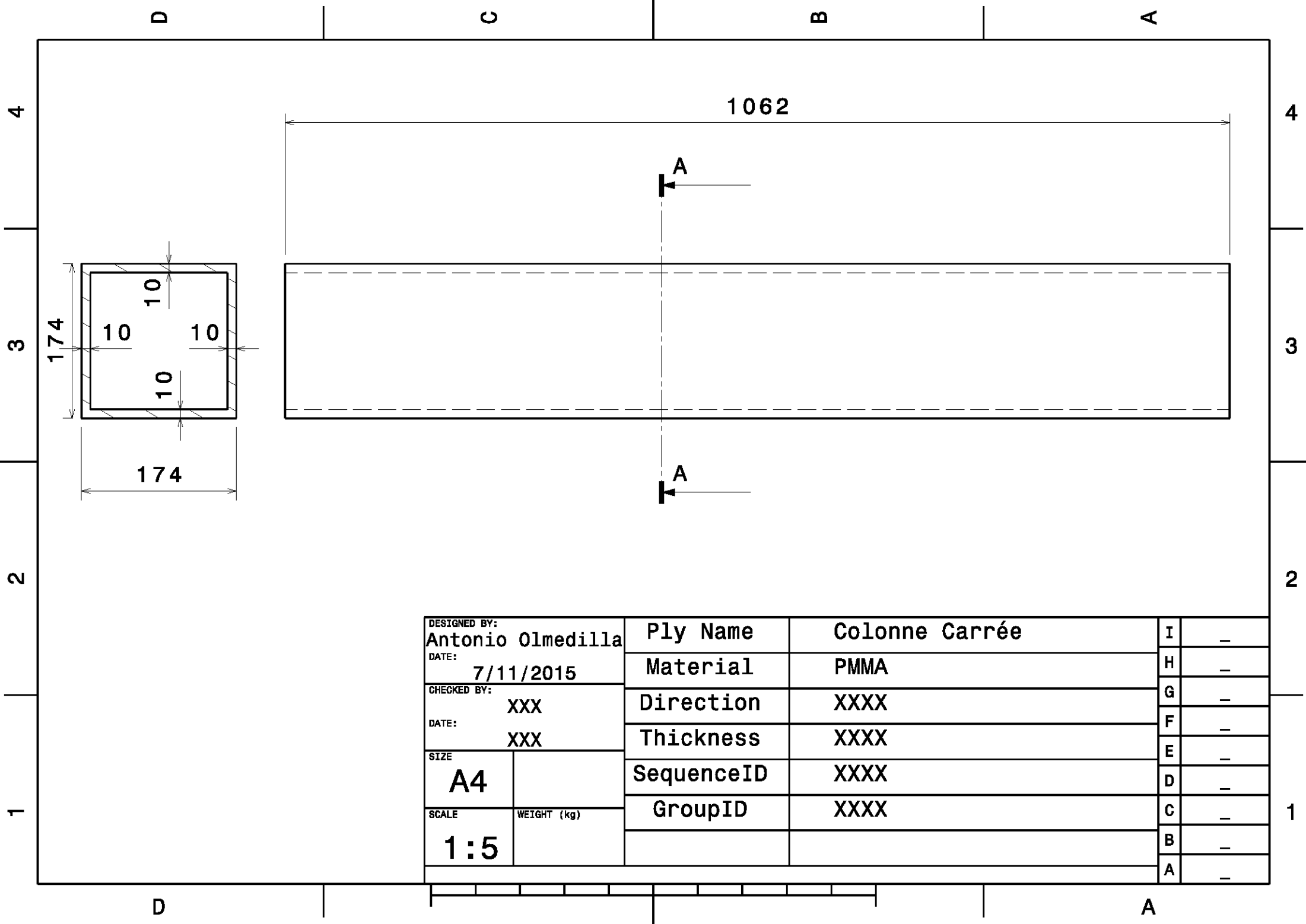
1

D

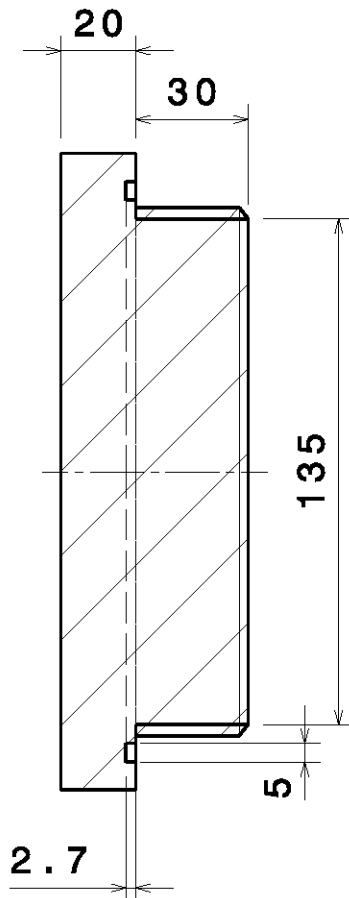
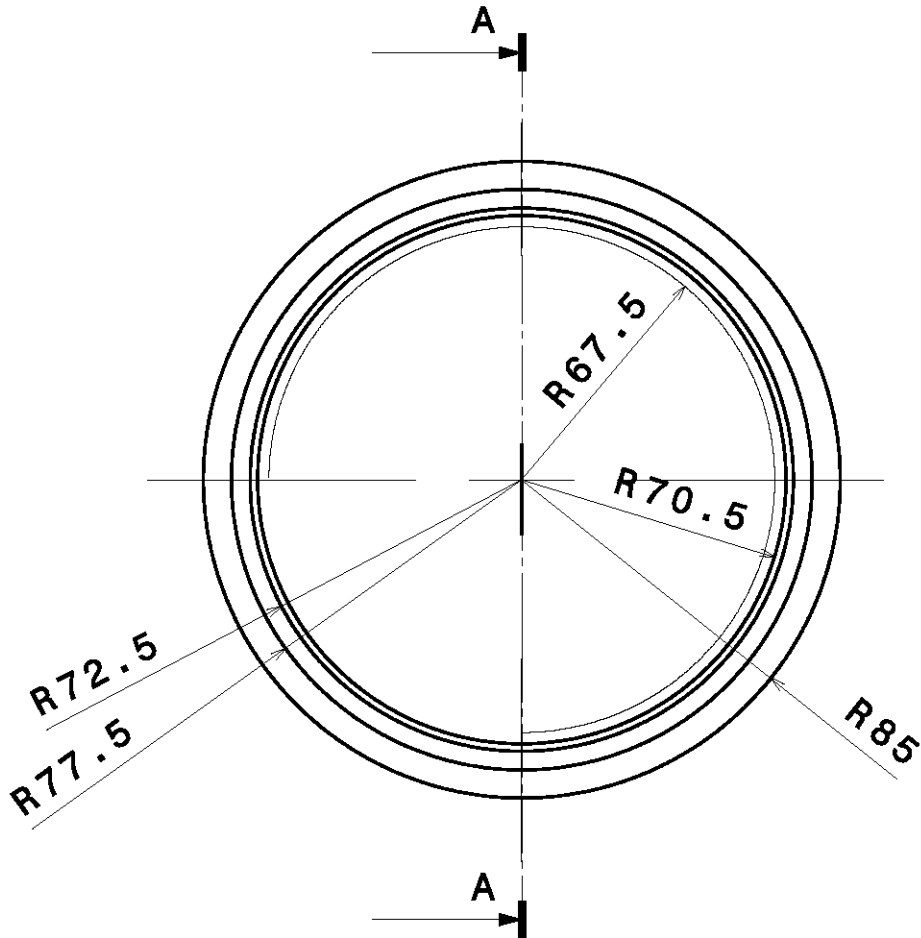
A

DESIGNED BY: Antonio Olmedilla		Ply Name	Colonne Cyclindrique	I	-
DATE: 7/11/2015		Material	PMMA	H	-
CHECKED BY: XXX		Direction	XXXX	G	-
DATE: XXX		Thickness	XXXX	F	-
SIZE A4		SequenceID	XXXX	E	-
SCALE 1:5		GroupID	XXXX	D	-
				C	-
				B	-
				A	-





DESIGNED BY: Antonio Olmedilla		Ply Name	Colonne Carrée	I	-
DATE: 7/11/2015		Material	PMMA	H	-
CHECKED BY: XXX		Direction	XXXX	G	-
DATE: XXX		Thickness	XXXX	F	-
SIZE A4		SequenceID	XXXX	E	-
SCALE 1:5	WEIGHT (kg)	GroupID	XXXX	D	-
				C	-
				B	-
				A	-



Section view A-A

DESIGNED BY: Antonio Olmedilla	Ply Name	Bouchon	I	-
DATE: 7/11/2015	Material	PVC	H	-
CHECKED BY: XXX	Direction	XXXX	G	-
DATE: XXX	Thickness	XXXX	F	-
SIZE A4	SequenceID	XXXX	E	-
SCALE 1:2	GroupID	XXXX	D	-
			C	-
			B	-
			A	-



D

C

B

A

4

4

3

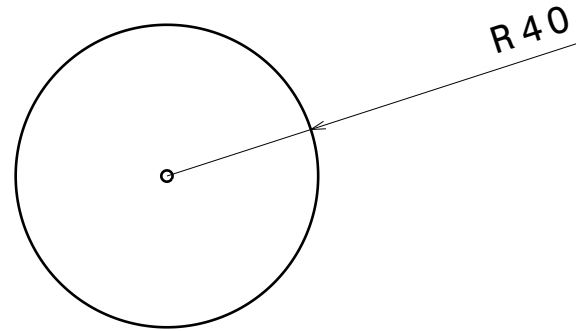
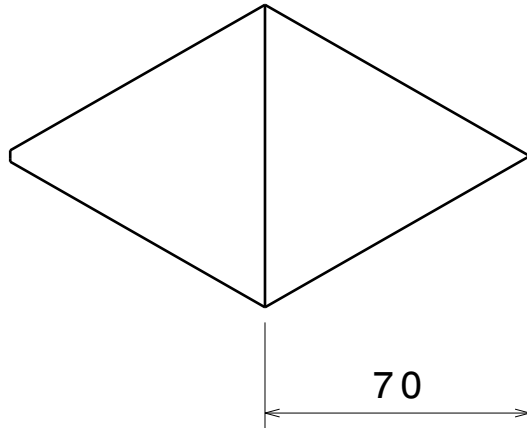
3

2

2

1

1



DESIGNED BY: Antonio Olmedilla		Ply Name	Conical_obstacle	I	-
DATE: 1/26/2016		Material	PVC	H	-
CHECKED BY: XXX		Direction	XXXX	G	-
DATE: XXX		Thickness	XXXX	F	-
SIZE A4		SequenceID	XXXX	E	-
SCALE 1:2	WEIGHT (kg) -	GroupID	XXXX	D	-
			C	-	
			B	-	
			A	-	

This drawing is our property; it can't be reproduced or communicated without our written agreement.

D

A

D

C

B

A

4

4

3

3

2

2

1

1

122

60

90

2

R 45

R 61

DESIGNED BY:

Antonio Olmedilla

DATE:

1/26/2016

CHECKED BY:

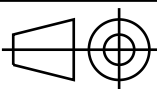
XXX

DATE:

XXX

SIZE

A4



SCALE

1:2

WEIGHT (kg)

-

		I	-
Material	PVC	H	-
Direction	XXXX	G	-
Thickness	XXXX	F	-
SequenceID	XXXX	E	-
GroupID	XXXX	D	-
		C	-
		B	-
		A	-

This drawing is our property; it can't be reproduced or communicated without our written agreement.

D

A

B.2 Friction coefficient of PAQC

The interparticle friction coefficient is an important parameter in order to understand the dry particle packing. A tribometer is used to characterize the polymer-polymer contact. The solid particles are manufactured in PAQC by additive manufacturing resulting a high rugosity surface state. Herein, two PAQC spherical particles (with identical surface roughness than the dendritic particles) are set in contact where one of them remains fixed and the other is rotating with an eccentric contact point (over 20% of diameter). A normal force of 5 N and constant rotation velocity are imposed. In this way, the time-evolution of the tangential force is measured and consequently the friction coefficient time-evolution.

In Fig. B.2 the resulting friction coefficient is plotted as function of time (green solid line) and fitted by means of a second-order response (blue dashed line). A peak is obtained when both surfaces enter in contact ($\mu_{fr} \approx 0.50$). Afterwards, the friction coefficient decreases until a steady value is reached ($\mu_{fr} \approx 0.18$) since the motion between both surfaces wears the surface rugosity.

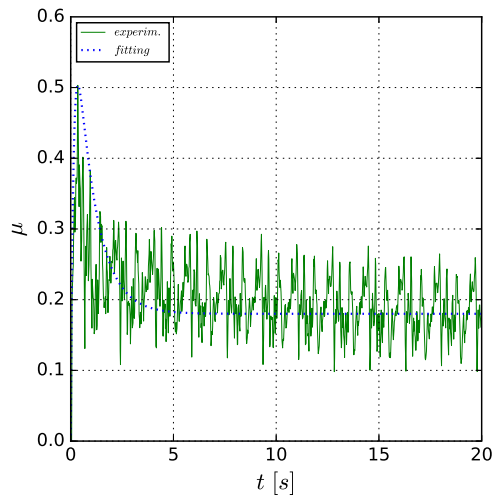


Figure B.2: PAQC-PAQC friction coefficient, μ_{fr} , vs time. The experimental tribometer data and a second-order fitting are shown in solid green and blue dotted lines, respectively.

In the dry packing phenomenon, the time of relative motion between two particle surface is thought to be relatively short (compared to the needed time to obtain the steady friction value). We assume that in the dry packing the surface roughness is not worn, therefore an interparticle friction coefficient of approximately 0.50 is used for both *static* and *dynamic* interparticle friction coefficients.

B.3 Theoretical sedimentation parameters

The theoretical Stokes number of the granular system for each fluid protocol is computed by $St = (\bar{\rho}_s \bar{d}_{eq} \bar{v}_s^{sed}) / (9\mu_f)$. In case of glycerol and water protocols, the limit sedimentation velocity is quickly reached. Assuming that the solid fraction of sedimentation is much lower than the solid packing fraction, $\phi_s^{sed} \ll \langle \phi_s \rangle_{\Omega_{pack}}$, the multi-particle influence on the drag is neglected, hence, \bar{v}_s^{sed} is given by the balance of apparent weight and drag for a single particle:

$$\bar{v}_s^{sed} = \left((4/3) C_D^{-1}(Re) \left(\frac{\bar{\rho}_s}{\rho_f} - 1 \right) g_o \bar{d}_{eq} \right)^{1/2} \quad (\text{B.1})$$

where the Reynolds number is given by $Re = (\rho_f \bar{d}_{eq} \bar{v}_s^{sed}) / (\mu_f)$ and the drag coefficient is computed assuming spherical geometry with the Oseen correction to Stokes drag coefficient when $Re < 5$, and the drag coefficient proposed in Ref. [Mikhailov and Freire, 2013] when $Re \geq 5$.

In case of settling in air, the grains do not reach the limit velocity in the column length. The granular sedimentation velocity previous to packing, \bar{v}_s^{sed} , is computed by Eq. B.2 with $h \approx 0.5m$. A similar velocity is obtained if the drag and buoyancy forces are maintained in the computation.

$$\bar{v}_s^{sed} = (2 g_o h)^{1/2} \quad (\text{B.2})$$

In Table B.1 the values of the fluid density, ρ_f , and the fluid dynamic viscosity, μ_f , are collected for each protocol.

Table B.1: Protocol properties, $T = 21^\circ$

Property	glycerol	glyc.-water	water	air
ρ_f [kg/m ³]	1262 [Cheng, 2008]	1201 [Cheng, 2008]	1000	1.2
μ_f [mPa.s]	1180 [Cheng, 2008]	50.4 (viscosimeter)	1.0	0.018

B.4 Average packing fraction measurement technique

The injection gate is intentionally designed for the packed granular system to form a convex top surface. Thereby, it is reasonable to use a revolution logic to estimate the occupied volume. In order to increase the accuracy a semi-revolution model is used: splitting the whole volume in a left and a right 180° semi-revolution volumetric elements of volumes $V_{1/2left}$ and $V_{1/2right}$. Each of the semi-revolution elements are composed by a semi-cylinder, of volume $V_{semi-cyl}$, and a upper semi-revolution volume based on a 2D profile, $V_{2D-prof}$. It is important to consider that in the taken photographs there is a depth deformation (deeper objects are slightly shrunken), so two scales are used: the wall scale, λ_w , and the center-of-vessel scale, λ_c , with $\lambda_w = \Delta H_{px}/\Delta H_{mm}$ and $\lambda_c = D_{px}/D_{mm}$. Where ΔH is a vertical reference length at the front wall and D is the vessel diameter. The sub-indexes px and mm indicate the unit of measurement of pixels and millimeters, respectively.

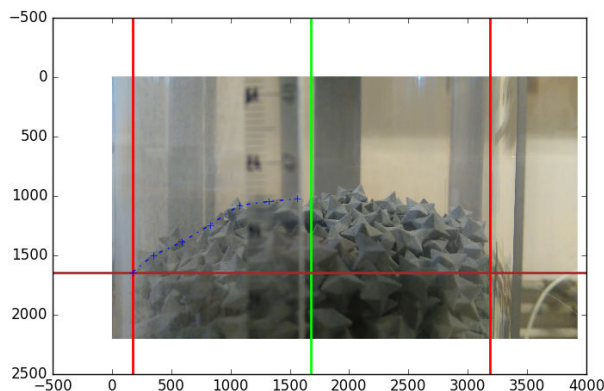


Figure B.3: Estimation of the total volume of the packed bed, $V_{\Omega_{pack}}$, from 2D image. Nonconvex dendrite grains in image. The horizontal and vertical axes are shown in pixels.

For each semi-revolution volume, we compute the semi-cylinder volume as $V_{semi-cyl} = \frac{\pi}{8} D^2 H_{semi-cyl}$, and later we compute the volume of the upper element, $V_{2D-prof}$, based on a 2D profile (see left blue profile in Fig. B.3) which is defined by N points whose radial and vertical coordinates are $\{r_i, z_i\}$ for $i \in (1, N)$. The pixel coordinates are converted into millimeters via λ_c . To compute the volume of the upper element, we discretize the upper element in N elements. The inner element, $i = 1$, has a circular section and a height of z_1 . The rest of the elements, $i = 2, N$, are characterized by a circular crown section defined by the radii $(r_{i-1} + r_i)/2$ and $(r_i + r_{i+1})/2$, and a height of z_i . We sum the volume of all these elements under the 2D profile:

$$V_{2D-prof} = \frac{\pi}{8} \sum_{i=2}^{N-1} (r_{i+1} - r_{i-1}) (r_{i+1} + r_{i-1} + 2r_i) z_i + (r_1 + r_2)^2 z_1 + [D^2 - (r_N + r_{N-1})^2] z_N \quad (\text{B.3})$$

Finally, we sum the volume of the four elements:

$$V_{\Omega_{pack}} = V_{1/2_{left}} + V_{1/2_{right}} = \{V_{semi-cyl} + V_{2D-prof}\}_{left} + \{V_{semi-cyl} + V_{2D-prof}\}_{right} \quad (\text{B.4})$$

The packing fraction experiment is repeated 10, 30 and 30 times for the glycerol, water and air protocols, respectively, for each collection of particles to obtain a mean and a standard deviation of the measured packing fraction. The measurement uncertainty of the packing fraction includes the uncertainties of the solid and the total volume: $\frac{\Delta\phi}{\phi} \approx \frac{\Delta V_s}{V_s} + \frac{\Delta V_{\Omega_{pack}}}{V_{\Omega_{pack}}}$, where ΔV_s and $\Delta V_{\Omega_{pack}}$ are the uncertainty in the solid and total volumes, respectively. The solid volume is given by the pycnometer uncertainty: $\frac{\Delta V_s}{V_s} \approx \frac{\Delta \rho_s}{\rho_s}$ and $\frac{\Delta V_{\Omega_{pack}}}{V_{\Omega_{pack}}}$ includes both the random character of the packing phenomenon and the systematic measurement error. We assume $\Delta V_{\Omega_{pack}}$ to be 2 standard deviations (level of confidence of 95%) of the total occupied volume of the experimental sample.

B.5 Sigmoidal model of fitting

We use a sigmoidal model of fitting for the influence of the packing hydrodynamic conditions on the packing, which is based on the Eqs. B.5, B.6 and B.7.

$$y(x) = y_0 + (y_1 - y_0) \left\{ 1 + e^{\lambda_{\Sigma} (\log_{10}(x) - \log_{10}(x_c))} \right\}^{-1} \quad (\text{B.5})$$

$$\log_{10}(x_c) = \frac{1}{2} (\log_{10}(x_1^*) + \log_{10}(x_0^*)) \quad (\text{B.6})$$

$$\lambda_{\Sigma} = \frac{2 \ln \left(\frac{\alpha}{1-\alpha} \right)}{\Delta x} \quad (\text{B.7})$$

where $\alpha = (y_0^* - y_0) / (y_1 - y_0) = (y_1 - y_1^*) / (y_1 - y_0)$ and $\Delta x = x_1^* - x_0^*$.

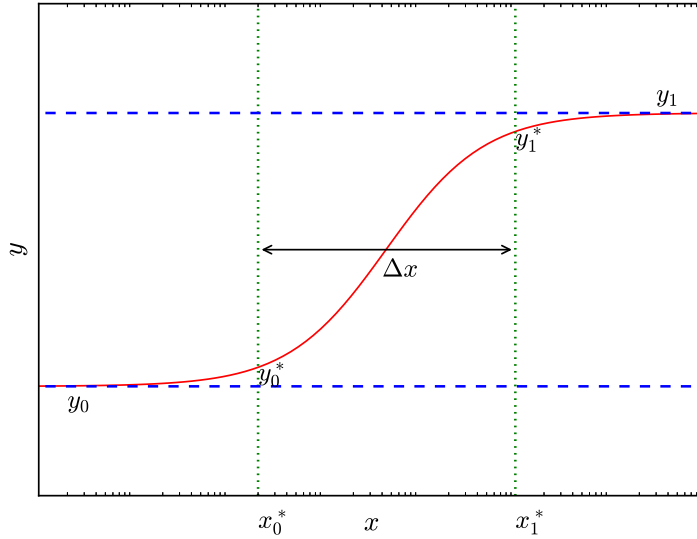


Figure B.4: Sigmoidal model $y = \Sigma(\log(x))$.

B.6 Particle contacts

To obtain the *contact number* and *contacting neighbors* (for non-spherical geometries) is not experimentally straightforward. In [Delaney et al., 2010] and [Jaoshvili et al., 2010]) an X-ray and MRI tomography system are used, respectively. Additionally, [Delaney et al., 2010] combines a tomography system with a DEM simulation tool to filter the mechanical contacts of a mono-disperse collection of spheres from the overall geometrical contacts.

Nonetheless, in case this thesis a tomography system to obtain the dendritic particle centers and orientations is not available. In this way, a simple technique to count the *geometrical contacts* is developed. The objective of this technique is that of obtaining an order of the *geometrical number of contacts* and *contacting neighbors* for a simply poured dry packing.

B.6.1 Description

Using a small recipient, we simply poured over 150 particles in it. Afterwards, we impregnate one dendrite in glue and dropped it over the previously packed particles. Now over 150 particles are simply poured over the impregnated particle covering it and packing around it. Finally, the cluster formed with the impregnated particle at the center is carefully extracted from the packing. In fig. B.5 the protocol (left) and particle cluster (right) are shown. Those particles attached to the impregnated particle (center of cluster) are counted, as well as, their double contacts with it. This operation is repeated 10 times to obtain the mean value and deviation. The obtained results are collected in table B.2. The same procedure is carried out for spheres with 5 tests.

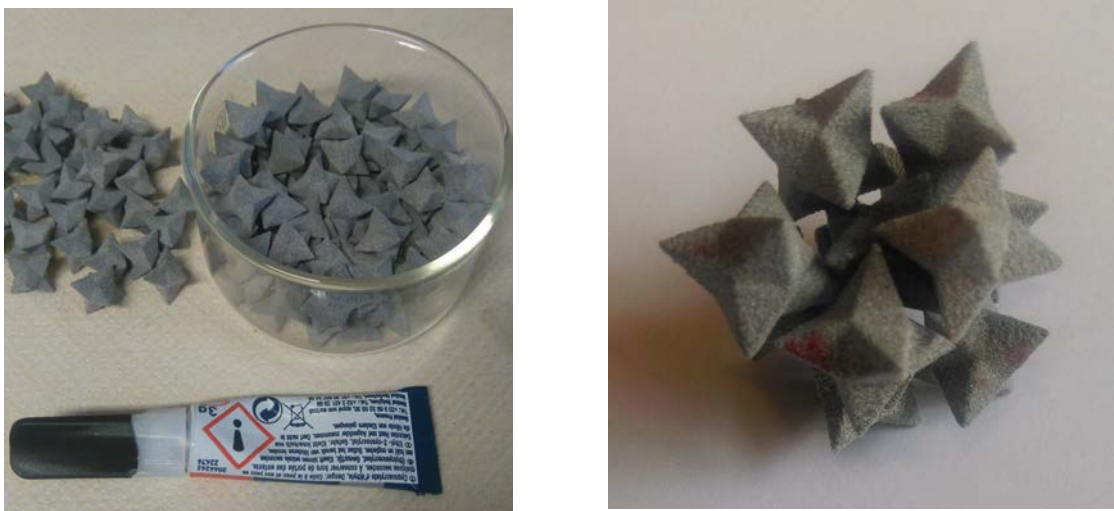


Figure B.5: Dendrite contact: protocol (left), formed cluster (right).

Table B.2: Dendritic envelope mechanical contacts, Z , and contacting neighbors, CN .

Z	9	5	7	8	5	8	8	7	8	8
CN	8	5	7	7	5	6	7	5	7	8

Table B.3: Spherical contacting neighbors, CN .

$Z = CN$	6	7	7	6	8
----------	---	---	---	---	---

In this way, for dendrites we obtained an average of 7.3 contacts with a sample standard deviation of 1.27 contacts. On the other hand, we obtain an average of 6.5 contacting particles with a deviation of 1.12 particles. Hence, in average there are $Z - cont. pt = 0.8$ double contacts per particle. The obtained contacts are thought to be *geometrical* since due to the glue those particles which are extremely close but without normal force at the contact can be attached and considered as contacts. Thereby, the number of mechanical contacts and mechanically contacting particles are ≤ 7.3 and ≤ 6.5 , respectively. In the case of spheres, we obtain the mean contact to be 6.8 whereas the sample standard deviation is 0.84 contacts. For spheres we obtain a slightly higher result than expected by 1 contact since by this protocol nearly touching particles are also attached by the glue, hence, $Z \leq 6.8$.

Assuming that the obtained packings are locally jammed, we consider, at least, 12 constraints per particle (isostaticity or hyperstaticity). In this way, 6.5 contacting particles generate 7.3 contacts which generate (at least) 12 linearly-independent constraints since the friction contacts can activate the tangential component and edge-edge, edge-surface or surface-surface contacts provide more that one constraint.

Appendix C

Mathematical support

C.1 Geometrical particle packing algorithm: flowchart

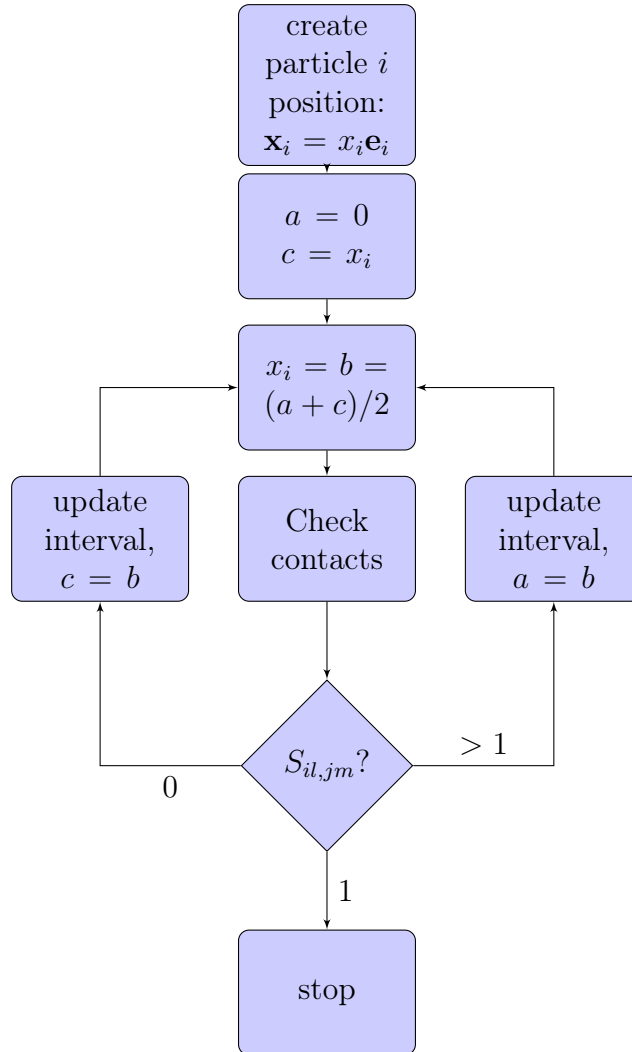


Figure C.1: Flowchart of the geometrical algorithm of particle packing. The steps to obtain the packing position of particle $i > 1$ based on a bisection method are shown. The position of the particle, \mathbf{x}_i , is expressed by the distance from the origin of the global reference frame in the direction of the unit vector \mathbf{e}_i . The bisection interval is defined by $[a, c]$. The parameter $S_{i,jm}$ indicates the number of marker pairs fulfilling the tolerance criterion between the particles i and j .

C.2 Random sequential addition algorithm: RSA

Herein this algorithm is defined in more detail. A rectangular prism domain which dimensions are L_x , L_y and L_z is used. Without loss of generality, the origin of that frame common to all particles can be defined at a corner of the domain, thus, the domain is defined as: $[0, L_x] \times [0, L_y] \times [0, L_z]$.

In this vein, N_{pt} particles will be generated in the domain. The position of the first particle is chosen randomly with a uniform probability distribution, where $\mathcal{U}[a, b]$ is the uniform probability distribution.

$$\mathbf{r}_1 = (x, y, z) / \{x : \mathcal{U}[0, L_x], y : \mathcal{U}[0, L_y], z : \mathcal{U}[0, L_z]\} \quad (\text{C.1})$$

For the rest of particles ($n \in [2, N_{pt}]$), see Eq. (C.2).

$$\mathbf{r}_n = (x, y, z) / \{x : \mathcal{U}[0, L_x], y : \mathcal{U}[0, L_y], z : \mathcal{U}[0, L_z]\} \text{ and} \\ \Omega_n \cap \left\{ \bigcup_{i=1}^{n-1} \Omega_i \right\} = \emptyset \quad (\text{C.2})$$

where Ω_n and Ω_i are the associated space regions to n -th and i -th particles (see Eq. (C.3) for n -th particle).

$$\Omega_n : (x, y, z) / (x - x_n)^2 + (y - y_n)^2 + (z - z_n)^2 \leq (l_{c_n}/2)^2 \quad (\text{C.3})$$

Moreover, a distinction needs to be made between initial positions in case of wall boundary conditions or periodicity boundary conditions. Thus, two different additional conditions are needed for the wall case and domain periodicity, Eq. (C.4) or Eq. (C.5), respectively.

$$\Omega_n \cap \partial\Omega = \emptyset, \quad \forall n \in [1, N_{pt}] \quad (\text{C.4})$$

$$\Omega_i|_{r,g} \cap \Omega_j|_{r,g} = \emptyset, \quad \forall i \in [1, N_{pt}], \quad \forall j \in [1, N_{pt}] / i \neq j \quad (\text{C.5})$$

where $\partial\Omega$ is the contour of the simulated domain. In Eq. (C.5), the sub-indexes r and g account for *real* and *ghost*, respectively. That is, the region of space occupied by a *real* i -th particle of any of its possible *ghosts* (see Sec. 4.3.7) cannot be occupied by a region of space $\Omega_j|_{r,g}$ associated to the j -th's particle itself of any of their ghosts.

C.3 Random orientation: Shoemaker algorithm

The particle initial quaternion components, $\hat{q}_o = [q_o, q_i, q_j, q_k]$, are computed following Eqs. C.6 and C.7.

$$\begin{cases} q_o = \sqrt{s_1} \cos(2\pi s_3) \\ q_i = \sqrt{1-s_1} \sin(2\pi s_2) \\ q_j = \sqrt{1-s_1} \cos(2\pi s_2) \\ q_k = \sqrt{s_1} \sin(2\pi s_3) \end{cases} \quad (\text{C.6})$$

where s_1 , s_2 and s_3 :

$$\begin{cases} s_1 : \mathcal{U}[0, 1] \\ s_2 : \mathcal{U}[0, 1] \\ s_3 : \mathcal{U}[0, 1] \end{cases} \quad (\text{C.7})$$

C.4 DEM numerical parameters

C.4.1 Low weight protocol

In this section, we show the criteria to select the linear stiffness, K_{eq} , the linear damping, C_{eq} , and the initial collision velocity, $\dot{\delta}_o$, for the low weight protocol. For this protocol, the selection of these numerical parameters is based on the acceleration of the DEM intergration of the granular system (reducing the computatinal time) and also maintaining a nil particle restitution coefficient, i.e. avoiding the rebounding.

From the *Linear Vibration Theory* it is known that the equation that describes the evolution of the overlap of a collision with time reads:

$$M_{eq} \frac{d^2\delta}{dt^2} + C_{eq} \frac{d\delta}{dt} + K_{eq}\delta = 0 \quad (\text{C.8})$$

with M_{eq} , C_{eq} and K_{eq} , the equivalent mass, damping and stiffness, respectively. In order to avoid the particle rebounding, a critical damping is chosen: $C_{eq} = 2\sqrt{M_{eq}K_{eq}}$. In a general case, the damping is related to the critical damping by the dimensionless parameter γ , $C_{eq} = 2\gamma\sqrt{M_{eq}K_{eq}}$. In this way, depending on the value of γ :

- $\gamma < 1$: oscillatory character of the collision, i.e. rebounding: $\delta(t) \propto \text{Re}(e^{(-|\lambda|+i\Omega)t})$.
- $\gamma \geq 1$: the linear dashpot element totally dissipates the elastic energy of the stiffness element during the contact: $\delta(t) \propto e^{-|\lambda|t}$.

With the critical damping condition, the solution of Eq. C.8 is given by:

$$\delta(t) = \dot{\delta}_o t e^{-\omega_o t} \quad (\text{C.9})$$

where ω_o is the natural frequency given by: $\omega_o = \sqrt{\frac{K_{eq}}{M_{eq}}}$.

The characteristic collision time between two particles reads:

$$t_{col} \approx \pi/\omega_o \quad (\text{C.10})$$

In the Discrete Element Method, the integration time step, Δt , must be n_t times shorter than the collision time in order to properly integrate the particle collision. The parameter n_t ranges from 25 up to 100 according to Ref. [Wachs et al., 2012a]. The integration time step reads:

$$\Delta t \approx \frac{t_{col}}{n_t} \quad (\text{C.11})$$

Now we present the numerical strategy that we have adopted in order to accelerate the DEM integration (especially in case of nonspherical particles), which consists of using a numerical particle stiffness much lower than the actual particle stiffness. Secondly, the opposite numerical strategy, which is appropriate to integrate the granular medium at quasi-static situations, is also presented.

- Decreasing the stiffness K_{eq} , maintaining the physical inertia (particle mass and inertia tensor): a new numerical fictitious stiffness is defined as: $K_{num} = K_{phys}/\beta$ where $\beta \gg 1$. In this way, the collision time is much larger and a larger integration time step is possible. The consequences of the reduction of stiffness is higher particle strains, i.e. a higher overlap.
- Increasing the particle physical mass, maintaining the physical stiffness [Christophe L. Martin, 2016]: a new numerical fictitious mass is defined as: $m_{num} = \beta m_{phys}$ where $\beta \gg 1$. Equivalently, the numerical stiffness of the collision is reduced. The consequence is that of obtaining a totally different trajectory than actual one. Useful in physical problems in which particle trajectory is not important but only the accurate reproduction of the particle overlap, i.e. quasi-static phenomena (e.g. powder sintering).

We compute the maximum overlap, $d\delta/dt = 0$, from Eq. C.9, obtaining:

$$\delta_{max} = \delta(t_{max}) = \frac{\dot{\delta}_o}{\omega_o} e^{-1} \quad (\text{C.12})$$

with $t_{max} = 1/\omega_o$. Finally, rewriting the previous equations:

$$\Delta t \approx \frac{\pi}{n_t} \sqrt{\frac{M_{eq}}{K_{num}}} \quad (\text{C.13})$$

$$\delta_{max} = \dot{\delta}_o e^{-1} \sqrt{\frac{M_{eq}}{K_{num}}} \quad (\text{C.14})$$

From Eq. C.13 we conclude that the higher the stiffness is, the lower is the integration time step. Normally, we can fix an integration time and obtain the numerical stiffness from this equation. Besides, using the maximum overlap during the collision as an input parameter and using the previously obtained value of the numerical stiffness, we use the Eq. C.16 to obtain the characteristic value of the initial velocity, $\dot{\delta}_o$. In the case of the low weight packing protocol, the acceleration applied to the particles is chosen to agree with $\dot{\delta}_o$.

C.4.2 Fluid protocol

In the fluid protocol, the particles sediment and pack with an important acceleration that ranges up to $0.1g_o$ where $g_o = 9.81 \text{ m/s}^2$. In this way, the choice of the numerical particle stiffness is not only based on the collision between two particles but also on the statics of the packed system.

In mechanical equilibrium, a particle is loaded with the apparent weight of the pile of particles above. Then, we can define a static overlap, given by $\delta_{st} = W_{pt}/K_{num}$, where W_{pt} is the apparent weight of the particles above. We compute it approximately as: $W_{pt} = N_{pt}(\pi/6)d_{eq}^3\Delta\rho g_o$, with N_{pt} the number of particles above.

We define a total maximum overlap by the superposition of the collision and static contributions:

$$\delta_{max}^{tot} = \dot{\delta}_o e^{-1} \sqrt{\frac{M_{eq}}{K_{num}}} + N_{pt}(\pi/6)d_{eq}^3\Delta\rho g_o/K_{num} \quad (\text{C.15})$$

We choose K_{num} in order to minimize the value of δ_{max}^{tot} and considering that the time step increases with the stiffness, as previously seen:

$$\Delta t \approx \frac{\pi}{n_t} \sqrt{\frac{M_{eq}}{K_{num}}} \quad (\text{C.16})$$

C.5 Polydispersity: mathematical relations

We are interested to develop a correlation between the average packing fraction of a collection of polydisperse particles with polydispersity, for low values of polydispersity. Next assumptions are considered:

- Fixed number of particles of the collection, N_{pt} .
- Large collection of particles.
- Symmetric size distribution of d_{eq} .

We expand by *Maclaurin series* the average packing fraction of the collection as a function of polydispersity:

$$\phi(\delta_p) = \phi(\delta_p = 0) + \left(\frac{d\phi}{d\delta_p} \right)_{\delta_p=0} \delta_p + \frac{1}{2} \left(\frac{d^2\phi}{d\delta_p^2} \right)_{\delta_p=0} \delta_p^2 + o(\delta_p^3) \quad (\text{C.17})$$

The term $\phi(\delta_p = 0)$ is the average packing fraction of the monodisperse particle collection, ϕ_0 . To compute the first derivative of the packing fraction with polydispersity, we assume a dependency of the solid volume of the collection and the total occupied volume of the collection on the polydispersity, i.e. $\phi(\delta_p) = V_s(\delta_p)/V_t(\delta_p)$. Then, we compute the first and second derivatives:

$$\left(\frac{d\phi}{d\delta_p} \right)_{\delta_p=0} = \phi_0 \left(\frac{d\tilde{V}_s}{d\delta_p} \right)_{\delta_p=0} - \phi_0^2 \left(\frac{d\tilde{V}_t}{d\delta_p} \right)_{\delta_p=0}, \quad (\text{C.18})$$

$$\left(\frac{d^2\phi}{d\delta_p^2} \right)_{\delta_p=0} = \phi_0 \left(\frac{d^2\tilde{V}_s}{d\delta_p^2} \right)_{\delta_p=0} - \phi_0^2 \left(\frac{d^2\tilde{V}_t}{d\delta_p^2} \right)_{\delta_p=0}, \quad (\text{C.19})$$

where $\tilde{V}_s = V_s/V_{s_0}$ and $\tilde{V}_t = V_t/V_{s_0}$. V_{s_0} is the solid volume of the monodisperse collection of particles.

To compute these derivatives of the solid volume with polydispersity, we relate the solid volume of the collection to the moments of the particle-size distribution (see Eq. C.25), knowing that d_{eq} follows a distribution whose mean value is d_{eq_0} (the equivalent particle diameter in the monodisperse case) and whose first, second and third central moments are $E[d_{eq} - d_{eq_0}] = 0$, $E[(d_{eq} - d_{eq_0})^2] = \sigma_p^2$ and $E[(d_{eq} - d_{eq_0})^3] = S_p\sigma_p^3$, respectively. Where σ_p and S_p are the *standard-deviation* and *skewness* of the particle size-distribution.

$$\tilde{V}_s = \frac{V_s}{V_{s_0}} = \frac{(\pi/6)N_{pt}d_{eq}^3}{(\pi/6)N_{pt}d_{eq_0}^3} \quad (\text{C.20})$$

$$\tilde{V}_s = \left(\frac{d_{eq}}{d_{eq_0}} \right)^3 = \left(1 + \frac{d_{eq} - d_{eq_0}}{d_{eq_0}} \right)^3 \quad (\text{C.21})$$

So we develop by means of *Newton's binomial*:

$$\tilde{V}_s = 1 + 3 \left(\frac{d_{eq} - d_{eq_0}}{d_{eq_0}} \right) + 3 \left(\frac{d_{eq} - d_{eq_0}}{d_{eq_0}} \right)^2 + \left(\frac{d_{eq} - d_{eq_0}}{d_{eq_0}} \right)^3 \quad (\text{C.22})$$

Since we assume that the systems are formed by a large number of grains, we relate the behavior of the system solid volume tendency with the polydispersity by means of the expectancy. E is the expectation operator.

$$\tilde{V}_s \approx E \left(1 + 3 \left(\frac{d_{eq} - d_{eq0}}{d_{eq0}} \right) + 3 \left(\frac{d_{eq} - d_{eq0}}{d_{eq0}} \right)^2 + \left(\frac{d_{eq} - d_{eq0}}{d_{eq0}} \right)^3 \right) \quad (\text{C.23})$$

$$\tilde{V}_s \approx 1 + \frac{3}{d_{eq0}} E [d_{eq} - d_{eq0}] + \frac{3}{d_{eq0}^2} E [(d_{eq} - d_{eq0})^2] + \frac{1}{d_{eq0}^3} E [(d_{eq} - d_{eq0})^3] \quad (\text{C.24})$$

$$\tilde{V}_s \approx E (\tilde{V}_s) = 1 + 3 \delta_p^2 + \delta_p^3 S_p \quad (\text{C.25})$$

And assuming the property of symmetry of the distribution, the skewness is nil:

$$\tilde{V}_s \approx E (\tilde{V}_s) = 1 + 3 \delta_p^2 \quad (\text{C.26})$$

In this way, we obtain:

$$\left(\frac{d\tilde{V}_s}{d\delta_p} \right)_{\delta_p=0} = 0 \quad (\text{C.27})$$

$$\left(\frac{d^2\tilde{V}_s}{d\delta_p^2} \right)_{\delta_p=0} = 6 \quad (\text{C.28})$$

We define \tilde{V}_t as a function of polydispersity with a polynomial:

$$\tilde{V}_t = \frac{1}{\phi_0} (1 + a_{V_t} \delta_p + b_{V_t} \delta_p^2) \quad (\text{C.29})$$

We rewrite Eq. C.17:

$$\frac{\phi(\delta_p)}{\phi_0} = 1 - a_{V_t} \delta_p + (3 - v_{V_t}) \delta_p^2 + o(\delta_p^3) \quad (\text{C.30})$$

C.6 Initial conditions

Table C.1: Influence of initial conditions on the packing parameters. Left: 10 simulation spherical results of packing fraction (ϕ^{sph}) and mechanical contacts (Z^{sph}). Right: 10 simulation dendritic results of packing fraction (ϕ^{den}), mechanical contacts (Z^{den}) and contacting neighbors (CN^{den}).

Simulation	ϕ^{sph} [%]	Z^{sph}	ϕ^{den} [%]	Z^{den}	CN^{den}
0	64.26	5.83	41.61	8.25	5.79
1	63.95	5.66	40.85	7.14	5.59
2	64.18	5.87	40.75	8.38	5.71
3	64.21	5.75	40.12	8.24	5.58
4	64.35	5.61	41.66	8.29	5.65
5	63.88	5.60	41.02	9.76	5.95
6	63.85	5.77	41.18	8.26	5.83
7	64.04	5.81	42.20	8.35	5.52
8	64.38	5.83	41.09	8.01	5.54
9	64.08	5.56	40.35	8.14	5.95

Appendix D

DEM simulations

Herein the time-evolution 3D and 2D postprocessings of the deposition and packing DEM simulations carried out by the *low inertia-to-dissipation protocol* are included. All particles are frictionless and noncohesive with a low vertical acceleration as a driving force of $a = 10^{-5}g_o$. In this way the particles achieve collision velocities up to 10mm/s .

Among the included geometries:

- Spherical.
- Dendritic (45° , 60° and 90°).
- Globular ($\xi = 1.0$).
- Ellipsoidal ($1.25 : 0.8 : 0.8$).

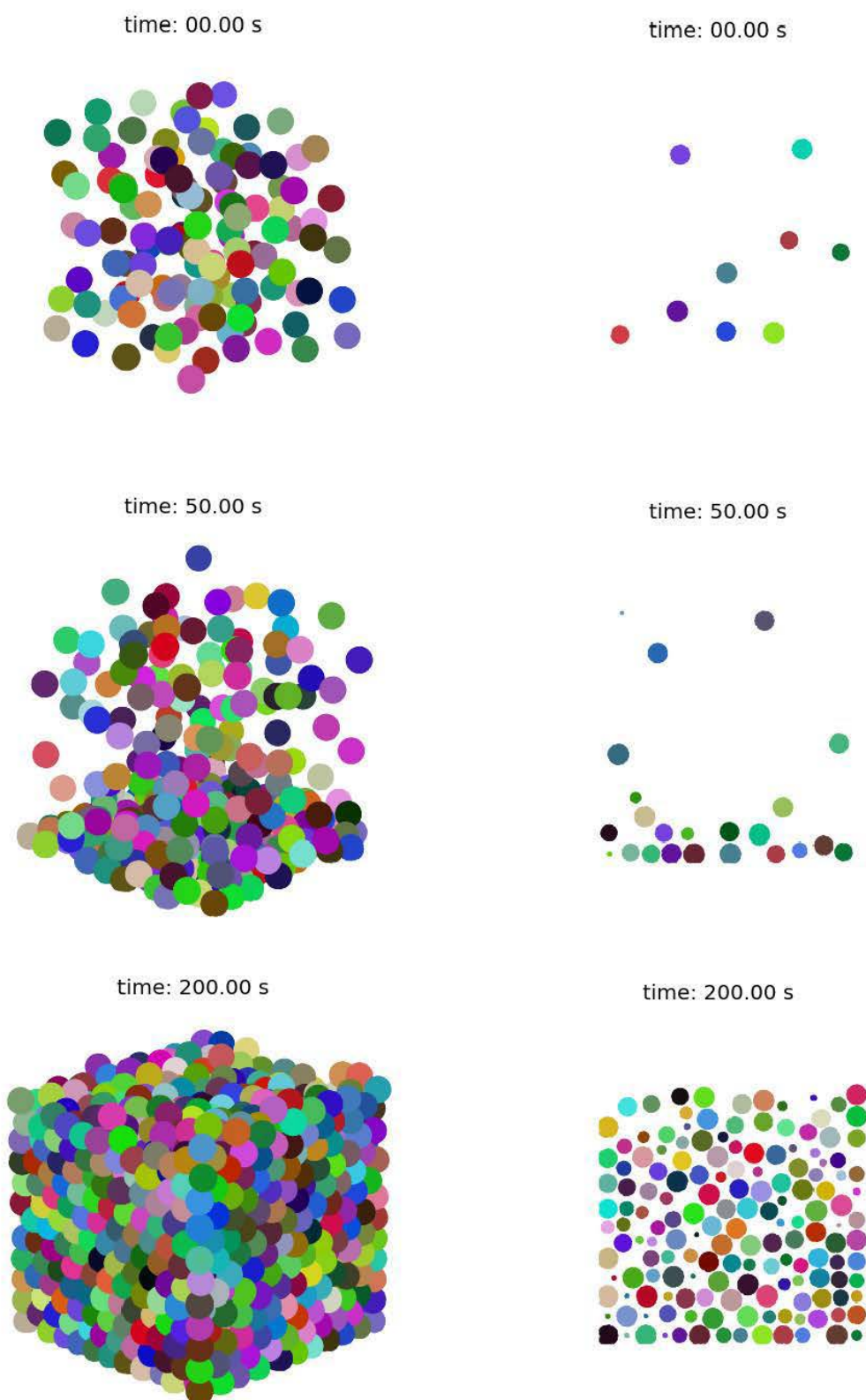


Figure D.1: Visual post-processing of 2000 spheres packing by means of the low inertia-to-dissipation vertical acceleration protocol: 3D and 2D at left and right, respectively; for the packing evolution at times 0, 50 and 200 s.

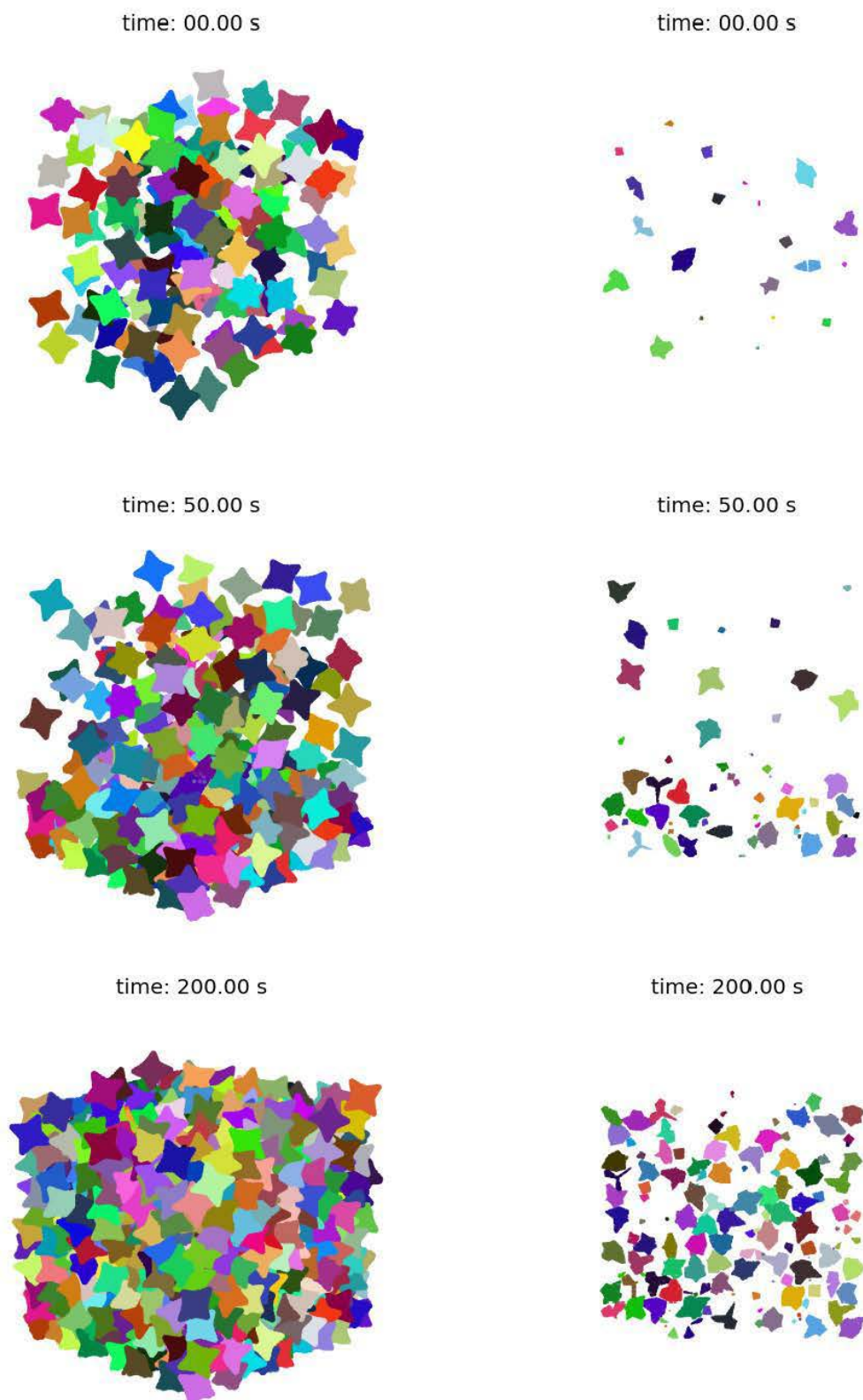


Figure D.2: Visual post-processing of 1000 dendritic envelopes 45° packing by means of the low inertia-to-dissipation vertical acceleration protocol: 3D and 2D at left and right, respectively; for the packing evolution at times 0, 50 and 200 s.

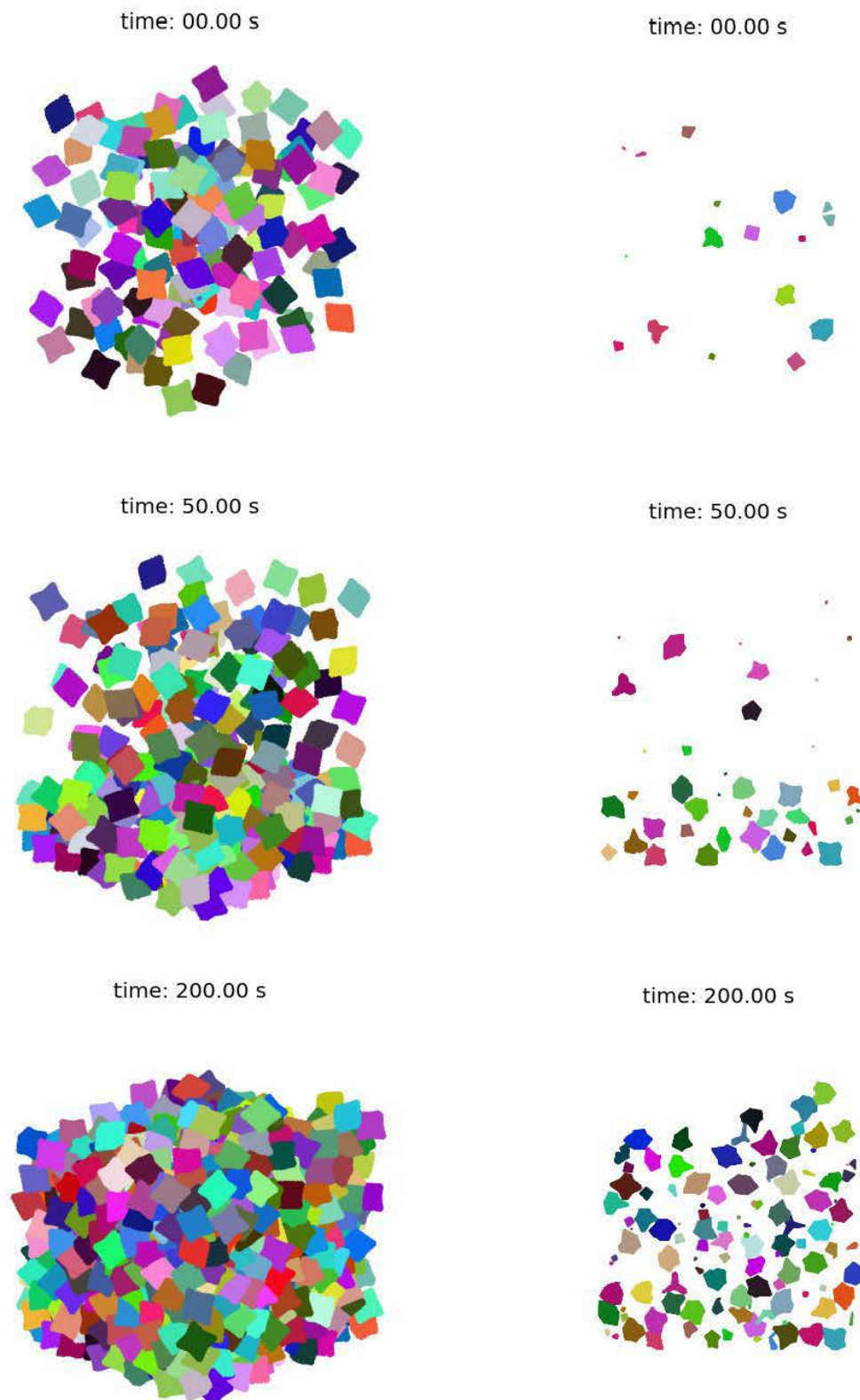


Figure D.3: Visual post-processing of 1000 dendritic envelopes 60° packing by means of the low inertia-to-dissipation vertical acceleration protocol: 3D and 2D at left and right, respectively; for the packing evolution at times 0, 50 and 200 s.

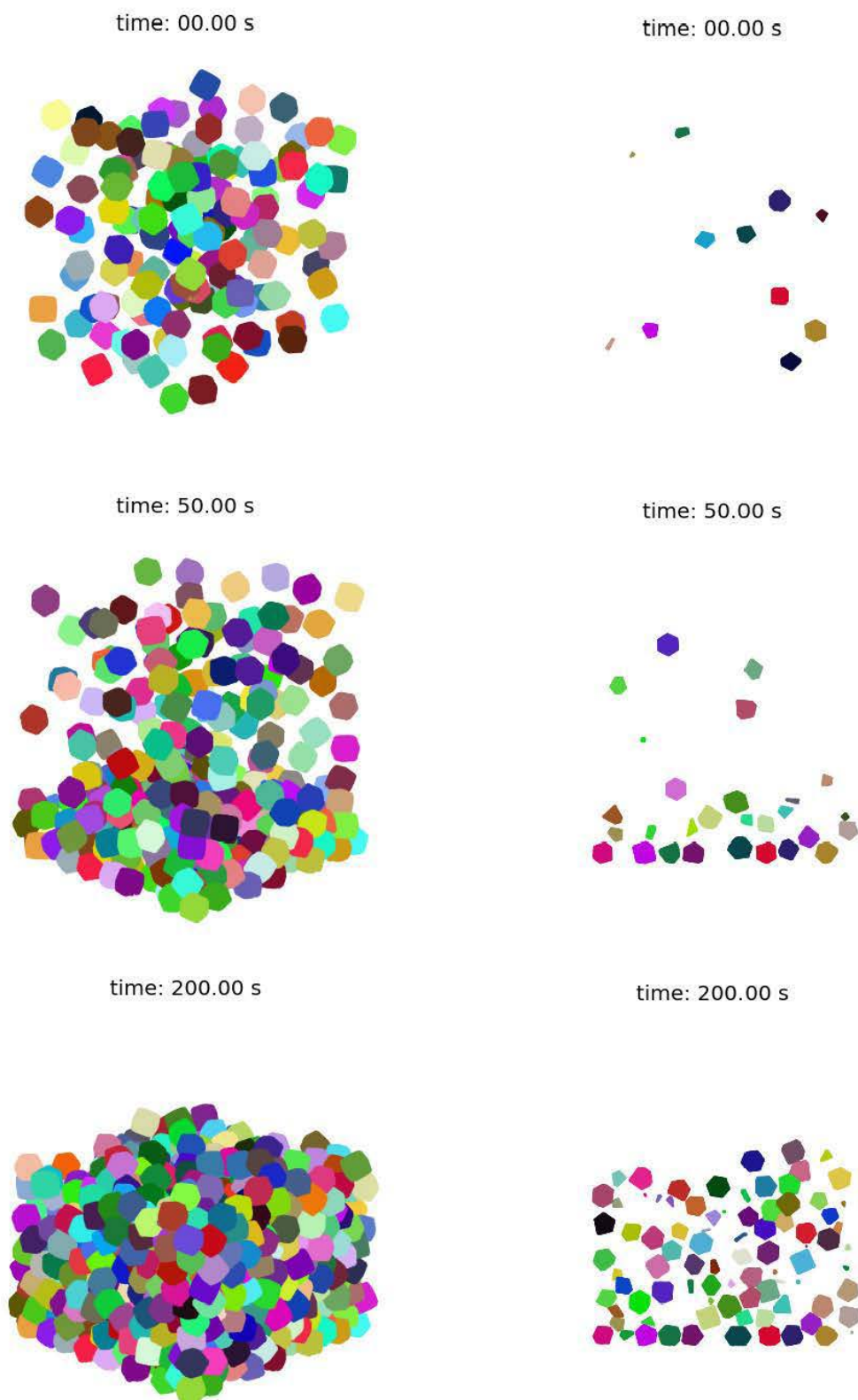


Figure D.4: Visual post-processing of 1000 dendritic envelopes 90° packing by means of the low inertia-to-dissipation vertical acceleration protocol: 3D and 2D at left and right, respectively; for the packing evolution at times 0, 50 and 200 s.

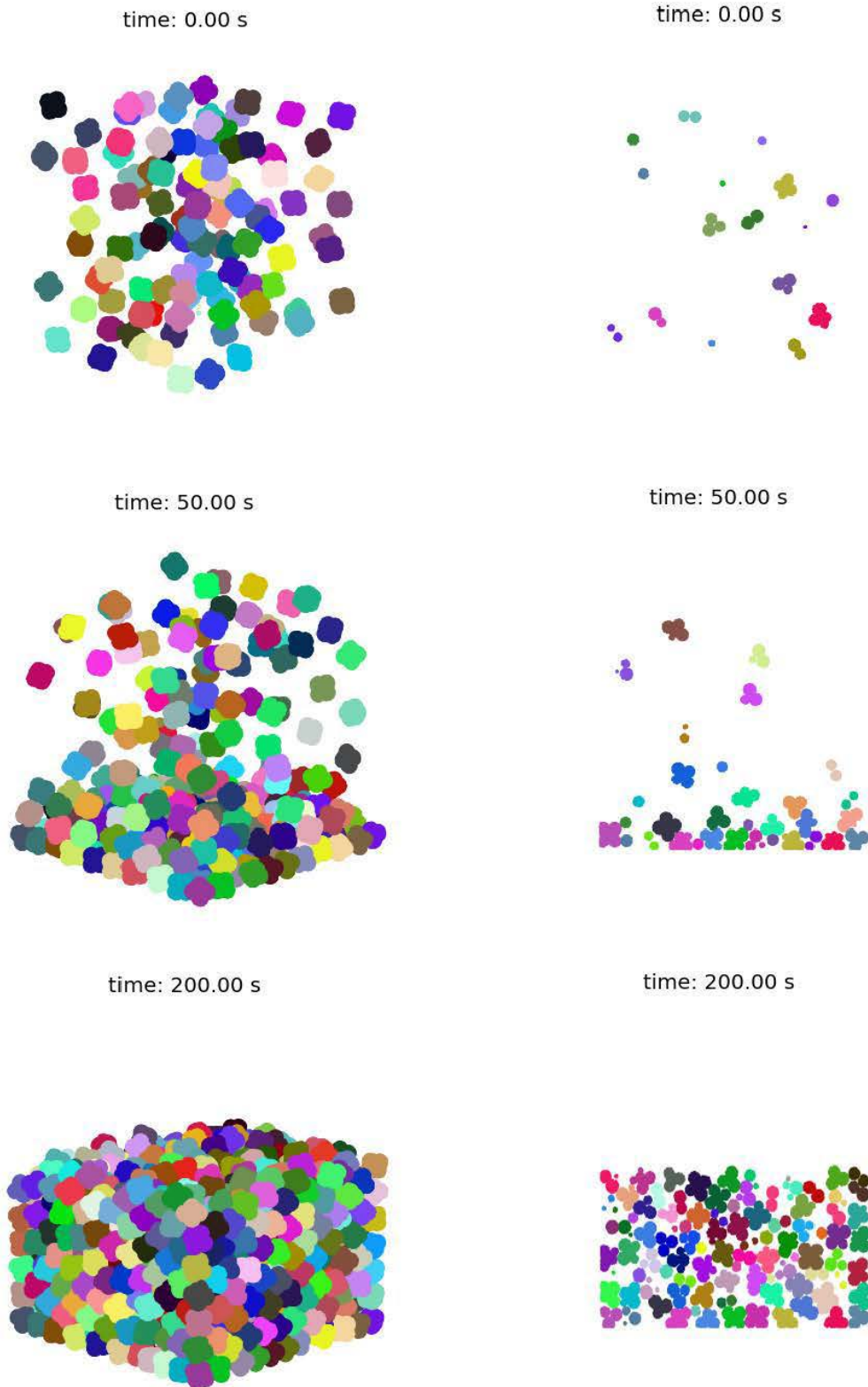


Figure D.5: Visual post-processing of 1000 globular envelopes $\xi = 1.0$ packing by means of the low inertia-to-dissipation vertical acceleration protocol: 3D and 2D at left and right, respectively; for the packing evolution at times 0, 50 and 200 s.

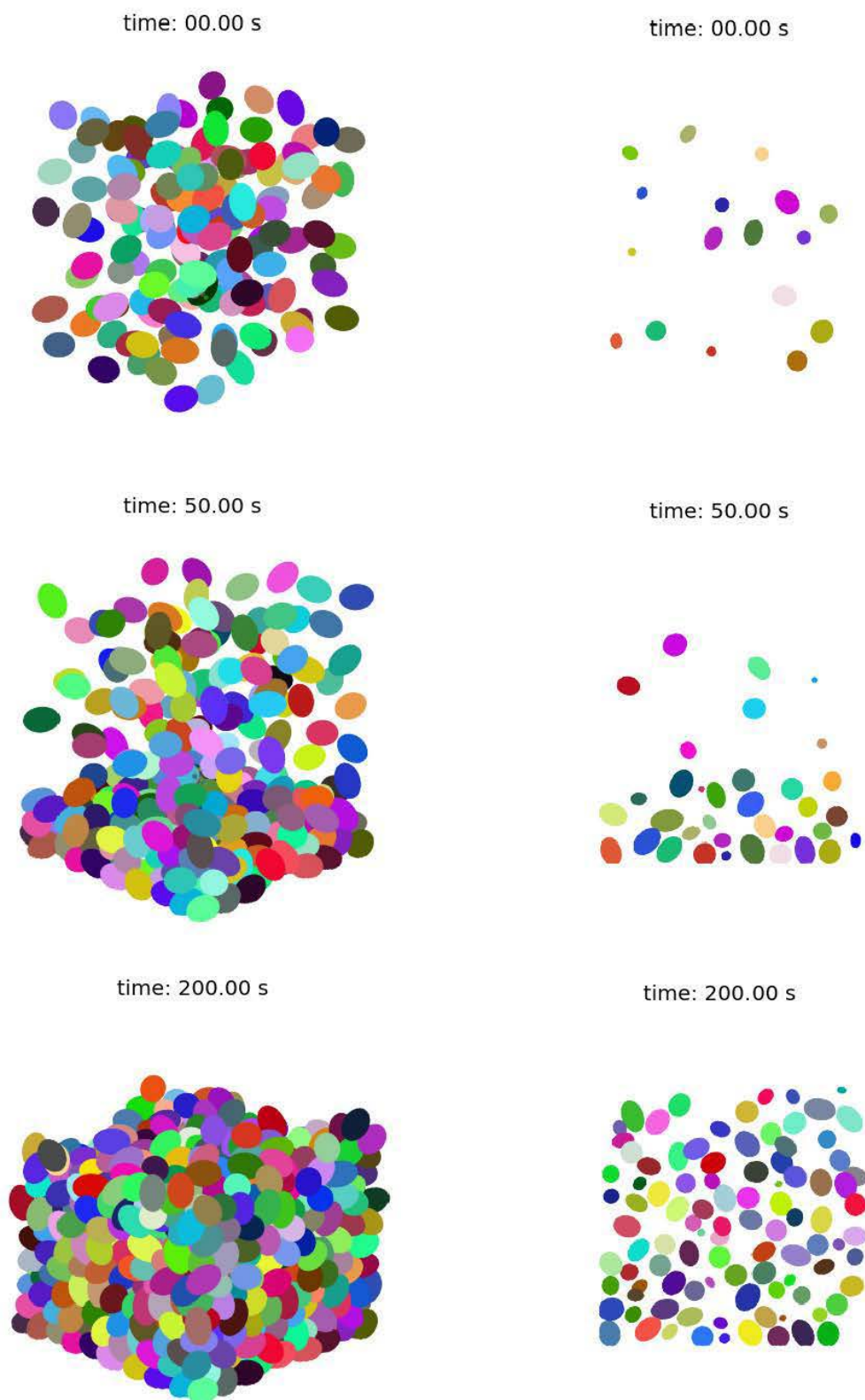


Figure D.6: Visual post-processing of 1000 ellipsoids $1.25 : 0.8 : 0.8$ packing by means of the low inertia-to-dissipation vertical acceleration protocol: 3D and 2D at left and right, respectively; for the packing evolution at times 0, 50 and 200 s.

Bibliography

- [Afkhani et al., 2015] Afkhani, M., Hassanpour, A., Fairweather, M., and Njobuenwu, D. O. (2015). Fully coupled les-dem of particle interaction and agglomeration in a turbulent channel flow. *Computers & Chemical Engineering*, 78:24–38.
- [Appolaire et al., 1999] Appolaire, B., Albert, V., Combeau, H., and Lesoult, G. (1999). Experimental study of free growth of equiaxed nh4cl crystals settling in undercooled nh4cl-h2o melts. *ISIJ international*, 39(3):263–270.
- [Appolaire et al., 2008] Appolaire, B., Combeau, H., and Lesoult, G. (2008). Modeling of equiaxed growth in multicomponent alloys accounting for convection and for the globular/dendritic morphological transition. *Materials Science and Engineering: A*, 487(1):33–45.
- [Aste and Di Matteo, 2008] Aste, T. and Di Matteo, T. (2008). Emergence of gamma distributions in granular materials and packing models. *Physical Review E*, 77(2):021309.
- [Aste et al., 2007] Aste, T., Di Matteo, T., Saadatfar, M., Senden, T. J., Schröter, M., and Swinney, H. L. (2007). An invariant distribution in static granular media. *EPL (Europhysics Letters)*, 79(2):24003.
- [ASTM, 2000] ASTM, D. (2000). 854-00 “standard test method for specific gravity of soil solids by water pycnometer.”. *American Society for Testing and Materials. Annual book of ASTM Standards*, 4:02.
- [Aussillous et al., 2013] Aussillous, P., Chauchat, J., Pailha, M., Médale, M., and Guazzelli, É. (2013). Investigation of the mobile granular layer in bedload transport by laminar shearing flows. *Journal of Fluid Mechanics*, 736:594–615.
- [Auwerda et al., 2010] Auwerda, G., Kloosterman, J., Winkelman, A., Groen, J., and Van Dijk, V. (2010). Comparison of experiments and calculations of void fraction distributions in randomly stacked pebble beds. *PHYSOR 2010-Advances in Reactor Physics to Power the Nuclear Renaissance, Pittsburgh, Pennsylvania, USA*, pages 9–14.
- [Baker and Kudrolli, 2010] Baker, J. and Kudrolli, A. (2010). Maximum and minimum stable random packings of platonic solids. *Physical Review E*, 82(6):061304.

- [Barés et al., 2017] Barés, J., Zhao, Y., Renouf, M., Dierichs, K., and Behringer, R. (2017). Structure of hexapod 3d packings: understanding the global stability from the local organization. In *Powders and Grains 2017*.
- [Berthier, 2011] Berthier, L. (2011). Entre géométrie et physique statistique: structure d'un empilement désordonné. *Images de la Physique, 2011*, pages 28–34.
- [Brenner, 1961] Brenner, H. (1961). The slow motion of a sphere through a viscous fluid towards a plane surface. *Chemical engineering science*, 16(3-4):242–251.
- [Cheng, 2008] Cheng, N.-S. (2008). Formula for the viscosity of a glycerol-water mixture. *Industrial & engineering chemistry research*, 47(9):3285–3288.
- [Christophe L. Martin, 2016] Christophe L. Martin (2016). Mechanics of Materials with Discrete Element Simulations. <http://simap.grenoble-inp.fr/gpm2/m-christophe-martin--430244.kjsp>. Online; accessed March 2016.
- [Combeau et al., 2009] Combeau, H., Založnik, M., Hans, S., and Richey, P. E. (2009). Prediction of macrosegregation in steel ingots: Influence of the motion and the morphology of equiaxed grains. *Metallurgical and materials transactions B*, 40(3):289–304.
- [Cox and Brenner, 1967] Cox, R. G. and Brenner, H. (1967). The slow motion of a sphere through a viscous fluid towards a plane surface—ii small gap widths, including inertial effects. *Chemical Engineering Science*, 22(12):1753–1777.
- [Dantzig and Rappaz, 2009] Dantzig, J. A. and Rappaz, M. (2009). *Solidification*. EPFL Press, 1st edition.
- [Davis et al., 1986] Davis, R. H., Serayssol, J.-M., and Hinch, E. (1986). The elastohydrodynamic collision of two spheres. *Journal of Fluid Mechanics*, 163:479–497.
- [de Moraes Franklin and de Andrade, 2015] de Moraes Franklin, E. and de Andrade, N. S. (2015). Granular flows in pressurized silos: Janssen effect versus hydrostatic pressure.
- [Delaney et al., 2010] Delaney, G. W., Di Matteo, T., and Aste, T. (2010). Combining tomographic imaging and dem simulations to investigate the structure of experimental sphere packings. *Soft Matter*, 6(13):2992–3006.
- [Delaney et al., 2011] Delaney, G. W., Hilton, J. E., and Cleary, P. W. (2011). Defining random loose packing for nonspherical grains. *Phys. Rev. E*, 83:051305.
- [Desmond and Weeks, 2009] Desmond, K. W. and Weeks, E. R. (2009). Random close packing of disks and spheres in confined geometries. *Phys. Rev. E*, 80:051305.
- [Desmond and Weeks, 2014] Desmond, K. W. and Weeks, E. R. (2014). Influence of particle size distribution on random close packing of spheres. *Physical Review E*, 90(2):022204.

-
- [Djurdjevic et al., 2012] Djurdjevic, M., Sokolowski, J., and Odanovic, Z. (2012). Determination of dendrite coherency point characteristics using first derivative curve versus temperature. *Journal of thermal analysis and calorimetry*, 109(2):875–882.
- [Donev, 2006] Donev, A. (2006). *Jammed packings of hard particles*. PhD thesis, Princeton University.
- [Donev et al., 2006] Donev, A., Torquato, S., Stillinger, F., and Connelly, R. (2006). Hypostatic jammed packings of nonspherical hard particles: Ellipses and ellipsoids. Technical report.
- [Dong et al., 2012] Dong, K., Yang, R., Zou, R., and Yu, A. (2012). Settling of particles in liquids: effects of material properties. *AIChE Journal*, 58(5):1409–1421.
- [Farrell et al., 2010] Farrell, G. R., Martini, K. M., and Menon, N. (2010). Loose packings of frictional spheres. *Soft Matter*, 6(13):2925–2930.
- [Faure et al., 2009] Faure, S., Lefebvre-Lepot, A., and Semin, B. (2009). Dynamic numerical investigation of random packing for spherical and nonconvex particles. In *ESAIM: Proceedings*, volume 28, pages 13–32. EDP Sciences.
- [Frankel and Acrivos, 1967] Frankel, N. and Acrivos, A. (1967). On the viscosity of a concentrated suspension of solid spheres. *Chemical Engineering Science*, 22(6):847–853.
- [Fu et al., 2017] Fu, X., Yao, Z., and Zhang, X. (2017). Numerical simulation of polygonal particles moving in incompressible viscous fluids. *Particuology*, 31:140–151.
- [García et al., 2011] García, X., Pavlidis, D., Gorman, G. J., Gomes, J. L., Piggott, M. D., Aristodemou, E., Mindel, J., Latham, J.-P., Pain, C. C., and ApSimon, H. (2011). A two-phase adaptive finite element method for solid–fluid coupling in complex geometries. *International Journal for Numerical Methods in Fluids*, 66(1):82–96.
- [Gerardin et al., 2001] Gerardin, S., Combeau, H., and Lesoult, G. (2001). Étude de l’effet du mouvement relatif cristal/liquide sur la croissance d’un cristal dendritique dans un liquide en surfusion. *Le Journal de Physique IV*, 11(PR6):Pr6–143.
- [Geuzaine and Remacle, 2009] Geuzaine, C. and Remacle, J.-F. (2009). Gmsh: A 3-d finite element mesh generator with built-in pre-and post-processing facilities. *International Journal for Numerical Methods in Engineering*, 79(11):1309–1331.
- [Gibbs et al., 2015] Gibbs, J., Mohan, K. A., Gulsoy, E., Shahani, A., Xiao, X., Bouman, C., De Graef, M., and Voorhees, P. (2015). The three-dimensional morphology of growing dendrites. *Scientific reports*, 5:11824.
- [Harada et al., 2000] Harada, S., Tanaka, T., and Tsuji, Y. (2000). Fluid force acting on a falling particle toward a plane wall. *Ret*, 6:25–8.

- [Heyvaert, 2015] Heyvaert, L. (2015). *Modélisation de la formation des structures et des microporosités durant la solidification d’alliages d’aluminium*. PhD thesis, Université de Lorraine.
- [Heyvaert et al., 2017] Heyvaert, L., Bedel, M., Založnik, M., and Combeau, H. (2017). Modeling of the Coupling of Microstructure and Macrosegregation in a Direct Chill Cast Al-Cu Billet. *Metallurgical and Materials Transactions A*, in press.
- [Higuti, 1961] Higuti, I. (1961). A statistical study of random packing of unequal spheres. *Annals of the Institute of Statistical Mathematics*, 12(3):257–271.
- [Izard et al., 2013] Izard, E., BONOMETTI, T., and LACAZE, L. (2013). Couplage ibm/dem pour la modélisation des milieux granulaires dans un fluide. *21ème Congrès Français de Mécanique, 26 au 30 août 2013, Bordeaux, France (FR)*.
- [Izard et al., 2014] Izard, E., Bonometti, T., and Lacaze, L. (2014). Modelling the dynamics of a sphere approaching and bouncing on a wall in a viscous fluid. *Journal of Fluid Mechanics*, 747:422–446.
- [Jackson and Hunt, 1965] Jackson, K. and Hunt, J. (1965). Transparent compounds that freeze like metals. *Acta Metallurgica*, 13(11):1212–1215.
- [Jackson et al., 1966] Jackson, K., Hunt, J., Uhlmann, D., and Seward, T. (1966). On origin of equiaxed zone in castings. *Transactions of the Metallurgical Society of AIME*, 236(2):149.
- [Jaoshvili et al., 2010] Jaoshvili, A., Esakia, A., Porrati, M., and Chaikin, P. M. (2010). Experiments on the random packing of tetrahedral dice. *Phys. Rev. Lett.*, 104:185501.
- [Jerkins et al., 2008] Jerkins, M., Schröter, M., Swinney, H. L., Senden, T. J., Saadatfar, M., and Aste, T. (2008). Onset of mechanical stability in random packings of frictional spheres. *Phys. Rev. Lett.*, 101:018301.
- [Jiao et al., 2009] Jiao, Y., Stillinger, F., and Torquato, S. (2009). Optimal packings of supe in this way, the pressure profile is not linear with the stocked particle height but it tends asymptotically to a saturation pressure.rballs. *Physical Review E*, 79(4):041309.
- [Kenzari et al., 2014] Kenzari, S., Bonina, D., Degiovanni, A., Dubois, J.-M., and Fournée, V. (2014). Quasicrystal-polymer composites for additive manufacturing technology. *Acta Physica Polonica A*, 126(2):449–452.
- [Kolonko et al., 2010] Kolonko, M., Raschdorf, S., and Wäsch, D. (2010). A hierarchical approach to simulate the packing density of particle mixtures on a computer. *Granular Matter*, 12(6):629–643.
- [Lecoq et al., 2004] Lecoq, N., Anthore, R., Cichocki, B., Szymczak, P., and Feuillebois, F. (2004). Drag force on a sphere moving towards a corrugated wall. *Journal of Fluid Mechanics*, 513:247–264.

-
- [Leith, 1987] Leith, D. (1987). Drag on nonspherical objects. *Aerosol science and technology*, 6(2):153–161.
- [Leriché, 2015] Leriché, N. (2015). *Étude de la Transition Colonnaire-Equiaxe dans les lingots et en coulée continue d’acier et influence du mouvement des grains*. PhD thesis, Université de Lorraine.
- [Liu et al., 2013] Liu, D., Bu, C., and Chen, X. (2013). Development and test of cfd–dem model for complex geometry: A coupling algorithm for fluent and dem. *Computers & Chemical Engineering*, 58:260–268.
- [Lubachevsky and Stillinger, 1990] Lubachevsky, B. D. and Stillinger, F. H. (1990). Geometric properties of random disk packings. *Journal of statistical Physics*, 60(5-6):561–583.
- [Mahmoud et al., 2008] Mahmoud, A., Fernandez, A., and Arlabosse, P. (2008). *Analysis of Electrical Phenomena Occurring in Thermally Assisted Mechanical Dewatering Processes (TAMD)-a Preliminary Study*. INTECH Open Access Publisher.
- [Malinouskaya et al., 2009] Malinouskaya, I., Mourzenko, V., Thovert, J.-F., and Adler, P. (2009). Random packings of spiky particles: Geometry and transport properties. *Physical Review E*, 80(1):011304.
- [Man et al., 2005] Man, W., Donev, A., Stillinger, F. H., Sullivan, M. T., Russel, W. B., Heeger, D., Inati, S., Torquato, S., and Chaikin, P. M. (2005). Experiments on random packings of ellipsoids. *Phys. Rev. Lett.*, 94:198001.
- [Mazet, 1995] Mazet, T. (1995). *Etude des structures de solidification et des ségrégations dans les lingots d’acier*. PhD thesis, Vandoeuvre-lès-Nancy, INPL.
- [Meyer et al., 2010] Meyer, S., Song, C., Jin, Y., Wang, K., and Makse, H. A. (2010). Jamming in two-dimensional packings. *Physica A: Statistical Mechanics and its Applications*, 389(22):5137–5144.
- [Mickel et al., 2013] Mickel, W., Kapfer, S. C., Schröder-Turk, G. E., and Mecke, K. (2013). Shortcomings of the bond orientational order parameters for the analysis of disordered particulate matter. *Journal of Chemical Physics* 138.4 (2013).
- [Mikhailov and Freire, 2013] Mikhailov, M. and Freire, A. S. (2013). The drag coefficient of a sphere an approximation using shanks transform. *Powder technology*, 237:432–435.
- [Mueller, 1992] Mueller, G. E. (1992). Radial void fraction distributions in randomly packed fixed beds of uniformly sized spheres in cylindrical containers. *Powder technology*, 72(3):269–275.
- [Mueller, 1993] Mueller, G. E. (1993). Angular void fraction distributions in randomly packed fixed beds of uniformly sized spheres in cylindrical containers. *Powder technology*, 77(3):313–319.

- [Nguyen et al., 2014] Nguyen, D.-H., Azéma, É., Radjai, F., and Sornay, P. (2014). Effect of size polydispersity versus particle shape in dense granular media. *Physical Review E*, 90(1):012202.
- [Nowak et al., 1998] Nowak, E. R., Knight, J. B., Ben-Naim, E., Jaeger, H. M., and Nagel, S. R. (1998). Density fluctuations in vibrated granular materials. *Physical Review E*, 57(2):1971.
- [Onoda and Liniger, 1990] Onoda, G. Y. and Liniger, E. G. (1990). Random loose packings of uniform spheres and the dilatancy onset. *Physical Review Letters*, 64(22):2727.
- [O’Reilly, 2013] O’Reilly, O. M. (2013). *Engineering dynamics: a primer*. Springer Science & Business Media.
- [Papanikolaou et al., 2013] Papanikolaou, S., O’Hern, C. S., and Shattuck, M. D. (2013). Isostaticity at Frictional Jamming. *Phys. Rev. Lett.*, 110:198002.
- [Pasha et al., 2016] Pasha, M., Hare, C., Ghadiri, M., Gunadi, A., and Piccione, P. M. (2016). Effect of particle shape on flow in discrete element method simulation of a rotary batch seed coater. *Powder Technology*, 296:29–36.
- [Pedrotti, 2012] Pedrotti, L. S. (2012). Basic geometrical optics. *Fundamentals of photonics*.
- [Peskin, 2002] Peskin, C. S. (2002). The immersed boundary method. *Acta numerica*, 11:479–517.
- [Pickard, 2010] Pickard, C. J. (2010). MS Windows NT kernel description. <http://www.tcm.phy.cam.ac.uk/~cjp20/old/lectures/topic2.pdf>. Accessed: 2016-01-28.
- [Pickering, 2013] Pickering, E. J. (2013). Macroseggregation in steel ingots: the applicability of modelling and characterisation techniques. *ISIJ international*, 53(6):935–949.
- [Reddy and Beckermann, 1995] Reddy, A. and Beckermann, C. (1995). ‘simulation of the effects of thermosolutal convection, shrinkage induced flow, and solid transport on macroseggregation and equiaxed grain size distribution in a dc continuous cast al-cu round ingot. *Materials Processing in the Computer Age II*, pages 89–102.
- [Rycroft, 2009] Rycroft, C. (2009). Voro++: A three-dimensional voronoi cell library in c++. *Lawrence Berkeley National Laboratory*.
- [Salvo et al., 2012] Salvo, L., Di Michiel, M., Scheel, M., Lhuissier, P., Mireux, B., and Suéry, M. (2012). Ultra fast in situ x-ray micro-tomography: Application to solidification of aluminium alloys. In *Materials science forum*, volume 706, pages 1713–1718. Trans Tech Publ.
- [Sánchez and Scheeres, 2016] Sánchez, D. and Scheeres, D. (2016). Angles of repose of granular beds using a soft-sphere discrete element method (ssdem). In *Lunar and Planetary Science Conference*, volume 47, page 1230.

-
- [Schröter et al., 2005] Schröter, M., Goldman, D. I., and Swinney, H. L. (2005). Stationary state volume fluctuations in a granular medium. *Phys. Rev. E*, 71:030301.
- [Scott and Kilgour, 1969] Scott, G. and Kilgour, D. (1969). The density of random close packing of spheres. *Journal of Physics D: Applied Physics*, 2(6):863.
- [Shoemaker, 1985] Shoemaker, K. (1985). Animating rotation with quaternion curves. In *ACM SIGGRAPH computer graphics*, volume 19, pages 245–254. ACM.
- [Silbert, 2010] Silbert, L. E. (2010). Jamming of frictional spheres and random loose packing. *Soft Matter*, 6(13):2918–2924.
- [Song et al., 2008] Song, C., Wang, P., and Makse, H. A. (2008). A phase diagram for jammed matter. *Nature*, 453(7195):629–632.
- [Souhar et al., 2016] Souhar, Y., De Felice, V. F., Beckermann, C., Combeau, H., and Založnik, M. (2016). Three-dimensional mesoscopic modeling of equiaxed dendritic solidification of a binary alloy. *Computational Materials Science*, 112:304–317.
- [Sperl, 2006] Sperl, M. (2006). Experiments on corn pressure in silo cells—translation and comment of janssen’s paper from 1895. *Granular Matter*, 8(2):59–65.
- [Steinbach, 2013] Steinbach, I. (2013). Why solidification? why phase-field? *JOM*, 65(9):1096–1102.
- [Sun and Xiao, 2016] Sun, R. and Xiao, H. (2016). Sedifoam: A general-purpose, open-source cfd–dem solver for particle-laden flow with emphasis on sediment transport. *Computers & Geosciences*, 89:207–219.
- [Suzuki and Taniguchi, 1981] Suzuki, K. and Taniguchi, K. (1981). The mechanism of reducing “a” segregates in steel ingots. *Transactions of the Iron and Steel Institute of Japan*, 21(4):235–242.
- [Tayeb et al., 2016] Tayeb, R., Dou, X., Mao, Y., and Zhang, Y. (2016). Analysis of cohesive microsized particle packing structure using history-dependent contact models. *Journal of Manufacturing Science and Engineering*, 138(4):041005.
- [Torquato and Stillinger, 2010] Torquato, S. and Stillinger, F. H. (2010). Jammed hard-particle packings: From kepler to bernal and beyond. *Rev. Mod. Phys.*, 82:2633–2672.
- [Torquato et al., 2000] Torquato, S., Truskett, T. M., and Debenedetti, P. G. (2000). Is random close packing of spheres well defined? *Phys. Rev. Lett.*, 84:2064–2067.
- [Villarruel et al., 2000] Villarruel, F. X., Lauderdale, B. E., Mueth, D. M., and Jaeger, H. M. (2000). Compaction of rods: relaxation and ordering in vibrated, anisotropic granular material. *Physical Review E*, 61(6):6914.

- [Vreeman et al., 2000] Vreeman, C. J., Krane, M. J. M., and Incropera, F. P. (2000). The effect of free-floating dendrites and convection on macrosegregation in direct chill cast aluminum alloys: Part i: model development. *International Journal of Heat and Mass Transfer*, 43(5):677–686.
- [Vreeman and Krane, 2002] Vreeman, Schloz, J. D. and Krane, M. J. M. (2002). Direct chill casting of aluminum alloys: Modeling and experiments on industrial scale ingots.
- [Wachs et al., 2012a] Wachs, A., Girolami, L., Vinay, G., and Ferrer, G. (2012a). Grains3d, a flexible {DEM} approach for particles of arbitrary convex shape — part i: Numerical model and validations. *Powder Technology*, 224:374 – 389.
- [Wachs et al., 2012b] Wachs, A., Girolami, L., Vinay, G., and Ferrer, G. (2012b). Grains3d, a flexible dem approach for particles of arbitrary convex shape—part i: Numerical model and validations. *Powder Technology*, 224:374–389.
- [Wang et al., 2005] Wang, T., Wu, M., Ludwig, A., Abondano, M., Pustal, B., and Bu «hrig-Polaczek, A. (2005). Modelling the thermosolutal convection, shrinkage flow and grain movement of globular equiaxed solidification using a three phase model. *International Journal of Cast Metals Research*, 18(4):221–228.
- [Wang et al., 2014] Wang, X., Shu, C., Wu, J., and Yang, L. (2014). An efficient boundary condition-implemented immersed boundary-lattice boltzmann method for simulation of 3d incompressible viscous flows. *Computers & Fluids*, 100:165–175.
- [Wu et al., 2014] Wu, C., Ayeni, O., Berrouk, A., and Nandakumar, K. (2014). Parallel algorithms for cfd–dem modeling of dense particulate flows. *Chemical Engineering Science*, 118:221–244.
- [Yang et al., 2007] Yang, R., Zou, R., Dong, K., An, X., and Yu, A. (2007). Simulation of the packing of cohesive particles. *Computer physics communications*, 177(1):206–209.
- [Yuan et al., 2012] Yuan, L., O’Sullivan, C., and Gourlay, C. (2012). Exploring dendrite coherency with the discrete element method. *Acta Materialia*, 60(3):1334–1345.
- [Založnik et al., 2011a] Založnik, M., Kumar, A., Combeau, H., Bedel, M., Jarry, P., and Waz, E. (2011a). Influence of transport mechanisms on macrosegregation formation in direct chill cast industrial scale aluminum alloy ingots. *Advanced Engineering Materials*, 13(7):570–580.
- [Založnik et al., 2011b] Založnik, M., Kumar, A., Combeau, H., Bedel, M., Jarry, P., and Waz, E. (2011b). Influence of transport mechanisms on macrosegregation formation in direct chill cast industrial scale aluminum alloy ingots. *Advanced Engineering Materials*, 13(7):570–580.
- [Zhao and van Wachem, 2013] Zhao, F. and van Wachem, B. (2013). A novel quaternion integration approach for describing the behaviour of non-spherical particles. *Acta Mechanica*, 224(12):3091–3109.

-
- [Zhao and Shan, 2013] Zhao, J. and Shan, T. (2013). Coupled cfd–dem simulation of fluid–particle interaction in geomechanics. *Powder technology*, 239:248–258.
- [Zhong et al., 2016] Zhong, W., Yu, A., Liu, X., Tong, Z., and Zhang, H. (2016). Dem/cfd-dem modelling of non-spherical particulate systems: theoretical developments and applications. *Powder Technology*, 302:108–152.
- [Zou and Yu, 1996] Zou, R. and Yu, A. (1996). Evaluation of the packing characteristics of mono-sized non-spherical particles. *Powder technology*, 88(1):71–79.

Abstract

Multiphase multiscale modeling of solidification of metal alloys is based on the combination of phenomena at the macroscopic scale of the product and at the microscopic scale of the solidification structures. The microscopic phenomena are incorporated via auxiliary microscopic models whose quality can remarkably affect the quality of the whole solidification modeling. This is the case for the phenomenon of equiaxed grain packing. In this thesis, the random packing of typical equiaxed grain morphologies in metal alloy solidification is investigated. The free-floating solid equiaxed grains, nucleated in the melt, sediment and pack driven by a low solid-liquid density difference. Firstly, we highlight the hydrodynamic dimensionless parameters governing the grain packing in the melt: the Stokes number, St , the Archimedes number, Ar , and the growth-to-motion ratio, Γ . Subsequently, an experimental setup is designed in order to investigate the influence of the equiaxed grain geometry and the hydrodynamic conditions on the average solid packing fraction. Two spherical and dendritic grain collections are experimentally investigated in conditions hydrodynamically similar to conditions encountered in solidification of metal alloys. Additionally, a numerical Discrete Element Method tool is developed to complement the experimental work by accessing to those granular variables which are difficult to obtain experimentally, such as the local packing fraction, the contacting neighbors and the particle orientation. The influence of the grain morphology on the packing fraction is found to be much more important than that of the hydrodynamic conditions, interparticle friction or grain size polydispersity. Packing fractions between approximately 0.53 and 0.67 are measured and computed for the spherical noncohesive grains, for different hydrodynamic, frictional and polydispersity conditions, whereas values down to approximately 0.30 are found for noncohesive dendrite envelopes. Besides, a numerical tool based on a geometrical packing is used to determine the packing fraction in case of very cohesive grains. In this case, the packing fraction could decrease down to approximately 0.27 and 0.15 for spheres and dendrites, respectively. Finally, we investigate the packing dynamics, which is the transition from a sedimentation regime to the mechanical equilibrium (packing). The evolution of the local solid fraction, contacting neighbors, mechanical contacts and grain orientation are given which showed that the hydrodynamic condition is the more influential on the packing dynamics than the grain morphology: faster packing dynamics is found for higher values of St number.

Keywords: metal alloy solidification, granular media, Discrete Element Method (DEM), nonconvex grain packing, hydrodynamic similarity.

Résumé

La modélisation multi-échelle multi-physique de la solidification d'alliages métalliques demande de combiner des phénomènes à l'échelle macroscopique du produit et microscopiques à l'échelle des structures de solidification. La qualité de la description des phénomènes microscopiques peut affecter notablement la qualité de la modélisation de la solidification. C'est le cas du phénomène d'empilement de grains équiaxes. Dans cette thèse, l'empilement aléatoire des grains équiaxes avec des morphologies typiques de solidification est étudié. La sédimentation des grains dendritiques est le résultat d'une faible différence de densité entre les phases solide et liquide. Nous mettons tout d'abord en évidence les paramètres hydrodynamiques adimensionnels qui régissent l'empilement de grains équiaxes : le nombre de Stokes, St , le nombre d'Archimède, Ar , et le rapport entre le temps caractéristique de la croissance et le temps caractéristique du mouvement, Γ . Un dispositif expérimental a été conçu afin d'étudier l'influence de la géométrie des grains équiaxes et l'influence des conditions hydrodynamiques sur la fraction d'empilement. Deux collections de grains sphériques et dendritiques ont été étudiées. En outre, un outil numérique basé sur la méthode des éléments discrets a été développé pour compléter le travail expérimental de détermination de : la fraction d'empilement locale, le nombre de particules voisines en contact et l'orientation des particules. Nous avons pu montrer que l'influence de la morphologie des grains sur la fraction d'empilement est beaucoup plus importante que l'influence des conditions hydrodynamiques, du frottement entre particules ou de la poly-dispersité des grains. Des fractions d'empilement entre environ 0,53 et 0,67 ont été mesurées et calculées pour les grains sphériques non-cohésifs, pour différentes conditions hydrodynamiques, de frottement et de poly-dispersité, alors que des valeurs allant jusqu'à environ 0,30 sont trouvées pour les grains dendritiques non-cohésifs. En outre, un outil numérique basé sur l'empilement géométrique a été développé pour déterminer la fraction d'empilement en cas de grains très cohésifs. Dans ce cas, la fraction d'empilement pourrait diminuer à environ 0.27 et 0.15 pour les sphères et les dendrites, respectivement. Enfin, nous étudions la dynamique de l'empilement, qui est la transition d'un régime de sédimentation à l'équilibre mécanique (empilement). L'évolution des variables comme par exemple, la fraction locale de solide, le nombre de particules voisines en contact, le nombre de contacts mécaniques et l'orientation du grain en fonction du temps est présentée. Ce qui a permis de montrer que l'influence des conditions hydrodynamiques est plus importante que l'influence de la morphologie des grains pour la dynamique d'empilement : une dynamique plus rapide est trouvée avec des valeurs du nombre de St plus élevées.

Mots-clés: solidification des alliages métalliques, milieux granulaires, Méthode des Éléments Discrets (DEM), empilement de particules non-convexes, similitude hydrodynamique.